Dynamic Plasmonic Metasurfaces in the Visible Spectrum

Richard Bartholomew

Department of Engineering
University of Cambridge

This dissertation is submitted for the degree of
Doctor of Philosophy

Jesus College

October 2017

Dynamic Plasmonic Metasurfaces in the Visible Spectrum

Richard Bartholomew

As visual display technologies move closer to producing true three dimensional displays, pixel technologies need to be ever smaller and more functional to keep pushing the boundaries. Plasmonic metasurfaces have been shown to control the phase, amplitude and/or polarisation of incoming electromagnetic radiation. Nano-fabrication advancements have resulted in the fabrication of the building blocks of such metasurfaces at nano-scale dimensions, allowing the surfaces to interact with visible light, opening up applications in visual displays. As pixel sizes shrink, smaller colour filters will be required. The excitation of plasmonic resonances in metallic nano-structure arrays have resulted in colour filters an order of magnitude smaller than what is currently commercially available. As colour filters, plasmonic metasurfaces offer numerous advantages over pigment-based colour filters used in modern commercial liquid crystal (LC) displays, including environmental, size and longevity factors. Furthermore, exploiting the wavelength and polarisation dependant scattering of nano-structures, optical components, including lenses, waveplates and holograms containing sub-wavelength pixels have been demonstrated in the visible wavelength spectrum. The metasurfaces are able to mould optical wavefronts into arbitrary shapes with sub-wavelength resolution by introducing spatial variations in the optical response of the light scatterers. The applications demonstrated so far are, on the whole, static devices, that is to say their optical properties may not be altered post fabrication. To realise the full potential of plasmonic metasurfaces to visual applications the devices must be made active. By activating structural colour surfaces, not only may pixel densities potentially be increased simply by removing the need for separate red, green and blue filters, but a new class of high definition ultra-thin display devices may be accessible, whilst the dynamic manipulation of the wavelength and polarisation properties of nano-scattering elements would open up the possibilities to create sub-wavelength holographic pixels. This thesis investigates ways to activate static metasurfaces for colour, flat optic, and holographic applications.

First, methods of dynamic control of the structural colour of plasmonic nano-hole arrays are investigated. By combining nano-hole arrays with liquid crystals, transmissive electrically tunable LC-nanohole pixels operating across the visible spectrum with un-polarised input light are experimentally demonstrated. An output analyser in combination with a nematic LC layer enables pixel colour to be electronically controlled through an applied voltage across the device, where LC re-orientation leads to tunable mixing of the relative contributions from the plasmonic colour input. Furthermore, exploiting the strong surface anchoring effects between an aluminium surface and LC molecules a twisted nematic LC cell, using a metallic grating as a combined colour filter, electrode and alignment layer, was shown to act a variable amplitude colour filter. The colour of these pixels was improved greatly utilising a grating-insulator-grating structure unique to this work.

Second, a new process for fabricating aluminium nano-rod structures embedded in an elastomeric medium, with high spatial accuracy, is presented. The process is used to create nano-rod plasmonic resonator arrays whose optical properties may be altered by mechanical deformation. The pattern transfer process is further utilised to create dynamic optical elements, including nano-rod arrays for colour filters, tunable focal length Fresnel zone plates and photon sieves, and stretchable holograms with dynamic replay fields.

Declaration

I hereby declare that except where specific reference is made to the work of others, the contents of this dissertation are original and have not been submitted in whole or in part for consideration for any other degree or qualification in this, or any other university. This dissertation is my own work and contains nothing which is the outcome of work done in collaboration with others, except as specified in the text and Acknowledgements. This dissertation contains fewer than 65,000 words including appendices, bibliography, footnotes, tables and equations and has fewer than 150 figures.

Richard Bartholomew
October 2017

Acknowledgements

I would like to acknowledge the help I have received from my fellow CMMPE group PhDs, in particular, Calum Williams for his help advice and knowledge and Ammar Khan for taking the time to teach me how to fabricate cells and general willingness to assist with fabrication techniques no matter how left field.

I would like to also acknowledge my supervisor Prof. Tim Wilkinson for giving me the opportunity to indulge my academic curiosities after a long break.

EPSRC and the David and Susan Hibbitt Scholarship for the financial support.

Lastly I would like to thank the patience and support I have received from my wife, Cally, as well as the encouragement I have received to submit this thesis in a timely manner.

Abstract

As visual display technologies move closer to producing true three dimensional displays, pixel technologies need to be ever smaller and more functional to keep pushing the boundaries. Plasmonic metasurfaces have been shown to control the phase, amplitude and/or polarisation of incoming electromagnetic radiation. Nano-fabrication advancements have resulted in the fabrication of the building blocks of such metasurfaces at nano-scale dimensions, allowing the surfaces to interact with visible light, opening up applications in visual displays. As pixel sizes shrink, smaller colour filters will be required. The excitation of plasmonic resonances in metallic nano-structure arrays have resulted in colour filters an order of magnitude smaller than what is currently commercially available. As colour filters, plasmonic metasurfaces offer numerous advantages over pigment-based colour filters used in modern commercial liquid crystal (LC) displays, including environmental, size and longevity factors. Furthermore, exploiting the wavelength and polarisation dependant scattering of nano-structures, optical components, including lenses, waveplates and holograms containing sub-wavelength pixels have been demonstrated in the visible wavelength spectrum. The metasurfaces are able to mould optical wavefronts into arbitrary shapes with sub-wavelength resolution by introducing spatial variations in the optical response of the light scatterers. The applications demonstrated so far are, on the whole, static devices, that is to say their optical properties may not be altered post fabrication. To realise the full potential of plasmonic metasurfaces to visual applications the devices must be made active. By activating structural colour surfaces, not only may pixel densities potentially be increased simply by removing the need for separate red, green and blue filters, but a new class of high definition ultra-thin display devices may be accessible, whilst the dynamic manipulation of the wavelength and polarisation properties of nano-scattering elements would open up the possibilities to create sub-wavelength holographic pixels. This thesis investigates ways to activate static metasurfaces for colour, flat optic, and holographic applications.

First, methods of dynamic control of the structural colour of plasmonic nano-hole arrays are investigated. By combining nano-hole arrays with liquid crystals, transmissive electrically tunable LC-nanohole pixels operating across the visible spectrum with un-polarised input light are experimentally demonstrated. An output analyser in combination with a nematic LC layer enables pixel colour to be electronically controlled through an applied voltage across the device, where LC re-orientation leads to tunable mixing of the relative contributions from the plasmonic colour input. Furthermore, exploiting the strong surface anchoring effects between an aluminium surface and LC molecules a twisted nematic LC cell, using a metallic grating as a combined colour filter, electrode and alignment layer, was shown to act a variable amplitude colour filter. The colour of these pixels was improved greatly utilising a grating-insulator-grating structure unique to this work.

Second, a new process for fabricating aluminium nano-rod structures embedded in an elastomeric medium, with high spatial accuracy, is presented. The process is used to create nano-rod plasmonic resonator arrays whose optical properties may be altered by mechanical deformation. The pattern transfer process is further utilised to create dynamic optical elements, including nano-rod arrays for colour filters, tunable focal length Fresnel zone plates and photon sieves, and stretchable holograms with dynamic replay fields.

Publications

1. Richard Bartholomew, Calum Williams, Ammar Khan, Richard Bowman, and Timothy Wilkinson. Plasmonic nanohole electrodes for active color tunable liquid crystal transmissive pixels. *Optics Letters*, 42(14):2810, jul 2017

Table of contents

List of figures

List of tables

Acronyms & Symbols

Roman Symbols

Δn	birefringence
ϵ	electric permittivity
Γ	nano-structure size
$\hbar$	$h/2\pi$
Λ	nano-structure pitch
λ_{LSPR}	resonant LSPR wavelength
λ_{SPP}	resonant SPP wavelength
μ_p	dipole moment
ω	angular frequency
ω_p	plasma frequency
ω_{res}	resonance frequency
E_F	Fermi energy
h	Planck constant
k	wavevector
m_e	mass of electron
2D	two dimensional

3D	three dimensional
CAD	computer aided design
CGH	computer generates holograms
CNT	carbon nanotube
DC	duty cycle
EBL	electron beam lithography
EM	electro-magnetic
EOT	extraordinary optical transmission
FDTD	finite-difference time-domain
FFT	fast Fourier transform
FL	focal length
FT	Fourier transform
FZP	Fresnel zone plate
GIG	grating-insulator-grating
GMR	guided mode resonance
HCM	high-contrast metastructure
HSQ	hydrogen silsesquioxane
IFFT	inverse fast Fourier transform
IFT	inverse Fourier transform
IFTA	iterative Fourier transform algorithm
IPA	isopropyl-alcohol
IR	infrared
ITO	indium-tin-oxide

LC	liquid crystal
LC-NH	liquid crystal nano-hole
LCD	liquid crystal display
$LiNbO_3$	lithium niobate
LSPR	localised surface plasmon resonance
MEMS	microelectromechanical systems
MIM	metal-insulator-metal
MIR	mid-infrared
MRWG	metallic resonant waveguide grating
n	refractive index
n_e	refractive index extraordinary axis
n_o	refractive index ordinary axis
NA	numerical aperture
PDMS	Polydimethylsiloxane
PMMA	poly(methyl methacrylate)
PS	photon sieve
PVD	physical vapour deposition
RA	Rayleigh anomaly
SCF	subtractive colour filter
SEM	scanning electron microscope
SLM	spatial light modulator
SP	surface plasmon
SPP	surface plasmon polariton

SPR	surface plasmon resonance
SRR	split-ring resonator
TE	transverse electric
TM	transverse magnetic
TN	twisted nematic
TN-LC	twisted nematic liquid crystal
TN-NG	twisted nematic nano-grating

Chapter 1

Introduction

1.1 Motivation

The ultimate aim in the development of display technologies is to be able to create a device that can display *true* three dimensional (3D) images. That is to say the display should be able to fully replicate what we see in the world. Traditional display technologies lack depth perception, and hence lack a dimension making them two dimensional (2D) displays; they lack a third dimension of information.

The motivation for 3D display technology comes from the need for additional information that could be used in medical imaging, computer aided design (CAD), exploration techniques and many other applications and disciplines. Current mainstream 3D technology is not true 3D imaging, it currently exploits the way the human brain creates the 3D objective views we see. Using two offset images, one from each eye, the human brain combines the two to create the 3D perspective of the world that we see every day. This type of display is called stereoscopic, and can be implemented in various techniques using glasses[2–4] to ensure different images reach each eye. Another technique is auto-stereoscopic, using the same principle but without using glasses to project 2 different images into each eye, such as parallax barriers[5], lenticular sheets[4, 5] or prism masks [6]. These types of technology have drawbacks due to limited field of views, eye fatigue [7], vergence accommodation[8] (figure 1.1(b)), interocular cross talk and various other human limiting factors[9].

An ideal 3D display is one where the display screen is a window to a virtual object behind. A schematic of an ideal display is shown in figure 1.1(a). It should “provide

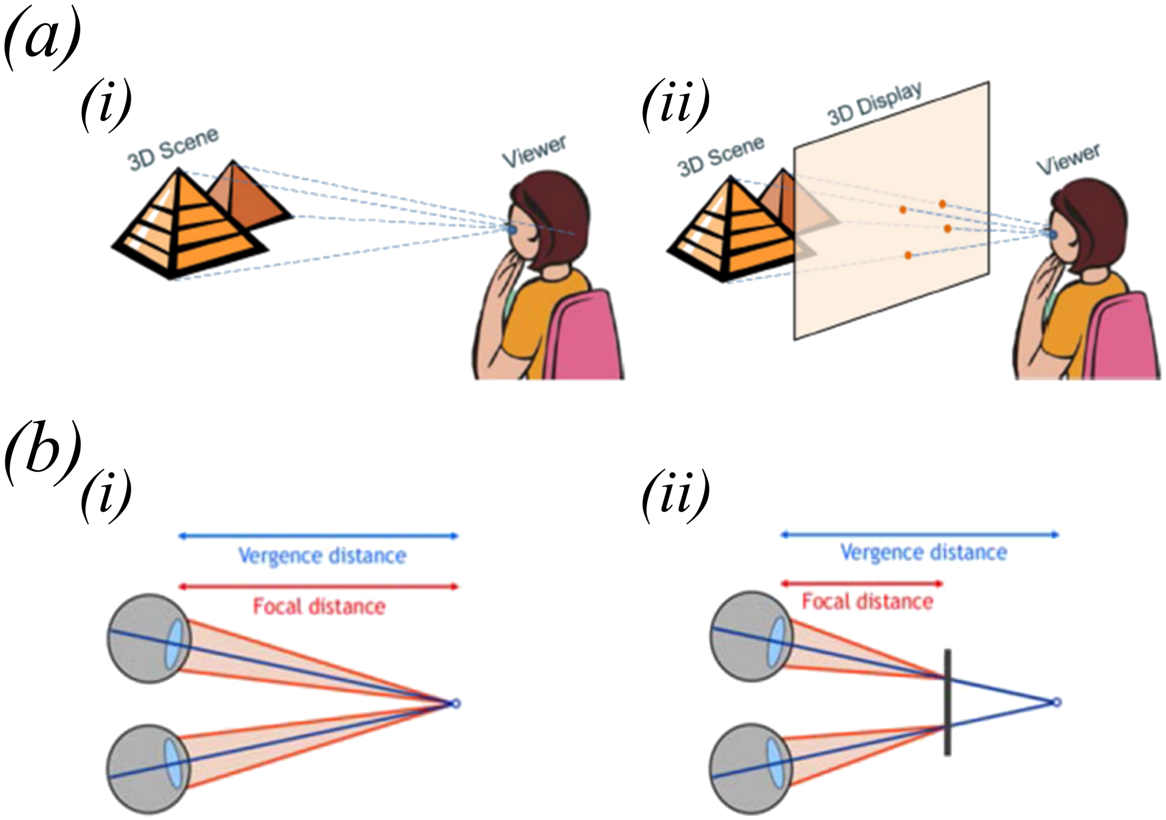

Figure. 1.1 Illustration of real and virtual objects, and vergence accommodation issues with 3D displays. (a) Illustration of (i) a person looking at an object and (ii) the same person viewing a virtual object through an ideal 3D display[10]. (b) Demonstration of (i)no vergence accommodation conflict and (ii) vergence accommodation conflict with a 3D display[8]. Figures adapted from references

high spatial resolution and depth perception with full depth cues including binocular disparity, motion parallax and ocular accommodation”[8].

One of the most promising technologies to create a 3D display is holography. Holography is the recreation of the phase and amplitude of a light wave front coming from an object using a physical diffraction pattern, known as a hologram. As such a hologram should be able to recreate the object such that there be no difference between what the human eye sees, whether looking at the object or the far field pattern of the hologram. However one of the major challenges that remains for holographic displays is reducing the pixel size[10, 8]. IMEC, a nano-electronic research company based in Belgium, have demonstrated a static poly-SiGe MEMS device with pixels of 500nm×500nm [11], whilst the CMMPE group at the University of Cambridge have demonstrated static holograms using optical nano-antennas with pixel pitch of 390nm[12].

It is the opinion of the author that plasmonic nano-structures offer the best route to achieving a *true* 3D display. In addition, plasmonic nano-structures can provide pathways to aid the miniaturisation of existing display technologies, opening up further opportunities for the development of high definition and 3D displays.

However, the technology in its present state is a long way away from achieving this goal. To be able to create an active display that comprises these nano-structures, one must be able to dynamically control their optical properties. The work in this thesis looks at potential means to dynamically control the optical properties of plasmonic metasurfaces, be it electronically, mechanically, thermally etc. such that they are able to be utilised in display devices for the visible spectrum, thus taking the first step, in what is a long journey, towards potentially using metasurface device in *true* 3D displays.

1.1.1 Dynamic plasmonic colour

As pixel sizes shrink, colour filters will need to too. Colour displays, such as emissive liquid crystal displays (LCDs), use pigment-based colour filters to absorb the complementary colours to produce red, green, and blue hues. Traditional pigment-based colour filters are however limited to printing dimensions of $\sim 10\mu$m. This is an order of magnitude higher that the theoretical diffraction limit of colour display optics. Yet even as the limits of fabrication technologies are pushed further, dye colourants suffer from fundamental limitations due to the low absorption coefficient of the dye material [13]. What is more, many of the pigments contain some toxic elements which could endanger the environment an give arise to disposal and recycling issues[13].

As we move towards higher-resolution imaging and displays, new innovations are needed to achieve higher resolution, lower power consumption and colour tunability in devices. Structural colour has been seen as a solution to these issues. Structural colour arises from the structural engineering of a device, such as diffraction optic devices, photonic crystals, and plasmonic structures. There are numerous examples of this type of colour in nature[14–16], typically due to the combined effects of thin film/multilayer interferences, grating diffraction, photonic crystals generating light scattering or partial absorption. To adapt the structural colour observed in nature into man-made optical devices, surface plasmon resonances (SPRs) have shown significant promise. The sub-wavelength nature of the plasmonic nano-structures not only make the elements ideal for high-resolution colour displays but also enable to the structure to be ultra-thin, easing the miniaturisation process. Utilising the various plasmonic modes which may arise at a metal-dielectric interface, plasmonic nano-structures have been shown to manipulate the intensity, phase, and polarisation of scattering light[17]. The majority of devices developed so far produce static colour. That is to say, once fabricated, the structural colour may not be altered. By activating these surfaces, not only may pixel density potentially be increased, simply by removing the need for separate red, green and blue filters, but a new class of high definition ultra-thin display devices may be accessible.

1.1.2 Dynamic plasmonic holographic elements

Conventional optical components designed to modify the wavefront of light, altering its phase, amplitude and polarisation in a desired manner, are based on refraction, reflection or diffraction of light. Typically wavefront shaping is achieved via propagation through media of given refractive indices that can be engineered to control the optical path of light beams. Secondary waves are created by diffractive optical components such as holograms, these waves propagate in air and interfere in the far-field to form complex patterns. A hologram is a physical structure, which, through diffraction, is able to record both the light and amplitude information of a light wave, in an intensity pattern[18]. In this way holograms may be used to reconstruct either 2D or 3D images.

Holography was first discovered in the 1940s by Gabor[19] and was achieved using light-sensitive materials which are used to encode an object interference fringe pattern in the recording materials surface topology[2]. Modern 3D holographic display technologies rely on spatial light modulators (SLMs), the two most common systems of which are Microelectromechanical (MEMS) and liquid crystal (LC) based. MEMS systems modulate the amplitude of the incoming wave and operate through arrays of tilting micro-mirrors, whilst LC devices, generally LC-on-Silicon (LCoS), use LCs to alter the phase of the wavefront. Due to their phase modulation capabilities, along with greater scalability, LCoS pixel elements provide the closest realisation of a *true* 3D holograph display, however commercially available SLM technologies consist of pixels over an order of magnitude larger than the diffraction limit. This restricts viewing angle, limits pixel density which combined with dispersive issues limit the quality and colour of the replay field image reconstructions[2].

Metasurfaces break our dependence on the propagation effect by introducing abrupt changes of optical properties. They can be made of arrays of nano-sized scatterers which, interacting with an incident light wave, form a spatially varying optical response moulding optical wavefronts into pre-determined shapes. Not only is the wavefront shaping accomplished by these nano-structures achieved within a distance much less than the wavelength from the interface but the sub-wavelength resolution of optical wavefronts makes it possible to funnel all incident optical power into a single useful beam while eliminating other diffraction orders circumventing the fundamental limitation of diffractive optical components, which typically produce multiple diffraction orders[20].

The optical properties of the nano-scatterers are wavelength and polarisation dependent[12]. The optical properties rely on the physical parameters of the scatterers such as size, shape, material and even proximity to other scatterers. Until now, like the structural colour structures previously discussed, the majority of these surfaces are static. In theory, the dynamic manipulation of the physical dimensions of a plasmonic metasurface will be able to tune the resonances of the sub-wavelength scattering elements. In this way a plasmonic metasurface would have the potential to act as a dynamic holographic element. For this to be achievable we must first find a way to fabricate the nano-structures in a way that allows the physical parameters for the meta-surface to be altered post fabrication.

1.1.3 Research Outlook

In summary, the use of plasmonic nano-structures for optical devices, including structural colour and flat optics, has been shown to shrink pixel sizes and lead to potential applications such as 3D displays. The majority of the devices presented in current literature are static. Should reliable methods be discovered to dynamically tune the optical properties these metasurfaces, it will open up the door to new and interesting display devices. The search for dynamic plasmonic devices continues, with ideas incorporating LC, electrochromic and mechanical deformation switching. In the cases where dynamic plasmonic devices have been fabricated, the devices typically operate in the infrared part of the electromagnetic (EM) spectrum, not the visible.

In this thesis, the work looks at *dynamic plasmonic metasurfaces in the visible range*, focusing on creating active colour pixels, and devising a method to dynamically manipulate the physical dimensions of plasmonic metasurfaces.

1.2 Structure of Thesis

The thesis compromises of a mixture of simulation, fabrication and characterisation work. A range of concepts and designs are proposed and investigated, based on the general rationale described previously. The structure of the thesis is as follows:

Chapter 2 presents the background information necessary for this work. First, the theory behind the physical mechanisms that occur in plasmonic metasurfaces are presented along with an overview of the science behind the applications to which plasmonics can be applied, starting with holography, leading onto liquid crystals and display pixel technology. Second, the current state of play of plasmonic metasurfaces has been summarised, looking at the most interesting and relevant results in the literature, highlighting the opportunities going forward.

Chapter 3 covers the methodologies for the simulation of EM waves interaction with nano-structures, and the fabrication and characterisation techniques used in this work. The simulation of nano-structures is performed using a commercial-grade simulator based on the finite-difference time-domain method[21]. The wider simulation of their applications (e.g. CGH), is performed using code written in MATLAB. The methods used to fabricated metallic nano-structures using electron beam lithography (EBL) and physical vapour deposition (PVD) on Si and on optically transparent substrates (e.g. glass) to operate in transmission are covered along with the construction of the fabricated structures into cells to be filled with liquid crystals. Lastly a pattern transfer process for the transfer of metallic nano-particles from a patterned chip to an elastomeric substrate with high spatial accuracy, developed in the course of this work and to be detailed in *chapter 5*, is summarised.

Chapter 4 looks at various methods of dynamic control of the structural colour of plasmonic nano-hole arrays. The devices described use plasmonic resonances to create structural colour. The structural colour of a plasmonic metasurface is a function of the physical dimensions of the nano-hole surface and the permittivities of the surrounding media and the metallic layer itself. The effects of altering these properties is discussed in detail along with methods of controlling the structural colour. The simulation, fabrication and characterisation of dynamic devices actively controlling the colour of light transmitted through plasmonic pixels are then presented.

The nano-hole arrays fabricated in an optically thin ($\sim$ 30nm) metallic layer were patterned on glass to allow the devices to operate in transmission. The metallic layer has the added advantage that it may act as an electrode to enable control of the pixel via application of an electric field to modulate the refractive index of the media surrounding the nano-structured layer. These include:

- *LC-nanohole continuously tunable device*[1] . Using an analyser, orientated at 45° to the nano-hole lattice in combination with a LC layer to filter the orthogonally-polarised plasmonic modes from a nano-hole layer, a liquid crystal nano-hole (LC-NH) device was created whose spectral output may be tuned across the visible spectrum.
- *LC twisted nematic cell integrated with a plasmonic grating.* Strong surface anchoring effects between an aluminium surface and LC molecules may be exploited to create a twisted nematic LC cell using a metallic grating as a combined colour filter, electrode and alignment layer. Utilising the nano-scale metallic grating as one half of a twisted nematic liquid crystal cell, it is possible to construct a plasmonic pixel which may switch between light and dark states when placed between crossed polarisers. The colour achieved with a nano-scale grating may be improved by introducing a second grating, separated from the first by a polymer layer.
- *Nano-hole on electro-optic substrates* The potential of dynamically tuning the plasmonic resonance of a metallic nano-hole layer utilising an electro-optic substrate is investigated. An electro-optic substrate is one whose refractive index may be modified with application of an electric field.

Chapter 5 presents a process for fabricating aluminium nano-rod structures embedded in PDMS, with high spatial accuracy, unique to this body of work. The process

---

[1] This work was published in Optics Letters Jul '17, "Plasmonic nanohole electrodes for active color tunable liquid crystal transmissive pixels"

builds on and simplifies similar existing pattern transfer processes. Furthermore the method can be used to transfer nano-particles down to 100nm in size with a pitch as low as 200nm.

The process is used to create nano-rod structures whose optical properties may be altered by mechanical deformation:

- *Dynamic plasmonic colour pixel by mechanical deformation.* Structural colour pixels whose colour changes under an applied strain.
- *Dynamic plasmonic lens.* Tunable focal length Fresnel zone plates and photon sieve, consisting of nano-rods embedded in PDMS.
- *Stretchable holograms.* Using aluminium nano-rods as the fundamental scattering element of the hologram pixels, the size of pixels in the replay field have an inversely proportional relationship to those in the hologram. Hence when a positive strain is applied to the hologram the replay field shrinks in size. The ability to fabricate plasmonic holograms in an elastomeric medium opens up a myriad of opportunities to develop holograms whose replay field may change when the hologram is physically stretched, due to the wavelength, polarisation and proximity dependence of the plasmonic resonance of the nano-rods.

Chapter 6 concludes the thesis with an overview of the main findings from the work, highlights some areas requiring further development, and describes some interesting avenues for further work.

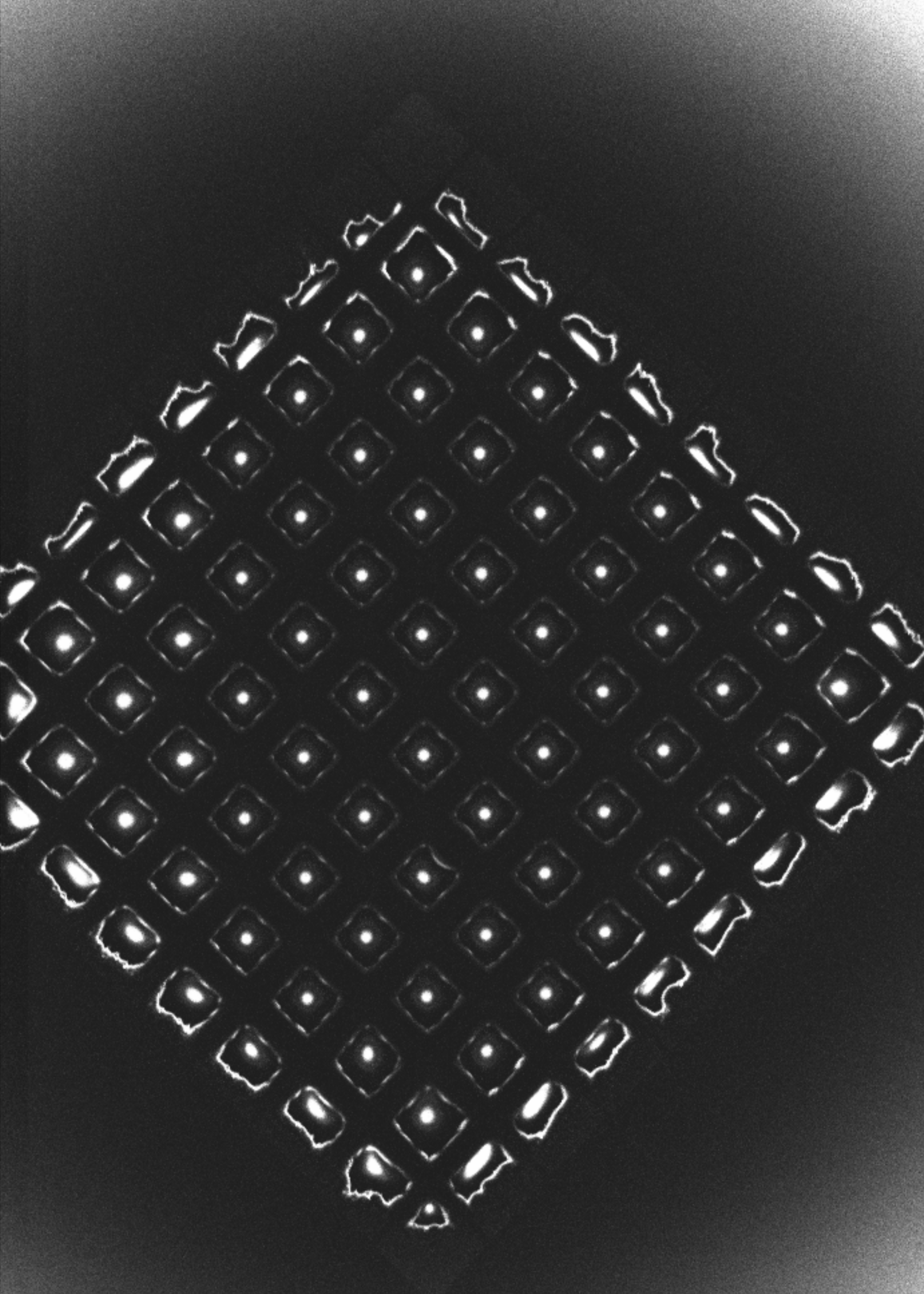

Chapter 2

Background

Introduction

It is important to understand the fundamentals of various aspects of the work presented in later chapters and to see where the work sits within the wider field of research into *plasmonic metasurfaces*. First this chapter presents theory behind the physical mechanisms that occur in plasmonic metasurfaces and then provides an overview of the science behind the applications to which plasmonics can be applied, starting with holography and leading onto liquid crystals and display pixel technology. Second this chapter summaries the current state of play of plasmonic metasurfaces, looking at the most interesting results in the literature, and highlighting some opportunities going forward.

2.1 Theory

2.1.1 Plasmonics

2.1.1.1 Surface plasmons

At the heart of any plasmonic metasurface are surface plasmons (SPs). The oscillations of the electron cloud in the surface of a metal at a metal-dielectric interface when excited by an applied electromagnetic (EM) field are referred to as SPs. The electrons in the surface of the metal respond to the EM field by collectively resonating. This resonant interaction between EM field and surface charge gives rise to unique properties originating from the characteristic dielectric response of metals at visible frequencies[22]. In the case where the oscillations propagate along a metal-dielectric or metal-air interface, this EM wave propagation is referred to as *surface plasmon polaritons* (SPP), referring to both the oscillating charge (SP) and the EM wave (Polariton). In the case where the oscillations are confined to an individual nano-structure they are referred to as *localised surface plasmon resonances* (LSPRs).

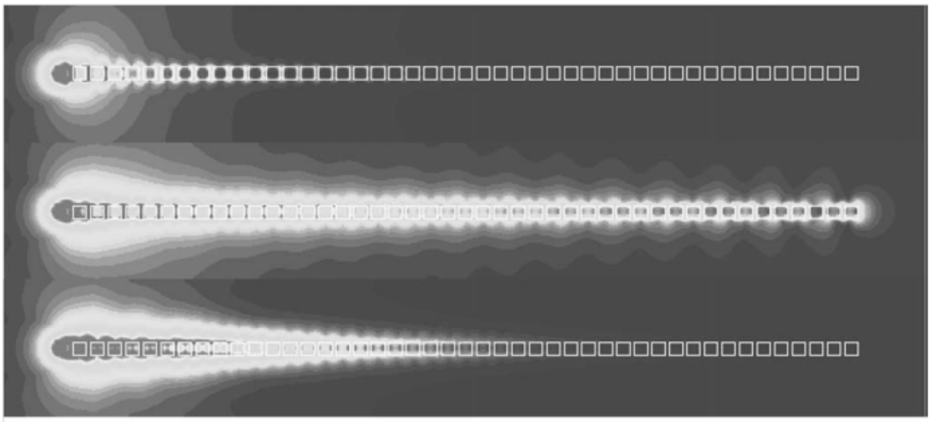

Figure. 2.1 Example of SPP field transmission. Electric-field distribution around nano-particle plasmon waveguides consisting of cubic 50nm Ag nano-particles in air excited using a longitudinally polarised point-dipole located to the left of the waveguide at $\lambda = 500$nm (top), 429nm (centre), and 390nm (bottom). In the case of resonant excitation of the interparticle-gap mode at 429nm, the energy is efficiently guided along the array. Image from [23]

In the case of nano-rods it is the LSPR that enhances near field intensities of an applied EM field as well as being accompanied by resonantly enhanced polarisability and enhanced scattering and absorption. Given that the nano-rods are small deposits of metal, the size and shape of the metal nano-particle have a large effect in restricting the oscillations of the SPs and hence the wavelength response of the nano-rods.

The oscillations of the electrons have been described or modelled in a variety of ways:

Mie theory

The response of a homogenous sphere to plane-wave illumination is analytically described in the framework of Mie theory, the solution to which describes the scattering of the EM wave in the form of an infinite series of vector spherical harmonics[22].

When applied to sub-wavelength particles, only the first-order dipolar term needs to be considered[24].

Consider a sphere of polarisable material with radius r and dielectric constant ϵ, embedded in a medium with dielectric constant ϵ_{env}, under the influence of a static electric field E_0. The dipole moment induced in the sphere by the external field can be written as[24]

$$\mu_p = 4\pi r^3 \epsilon_0 \frac{\epsilon - \epsilon_{env}}{\epsilon + 2\epsilon_{env}} E_0 \tag{2.1}$$

When $\epsilon_{env} = 1$ the dipole moment tends towards ∞ and hence the expression demonstrates a resonance when the real part of ϵ approaches -2.

If we now consider a plane wave with wavelength λ_0, incident upon a very small spherical metallic nano-particle such that $r \ll \lambda_0$, the external field can be considered constant over the particle. In this quasistatic approximation the phase is also constant over the particle and retardation effects can be neglected, and hence equation 2.1 is still valid. Furthermore, as we are considering the case of a metallic nano-particle, the dielectric constant ϵ is replaced by a complex dispersive material model with $\epsilon(\omega) = \epsilon'(\omega) + i\epsilon''(\omega)$. Resonance still occurs when the real part of the dielectric constant, ϵ', tends to -2. This condition is met in the visible range for the metals Au, Ag and Cu, and in the near-ultraviolet for Al. On resonance, the vanishing real part of the denominator of equation 2.1 leads to a strongly increased induced dipole moment and therefore to enhanced local fields and scattering. However, due to the spectral position of the interband transitions, particles consisting of different materials still show different optical properties[22], and are therefore suitable for applications in different spectral regimes.

Nano-particles are rarely spherical. If we now consider the plasmonic resonances of elongated prolate particles, we are interested in charge oscillations along the main axis (length d) of such an ellipsoid. Quantitatively, by transforming 2.1 one can obtain the induced dipole moment of a prolate ellipsoid of volume V, being the prototype of an elongated particle, which reads as[24]

$$\mu_p = V\epsilon_0 \frac{\epsilon - \epsilon_{env}}{P_j\epsilon + (1 - P_j)\epsilon_{env}} E_0 \tag{2.2}$$

Here P_j is a function of the aspect ratio, R, (the ratio of the long axis radius, $d/2$, to the short axis radius r) of the ellipsoid. A detailed analysis of 2.2 shows that the resonance depends approximately linearly on the aspect ratio, such that an increased aspect ratio leads to a red-shift of the resonance[24].

Mass and spring model

In the mass and spring model the plasmon resonance is represented as a simple mass-and-spring model with a resonant frequency of $\omega_{res} = (\frac{D}{m})^{\frac{1}{2}}$ where D and m are the elastic constants of the restoring force and the total effective mass of the electron system respectively[22].

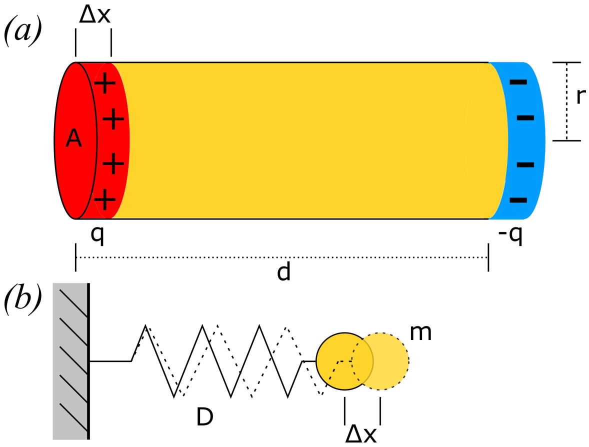

Figure. 2.2 Mass-and-spring model for plasmonic resonances. (a) Sketch of a plasmonic particle whose electron cloud has been displaced by Δx. The resulting positive and negative charge at the ends are treated as point-like charges that possess potential energy due to Coulomb interaction. (b) The resulting oscillation can be modelled by an effective spring constant D and the effective mass m of the moving electron cloud. Figure reproduced from [22].

To estimate the restoring force we consider a cylindrical nano-rod, in which the electron cloud has been displaced by Δx. When the electron cloud has been displaced, opposite point charges $\pm q$ build up at both ends whose magnitude depends on the charge carrier density n and the cross sectional area of the nano-rod, A, such that $q = neA\Delta x$, where e is the elementary charge of an electron. The coulomb potential energy, W, of the two charges is then

$$W(\Delta x) = \frac{1}{4\pi\epsilon_0}\frac{q^2}{d} = \frac{1}{4\pi\epsilon_0}\frac{(neA)^2}{d}\Delta x^2 \tag{2.3}$$

The restoring force can now be determined as

$$F(\Delta x) = \frac{-\delta W(\Delta x)}{\delta \Delta x} = \frac{-1}{2\pi\epsilon_0}(ne)^2\frac{A^2}{d}\Delta x = -D\Delta x \tag{2.4}$$

from which the spring constant D is obtained. The linear relationship between the displacement and the resulting force leads to oscillations in the system. The total effective mass of the system, is the mass of the electron cloud, which is given, by $m = nm_e Ad$, where m_e is the effective electron mass.

Therefore we obtain the approximate resonance frequency of the SP of an elongated particle

$$\omega_{res} = \frac{\omega_p}{2\sqrt{2}}\frac{1}{R} \tag{2.5}$$

where we have now substituted, the aspect ratio, $R = \frac{d}{2r}$, and the plasma frequency, $\omega_p^2 = ne^2/(\epsilon_0 m_e)$, as well as the area, $A = \pi r^2$. This model assumes the charges are point-like, which means that we cannot expect the result to reproduce the exact frequencies for shorter and thicker antenna, however it does demonstrate that the resonance is inversely proportional to the aspect ratio, R, the physical reason for which lies in the fact that the electric field of the charge distribution has a dipolar character.

In a spring, potential energy is transferred into kinetic energy and then back again. In comparison, when the EM mode oscillates inside a resonator, in cases where the size of the nano-rod is larger than that of the wavelength, every half period the energy is transferred from the electric field energy $u_E \approx \frac{1}{2}\epsilon E^2$ to the magnetic field energy $u_H \approx \frac{1}{2}\mu H^2$ and back, where μ is the permeability. Solving Maxwell's equation at this scale gives $u_E = u_H$ and energy is conserved while being transferred from one form to another[25]. However, from Maxwell's equations, it also follows that in truly sub-λ mode, when the nano-rod is smaller than $\frac{\lambda}{2}$n, where n is the refractive index, the magnetic energy is much smaller than the electric energy, which makes self-sustaining oscillations impossible as expected from the diffraction limit[25]. If, however, one introduces free carriers into the mode, the energy can also be stored in the form of kinetic energy $u_K \approx \frac{1}{2}\epsilon(\omega_p^2/\omega^2)E^2$ (here ϵ_0 is the vacuum permittivity, ω is frequency, and ω_p is the plasma frequency that for noble metals lies in the ultraviolet). Thus, depending on the exact geometry, the energy balance $u_H + u_K = u_E$ can be restored at certain frequencies ω_{res} (typically on the scale of a fraction of ω_p), precisely the frequencies of sub-λ SPPs. Free carriers may be used to exceed the diffraction limit, however, unlike when $d > \lambda$ and energy is conserved, almost half of the time the energy is stored in the form of kinetic energy, and therefore it is lost at the rate that is comparable with the rate of scattering of electrons in metal, γ, which is on the scale of 10 fs[22, 26]. Thus, once the optical mode becomes sub-λ in all three dimensions, independent of its shape, the SPP energy will be lost on the 10-fs scale.

Coupling surface plasmons

If we now consider, rather than a metallic nano-particle, a continuous metal-dielectric interface. As opposed to being confined the charge oscillations may now propagate and are thus SPPs. The simplest system supporting these collective oscillations is an infinite flat metallic surface. Assuming we have a dielectric with positive permittivity ϵ_1 and a metal with negative real permittivity ϵ_2, for simplicity sake we ignore any losses at this stage. The E-field vector of the incident radiation is in the plane of incidence, hence we are only considering p-polarised (transverse magnetic, TM) EM waves; this is due to the requirement of the normal E-fields to create surface charges. We take the x-y plane to be the interface of the plane, the positive z half space as medium 2, then for wave propagation in the x direction we have[32]

$$E_1 = (E_{x1}, 0, E_{z1}) \exp[i(k_x x - \omega t)] \exp(ik_{z1} z) \tag{2.6a}$$

$$H_1 = (0, H_{y1}, 0) \exp[i(k_x x - \omega t)] \exp(ik_{z1} z) \tag{2.6b}$$

$$E_2 = (E_{x2}, 0, E_{z2}) \exp[i(k_x x - \omega t)] \exp(ik_{z1} z) \tag{2.6c}$$

$$H_2 = (0, H_{y2}, 0) \exp[i(k_x x - \omega t)] \exp(ik_{z1} z) \tag{2.6d}$$

If we now apply Maxwell's Equation $\nabla . E = 0$,

$$E_{z1} = -E_{x1} \frac{k_x}{k_{z1}} \tag{2.7a}$$

$$E_{z2} = -E_{x2} \frac{k_x}{k_{z2}} \tag{2.7b}$$

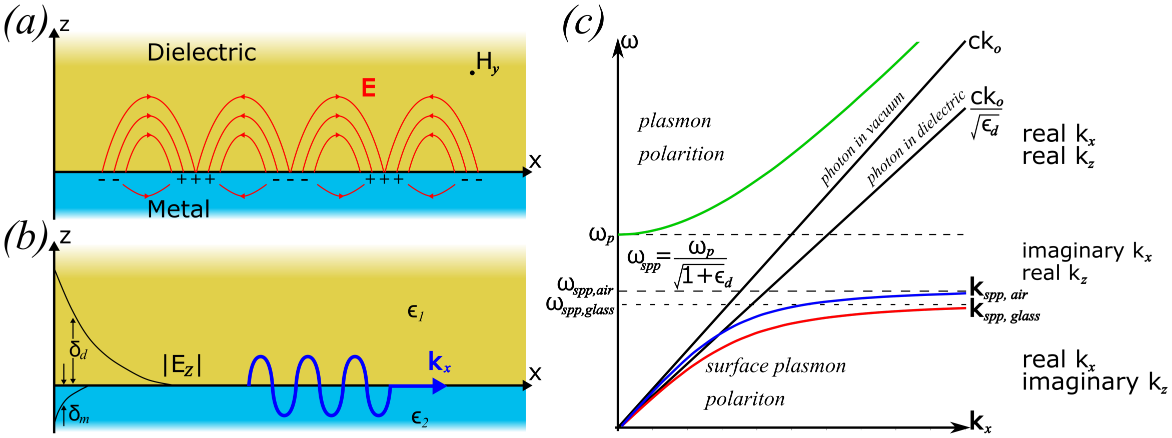

Figure. 2.3 Surface plasmons (SPs) at the interface between a metal and a dielectric. The surface charge and electromagnetic (EM) field characteristics are shown in (a). The SPs are transverse magnetic (TM) in nature, with H in the y direction. E is normal to the surface. The propagation of SPP is in the x direction along the metal-dielectric interface (b). The perpendicular E-field component, enhanced at the interface, decays exponentially away from the interface. The decay length in the dielectric is approximately $\lambda/2$ of the wavelength of light in the medium, and in the metal is approximately the skin depth. (c) The dispersion curve (ω v k) for a SP mode. Shows the momentum mismatch, with the SP mode always lying beyond the light line, that must be overcome to couple light and SP modes together. This can be done using prism coupling, nano-scale defects or surface undulation[27–31]. (a,b) reproduced from [27].

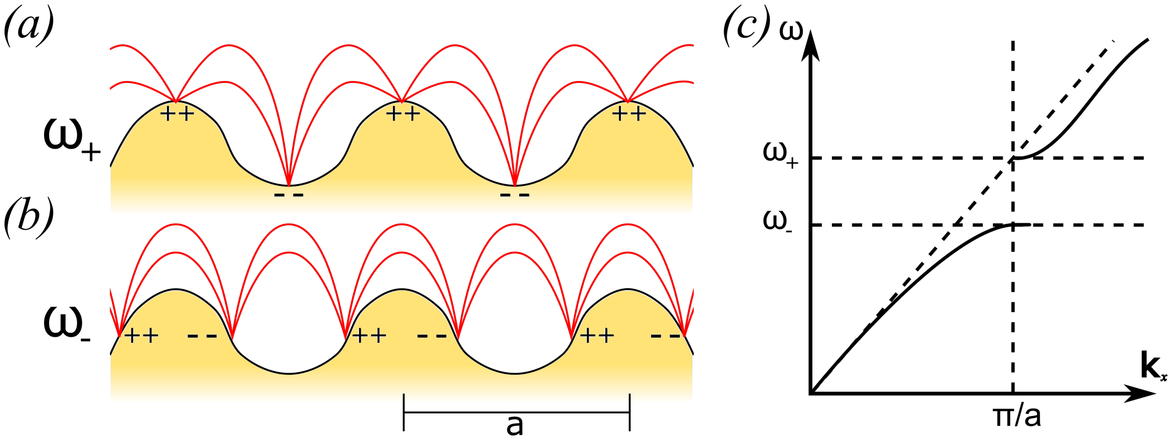

Figure. 2.4 Photonic bandgaps can be created with periodic texturing of a metallic surface. The bandgap occurs when the period, a, is equal to half the wavelength of the SP, as shown in (c). There are two standing wave solutions, (a) &(b), however owing to their different field and surface charge distributions they have different frequencies. ω_+ is of higher energy due to the greater spacial distance between the surface charges and the greater distortion of the field. Figure reproduced from[27].

To find the relationship between H_y and E_x we use Maxwell's equation $\nabla \times E = -\mu\frac{\delta H}{\delta t}$ which with $\mu = \mu_0$ gives the following relationships between the field components, the permittivities and the normal component of the wavevectors in the two media:

$$H_{y1} = \omega E_{x1}\epsilon_1\epsilon_0/k_{z1} \tag{2.8a}$$

$$H_{y2} = \omega E_{x2}\epsilon_2\epsilon_0/k_{z2} \tag{2.8b}$$

Finally we need to apply the boundary conditions at $z = 0$. We know tangential H is continuous and so is tangential E, thus $H_{yl} = H_{y2}$ and $E_{x1}, = E_{x2}$, leading to the following simple relationship between the relative permittivities and the normal components of the wavevectors in both media:

$$\frac{\epsilon_1}{k_{z1}} = \frac{\epsilon_2}{k_{z2}} \tag{2.9}$$

We also have

$$k_{z1} = -i(k_x^2 - \epsilon_1 k^2)^{\frac{1}{2}}, \text{ requiring } k_x^2 > \epsilon_1 k^2 \tag{2.10a}$$

and

$$k_{z2} = -i(k_x^2 - \epsilon_2 k^2)^{\frac{1}{2}}, \text{ requiring } k_x^2 > \epsilon_2 k^2 \tag{2.10b}$$

where $k = \omega/c$. If the wave is truly trapped in the surface then we need $ik_{z1} > 0$ and $ik_{z2} < 0$. Thus both k_z are imaginary with opposite signs and so ϵ_1 and ϵ_2 are of opposite sign. The first condition, in the dielectric characterised by ϵ_1, tells us the surface mode wavevector k_x is greater than the maximum photon wavevector available in the dielectric, $\sqrt{\epsilon_1}k$. The second condition, for the metal, is automatically satisfied, with ϵ_2 negative.

Substituting expressions 2.10 for k_{z1} and k_{z2} into 2.9 gives

$$k_x = k\sqrt{\frac{\epsilon_1\epsilon_2}{\epsilon_1 + \epsilon_2}} \tag{2.11}$$

and we see that for k_x to be real, the requirement for a propagating mode, with ϵ_2 negative, is that $|\epsilon_2| > \epsilon_1$.

The SPP mode propagates along the surface, however the field perpendicular to the surface is evanescent and decays exponentially into the two media. The typical penetration of this evanescent field into the dielectric is $\lambda/2$ of the wavelength in the medium, whereas it is typically the skin depth of the metal ($\sim$ 10nm for noble metals in visible light). This is a consequence of the bound, non-radiative nature of SPPs, and prevents propagation of power away from the surface.

If the requirement is met for SPP propagation $k_x > k$. This means that the momentum of a SP mode is higher than that of a photon with the same wavelength. The extra momentum required is due to the binding of the SP mode to the surface. Hence if we wish to use light to generate SPPs there is a momentum gap that needs to be compensated for. There are three main techniques by which the missing momentum can be provided[27]. The first makes use of prism coupling to enhance the momentum of the incident light[28]. The second involves scattering from a topological defect on the surface, such as a sub-wavelength protrusion or hole, which provides a convenient way to generate SPs locally[29, 30]. The third makes use of a periodic undulation in the metal's surface[31]. When the period of the nano-structure is half that of the wave length of the SP mode, standing waves may form creating a SP stop band, shown in figure 2.4. When the surface is manipulated in both in-plane directions, for example by a periodic array of bumps, SP modes may be prevented from travelling in any in-plane direction. At frequencies within a bandgap no SP modes can be supported, however, at the band edges, the SP mode dispersion is flat and the associated density of SP modes is high. The consequences of this are that there is large field enhancement close to the metal surface and that the SP modes can be excited by photons over a wide range of angles (due to the nature of the flat band edges), making such surfaces good for frequency selective applications. Furthermore, flat bands are also associated with the localised SP modes of metallic nano-particles. The frequency and width of these modes are determined by the particle's shape, material, size and environment.

2.1.1.2 Optical properties of metals

The optical properties of metals can best be described using the permittivity, ϵ, of the metal. The permittivity is a measure of a materials ability to resist an electric field. It relates the electric field, E, in a material to the electric displacement, D, in a material such that $E = \epsilon D$. In a dielectric material, the electrons are fully bound to the atoms in the material, and the permittivity is real and relatively constant. In the case of metals interacting with EM waves it is a complex frequency-dependant value.

Up until now we have been talking about charge oscillations in metals under the assumption of that the electrons in a metal act as a free-cloud of electron gas. In reality, whilst the valence electrons can be assumed to be completely detached from their ions, electron-electron interactions and other loss mechanisms have been neglected and need to be taken into account. The *Drude* model presents a framework for the response of electrons in metals to EM waves at visible wavelengths. Originally proposed by Drude in 1900[33] the model was later extended by Lorentz and Sommerfeld and Bethe[34, 35]. Lorentz introduced damping into the equation of motion of electrons due to collisions in their motion and this leads to a relaxation time, τ. Sommerfeld assumed that electrons in metals are described by Fermi–Dirac statistics instead of Maxwell–Boltzmann statistics.

The fast response of conduction electrons, which can move quasi-freely in the bulk material, when experiencing an external EM excitation, can be described through the equation of motion of a forced, damped harmonic oscillator, driven by an external harmonic field $E(\omega) = E_0 e^{i\omega t}$[36, 37]

$$m_e \frac{d^2x}{dt^2} + m_e \Gamma \frac{dx}{dt} = -qE_0 e^{-i\omega t} \tag{2.12}$$

The first term in equation 2.12 is the acceleration of electrons by the electric field, the second is the damping of electrons by electron-electron scattering with damping coefficient $\Gamma = v_F \langle l \rangle$, where v_F is the Fermi velocity and $\langle l \rangle$ the mean free path of the electrons.

Assuming that the system oscillates at the driving frequency, we can say $x = x_0 e^{i\omega t}$ and obtain[37]

$$x(-\omega^2 m_e - i\omega m_e \Gamma) = -qE \tag{2.13}$$

Defining the polarisation, the sum of all electric dipole moments of the electrons in a certain volume, as $P(\omega) = nqx = \epsilon_0 \chi(\omega) E(\omega)$ we obtain the expression

$$\epsilon(\omega) = \epsilon'(\omega) + i\epsilon''(\omega) = 1 - \frac{\omega_p^2}{\omega^2 + i\omega\Gamma} \tag{2.14}$$

This expression shows the relation between the frequency dependant permittivity and the plasma frequency, $\omega_p = \frac{nq^2}{m_e \epsilon_0}$.

In noble metals the real part of the permittivity, ϵ', is negative in the visible wavelength range, and fits well with experimentally measured dielectric functions[38] at longer wavelengths, but diverges at higher energies. To improve the fit between theoretical model and experimental techniques, the unity part of equation 2.14 can be replaced by $\epsilon_\infty = 1 + \delta\epsilon$, with the value of $\delta\epsilon$ adjusted to fit the experimental data[37]. However, the cause of the disparities is generally due to interband transitions, when the energy of an incoming photon is large enough to overcome the band gap of a metal and promote valence electrons to the conduction band of the material. The crude modification to the *Drude* model can be replaced by adding Lorentzian terms to the Drude expression to replicate the interband transitions:

$$\epsilon(\omega) = 1 - \frac{\Omega_p^2}{\omega^2 + i\omega\Gamma_0} + \sum_{j=1}^{m} \frac{f_j\omega_p^2}{(\omega_j^2 - \omega^2) + i\omega\Gamma_j} \tag{2.15}$$

where m is the number of oscillators. Each oscillator has a lifetime Γ_j, with strength and frequency of f_j and ω_j respectively. The modified plasma frequency, $\Omega_p = \sqrt{f_0}\omega_p$, is adjusted to include the oscillator strength f_0. In general, several Lorentzian terms

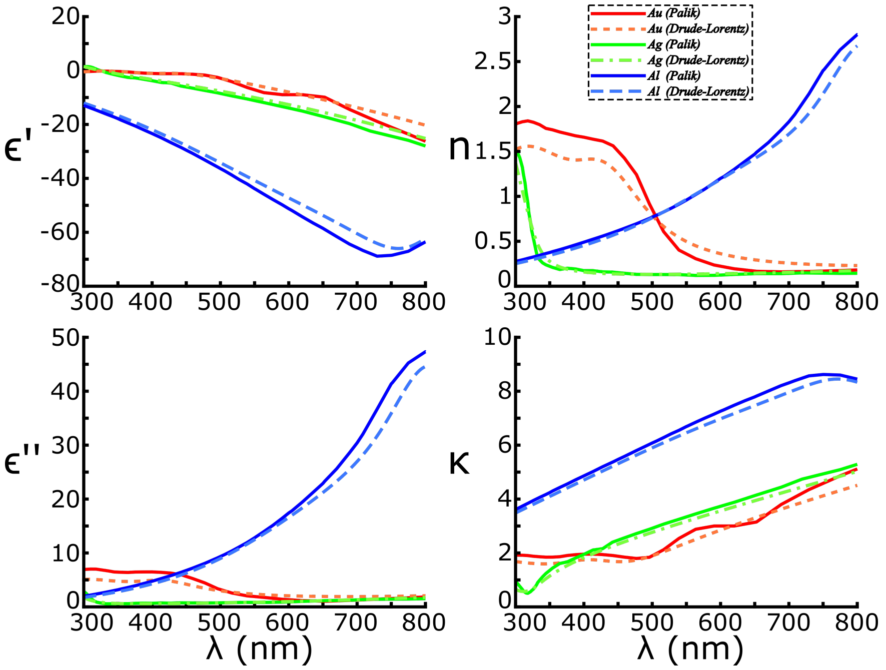

Figure. 2.5 The permittivity (real, ϵ', and imaginary, ϵ'') and refractive index (real, n, and imaginary, κ) of common noble metals across the visible wavelengths. Experimentally observed data are taken from Palik[38] and the Drude-Lorentz multiple oscillator model is taken from[39].

can be added to $\epsilon(\omega)$ to describe the effect of different interband transitions and enable a better fit to experimental data as shown in figure 2.5.

The refractive index of a material is related to the permittivity by $\mathrm{n} = \sqrt{\epsilon}$ when the materials relative permeability is 1, which is the case for most materials at optical frequencies. In metals, as the permittivity is complex, so will the refractive index be, and will take the form $\bar{\mathrm{n}} = \mathrm{n} + i\kappa$. The real part of the solution, n, gives the phase velocity of an EM wave travelling through the material whilst the imaginary part, κ, referred to as the extinction coefficient, indicates the amount of attenuation when an EM wave travels through the material.

2.1.1.3 Loss mechanisms in metals

In the previous section we have a defined damping factor, Γ, to model the losses in the optical properties of metals. Here we take a look further into the physical processes that contribute to the damping factors.

Absorption assisted by a phonon This absorption mechanism, requiring a phonon or an imperfection, results in an electron and a hole, referred to as 'hot' carriers, whose energy can be harvested should they reach the surface of the metal. Consider two states with wavevectors k_1 and k_2 in the simplified band structure of a metal shown in figure 2.6(a), occurring above and below the Fermi Level. Each momenta has the energy E_1 and $E_2 = E_1 + \hbar\omega$, respectively. The difference in the magnitude of these two momenta is typically of the order of 3nm^{-1} ($\Delta k_{1,2} > \Delta k_0 \sim \omega v_F$, where $v_F \sim 10^8$cm s^{-1} is the Fermi velocity) and too large to be provided by a photon or SPP, hence the need for a phonon. The process occur as the simultaneous absorption of the photon and phonon or as absorption of a photon, followed by thermalisation due to electron-phonon interaction. The probability of absorption by this mechanism is proportional to $\gamma_{ph}(\omega)^{\omega_p^2}/_{\omega^2}$, it is weakly dependent on frequency and is typically $\gamma_{ph}(\omega) \sim 10^{14}$s^{-1} (the reason for this large value, as follows from Fermi's golden rule, is a huge density of states above the Fermi level available for the transition)[25].

Electron-electron (e-e) scattering e–e scattering is the other momentum-conserving process that can lead to absorption. This so-called Umklapp process, figure 2.6(b), works by two electrons making the transition from the states k_1 and k_2 below the Fermi

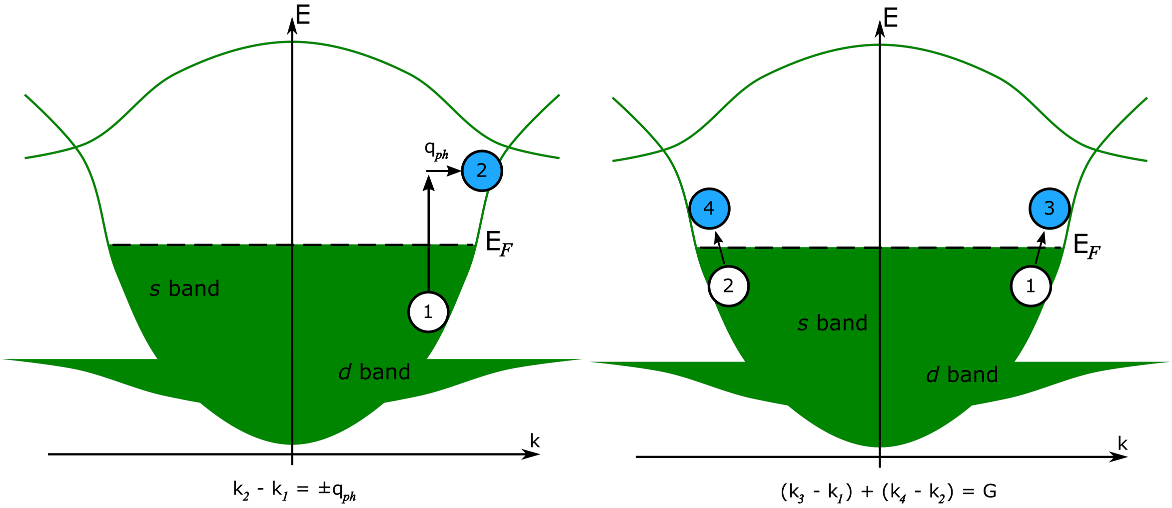

(a) Absorption of electromagnetic energy $\hbar\omega$ assisted by a phonon with wavevector q_{ph}. Creates hot hole (1) with wavevector k_1 and hot electron (2) with wavevector k_2, with energy E_2 above the Fermi level, E_F

(b) Electron–electron scattering assisted absorption of energy $\hbar\omega$. An *Umklapp* process involving reciprocal lattice vector G creates four lukewarm carriers - two holes (1,2) and two electrons (3,4)

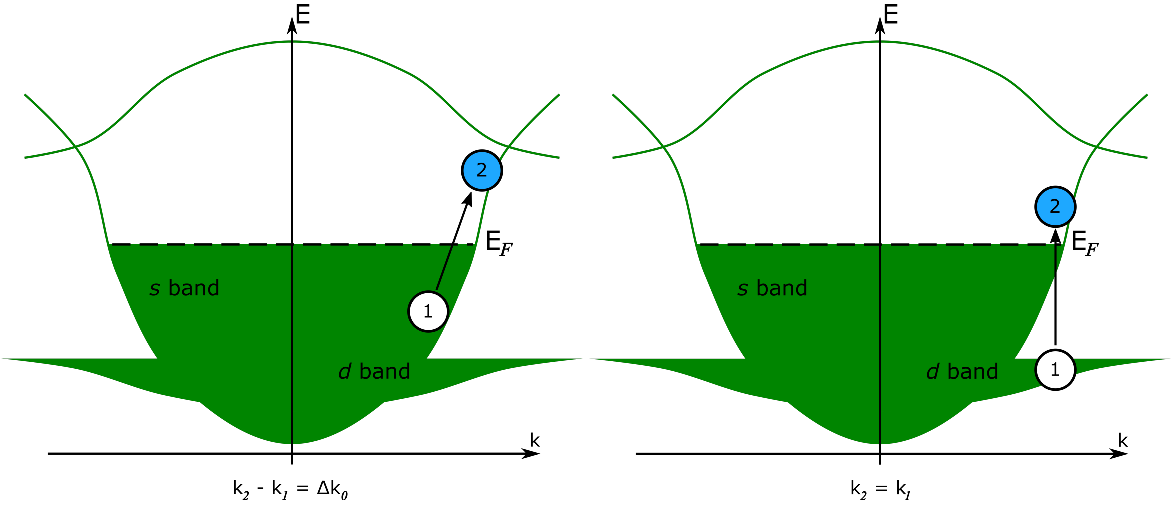

(c) Direct absorption of energy $\hbar\omega$ (Landau damping) assisted by the SPP momentum Δk_0. Creates hot hole (1) and hot electron (2)

(d) Interband absorption of energy $\hbar\omega$ from the d to s shell. Does not create hot carriers because hole (1) in the d band has low velocity and excited electron (2) is too close to the Fermi level

Figure. 2.6 Absorption of a quantum of electromagnetic energy $\hbar\omega$ in a metal. Figure recreated from [25] level to the states k_3 and k_4 above the Fermi level. The momentum conservation is $k_3 + k_4 = k_1 + k_2 + G$, where G is the reciprocal lattice vector and the energy conservation relation is $E_3 + E_4 = E_1 + E_2 + \hbar\omega$. The energy conservation equation suggest that, rather than in the case of absorption assisted by a phonon we get two hot carriers which share the energy term $\hbar\omega$, you get four 'lukewarm' carriers having kinetic energies of the order of $\hbar\omega/4$ each. This fact can cause issues in photo-detection and energy harvesting applications, where the energy of the hot carriers has to overcome certain barriers to be useful. Similarly to absorption assisted by a phonon, the probability of e–e scattering is frequency dependent. However, in the case of e-e scattering this dependency is strong since high photon energy means more electrons and holes are involved in the process. It can be written that the probability of e-e scattering is approximately $\gamma_{ee}(\omega) \sim \gamma_0 \frac{\hbar\omega}{E_F}$, where $\gamma_0 \sim 10^{15} s^{-1}$. $\gamma_{ee}(\omega)$ becomes comparable to γ_{ph} in the visible range[25].

Landau damping Landau damping is a 'diagonal' process that is associated with the finite size of SPP modes. The absorption process, shown in figure 2.6(c) can occur if the effective size of the SPP mode inside the metal $a_m \ll \lambda/2$. If the mode is at this length scale it will include spatial frequencies larger than Δk_0, which can lead to an additional 'confinement' contribution to the absorption $\gamma_c \sim v_F/a_m$. When $a_m \sim$ 10nm, γ_c becomes comparable to the other 'bulk' contributions γ_{ph} and γ_{ee}. The implications of this are significant as even if you could find an 'ideal' metal, with no bulk losses, in sub-λ SPP modes, Landau damping would still introduce significant losses. This is because electrons will still make the transition as there are plenty of states available to move into. The only way around this would be to have a band structure with a band gap[25].

Interband absorption Lastly, of note, there is band-to-band absorption, shown in figure 2.6(d), which occurs in all metals. No hot carriers are formed however, as the 'hot' electron is created near the Fermi, while in the d band the effective mass of the 'hot' hole is higher, so despite its high energy it has a low velocity. Interband absorptions are significant around 600nm for Au, 400nm for Ag, and 800nm for Al[25, 40].

2.1.1.4 Materials for plasmonics in the visible range

The case for which material to use, when fabricating plasmonic structures, comes down to fundamental and practical reasoning. The most commonly used materials for plasmonic nano-structures are aluminium (Al), gold (Au) and silver (Ag). This is due to their negative permittivity and relatively low interband losses in the near infra-red and visible wavelength ranges, and the ease with which they can be used to fabricated plasmonic devices.

As shown in figure 2.5, none of the metals mentioned are lossless throughout the visible wavelength spectrum. Al is most suited for UV applications, however, interband losses build up quickly as the wavelength increases, making the metal non-ideal for the visible range of wavelengths. Au has significant losses at the lower end of the visible spectrum due to interband transitions, and whilst Ag has similar issues they are more significant at shorter wavelengths for Ag than for Au, making silver the material of choice for most plasmonic applications at visible wavelengths.

This raises the question, given their losses in the visible range, whether or not noble metals are suitable at all for plasmonic applications. However, plasmonic elements smaller than the diffraction limit require a negative real part of the materials permittivity, ϵ', and positive imaginary part,ϵ''. This is typical for conductors due to the fact that they have free carriers, and free carriers, as discussed in section 2.1.1.1, are necessary for all plasmonic materials looking to break the diffraction limit. Below this limit the magnetic energy is too small to sustain oscillations with the electric field energy and must be compensated using the kinetic energy of these free carriers. The condition may be met for semiconductors or polar insulators when their ions are driven past their resonance frequency. There are no naturally occurring materials that have negative real permittivity and are lossless in any part of the EM spectrum[41][42][43].

When looking at alternative metals, those with the lowest losses in the visible regime are alkali metals, notably sodium and potassium. Yet their suitability as an alternate material for plasmonic nano-structures is low due to their high reactivity in air and water making the feasibility of using the metals in nano-fabrication procedures is low. Due to this there have been no reported applications using alkali metals.

Copper (Cu), given its high conductivity, is expected to be a good plasmonic material, however it has similar absorption to Au in the 600-750nm wavelength range and also readily forms its oxides making fabrication with the metal challenging[42].

That is not to say that such issues do not hamper noble metals commonly used as plasmonic materials. Whilst Au is very stable in air, Ag is sensitive to sulfidation and tarnishes to form a layer of silver sulfide, increasing the optical losses of the material significantly[41].

An alternative option is metallic alloys. If you could shift the interband transitions of a metal into an alternative part of the EM spectrum that is not relevant for a particular application one could create a more suitable material. Bivalent transition metals, such as cadmium (Cd) and zinc (Zn), when doped into monovalent noble metals contribute one extra electron to the free-electron plasma[44]. This n-type doping raises the Fermi level, increases ω_p and shifts the threshold for interband transitions. The work detailed by Dobb et al. ,[44] doped gold with cadmium, creating a unique band structure and shifting the interband to new wavelengths. Unfortunately, in this case the losses were not shifted out of the visible wavelength range, and the technique needs more research for visible wavelength applications. One could also look at combining alkali metals with a noble metal[45]. The compound predicted to show most promise is potassium gold (KAu), however is not suitable as it does not have negative ϵ' values in the visible range, along with various fabrication difficulties.

Semiconductors are another potential material for plasmonics, however for the material to be feasible it needs to be wide bandgap (low interband transitions), heavily doped and have high carrier mobility to qualify as a low loss plasmonic material in the visible spectrum. Unfortunately, whilst there are numerous semiconductors with large bandgaps and high carrier mobility, very high doping levels are needed to bring the crossover frequency (where ϵ' changes from negative to positive) into the visible range. Doping semiconductors to this level creates issues such as concerns about the solubility limit, the fraction of dopants that would be active and retaining a high carrier mobility that is necessary for low losses. Hence currently semiconductors are not suitable for plasmonic materials in the visible range.

Metal nitrides, such as titanium nitride (TiN) can exhibit metallic properties in the visible wavelength range ($>$ 500nm). These are non-stoichiometric, interstitial compounds with large free-carrier concentrations and allow for tuning of their optical properties by varying their composition[46]. In fact TiN, as shown in figure 2.7, exhibits losses comparable to silver and gold in the visible regime, however the exact optical properties are process-dependant given the compound is non-stoichiometric.

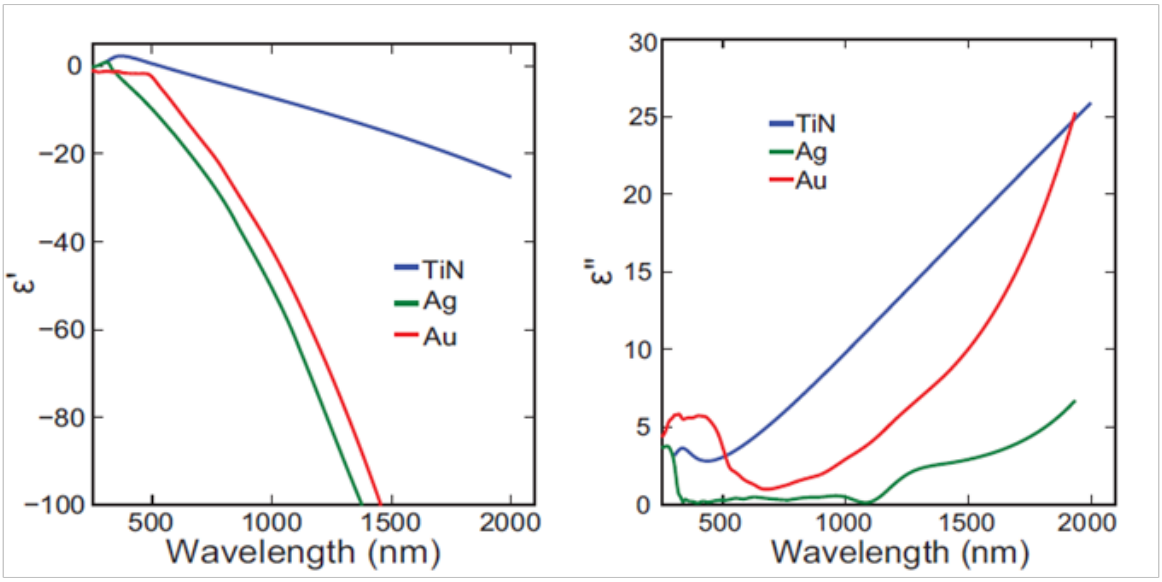

Figure. 2.7 Dielectric function of TiN in comparison with conventional plasmonic materials: gold and silver. Charts taken from[46].

Graphene, due to its high carrier mobility, can be considered as a potential plasmonic material. It has been demonstrated that a widely tunable metasurface composed of optical antennas on graphene can be incorporated into a sub-wavelength thick optical cavity to create an electrically tunable perfect absorber[47]. However, potential applications have been targeted at the mid-IR spectrum due the fact that the material is subject to losses in the near IR and at visible wavelengths.

2.1.2 Holography

When light is scattered from an object the light waves from the object consist of *phase*, *amplitude* and *polarisation*. In traditional photographic techniques, the information recorded is the amplitude of the light from the object, and in that process information from the original object is lost. The result of this loss of information is that the image recorded is only 2-dimensional (2D), that is to say that information regarding the depth of the image is lost, and the image will look the same from any angle of viewing. In holography, the information recorded includes the phase information, that is to say, the light-field is recorded.

The interference of light, diffracted from a hologram, creates an image in the far field, creating a virtual-object that you can view from different angles. The wavefront from an object whose image we wish to record can be written as

$$\Psi = A(x,y)e^{i\phi(x,y)} \tag{2.16}$$

where $A(x,y)$ contains the amplitude information of the wavefront varying in the x and y directions, and $\phi(x,y)$ contains the phase distribution. If we were to reconstruct the image directly, we would need a source or modulator that could manipulate both the phase and amplitude or two separate modulators which can do each job individually. However, if we were to use a reference wave, $A_0e^{i\alpha x}$ to record the image all the information (both *phase* and *amplitude*) from the original wavefront is recorded in the intensity profile of the two combined light waves[48][18]. A schematic of the recording setup is shown in figure 2.8(a,i). $\alpha = sin\theta/\lambda$ where θ is the angle between the wavefront of the image to be recorded and the reference wave, and λ is the wavelength of the reference wave. The intensity of the combined wave can be written as

$$I = A_0^2 + A_{(x,y)}^2 + 2A_0A(x,y)\cos[\alpha x - \phi(x,y)] \tag{2.17}$$

The first term represents the directly transmitted beam, the second can be neglected as the intensity of the image wavefront will be significantly smaller than that of the reference beam ($|A(x,y)| \ll A_0$). The third term is the complex amplitude of the scattered wave from the image object and a conjugate object, with the same wavefront from the original image, but with opposite curvature. The result is that the amplitude and the phase of the original object are encoded in the intensity profile of the photographic plate. This method of recording holograms was developed by Leith and Upatnieks, as an improvement to Gabor's original on axis arrangement, resulting in the reconstructed images at different angles to the reference beam, which means at large enough values of θ the images will not overlap. Thus the hologram needs only to be either a *phase hologram*, which spatially modulates the phase of the illuminating reference wave, or an *amplitude hologram*, which spatially modulates the amplitude of the illuminating reference wave.

An alternative method for recording holograms is shown in figure 2.8(b). Here the object is a transparency located in the front focal plane of a lens, and is illuminated by a collimated beam of monochromatic light[18]. The complex amplitudes of the waves from the object and a separate reference pass through a lens, and hence the waves that interfere at the hologram are the Fourier transform of the original waves.

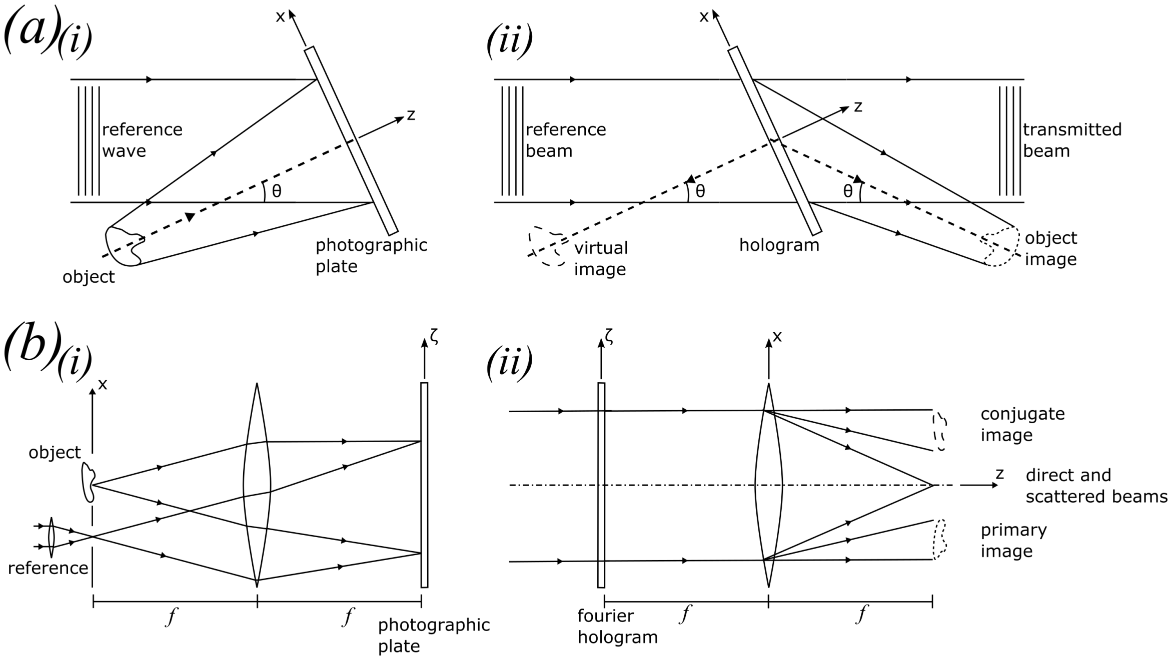

Figure. 2.8 Optical setups for Hologram (i) recording and (ii) reconstruction using an (a) off-axis reference beam and (b) Fourier hologram setup. Reproduced from [18]

To reconstruct the image, the processed hologram is placed in front of the lens and illuminated with a collimated beam of monochromatic light. A hologram with the same properties as a Fourier hologram can be obtained without using a lens, if the reference wave comes from a point source in the plane of the object[18].

2.1.2.1 Scalar diffraction theory

The physical basis for any hologram is diffraction and interference. Diffraction is the bending or change of direction of EM waves when encountering an object or aperture. These waves interfere after the object or aperture and the superposition of these wave is known as the interference. Whilst diffraction occurs whenever waves encounter an object or aperture the effects are most significant when the dimensions of the object or aperture are comparable to the wavelength of the EM waves.

The diffraction of a wave when encountering an object can be determined by solving Maxwell's equations, however this can be overly complex and computationally dense. An alternative solution is *scalar diffraction theory*, which simplifies the problem by using the Huygens-Fresnel principle. The principle states that every unobstructed point on a wavefront acts, at a given instant, as a source of outgoing secondary spherical wavelets. The resulting net light amplitude at any position in the scattered light field is the superposition of the amplitudes and relative phases of all the individual wavelets.

If you consider an arbitrary hole (or aperture) $A(x, y)$ in a plane surface as shown in figure 2.9(a), when light is shone onto the surface the light passing through the hole will be diffracted at its edges. To calculate the pattern the diffraction of this light creates, you can split the hole into infinitely small areas of dS, which can be modelled as point sources of spherical *Huygens* wavelets. If you take the superposition of all the wavelets across the hole and evaluate at a surface in the far field you can calculate the diffraction pattern of the initial aperture.

If we consider only the part of the wavelets which are propagating forward ($z > 0$), and are contained in a cone of small angles away form the z-axis, then we can evaluate the change in field dE at the point P due to dS[49]. As the wavelet dS acts as a point source, we can say that the power radiated is proportional to $1/r^2$, hence the field dE will be proportional to $1/r$. We can see that for a propagating wave of frequency ω and wave number k ($k = 2\pi/\lambda$), we have

$$dE = \frac{A(x,y)}{r} e^{j(\omega t - kr)} dS \tag{2.18}$$

The co-ordinate system needs to be translated from the aperture plane to the plane containing point P, which are defined as $[\alpha, \beta]$

$$R^2 = \alpha^2 + \beta^2 + z^2, \quad r^2 = (\alpha - x)^2 + (\beta - y)^2 + z^2 \tag{2.19}$$

where R is the distance from the centre of the aperture plane to the point P[49].

The final full expression in terms of x and y ($dS = dxdy$) for dE will now be

$$dE = \frac{A(x,y) e^{j\omega t} e^{-kR\sqrt{1 - \frac{2\alpha x + 2\beta y}{R^2} + \frac{x^2+y^2}{R^2}}}}{R\sqrt{1 - \frac{2\alpha x + 2\beta y}{R^2} + \frac{x^2+y^2}{R^2}}} dxdy \tag{2.20}$$

Such an expression can only be solved for a few specific aperture functions. To account for an arbitrary aperture the region over which the diffracted pattern is evaluated needs simplification, restriction and approximation. By assuming $R \gg \alpha, \beta$ and $A(x, y) \ll R$, then the denominator of equation(2.20) can be assumed to be constant and that for all intents and purposes $r = R$. Considering only the region

region where $R \ll x^2 + y^2$ and simplifying using the binomial expansion, the expression for dE becomes[49]

$$dE = \frac{A(x,y)}{R} e^{j(\omega t - kr)} e^{jk\frac{\alpha x + \beta y}{R}} dxdy \tag{2.21}$$

We are only interested in the relative scaling of points in the plane containing P, hence we can assume

$$\frac{1}{R} e^{j(\omega t - kr)} = 1 \tag{2.22}$$

as this term only contains information about the original wave incident on the aperture. Hence total effect of the dS wavelets can be be found by integrating dE across the aperture to give us the expression for the far field diffraction pattern

$$E(\alpha, \beta) = \iint_A A(x,y) e^{(jk(\alpha x + \beta y)/R)} dxdy \tag{2.23}$$

The region where the approximations we have made hold is referred to as the *Fraunhofer region.* $E(x,y)$ only changes in size with increasing z. In cases where the approximation is moderately accurate, we are in the *Fresnel region.* Before the Fresnel region, the evaluation of $E(x,y)$ is very difficult, and is defined as the near field diffraction pattern[49, 50]. These regions are shown schematically in figure 2.9(b).

Equation 2.23 is directly comparable to the *2D Fourier transform* of an arbitrary function

$$F(u,v) = \iint_{\pm\infty} f(x,y) e^{2\pi j(ux+vy)} dxdy \tag{2.24}$$

This has the convenient consequence that it is possible to calculate the inverse, i.e. the original shape of the aperture can be obtained from the far field pattern.

$$f(u,v) = \iint_{\pm\infty} F(x,y) e^{2\pi j(ux+vy)} dudv \tag{2.25}$$

This result is incredibly useful in the process of computer generated holograms as will be shown in the next section.

One downside of this result is the fact that the far-field is actually spatially quite far away. For example an aperture of size 1mm square, if illuminated by a wavelength of light of 630nm, the far field pattern can only be measured approximately 10 metres away from the aperture. To overcome this limitation you can introduce a lens, as shown in figure 2.8(b), into the optical system. The lens converts plane waves incident upon it into spherical waves convergent on its focal plane. Hence now the far field pattern occurs at the focal plane of the lens. The introduction of the lens however introduces a phase distortion in the Fourier transform, which in compressed optical systems must be corrected for. The most convenient method of correcting for this, should space not be a constraint, is to place the lens its focal length away from the aperture. Beyond this the introduction of a lens will unfortunately, due to its non-perfect nature, introduce chromatic and spherical aberrations resulting in a distorted image.

2.1.2.2 Computer generated holograms

Holograms generated by a computer are able to produce a wavefront with any prescribed amplitude and phase distribution, hence a computer can be used to create a hologram of any object, without the need for the object to actually exist. However, the full wave simulation in 3-dimensions (3D) of the scattering and interference of light from an object is computationally dense. To reduce the computational effort we can use the result of *scalar diffraction theory*, that the Fourier transform of an arbitrary aperture is its far field diffraction pattern. In fact it can be shown, by means of sampling theorem, that if an object wave is sampled at a sufficiently large number of points, it can be done with no loss of information[18].

The process by which computers generate holograms can be summarised as follows. It starts with the virtual object, which can either be created by the computer or can be recorded from a real object. Wave propagation is computed with theories appropriate for Fraunhofer, Fresnel, or near-field diffraction, however, as previously mentioned, for simplicity in this work, it is the Fourier transform of the original object that is calculated. The object-scattered field is evaluated on a hypothetical surface which is usually flat, interfering with a reference wave to compute the Hologram. The computer generated hologram (CGH) can then either be displayed on a spatial light modulator (SLM) or fabricated using various techniques[51].

The hologram can be phase-only, where the hologram is able to modulate only the phase of an incoming wavefront; amplitude-only, where the hologram is able to modulate only the amplitude of an incoming wavefront, the transmitted phase being

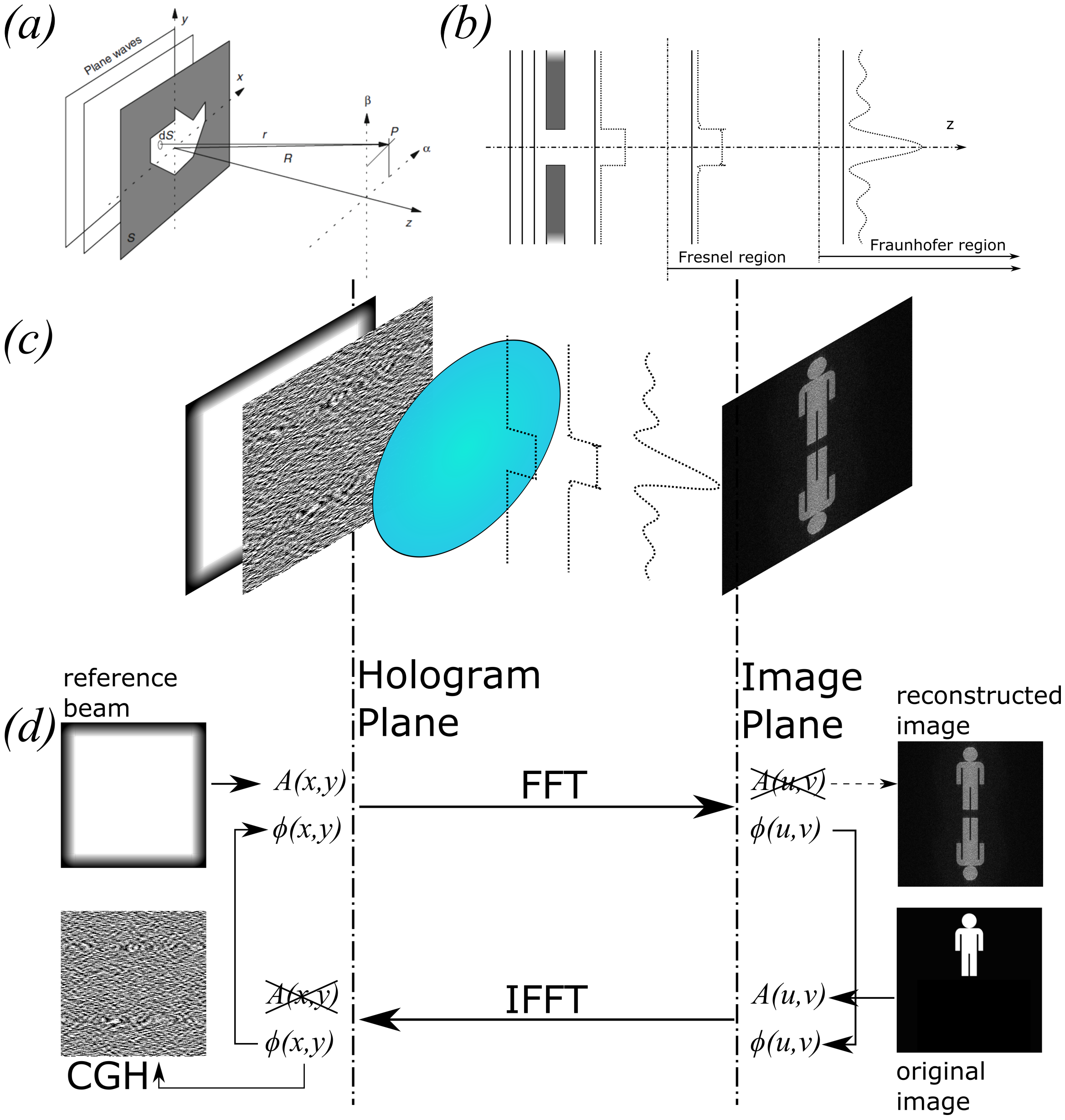

Figure. 2.9 Aperture and diffraction co-ordinate system[49] and diffraction regions or scalar diffraction theory. (c) Graphical representation of image reconstruction of a Fresnel Hologram, the reference beam illuminates the binary amplitude hologram in the Hologram plane, resulting in a reconstructed image in the far field (image plane) (note zero order has been removed from reconstructed image). (d) Information flow in iterative GS algorithm for producing CGHs.

equal to a constant; or complex-amplitude, where the hologram is able to modulate both the phase and amplitude of an incoming wavefront.

To reconstruct the original object (virtual or real) the hologram is illuminated by a reference beam[52], in the configuration shown in figure 2.8(b).

The quality of the recreated image can be improved by using an iterative Fourier transform algorithm (IFTA)[53, 51]. In the case of this work a Gerchberg-Saxton (GS) algorithm, commonly used in the optimisation of holograms, is utilised. IFTAs are computationally time consuming and introduce speckle noise into the reconstruction plane. A hundred or more iterations are needed, depending on the complexity of the design and on the desired light distribution $A(u, v)$ in the CGH reconstruction plane. Alternatively a cost function can be introduced, that the algorithm will run until it is minimised or maximised, depending on how the cost function designed.

The algorithm, displayed graphically in figure 2.9(d), cycles between the image plane in the far field and the hologram plane by means of Fourier (FT) and inverse Fourier (IFT) transforms. The GS algorithm can be run looping either amplitude or phase, with the property not being looped discarded at each plane and replaced by the respective properties of either the reference beam (in the hologram plane) or the original image (at the image plane).

The reason for this is that a digital display is typically only able to modulate either the phase or the amplitude of a reference beam, not both. Which property to constrain is a matter of choice for the user generating the hologram, however, since the majority of information of an image is stored in phase, in this work the phase will be used to generate the hologram. In fact a binary amplitude-only CGH can be produced by considering only binary-phase in the GS algorithm. By replacing the phase of $\pm\pi$ with $[0, 1]$, it can be mathematically shown that a binary phase is equivalent to binary amplitude, with a constant offset, representing a zero-order term[54, 51].

2.1.3 Liquid crystals

Conventionally, matter can exist in four different phases solids, liquid, gas or plasma. The two most common condensed matter states are solids and liquids, with the main difference between the two being the degree of order of the molecules within the states, solids being highly ordered and liquids not at all. Within solids, which can also be referred to as crystals, there are degrees of orientational order and positional order, due to the solids' molecules being rigidly held together by intermolecular bonds. In liquids molecules move around with little restriction, moving freely and rotating around their molecular axis, resulting in random order and isotropic properties (i.e. its physical properties do not depend on its orientation).

In-between the liquid and crystal phases numerous other phases exist with varying degrees of order. These phases are called liquid crystal (LC) phases. They are fluidic in nature, like a liquid, but also exhibit a degree of molecular order similar to (but weaker than) that observed in crystalline solids. Not all materials will exhibit liquid crystalline properties, but instead are limited to molecules that have a structural anisotropy, eg: rod-shaped molecules (calamatic LCs), disc-shaped molecules (discotic LCs) and board-like molecules (sanidic LCs).

LCs can be classified into two main categories, separated by the cause of transitional mechanism into a LC phase; thermotropic LCs, which are influenced by change of temperature and lyotropic LCs, which are influenced by the change of solvent. Lyotropic LCs are not applicable to electro-optic devices and as such will not be discussed in this thesis.

Either by heating a thermotropic LC above the crystalline solid phase or cooling from the isotropic liquid phase a liquid crystal mesophase will appear. The temperature at which, on heating, the state of matter changes from that of a solid to that of a liquid crystal is called the melting point (T_m). The temperature at which, on cooling, the state of matter changes from isotropic liquid to liquid crystal is referred to as the clearing point (T_c).

Liquid crystals are further characterised into different mesophases depending upon the degree of orientational and positional order that they possess. Some liquid crystals may only exhibit one particular type of liquid crystal mesophase, whilst others may exhibit many different phases at different temperatures.

In this work, calamatic liquid crystals (i.e. rod-shaped) are used. The LC structure may consist of positional order (the extent to which an average molecule or group of molecules show translational symmetry), orientational order (the tendency of the molecules to align along the director on a long range basis) or bond orientational order (describing a line joining the centres of nearest-neighbour molecules without requiring a regular spacing along that line), or any combination of the three.

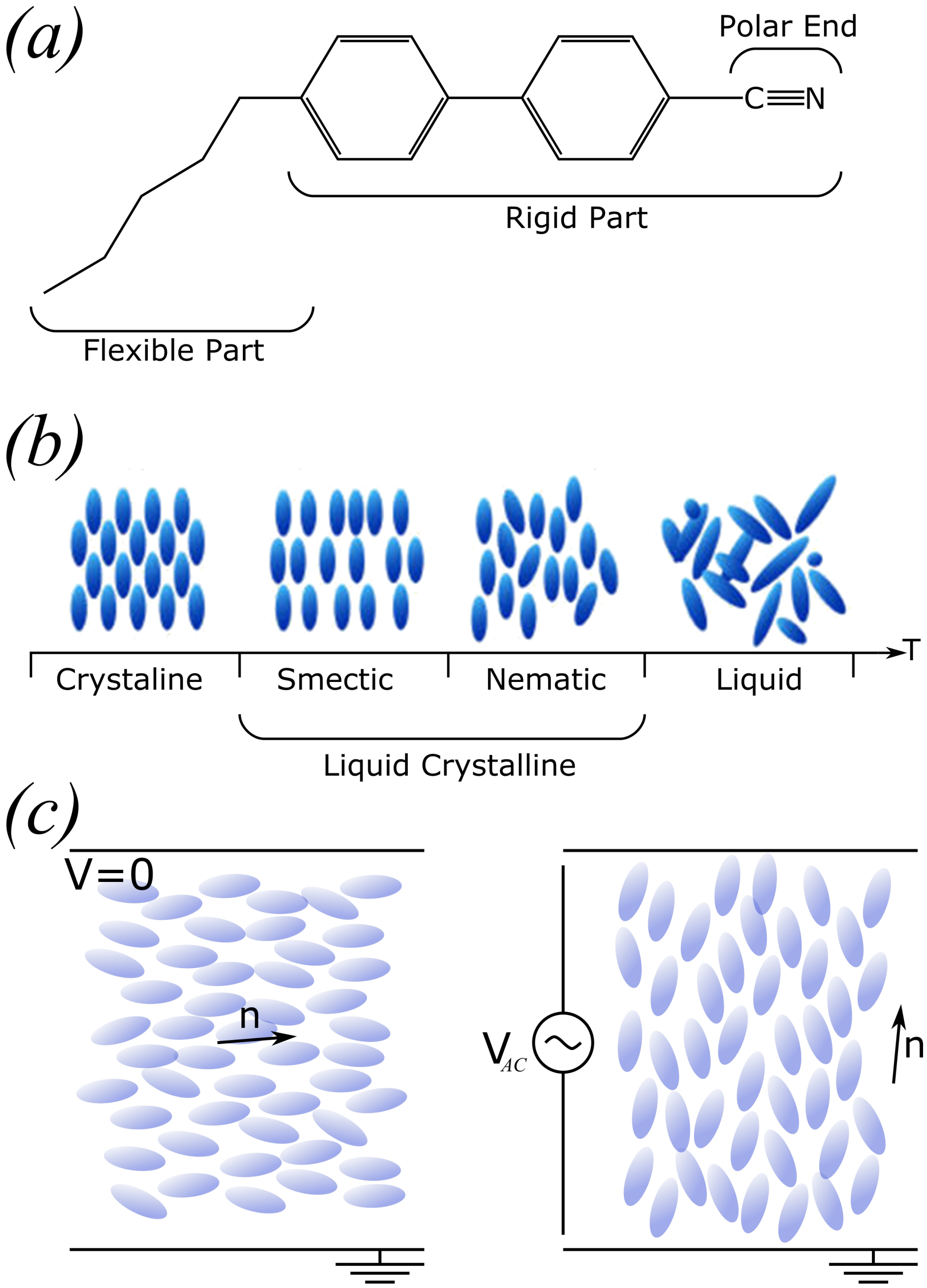

Figure. 2.10 Liquid crystal structure, phases and action under an applied field. (a) Typical Thermotropic Liquid Crystal Molecule Structure. (b) Appearance of Liquid Crystal Phases in a Temperature Profile[55]. (c) Alignment of nematic LC in a planar aligned cell with and without AC signal applied between the top and bottom of the cell, director (n) is average orientation of LC molecule axes.

The least ordered of the LC phases is called the nematic phase, as its constituent molecules do not have any translation or long-range positional order but only short range orientational order (figure 2.10(b))

This anisotropy of the LC molecule, coupled with the degrees of order that a given LC posses, results in the anisotropic material properties of a LC.

The LC molecule, shown schematically in figure 2.10(a), will consist of a rigid part, a flexible region and a polar group. The anisotropic geometry of the molecules allows for preferential alignment of the molecules along one spatial direction, also referred to as the director, n, illustrated in figure 2.10(c). The rod like shape of the molecule is the cause of the anisotropy in the dielectric constant of the LC molecules. As light approaches the molecule, depending on the direction of approach, the wave will interact with more or less electrons in the LC molecule, resulting in higher or lower permittivity. The refractive index of a material is related to the permittivity by n= $\sqrt{\epsilon}$, hence as a LCs permittivity is anisotropic so its refractive index will be. The speed that light propagates through isotropically structured transparent materials is determined by the refractive index, n. Light therefore travels at a different speed in one direction through LCs than it will in another. Materials with such a property are referred to as *birefringent*. Birefringent materials will have different refractive indices not only in different directions, but also for light of different polarisations, hence different polarisations of light will travel through a birefringent material at different speeds. If one considers two rays of light approaching a birefringent material, with polarisation orthogonal to each other, the polarisation of light that sees the 'short' axes of the material is referred to as the 'ordinary ray' (which has been modulated by the ordinary refractive index, n_o) and the polarisation that sees the long axis is called the 'extraordinary ray' (which has been modulated by the extraordinary refractive index, n_e). The difference between ordinary and extraordinary refractive index ($n_e - n_o$) is called the birefringence, Δn. As a LC molecule has two short axes there exists a single, uniaxial, orientation of a birefringent material for which there is no difference in refractive index. This direction is referred to as the 'optic axis' of the crystal.

Furthermore, the polar end of the LC molecule results in an anisotropic distribution of charge across the LC molecules resulting in a dipole moment. The electrically polar nature of LC molecules means that the lowest energy configuration state for them to be in, is one in which their electric dipole (usually parallel to the liquid crystal director for positive dielectric anisotropy materials) aligns with any externally applied electric field. This fact combined with the fluidic nature of LCs means that orientation of the LC molecule, and hence the director of a LC material, will preferentially align to a low frequency electric field. When the LC molecules rotate so do their optical properties, hence LCs are ideal for electro-optic switching applications.

Intensity modulation of transmitted light using nematic liquid crystals can be achieved by simply placing a planar aligned liquid crystal cell between crossed polarisers, with the director aligned ±45° to the crossed polarisers, and modulating the applied voltage. The birefringence (Δn) that the light 'sees' when the LC molecules are planar aligned is $\Delta \mathrm{n} = \mathrm{n}_e - \mathrm{n}_o$. As a voltage is applied to the cell, the LC molecules re-align to the field. The birefringence seen by the light is then

$$\Delta \mathrm{n}(\theta) = \frac{\mathrm{n}_e \mathrm{n}_o}{\sqrt{\mathrm{n}_e^2 \sin^2\theta + \mathrm{n}_o^2 \cos^2\theta}} - \mathrm{n}_o \tag{2.26}$$

The phase difference between the two orthogonal component of propagation light,($\gamma = \phi_x - \phi_y$), also known as the retardance, Γ, at a given wavelength, λ, is dependant on the Δn and thickness, t, of the LC layer by

$$\Gamma = \frac{2\pi \Delta \mathrm{n}(\theta) t}{\lambda} \tag{2.27}$$

At phase differences equalling π radians (or odd integer multiples thereof) the resulting light is not polarised in a direction to pass through the second polariser, and a dark state results. At phase differences equalling 2π (or even integers of π), the resulting light does pass through the second polariser, and a bright state results. Intermediate brightnesses are achieved by driving at intermediate voltages.

If there are no polarisers and $\Gamma = \pi/2$ then the cell can be called a quarter wave plate.

Twisted Nematic displays operate by having a cell with crossed planar alignment layers. The result is a quarter twist in the alignment of the LC from the bottom of the cell to the top. This twist will rotate the polarisation of light by 90°. If an E-field is applied between the two plates the LC molecules align vertically to the field and hence will not rotate the polarisation of light. If the cell is placed between cross polarisers with the LC director aligned to the polarisers axes at each end of the cell, with no voltage applied the light polarisation with be rotated to match the output polariser and light will be transmitted, if an E-field is applied the polarisation of light is not rotated and no light will be transmitted.

2.2 The world as we know it; Plasmonic metasurfaces

The basis for this section comes from several recent review papers that provide excellent summaries of where plasmonic metasurface technologies are currently positioned[2, 56, 20, 17, 13, 57, 58].

2.2.1 Passive metasurfaces

2.2.1.1 Colour generation by plasmonics

Unlike the photon absorption in pigments, which is determined by the energy level transitions of the molecules, it has been shown in section 2.1.1 that the scattering and absorption of plasmonic nano-structures are determined by the geometry, dimensions and optical properties of the nano-structured material and dielectric medium in which the nano-particle sits. Coupled with advances in nano-fabrication that have resulted in nano-particles being able to be reliably fabricated down to sub-10nm dimensions, plasmonics now offer a viable alternative to pigment based colour filters[17].

The following sections present the various fabricated structural colour devices from the literature, organised by the structural colour generating mechanism.

Structural colour from localised surface plasmon resonances (LSPR)

Polarisation independent nano-rods A plasmonic colour filter consisting of an array of nano-rods, operating in reflection mode has been shown by Si et al.[59]. The structure of the array is common amongst plasmonic colour filters. An SEM of the nano-rod array is shown in figure 2.11(a). The circular Ag nano-rods are on a quartz substrate with regular size and period. The image in figure 2.11(a,i) shows an array with periodicity of $p = 550$nm. Also shown is a table with the dimensions required for a range of colours, and the spectra for the colours are shown in figure 2.11(a,ii).

When the nano-rod resonator is excited, it radiates a scattering field in proportion to its dipole moment. By altering the diameter and periodicity of the nano-rod array, the array dimensions are optimised to enhance the LSPR efficiencies and to control the reflected colour. To be able to reflect across the entire visible spectrum, the ratio of the diameter of the circular nano-particles to the periodicity was found to be high, up to 0.938. This requires very high nano-fabrication accuracy as the gaps between nano-rods are required to be as low as 20nm. As the nano-rod is circular it responds equally to any polarisation of incident light[17].

Polarisation dependent nano-rods By changing the axial symmetry of the nano-particle it is possible to add another degree of freedom to employ in altering the spectral response of a plasmonic metasurface. Aluminium nano-structures composed of metallic crosses with different arm lengths exhibit strong dependence on the polarisation states[60]. A schematic of the structure is shown in figure 2.11(b,i). The incoming light excites LSPRs in each arm, the amount of light polarised along the axis of each arm determines the overall transmission spectra. Hence as the polarisation of incoming light varies, so does the transmission spectra, and so does the colour. The simulated transmission spectra as the polarisation angle, ϕ of the incoming light rotates is shown in figure 2.11(b,ii). The modelled spectra varies from $\phi = 0°$(blue) to $\phi = 90°$ (yellow) with steps of $\Delta\phi = 10°$. The transmission spectra at an arbitrary value of ϕ is a linear superposition of the vertical ($\phi = 90°$) and horizontal($\phi = 0°$) states[60]

$$T(\phi, \lambda) = T_V(\lambda)\sin^2\phi + T_H(\lambda)\cos^2\phi \tag{2.28}$$

where $T_V(\lambda)$ and $T_H(\lambda)$ are the transmittances for the light polarised vertically and horizontally[60, 17, 58, 13]. The experimental transmission spectra dip is plotted against the cross arm length, L, in (b,iii). The relationship is linear, resulting in a colour shift of the array as the arm length is increased, as shown in the images of the arrays with corresponding arm lengths.

A similar effect can be obtained, with simpler structures than crosses. A rectangular nano-rod, with different width and length will excite two plasmonic resonances across it. Halas et al.[61] fabricated sparse arrays of aluminium on ITO-coated silicon substrate by electron beam lithography (EBL) which exhibit vivid colour of visible spectrum by changing the geometry of the nano-features. The pixels are shown in figure 2.11(c). The schematic and SEM image in (c,i-ii) shows the dimensions and structure of the

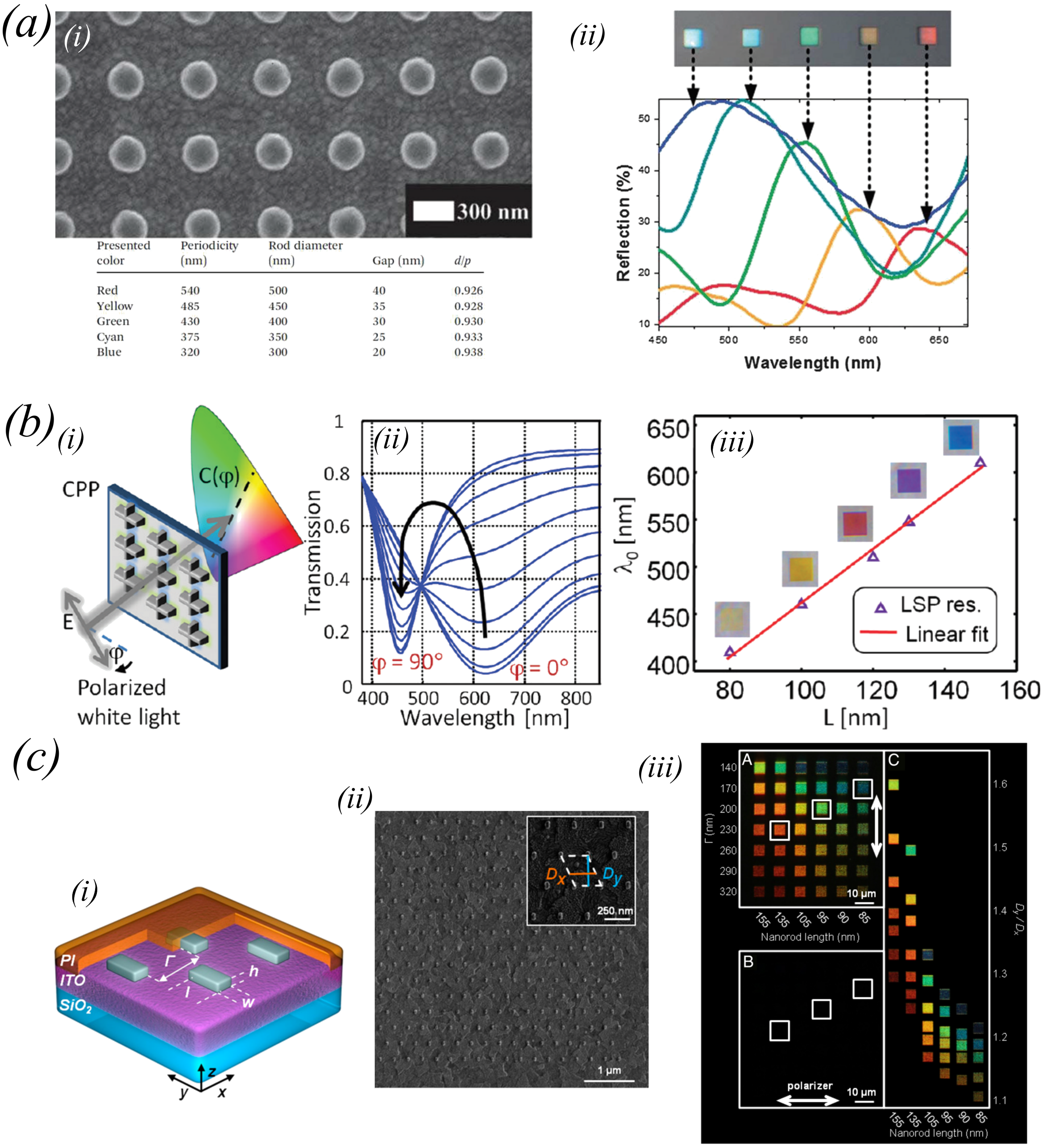

Presented color	Periodicity (nm)	Rod diameter (nm)	Gap (nm)	*d*/*p*
Red	540	500	40	0.926
Yellow	485	450	35	0.928
Green	430	400	30	0.930
Cyan	375	350	25	0.933
Blue	320	300	20	0.938

Figure. 2.11 Localised Surface Plasmon Resonance (LSPR) Colour Generation. (a) Typical Ag nano-rod array[59]. (a,i) SEM image of array and table of dimensions for selected reflected colours. (a,ii) Optical image and experimentally measured spectra of selected reflective colours. (b) Polarisation dependent colour generation[60]. (b,i) Illustration of cross nano-structure operation. (b,ii) Simulated transmission spectra varying input polarisation angle ϕ ($\delta\phi = 10°$). (b,iii) Experimental transmission spectra dip vs cross arm length, L. (c) Al nano-rod pixel[61]. (c,i) Schematic of and (c,ii) SEM image of a $5x5\mu$m plasmonic pixel. (c,iii) Scattering DSLR camera images of Al pixels with light polarised (A) parallel (B) perpendicular to y axis varying size (l) and spacing (Γ) of nano-rods, and (C) as a function of D_y/D_x ratio and nano-rod length l. Red, green, and blue pixels highlighted. Figures re-worked from references.

array. In fact the colour is not only generated by the LSPR of each individual nano-rod but also by diffractive coupling effects. In their paper they show how the size of the nano-rod and the periodicity of the array can vary the colour spectra from the surface as well as narrowing the line shape, intensifying the scattering of light and shifting the scattering peak[61, 58, 13]. The varying colour is shown in figure 2.11(c,iii). The scattering DSLR camera images of the Al pixels polarised (A) parallel and (B) perpendicular to y direction varying size (columns) and spacing (Γ, rows) nano-rods are shown. Whilst in (A) the colours of the pixels span the visible spectrum, under illumination polarised perpendicular to the y-axis, no LSPR modes are excited, hence no colours are reflected. The highlighted pixels in (A) display red, green, and blue colours. (C) shows un-polarised illumination of the pixels with the composite DSLR camera image of individual pixels plotted as a function of D_y/D_x ratio and nano-rod length l.

Structural colour from metallic gratings Metallic gratings offer an alternative to the nano-particle for subtractive filters[62, 17]. The filtering effect is a combination of LSPR and the interaction of short range surface plasmon polariton (SRSPP) between nearest-neighbour nano-structures. For shorter periodicity, the contribution of the SRSPPs was found to be greater than the LSPRs. The result is low transmission at the resonant wavelengths whilst, by using an ultrathin ($<$ 30nm) layer of metal, the transmission away from the resonant wavelengths is high ($60-70\%$) as shown in figure 2.12(a). The grating acts as plasmon coupler and increases the momentum of the incident light to match that of plasmon[13]. By altering the geometric properties of the grating[63], the interaction of light with the grating can be controlled and hence the reflective and transmissive properties can be manipulated[13].

Alternatively, plasmonic gratings can be used for additive colour filters. Combining the grating with a high-index dielectric waveguide layer[65] can result in transmission efficiencies of over 70%. The colour filtering is achieved by the guided mode resonance (GMR) effect. The GMR between the diffracted modes of grating and the guided modes of the planar dielectric waveguide (with Al grating as the upper cladding and a quartz substrate as the lower cladding) is readily induced as long as phase matching is achieved between them. This can be improved once again by constructively interfering the incident wave with the coupled mode[65, 17].

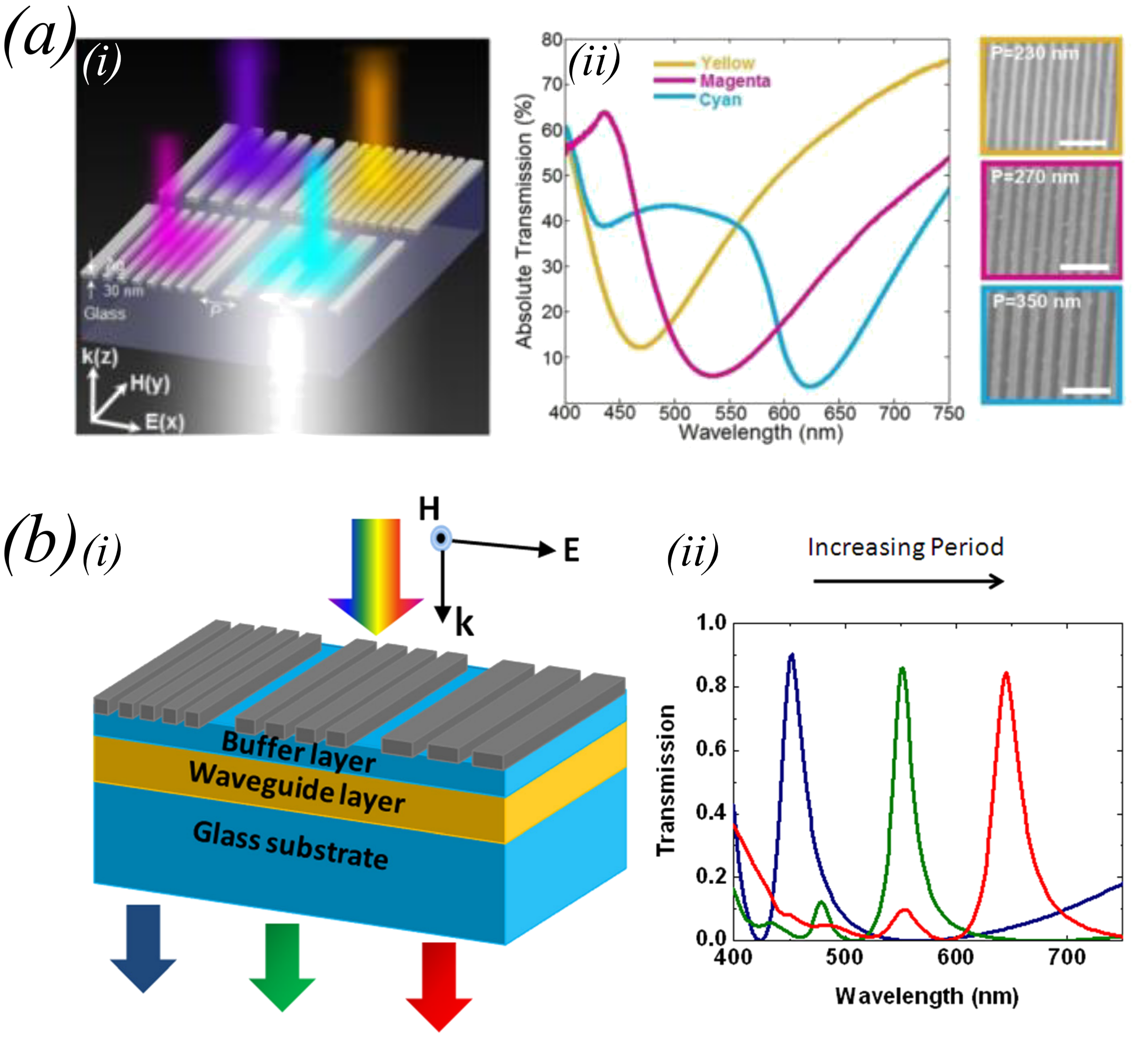

Figure. 2.12 Metallic gratings for plasmonic colour generation (a) Plasmonic subtractive colour filters (SCFs)[62]. (a,i) Schematic diagram of plasmonic SCFs. (a,ii) Measured T_M transmission spectra for cyan (Pitch=350nm), magenta(280nm) and yellow(230nm) SCFs, with SEM images of fabricated nano-gratings. Scale bars, 1μm. (b) Metallic resonant waveguide grating (MRWG) structure[64]. (b,i) Schematic of the transmissive colour filter structure. (b,ii) Simulated transmission spectra of RGB filters. Figures re-worked from references.

Similar structures, shown in figure 2.12(b), using a low-index buffer between the waveguide and the metallic grating have shown a transmittance of ≈ 90%[64]. The thickness of the buffer layer can control the loss of the guided mode in metallic gratings, which can be explained by theory of metal cladding dielectric waveguide[64]. Incident light scattered from the grating couples into waveguide modes at a specific resonant wavelength. When propagating along the waveguide layer, the coupled modes will be scattered again by the wide line-width metal grating. The scattered waves, consequently reflected by the metal grating, will radiate into far field in the forward direction, realising the spectrum filtering effect at the resonant wavelength. The nano-grating with a buffer layer can achieve narrow band resonances and high efficiency in the transmission spectra. This characteristic of high and sharp peaks is suitable for producing colours with high purity[17].

Structural colour from propagating surface plasmons The LSPR in metallic nano-rods produce peaks in the reflection spectrum and dips in the transmission spectrum. According to the Babinet's principle, nano-hole arrays in metal films, being the compliment of nano-rods, the LSPR resonant modes result in dips in the reflection spectra and peaks in the transmission spectra[17, 13]. Whilst this is true, propagating SPPs, excited in the metallic layer of a nano-hole surface, introduce further resonant modes affecting the optical response of a nano-hole surface.

Polarisation independent nano-hole arrays When comparing to nano-rods, which are subtractive colour filters, nano-holes are additive filters. A single nano-hole in an optically thick metallic film has a transmission efficiency proportional to the radius of the hole, r, by $\left(\frac{r}{\lambda}\right)^4$, where λ is the wavelength of the incident light[66]. The resulting transmission from an individual nano-hole is very low. However, a periodic array of nano-holes provides the momentum to convert photons into surface plasmons by the interference of SPPs between neighbouring holes. This is the principle behind the extraordinary optical transmission (EOT) effect, first reported in 1998[67]. Using the EOT effect, a nano-hole array can act like a tunable filter as the transmission spectra can be adjusted just by varying the array period, size of the nano-hole, metal material, and the surrounding environment[13].

The peak transmission, at normal incidence can be approximated by the equation

$$\lambda_{max} = \frac{P}{\sqrt{(i^2 + j^2)}} \sqrt{\frac{\epsilon_m \epsilon_d}{\epsilon_m + \epsilon_d}} \tag{2.29}$$

for a square array, and

$$\lambda_{max} = \frac{P}{\sqrt{\frac{4}{3}(i^2 + ij + j^2)}} \sqrt{\frac{\epsilon_m \epsilon_d}{\epsilon_m + \epsilon_d}} \tag{2.30}$$

for a triangular array. P is the periodicity of the array, ϵ_m and ϵ_d are the relative permittivities of the metal and dielectric material, and i and j are the scattering orders of the array[67, 66]. The lowest order mode ($i = \pm 1, j = 0$), the λ_{max} of the triangular array is smaller than that of the square array with the same period and metallic material. The difference between the first 2 modes of the triangular array are larger than that of the square array, with the consequence that the spectra peaks will be narrower, resulting in less colour cross-talk and 'purer' colours[17, 68, 69]. This fact is supported experimentally with colours achieved shown in figure 2.13(a,b)[68, 69]. Figure 2.13(a) shows structural colours from transmissive nano-hole arrays of varying shape and geometry in an aluminium layer. Optical microscope images the arrays as the periodicity of the arrays vary shown in (a,i), with the triangular array showing a greater colour range and more vivid colours. The microscope images are supported by the spectra measurements shown in (a, ii) with the triangular arrays showing higher and relatively narrower transmission peaks for red (period= 420nm), green (340nm) and blue (300nm) colour filters. Furthermore, what can also be deduced is that the period of the nano-hole array has a more significant effect on the colour than the nano-hole size. Figure 2.13(a,b) shows optical microscope images of a transmissive circular nano-hole arrays with triangular lattice[68]. Variation in the diameter of the nano-hole has relatively little effect on the colour of the nano-hole array, where as the variation in pitch of the array has a significant impact.

Metallic nano-hole layers are generally fabricated on a glass substrate to allow for transmissive operation, this however has the consequence that the permittivities are different on the each side of the nano-hole layer. This asymmetry results in two SP modes, one on each side of the nano-hole layer, with different λ_{max}, resulting in cross talk and less pure colours, whilst the momentum mismatch of the modes reduces transmittance[17].

The resolution of metallic hole arrays is higher than what can be achieved with chemical pigments, which with current printing techniques can reach $\sim 10\mu$m. In figure 2.13(c) the letters h and v are nano-holes in a dimple array. The dimples were fabricated by focused-ion-beam milling an Ag film while the holes were dimples milled through the film, to allow transmission of light. When illuminated the colour of the letter is due to the periods of the nano-holes have hole spacing of 550nm and 450nm resulting in the different colours as well as demonstrating the resolution capability is an order of magnitude greater than that of pigments[66].

Polarisation dependent nano-hole arrays Just as with nano-rods, nano-hole arrays can be made polarisation sensitive by varying their dimensions. Analogous to Ellenbogen et al.[60], Li et al.[70] showed a polarisation-sensitive colour filter by an asymmetric cross-shaped nano-hole made in an aluminium film. By changing the axial symmetry of the nano-hole, it is once again possible to add a degree of freedom to employ in altering the spectral response of the nano-hole surface[13]. Equation 2.28 is still valid in the case of nano-holes hence the spectra from the surface once again depends on the polarisation of light illuminating the surface (in additional to nano-hole geometry) as shown experimentally in figure 2.13(d).

Structural colour from plasmonic mode coupling Colour filters can also be fabricated using a plasmonic waveguide in conjunction with a cavity. The metal-insulator-metal (MIM) structure consists of a finite thickness of dielectric sandwiched between two metal layers. The two metal/dielectric interfaces each support a confined wave of planar SPPs. When the separation between adjacent interfaces is small enough to induce interactions between two planar SPPs, it gives rise to coupled modes of symmetric or antisymmetric profiles with respect to the magnetic-field distributed at the two interfaces. Such modes, propagating along the interface direction, belong to waveguide modes, with the field mainly confined inside the middle dielectric region[56].

Sandwiching of a dielectric between two partially reflective metallic films establishes the resonance condition and provides the selective transmission of the light through the stack[13]. As one might expect the type of metal either side of the dielectric cavity, the thickness of the cavity and the refractive index of the cavity material are the major

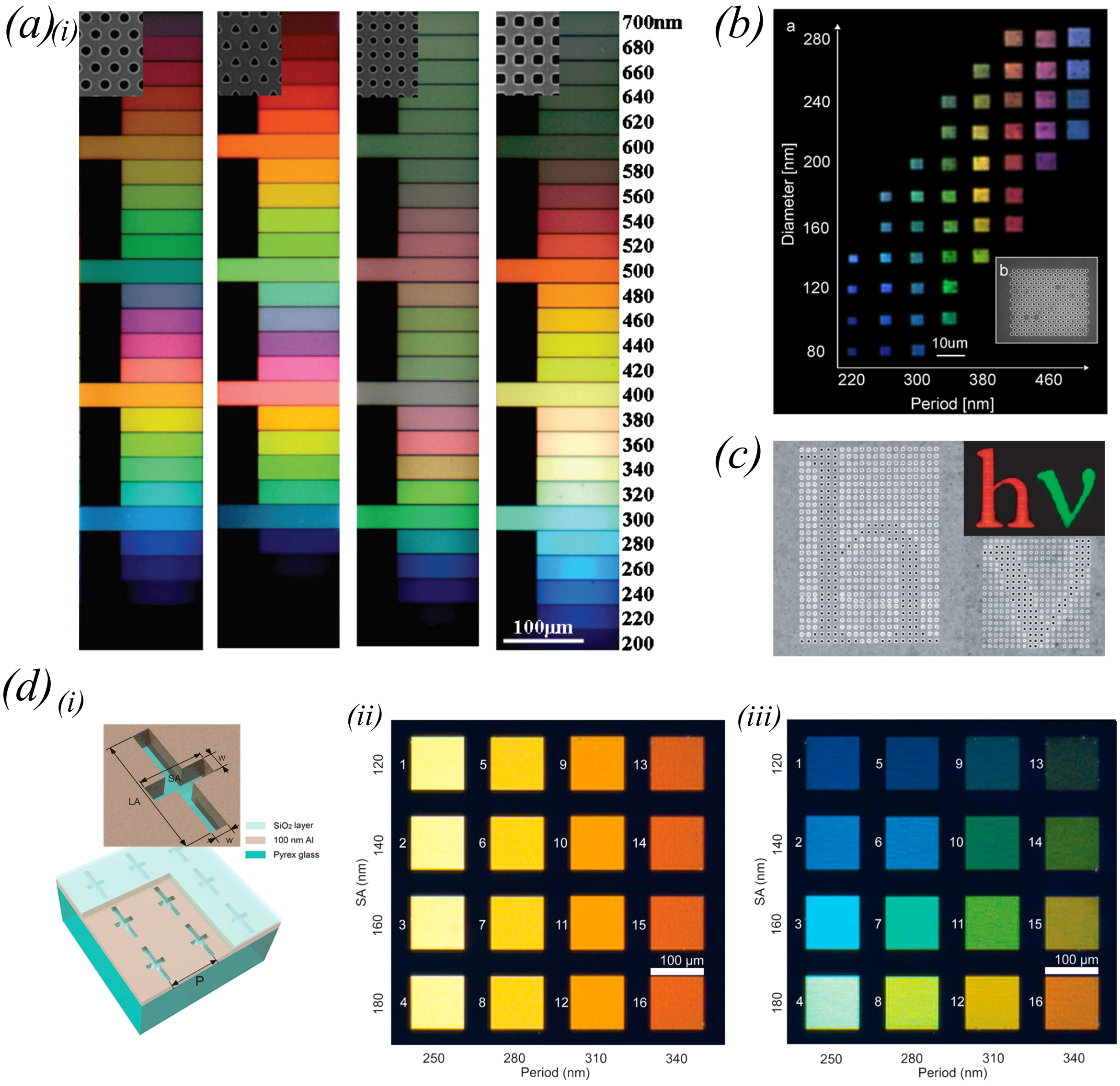

Figure. 2.13 Structural Colour from Propagating Surface Plasmons (a) Colours from transmissive nano-hole arrays of varying shape, geometry and periodicity[69]. Inset: SEM image of nano-hole arrays. (b) Colours from transmissive circular nano-hole arrays with triangular lattice varying hole diameter (y axis), and hole period (x axis)[68]. Inset: SEM image of nano-hole array filter with $p = 420$nm and $d = 240$nm. (c) Nano-holes in a dimple array generating the letters *hv* in Ag film[66]. SEM images shows structure of array which when illuminated (inset) produces different colours due to the pitch of the nano-holes (red= 550nm, green= 450nm). (d) Polarisation dependent nano-hole structure and colours[70]. (d,i) Schematics of nano-holes, showing aperture geometry and arrangement. (d,ii-iii) Images of polarisation switchable colour palette in transmission with illumination polarised along (iii) x- (short arm) and (iv) y-axis (long arm). Images taken using optical microscope unless otherwise stated. Figures re-worked from references.

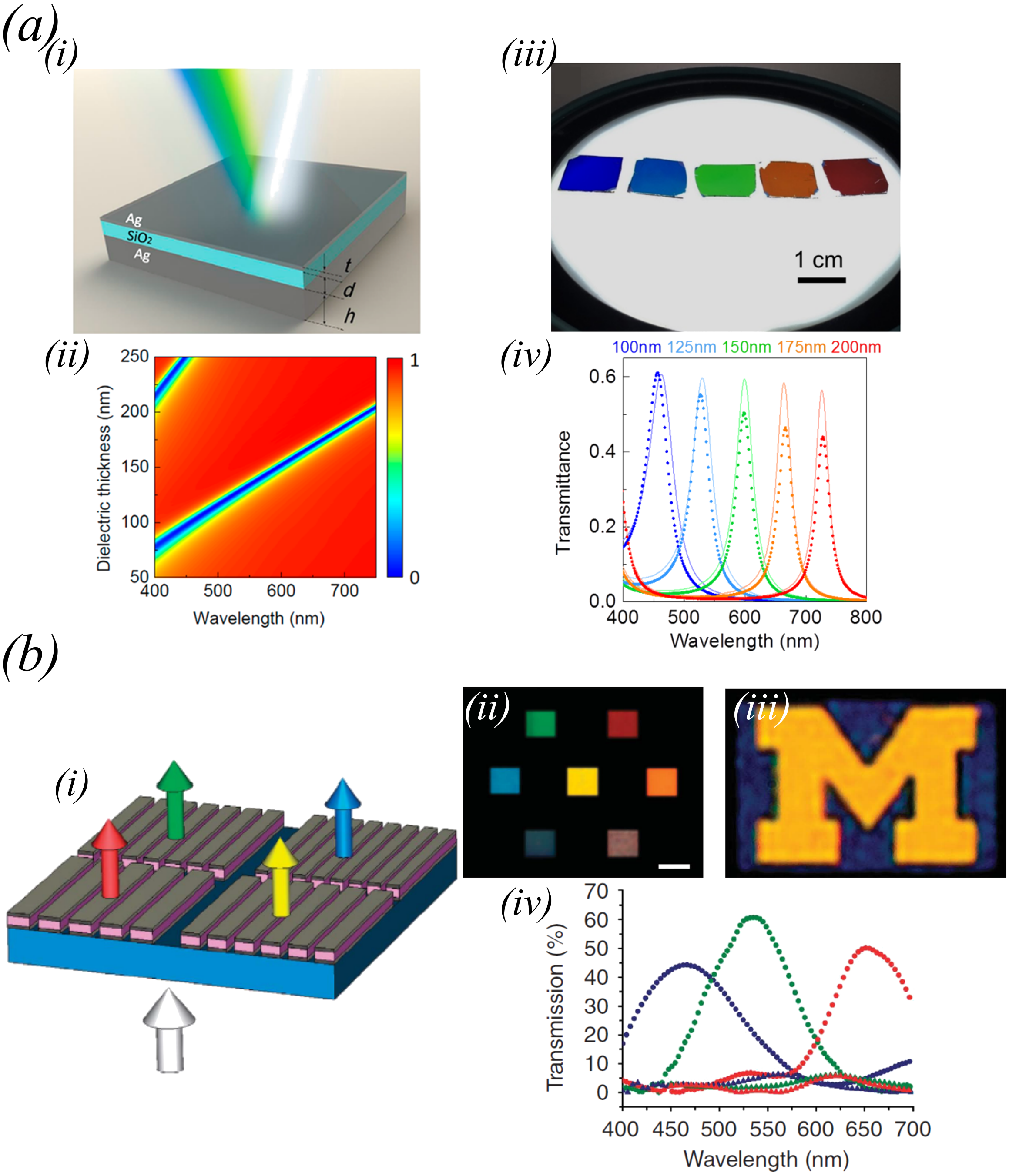

Figure. 2.14 Structural Colour from Plasmonic Mode Coupling. (a) Planar MIM structure for colour filtering[71]. (a,i) Schematic configurations of planar thin-film MIM cavity. (a,ii) Reflectance plotted as a function of wavelength and dielectric thickness d with optically thick backplane ($h \sim 100$nm). (a,iii) Planar MIM structure with optically thin backplane ($h \sim 30$nm) in transmission with corresponding measured (dots) and simulated (solid line) transmission spectra. Colour variation is due to change in SiO_2 layer thickness ($d = 100 - 200$nm). (b) Plasmonic nano-resonators formed by MIM stack arrays[72]. (b,i) Schematic diagram of plasmonic nano-resonators. (b,ii) Optical microscopy images of seven plasmonic colour filters varying grating periodicity from 200 – 360nm. Scale bar, 10μm. (b,iii) Experimentally measured transmission spectra of RGB colour filters for T_M (circle) and T_E (triangle) illuminations. (b,iv) Image of yellow 'M' (period=220nm) on blue background (p=310nm) pattern illuminated with white light. Figures re-worked from references.

factors that determine the wavelength of light transmitted. Li et al.[71] demonstrated a planar thin-film MIM cavity device with a 100nm zinc-selenide film sandwiched by two 40nm thick aluminium layers fabricated on top of MgF_2 used as transparent substrate. A schematic of the structure is shown in figure 2.14(a). The device may be used in reflection or transmission, by utilising either an optically thick or thin lower metallic layer. When the back layer of metal is optically thick, the lower layer acts as a mirror and a super absorber can be constructed. The device can absorb up to $\approx 97\%$ of the incident light, with a narrow peak. The absorption is due to coupling of incident light to the fundamental Fabry-Perot resonance mode of the structure[71, 72]. These devices are planar, hence do not have a small pixel dimensions, and do not utilise any plasmonic resonance as there is no mechanism to overcome the momentum mismatch between the incident radiation and plasmonic resonant mode. They are essentially an asymmetric Fabry-Perot type resonator, comprised of lossless core dielectric with partially reflective top metal layer and, depending on the device, an optically thick highly reflective mirror or a lower partially reflective bottom metal layer.

By reducing the planar dimesnions of the MIM structure, Guo et al.[72] created a MIM grating structure, illustrated in figure 2.14(b), in which plasmonic resonances may be excited. The bottom Al grating is used to couple selectively the incident light into plasmon waveguide modes by diffraction, whereas the top Al grating efficiently reconverts the confined plasmons to propagating waves by scattering, transmitting the light, forward out of the device[13].

By combining the MIM structure with other nano-structures, different plasmonic modes can be coupled to the benefit of colour generation. For example a MIM nano-structure of nano-rods over a nano-hole surface with a dielectric partitioning layer, shown in figure 2.15(a), has been shown to generate strong colours. The top layer of nano-rods provide LSPRs and the bottom nano-hole layer provides propagating SPPs. The degree of coupling between the two layers is determined by the thickness of the dielectric layer between them. In fact, when sub-wavelength-sized holes in an optically opaque metal film are completely covered by opaque metal disks larger than the holes, the light transmitted through the holes is not reduced, but rather enhanced[73]. Using the structure in reflection Kumar et al.[74] deposited a thin layer of Au-Ag on hydrogen silsesquioxane (HSQ) pillars on a silicon substrate. Once again by varying the size of the nano-rods, the nano-holes and the thickness of the spacing layer the colour reflected can be tuned, whilst both periodic and aperiodic structure can result in various colours,

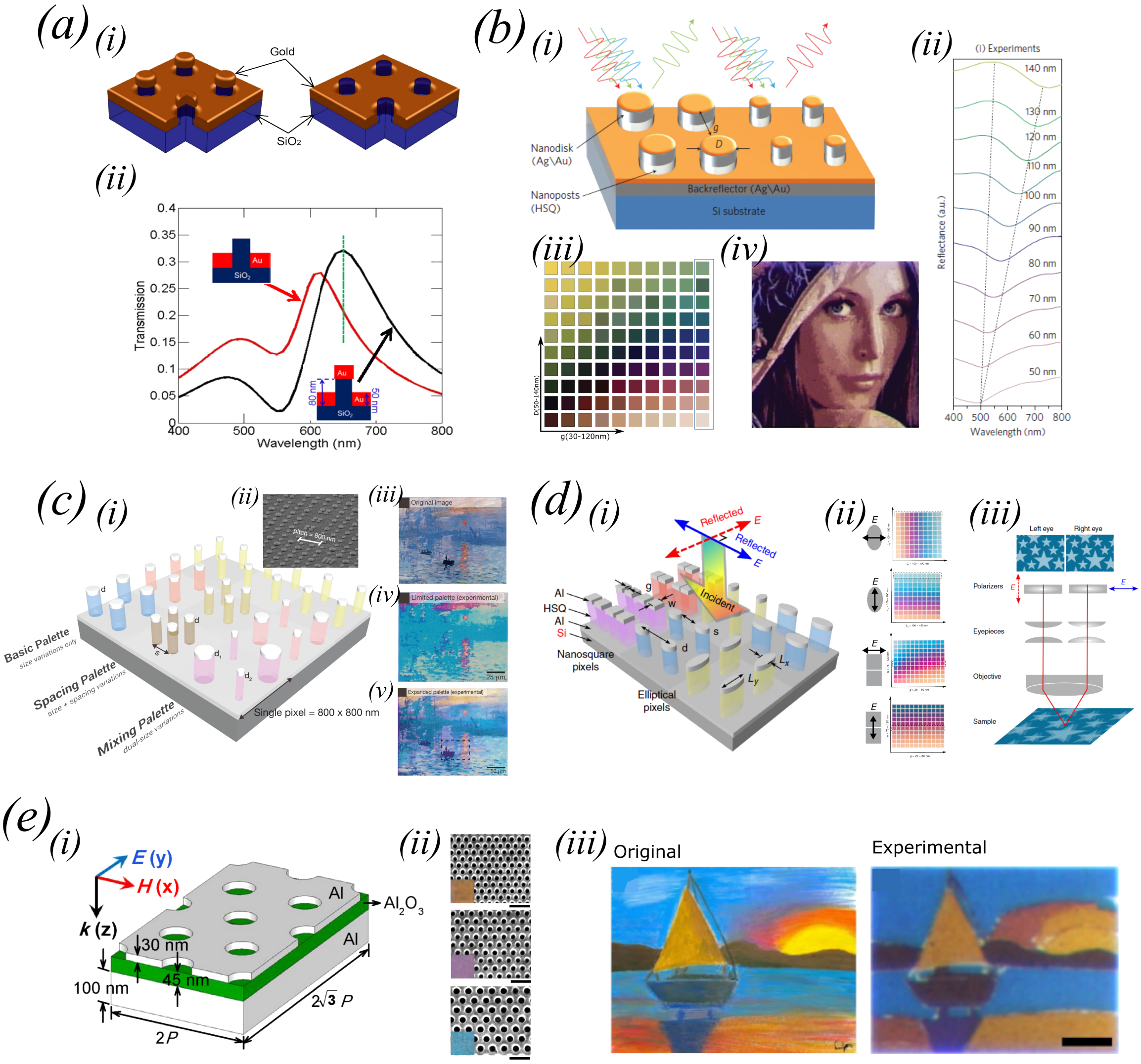

Figure. 2.15 Structural Colour from Plasmonic Mode Coupling. (a) Sub-wavelength metallic hole arrays with and without metal nano-disk blockers[73]. (a,i) Schematic of and (a,ii) simulated transmission spectra of Au pixels. (b) Plasmonic colours from MIM nano-hole/disk array[74]. (b,i) Schematic of and (b,ii) experimentally measured reflection spectra of pixel varying D,($g = 120$nm). (b,iii) Image of nano-structure arrays varying D and g. (b,iv) Image of Lena created using pixels. (c) Plasmonic colours from MIM nano-hole/disk array varying dimensions within 4x4 structure pixel[75]. (c,i) Schematic and (c,ii) SEM of Al plasmonic pixels. (c,iii-v) Original of Monet's Impression and recreations using (iv) RGB and (v) full colour range MIM nano-hole/disk structure. (d) Polarisation-dependent plasmonic MIM pixels[76]. (d,i) Schematics of and (d,ii) Images of elliptical and nano-square arrays with varying dimensions, illuminated under y- and x-polarised light. (d,iii) Schematic of a stereomicroscope setup, resulting in depth perception. (e) Colour using MIM nano-hole[77]. (e,i) Schematic of pixel. (e,ii) SEM images of three distinct colour samples. Insets: colour image of array. Scale bar= 500nm. (e,iii) Original and recreated image using MIM nano-hole pixels. Scale bar= 500μm. Images taken using optical microscope unless otherwise stated. Figures re-worked from references

the latter is angle insensitive[13]. The effect of the coupling is that the variation in peak transmittance or reflectance is more sensitive to the change in physical parameters. In figure 2.15(b,iv) the image of Lena is produced by only varying the nano-disk size, whilst the pitch is constant at 125nm. The colour map obtained by varying the nano-rod/hole size and periodicity of the array is shown in figure 2.15(b,iii). Tan et al. took this a step further, by using the MIM nano-structures, but defining a pixel as 4 nano structures within an 800nm×800nm square, and then varying the nano-rod/hole size and pitch within the pixel to produce a mixed colour palette[75] shown in figure 2.15(c). By adding the extra dimensions of varying the structures within a pixel, a larger range of the colour spectrum is accessible as demonstrated in their reproduction of Monet's "Impression, Sunrise" painting that was poorly reproduced by the primary plasmonic colour palette, but was vastly improved with the mixing palette (figure 2.15(c,iii)). This extra flexibility, also means that as opposed to using a mix of Au and Ag, only Al was used which is preferable as it has a neutral tint (unlike Au), is durable and low cost[17].

As with simple nano-rod or nano-hole arrays, by using an asymmetric geometry of the nano-structures, the spectral response can be made polarisation dependent. Goh et al.[76], not only demonstrated the ability to control the reflection spectra of orthogonally polarised light enabling two different colour images to be encoded into the same area, but used this to create stereoscopic effects, by modulation of the two alternatively polarised images to realise 3D plasmonic stereoscopic prints[76, 17].

If the lower layer is continuous, rather than a nano-hole layer, another mechanism can be used for colour generation. Gap surface plasmons (GSPs) can be generated using a MIM nano-structure containing Au nano-rod arrays on the top of a thin dielectric layer, with a continuous layer of Au underneath[78]. By adjusting the geometry of the nano-rods and te thickness of the dielectric layer, the reflected colour can be tuned. The advantages of using such a nano-structure include the angle independence of the reflection spectra and the relative insensitivity of the spectra to the surrounding index (the separating dielectric layer not included in this definition of surrounding index). Both of these advantages are of great value in practical applications[17]. Similar results can be seen when using a nano-hole layer in a MIM structure as shown in figure 2.15(e)[77]. The structural colour came from an Al nano-hole surface separated from a continuous optically thick surface of Al by a dielectric layer. The fabricated device supported near perfect light absorption with a narrow-band spectral response tunable across the visible spectrum, with the same advantages as seen in the MIM nano-rod structure.

2.2.1.2 Wavefront modulation by plasmonics

In addition to structural colour, plasmonic nano-structures offer a way to control the wavefront of EM waves. As opposed to conventional devices, which shape the wavefront via propagation through media of given refractive indices that can be engineered to control the optical path of light beams, a plasmonic metasurface can create abrupt changes in the phase of a wavefront. Furthermore the abrupt changes also reduce the dependence of light propagation for diffractive effects. This means plasmonic metasurfaces are able to realise extraordinary light manipulations, such as light bending, focusing, waveplate, vortex beam generation and holograms, in a confined region[20, 57].

Plasmonic phase discontinuities The resonant LSPR mode in a nano-rod will occur at a given wavelength, λ_{res}, when the rod is of a length L_{res}. Assuming our rod is excited by a single fixed wavelength, if we increase/decrease the length of the nano-rod the charge oscillations in the nano-rod lags/leads the driving E-field. Hence by choosing different rod lengths it is possible to control the phase of the scattered waves[20]. Using a single nano-rod one can achieve a phase change of $0 - \pi$, however using multiple resonances in a nano-structure, a phase response can be tuned over the full $0 - 2\pi$ range.

V-shaped sub-wavelength antennas were first proposed and experimentally demonstrated to control the propagation of linearly polarised light at mid-infrared (MIR) range[79]. The V-shaped antenna support a symmetric and antisymmetric modes, shown schematically in figure 2.16(a,i), excited by components of the incident field along $\hat{s}$ and $\hat{a}$ axes. When the incident radiation is polarised along the $\hat{s}$ and $\hat{a}$ axes only the symmetric or anti-symmetric mode is excited, and thus the scattering is polarised the same an the incident radiation. For an arbitrarily polarised illumination, both antenna modes are excited but with very different phase and amplitude, owing to the distinct resonance conditions, resulting in scattered light which can have a polarisation different to the illumination polarisation. For example, when illuminated with light polarised at 45° to the $\hat{s}$ and $\hat{a}$ axes, observing the scattered light that is polarised orthogonally to the incident light, the combination of the two modes in the antenna

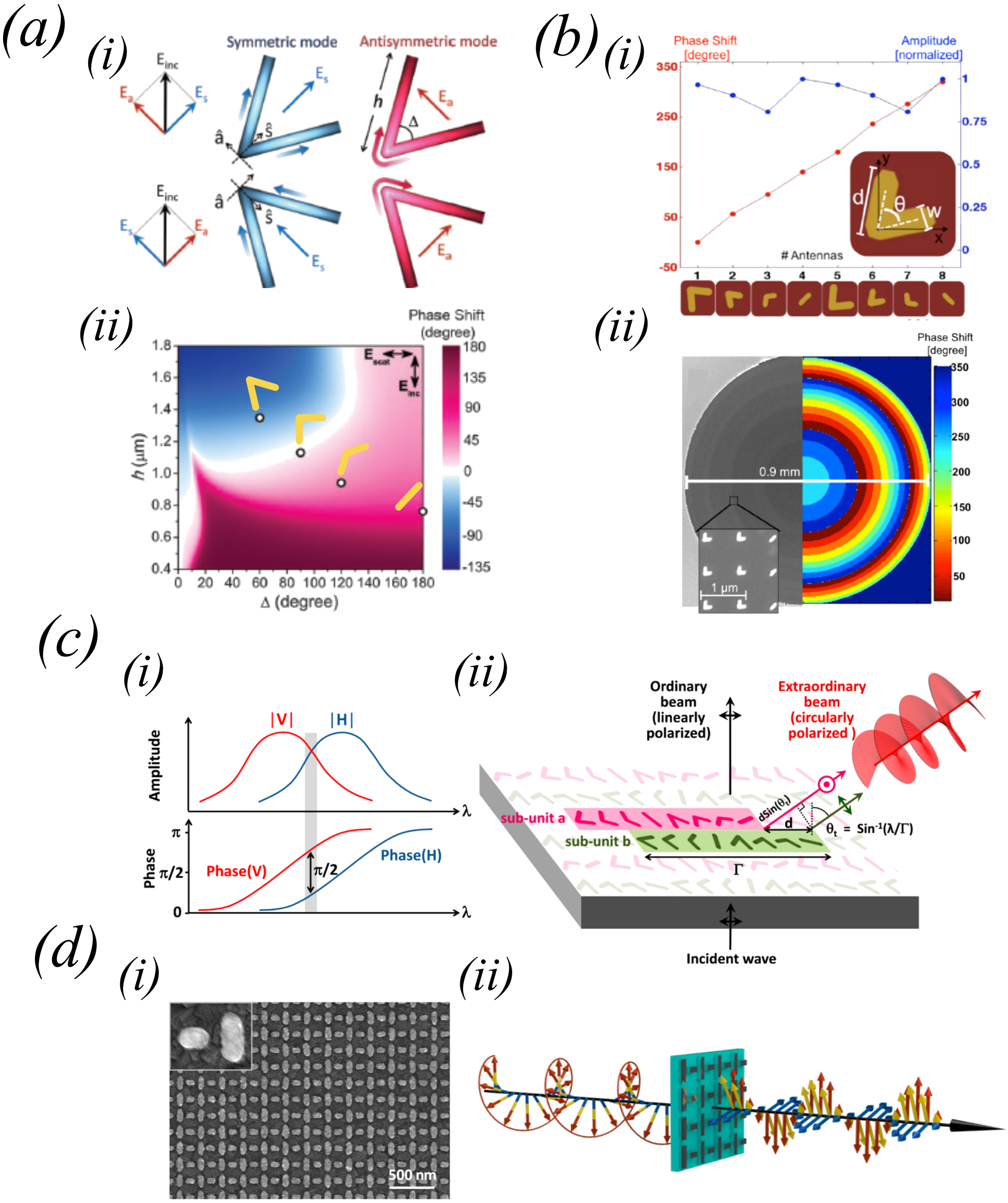

Figure. 2.16 Plasmonic Phase Discontinuities in the IR. (a) Phase control of scattered EM-wave using V-shaped antenna[79]. (a,i) Schematic of symmetric and antisymmetric modes supported. (a,ii) FDTD simulated phase of scattered light varying V-shape antenna arm length(h) and angle(δ) ($\lambda = 8\mu$m). (b) Plasmonic phase discontinuities in the IR to create a Fresnel Lens[80]. (b,i) FDTD simulated phase shifts and scattering amplitudes of V-shaped antenna ($\lambda = 1.55\mu$m). (b,ii) SEM image and and corresponding phase shift profile of the fabricated lens with 3cm focal length. (c) Plasmonic quarter-wave plate (QWP)[81]. (c,i) Amplitude and phase of orthogonal plasmonic eigenmodes (V,H), shaded area is region where phase difference of $\psi \sim \frac{\pi}{2}$. (c,ii) Schematic of device operation, showing excitation by linearly polarised light generating a circularly polarised beam. (d) Plasmonic quarter-wave plate (QWP) at visible wavelengths, circular to linear polarisation[81]. (d,i) SEM of QWP nano-structure. (d,ii) Schematic of device operation Figures re-worked from references.

results in scattered light with an alternate phase. The phase and amplitude of the scattered light depends on the length, h, of the arms of the V and the angle, Δ, between them. Figure 2.16(a,ii) plots the dependence of the phase on h and Δ when illuminated with an EM wave of $\lambda = 8\mu$m. By altering h and Δ, phase shifts of almost $\pm\pi$ may be achieved.

In order to increase the efficiency of phase change structures, MIM-structures can be used[82]. The idea is to use antennas coupled with their bipolar images in the back plane to achieve a phase coverage of 2π. This approach has the advantage that the antenna scattering efficiency is significantly higher than that of the single-layered design (for example, 80% v. 20% in reflection)[83] because transmission is suppressed by the back plane with the additional advantage that the polarisation of the reflected light is the same as that of the incident light[20].

Using the phase alteration properties of plasmonic metasurfaces, optical components can be created. Aeita et al.[80] fabricated flat lenses based on V-shape antenna, using the phase change of the different V-shaped antennas to recreate a Fresnel lens (figure 2.16(b)). Yu et al.[81] demonstrated a metasurface quarter-wave plate. The QWP only operates when the two orthogonal eigenmodes, V and H, of arrays of identical anisotropic plasmonic structures, have approximately equal scattering amplitudes and phase difference of $\psi = \pi/2$. This region, shown in figure 2.16(c,i), only occurs in a narrow wavelength range. A schematic of the surface is shown in figure 2.16(c,ii). Using a combination of antenna rotation and dispersion both the phase and polarisation response of the metasurface is engineered so that when a linearly polarised beam normally encounters the metasurface it creates a circularly polarised beam, comprising of two generated co-propagating waves with equal amplitudes, orthogonal linear polarisations and a $\pi/2$ phase difference, propagating away from the surface normal[57].

The examples so far have demonstrated how sub-wavelength plasmonic structures can control the phase of EM waves at IR wavelengths. To interact with visible light sub-wavelength structures become nano-structures. By arranging nano-rods in a broken T-configuration, shown in figure 2.16(d), Zhao et al.[84] created a surface that is able to modify the polarisation of visible light by 90°. The quarter wave plate (QWP) introduces an orthogonal phase delay, utilising the detuned resonances of two nano-rods by tailoring their lengths. The QWP operates over a broad bandwidth 615-835nm with peak conversion efficiency of $\approx 50\%$. The transmitted beam is linearly polarised at different angles as a function of the impinging wavelength.

Plasmonic Holograms By shrinking the dimensions of the antennae, arrays of V-shaped nano-structures can be used to control the phase of visible light. This approach can be used to create a Fresnel zone plate for visible wavelengths, and can also be used to make phase holograms.

The fact that a metasurface has the ability to create an abrupt change in the phase and/or amplitude of an incoming wavefront to a nano-scale dimensions makes them ideal for creating holograms with nano-scale pixels which have the potential to alleviate issues such as high-order diffraction and twin-image issues[57]. To create phase only holograms Shalaev et al.[85] used V-shaped nano-holes to control the phase of linearly polarised light as it passed through the metasurface. Shown in figure 2.17(a,i), illumination of the hologram results in an image in the far field that has no conjugate, which has been hypothesised to be due to the sub-wavelength nature of the hologram pixels[86]. By changing the angle between the two arms and modulating their length, eight discrete phase changes were used to create the image of letters in the far field, shown in (figure 2.17(a,ii)). The hologram, designed to operate at 676nm, whilst no energy is diffracted into higher order modes, has an efficiency of $\approx 10\%$. Despite being low this is better than other demonstrated metasurface holograms.

In addition, nano-features can be used to create amplitude only holograms. In this case nano-structures of consistent size are used to scatter light. The scattering from each element will be in phase and each scattering element can be used as an individual amplitude modulating pixel. Huang et al.[86] used nano-holes distributed in a quasi-random distribution to create a hologram with a far field image, shown in figure 2.17(b,i), which once again has no conjugate image and loses no energy to high order diffraction modes.

Furthermore Huang et al. used a quasi-periodic distribution to recreate a lens to focus light with high resolution circular focusing spot shown in figure 2.17(b,ii). The lens comprised of nano-holes, uniformly allocated in concentric non-periodically distributed rings as shown in figure 2.17(b,iii). As the ring radius (R_n) increases the radius of the nano-holes (a_n) decreases. Hence, the overall structure exhibits aperiodic behaviour in a_n and R_n, which allows it to sieve light with appropriate amplitude and phase for achieving a small spot[86].

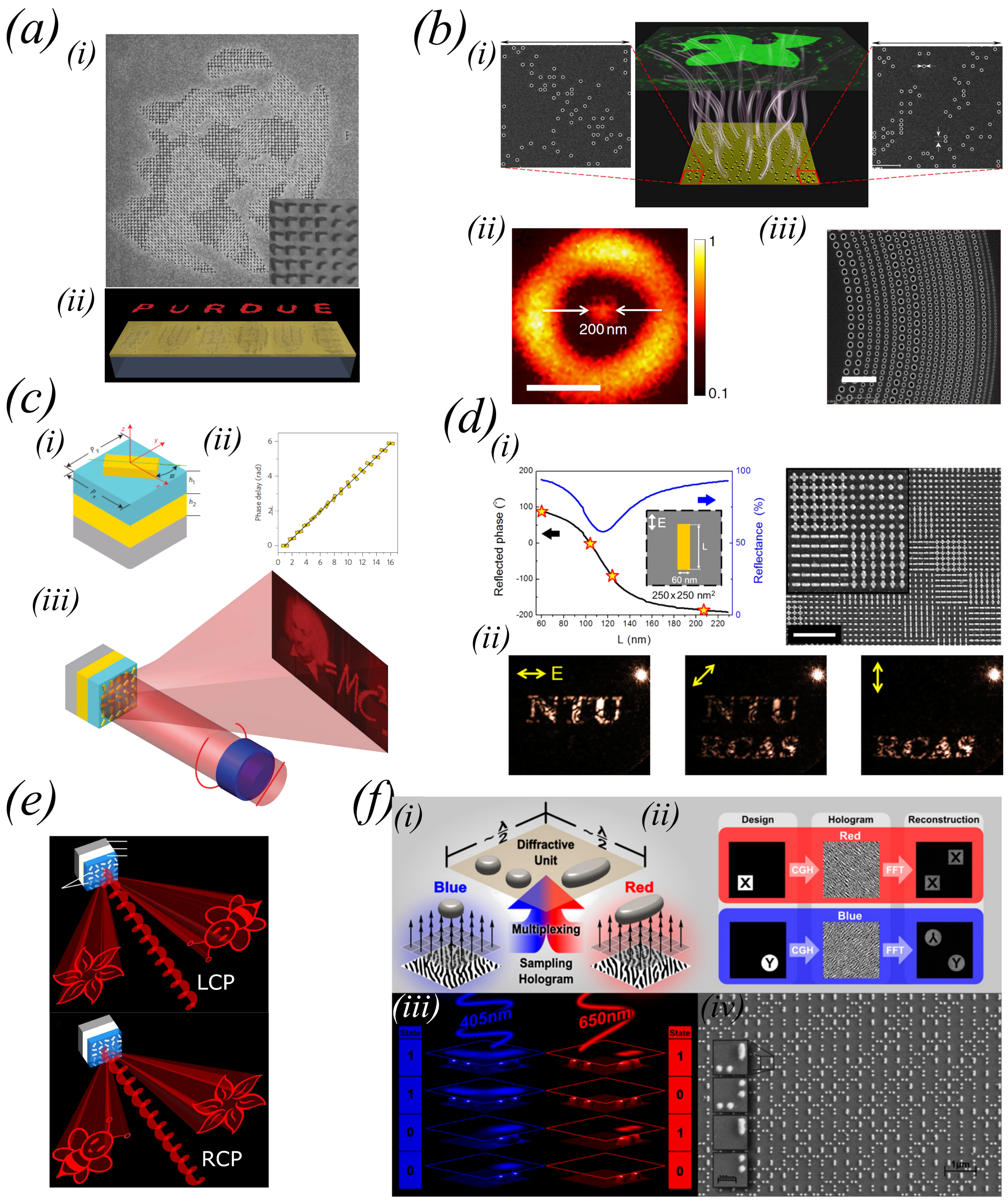

Figure. 2.17 Plasmonic Holograms for visible light. (a) V-shaped nano-antennas for visible light holograms[85]. (a,i) SEM image and (a,ii) schematic of hologram with subsequent far-field images. (b) Holograms designed with sub-wavelength nano-holes[86]. (b,i) SEM images of hologram and far-field image that lacks conjugate image. (b,ii) Measured focal spot of 200nm and (b,iii) SEM of focus hologram. (c) High efficiency phase holograms, using MIM structure[87]. (c,i) Schematic of unit cell of phase hologram. (c,ii) Plot of phase delay versus the orientation angle (ψ) of the nano-rod in the x-y plane. (c,iii) Illustration of the reflective nano-rod-based CGH under a circularly polarised incident beam. (d,e) Polarisation dependent hologram[88, 89]. (d,i) Reflected phase and amplitude versus length of periodic nano-rods. (d,ii) SEM image of the hologram. Scale bar is 2μm. (d,iii) Image of far field pattern of hologram under different polarisation states. (e) Illustration of circularly polarisation dependant hologram by Wen et al.[89]. (f) Colour and polarisation multiplexed holograms[12]. (f,i-ii) Design process for dual colour hologram. (f,iii) Simulation of dual-colour pixel scattering. (f,iv) SEM image of the fabricated hologram. Figures re-worked from references.

The efficiency of metasurface holograms can once again be increased by introducing a MIM structure. Zhang et al.[87] created a phase only hologram using nano-rods separated from a metallic back plane by a dielectric layer. The degree of phase modulation is dependant on the planar orientation of the nano-rods. The phase only hologram is patterned on a dielectric (MgF_2) spacer layer on top of an optically thick gold layer. The 16-level-phase computer-generated hologram combines a geometric metasurface for control of the phase profile with a reflect arrays for achieving high polarisation conversion efficiency (figure 2.17(c)). The result is a phase only reflection hologram, operating with circularly polarised light, with diffraction efficiency $\approx 80\%$.

Polarisation dependant holograms As with colour generation using plasmonic nano-structures, by asymmetrically altering their shape, the plasmonic nano-structures that make up the hologram the pattern in the far field can be designed to be polarisation dependant. One way that has been shown to achieve this is using a cross as a base pixel, picking 4 lengths of each cross arm to correspond to 4 discrete phase levels, with phase separation of $\pi/2$, for the hologram. Combining the 4 lengths of the discrete phase levels on the two orthogonal axes of the cross, the result is 16 different pixels that can multiplex 2 polarisation dependent holograms onto the same surface[88] (figure 2.17(d)). The cross design is one that operates with linear polarised light, however, it is possible achieve similar results with circularly polarised light[89]. This achieved by once again using nano-rods with spatially varying orientations. By overlaying two holograms with pixel pitch d, sensitive to left-hand circularly polarised light (LCP) to end up with a single hologram with pixel pitch of $d/2$, the far field contains both the images of the individual holograms. If such a hologram is then illuminated with right-hand circularly polarised light the spatial image location of the two images in the far field is then inverted as shown in figure 2.17(e).

Multicolour polarisation dependant holograms By combining the wavelength sensitivity of plasmonic nano-structures with their polarisation sensitivity, Montelongo et al.[12] demonstrated holograms that were not only sensitive to the polarisation of incoming light but to the wavelength of the illuminating radiation also. The holographic structures previously discussed in this chapter are either designed to be broadband or whilst they have different sensitivities to different wavelengths, a change in wavelength affects the diffraction efficiency of the hologram it does not change the target image into the far field. When multiple arrays of plasmonic nano-particles are multiplexed without coupling, they carry independent information such as polarisation and wavelength to the far field. The colour and polarisation dependent hologram, shown in figure 2.17(f), is designed by taking two CGH amplitude holograms then multiplexing them into one hologram. Each pixel of the multiplexed hologram has 4 states. The pixels themselves are fabricated by spatially multiplexing two different nano-particles with different spectral emissions on a SiO_2 substrate. In the case of Montelongo et al.[12], blue and red colours of light are used coming from the scattering of 60nm diameter nano-spheres and nano-rods of 60nm width and 165nm length, respectively. To balance the intensity emission of both colours, the nano-spheres were placed in pairs, whilst the 'red' nano-rods showed a secondary peak in the blue region, and as a consequence, to remove the blue peak and the resulting secondary blue hologram, a pair of nano-spheres is used as an alternative to a missing nano-rod when the red hologram is required to show a 'zero'.

2.2.2 Dynamic metasurfaces

Plasmonic metasurfaces open up a large range of possibilities in flat optics, colour generation, holography etc. however the full potential of metasurfaces is yet to be realised. In areas such as optical switches or displays, dynamic tuning of the optical responses is highly desirable. Despite the progress of passive plasmonic surfaces, dynamic tuning of the optical responses still remains a challenge.

2.2.2.1 Dynamic plasmonic colour generation

Despite the challenges there are several ways in which efforts have been made to dynamically tune the colour response of plasmonic pixels

Electrochromic switching Electrochromic materials, including various transition metal oxides and conducting polymers, show a reversible colour change on electrochemical reduction, or oxidation, by application of a small voltage. By incorporating electrochromic materials into an array of nano-slits, Xu et al.[90] created dynamic pixels with binary on/off states, whose colours in the on state depends on the pitch of the nano-slits. The structure for the pixels is shown in figure 2.18(a). The working electrode designed for monochromatic operation incorporates an Au film patterned with a nano-slit array, conformally coated with a thin layer of electrochromic material

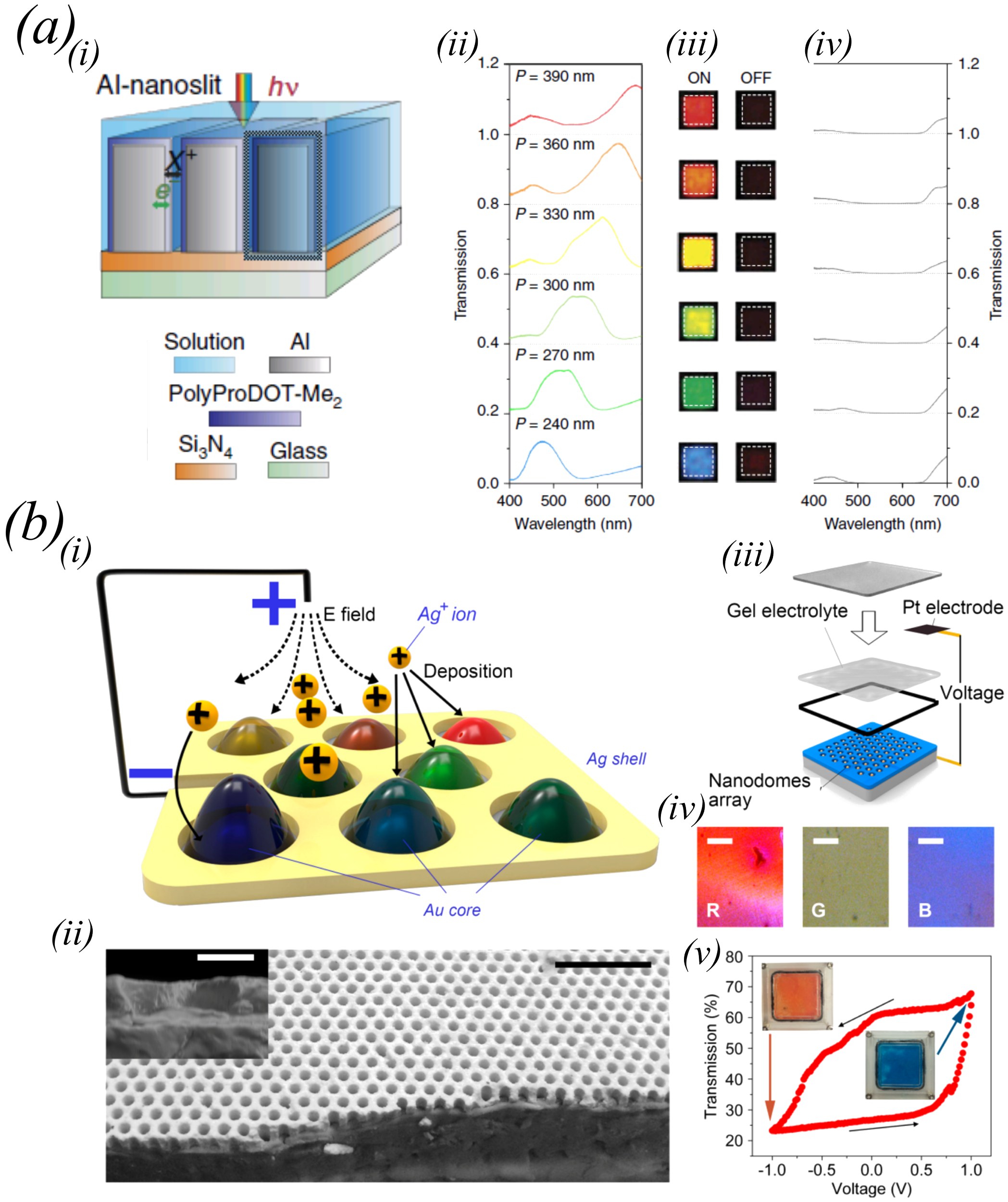

Figure. 2.18 Electrochromic switching for plasmonic surfaces. (a) Plasmonic electrochromic nano-slit electrodes[90]. (a,i) Schematic of a plasmonic electrochromic electrode incorporating Al-nanoslit array of pitch ($P = 240 - 390$nm). (a,ii,iv) Transmission spectra of plasmonic electrochromic electrodes in on(ii) and off(iv) states, with varying period and corresponding (a,iii) images. (b) Plasmonic electrochromic nano-dot electrodes[91]. (b,i) Structure and function of the plasmonic cell devices. (b,ii) SEM image of the SiO$_2$ nano-hole array formed after etching. Scale bar= 100nm. Inset: Cross-sectional SEM image of one SiO$_2$ nano-hole. Scale bar= 50nm. (b,iii) Formation of the working plasmonic cell. (b,iv) Image of the device's RGB colours. Scale bar= 50μm. (b,v) Transmission of 600nm light as a function of electro-deposition voltage. Inset: Photo of the plasmonic cell device at the start and end voltage. Figures re-worked from references.

immersed into electrochemical cells. The pixels operate by applying various voltages to the cells. When the voltage is applied the polymer switches between the reduced and oxidised states, causing a change in the refractive index of the environment surrounding the slits and thus altering the optical absorption characteristics of the pixel. As a result strong optical absorption can be realised using a thin electrochromic polymer layer, while simultaneously achieving a fast switching time due to correspondingly small charge-propagation distance, in pixel of size the order of microns[90, 13].

Wang et al. demonstrated dynamic tunable colour changes in metasurfaces based on bimetallic nano-dots arrays[91, 13]. Shown in figure 2.18(b) the cell consists of an array of nano-holes filled with Au. The array of gold nano-dots is one side of a cell filled with gel electrolyte containing Ag+ ions. When a voltage is applied across the cell, electro-deposition of Ag occurs on the gold nano-dots, altering the permittivity, and thus the plasmonic resonance, of the nano-dot and thus its spectral response under illumination. In their work they experimentally demonstrated robust dynamic colour change and even developed a mechanical chameleon based on this concept[91, 13]. There is, however, a lack of reproducibility of the Ag electro-deposition onto the nano-dots and the long term stability of silver is poor due to it sulfidation[41].

Liquid crystal switching As the plasmonic resonance of a plasmonic metasurface is dependent on the permittivity of the medium in which the structure sits, liquid crystals, due to their anisotropic optical properties have the potential to be integrated into active colour plasmonic devices. The potential of liquid crystals is hindered by the significant surface anchoring forces they encounter, preventing full re-orientation of the liquid crystal and hence limiting the birefringence than can be utilised in such devices.

Buchnev et al.[92] proposed a hybrid plasmonic metasurface-liquid crystal device, with a novel surface structure to overcome surface anchoring and engage in-plane switching of liquid-crystal molecules on the nano-scale. The metasurface, shown in figure 2.19(a,i), is based on a double-periodic array of connected V-shaped plasmonic resonators forming a continuous *zig-zag* wire pattern. The LC is set-up with a twist structure, and the re-orientation of the LC at the plasmonic metasurface was from aligned to the zig-zag structure to aligned in-plane between the zig-zags as the re-alignment E-field was applied in-plane between the nano-wires. The overall shift in plasmonic resonance was 7%, however the pixels operate at the near IR wavelengths, hence whilst effective electro-optic switching is demonstrated, it is not in the visible wavelength range.

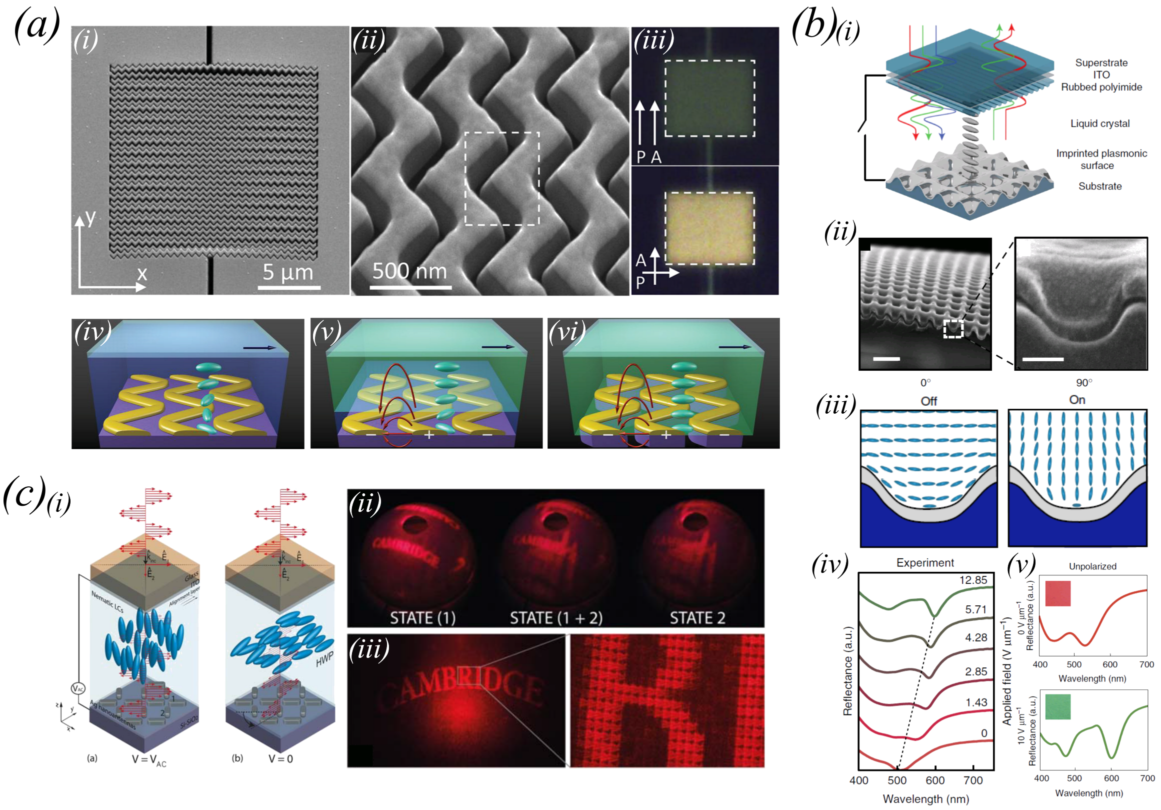

Figure. 2.19 Liquid crystal(LC) switching for plasmonic surface. (a) Suspended zig-zag metasurface to overcome LC surface anchoring effects[92]. (a,i,ii) SEM image of metasurface. (a,iii) Polarising optical microscope images of metasurface-LC cell. Polariser(P) and analyser(A) orientation indicated. (a,iv-vi) Schematic of metasurface-LC cell in off (iv), partially aligned LC(v), on fully aligned LC state(vi). (b) LC tunable undulating plasmonic surface[93]. (b,i) Schematic of the plasmonic-LC cell. (b,ii) SEM images of the nano-well structure. Scale bars=500nm,100nm. (b,iii) Modelled LC orientation on undulating surface with and without an E-field applied. (b,iv) Experimentally observed reflectance spectra with varying field applied across cell. (b,v) Spectra and microscope images showing the un-polarised reflected colour in off and on states of surface with period $p = 320$nm. (c) Liquid crystal(LC) image switching of polarisation sensitive plasmonic holograms[94]. (c,i) Schematic of LC-nano-rod element on Si, excited by different polarisation of illumination depending on applied voltage. (c,ii) Images of far-field with cell off, with polarisation aligned to excite a single image (State 1,2), and cell on (state1+2) where both images are excited. (c,iii) Enhanced images showing pixels in far-field. Figures re-worked from references.

Franklin et al.[93] demonstrated a plasmonic device, operating as a reflective device at visible wavelengths, that, using the re-orientation of a high-birefringent LC, can tune the resonance of the plasmonic metasurface. The surface selectively absorbs light, the wavelength of which depends on the LC orientation at the metal interface, while reflecting the rest back out of the device. The plasmonic metasurface, shown in figure 2.19(b) was a thin Al undulating surface, consisting of nano-wells, whose size and periodicity determines the initial colour of the surface. The nano-well surface also acts to reduce the surface anchoring forces between the LC and the metallic nano-structured surface, as there are no hard edges. This, combined with the high-birefringent LC, resulted in a large enough shift in permittivity around the nano-wells, when a voltage was applied to the device, that a single pixel could see a significant shift in colour (e. g. red to green), as shown in figure 2.19(b,v)

In addition liquid crystals have the potential to create dynamic plasmonic holograms however to date a device that can dynamically change the far field of a plasmonic hologram has not been demonstrated. That is not to say efforts are not ongoing. Williams et al.[94] used a LC layer as an electro-optic half wave-plate switch that can alternate between orthogonal polarisations of transmitted light to switch between the two far field images encoded at orthogonal polarisations in a plasmonic metasurface hologram (figure 2.19(c)).

2.2.2.2 Mechanical deformation

The optical response of a plasmonic metasurface can be tailored by altering the geometry, dimensions and optical properties of the material and dielectric medium in which the nano-particle sits. Dynamic tunability has been demonstrated by changing the dielectric environment of the resonator with electrochromic materials and liquid crystals. By substituting the substrate on which the nano-structures sit with an elastic material, the physical dimensions of the metasurface can be modified using high-strain mechanical deformation. Thus, by applying a strain to the substrate, and altering the plasmonic coupling between resonator elements, the resonant condition of the metasurface can be controlled. Pryce et al.[95] fabricated coupled split-ring resonator (SRR) arrays on a Polydimethylsiloxane (PDMS) substrates, designed to operate in the IR range. U-shaped SRRs can be modelled as electrical LC resonators with a resonant frequency of $\omega_{res} = (LC)^{-\frac{1}{2}}$ where the effective capacitance C depends on the gap size, and the inductance L is proportional to the total effective length of each SRR. By physically deforming the substrate the effective capacitance is modified and hence the resonant frequency altered (figure 2.20(a)).

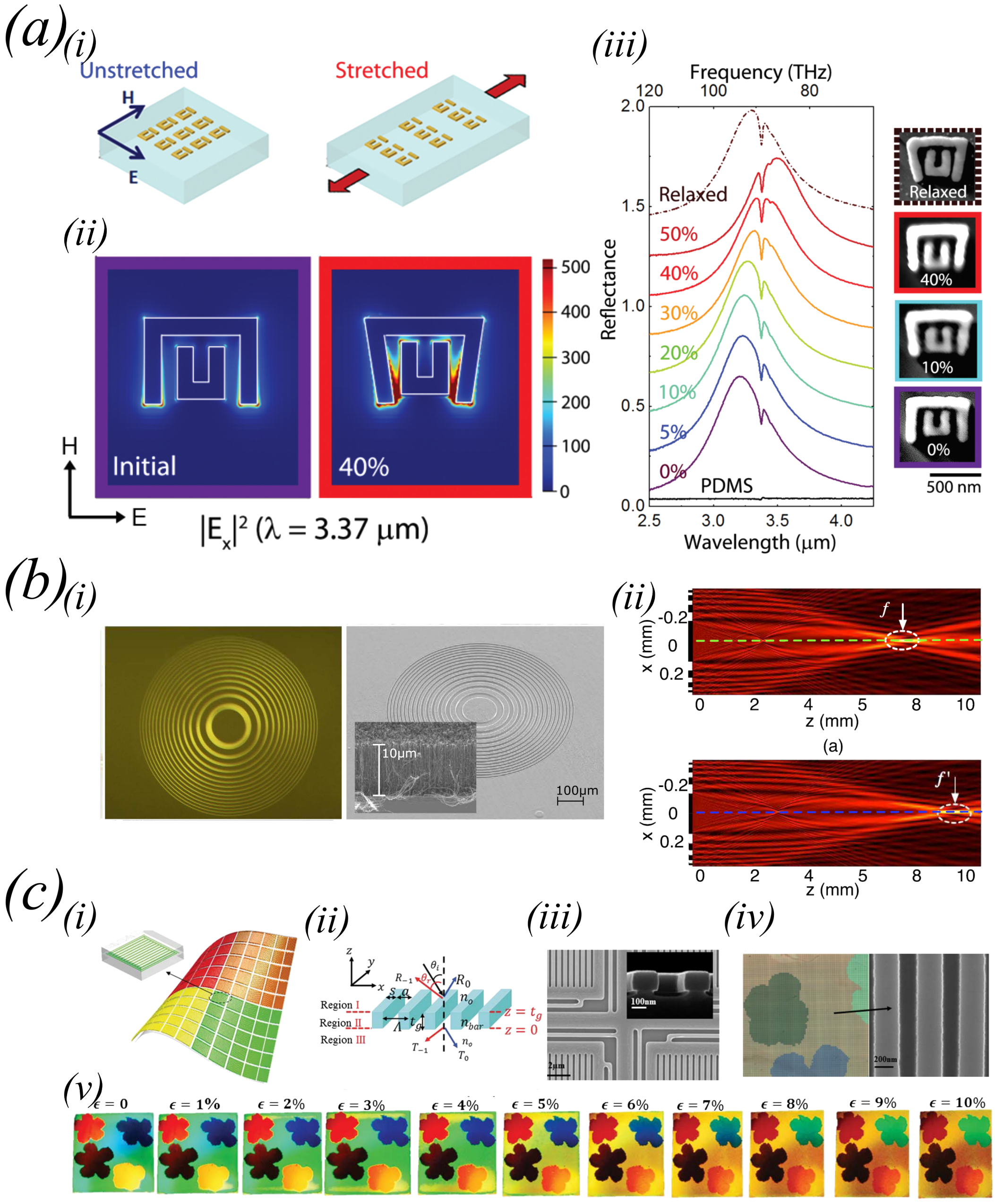

Figure. 2.20 Mechanical Deformation for tuning of plasmonic surfaces. (a) Plasmonic resonators on PDMS for resonance tuning[95]. (a,i) Schematic of SRR deformation. (a,ii) Double-SRR (DSRR) E-field intensity plots at $\lambda = 3.37\mu$m for 0% and 40% strain. (a,iii) Experimentally measured reflection spectra, with ESEM images, for varying tensile strains. (b) Fresnel zone plate with tunable focal length consisting of carbon nanotube (CNT) absorbers on PDMS substrate[96]. (b,i) Optical microscope image of lens and tilted SEM image of the diffractive CNT pattern. SEM inset shows vertically aligned CNTs. (b,ii) Computed wave propagation and focal length (FL) change when the lens size is changed. ΔFL $=$ 1.47mm under 10% strain. (c) Flexible photonic high-contrast metasurfaces (HCMs) for tunable colour[97]. Schematic of (c,i) colour from HCM and of (c,ii) a one-dimensional HCM. (c,iii) SEM images of HCM on Si on insulator after etching. (c,iv) Microscopic ($1cm^2$) and SEM images of transferred flower pattern. (c,v) Images of flower pattern HCM under increasing strain from $\epsilon = 0\%$ to 4.9%. Figures re-worked from references.

PDMS has also been used to create flat optical elements. Li et al.[96] demonstrated a binary amplitude Fresnel zone plate with tunable focal length by encapsulating lithographically defined vertically aligned carbon nanotube (CNT) bundles inside a PDMS layer, shown in figure 2.20(b). The operation of the lens does not in fact use any plasmonic effect to operate as a lens, but combines the excellent optical absorption properties of the CNT with the transparency and stretchability of the PDMS. By stretching the elastomeric composite in radial direction, the lens focal length is tuned. Good focusing response is demonstrated and a large focus change ($\geq 24\%$) was achieved by stretching lenses up to 11.4%.

Dynamic colour pixels have been created using grating structures in a PDMS substrate[97]. The grating, made of Si, is referred to as a high-contrast metastructure (HCM), a periodic structures made of one single-layer, high-refractive-index material fully surrounded by low-index material, and a periodicity of nearly one wavelength[97]. The colour of the grating is not generated by plasmonic resonance effects but is generated by the structure annihilating the 0th order diffraction while enhancing the -1st order, a new phenomenon made possible with a large index contrast. The colour depends on the periodicity and hence by stretching the substrate the colour can be varied. The metasurfaces were designed by Zhu et al.[97] to exhibit green, yellow, orange, and red colours as a colour palette, as well as an example display of flower patterns, shown in figure 2.20(c), whose colour change under a strain.

Whilst these dynamic pixels fundamental operations are not necessarily due to plasmonics or are not in the visible wavelength range, what they do show is that there is huge potential to use mechanical deformation to create dynamic plasmonic metasurfaces.

2.3 Summary

To create *true* 3D displays, an increase in the pixel density and decrease in physical size of pixels from what is currently commercially available is required. In the current state of the art for spatial light modulators (SLMs) for holographic displays the full-complex modulation of light is not possible and pixels are the order of a few microns up to tens of microns in size.

Plasmonic metasurfaces have been demonstrated to be able to control the phase, polarisation, amplitude and wavelength of a wavefront with pixels smaller than the wavelengths of visible light and thus have shown huge potential in being able to realise an 'ideal' SLM. So far, however, the transition from passive to active devices has been slow and challenging. Therefore, if a reliable method to control the optical properties of a plasmonic metasurface can be found, it will go a long way to realising their potential for active wavefront modulation devices.

In this chapter the theory behind the physical mechanisms that occur in plasmonic metasurfaces have been presented along with an overview of the science behind the applications to which plasmonics can be applied, starting with holography, leading onto liquid crystals and display pixel technology. In addition the current state of play of plasmonic metasurfaces has been summarised, looking at the most interesting and relevant results in the literature, highlighting opportunities going forward. In particular utilising LCs to modulate the refractive index of the medium surrounding plasmonic nano-structures, and mechanical deformation to alter the dimensions of plasmonic arrays.

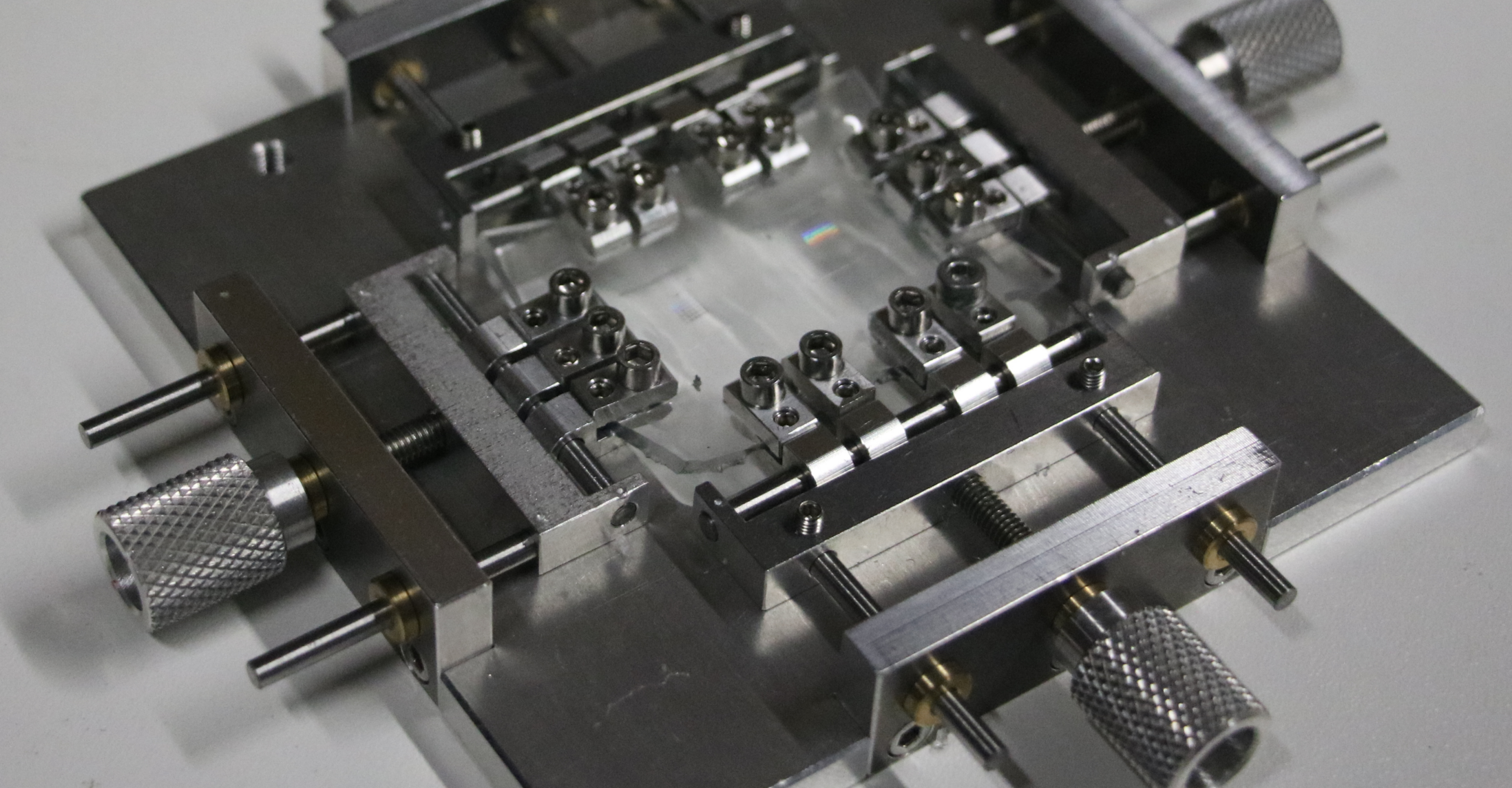

Chapter 3

Methods

Introduction

The experimental methods undertaken to investigate devices that have the potential to operate as *dynamic plasmonic metasurfaces in the visible spectrum* are outlined in this chapter. The chapter is structured similarly to the design and fabrication, and characterisation processes for the experimental work presented in this thesis. First, the modelling and design methods are described. Second, the cleanroom processes employed in fabricating the metasurfaces, followed by the processes employed in turning the passive metasurfaces into active devices. Lastly, the processes by which the devices were characterised are presented.

3.1 Simulation

The design and simulation of plasmonic nano-structures is centred around the *the Finite-Difference Time-Domain* (FDTD) method for solving Maxwell's equations. As a tool for predicting the interaction of light with a structure, FDTD simulation is very powerful, however it can also be computationally expensive and complex. In cases where there exist succinct solutions approximations may be used, e.g. the diffraction of light through a grating, or the far-field pattern of a hologram, as the FDTD method is slow, overly complex and unnecessary. In these cases the simpler methods may be implemented via code in MATLAB.

3.1.1 The finite-difference time-domain (FDTD) method

Given the complexities of setting up an FDTD solver, a commercial-grade simulator based on the finite-difference time-domain method was used to perform the calculations[21]. The FDTD method is a full-wave technique used to solve problems in electromagnetics, employing finite differences as approximations to both the spatial and temporal derivatives of Maxwell's equations (specifically Ampere's and Faraday's laws).

To gain a basic understanding of the workings of an FDTD solver we will look at the FDTD method in 1-dimension (1-D). The following description of the FDTD method in 1-D is adapted from reference [98].

Starting from the Taylor series expansion of an arbitrary function $f(x)$ expanded about the point x_0 with an offset of $\pm\delta/2$ wet get

$$f\left(x_0+\frac{\delta}{2}\right)=f(x_0)+\frac{\delta}{2}f'(x_0)+\frac{1}{2!}\left(\frac{\delta}{2}\right)^2 f''(x_0)+\frac{1}{3!}\left(\frac{\delta}{2}\right)^3 f'''(x_0)+\dots \tag{3.1a}$$

$$f\left(x_0-\frac{\delta}{2}\right)=f(x_0)-\frac{\delta}{2}f'(x_0)+\frac{1}{2!}\left(\frac{\delta}{2}\right)^2 f''(x_0)-\frac{1}{3!}\left(\frac{\delta}{2}\right)^3 f'''(x_0)+\dots \tag{3.1b}$$

Subtracting equation 3.1b from equation 3.1a results in

$$f\left(x_0+\frac{\delta}{2}\right)-f\left(x_0-\frac{\delta}{2}\right)=\delta f'(x_0)+\frac{2}{3!}(\frac{\delta}{2})^3 f'''(x_0)+\dots \tag{3.2}$$

Dividing by δ gives

$$\frac{f(x_0+\frac{\delta}{2})-f(x_0-\frac{\delta}{2})}{\delta}=f'(x_0)+\frac{2}{3!}\left(\frac{\delta}{2}\right)^2 f'''(x_0)+\dots \tag{3.3}$$

where the difference equation about point x_0 is equal to the derivative of $f(x)$ at the point x_0 plus a term that depends on δ^2 and an infinite set of higher order terms. Assuming that δ is sufficiently small it is reasonable to ignore the δ^2 and higher power terms resulting in the central difference approximation:

$$\left.\frac{df(x)}{dx}\right|_{x=x_0} \approx \frac{f(x_0+\frac{\delta}{2}) - f(x_0-\frac{\delta}{2})}{\delta} \tag{3.4}$$

The central difference function is providing an approximation of $f'(x_0)$ by sampling data not at x_0 but at the neighbouring points $x_0 \pm \delta/2$, and is of second order accuracy, given we are ignoring δ^2 terms and higher

The Yee algorithm The FDTD algorithm as first proposed by Kane Yee in 1966[99] employs second-order central differences.

The algorithm can be summarised as follows:

1. Replace all the derivatives in Ampere's and Faraday's laws with finite differences. Discretise space and time so that the electric and magnetic fields are staggered in both space and time.
2. Solve the resulting difference equations to obtain*update equations* that express the (unknown) future fields in terms of (known) past fields.
3. Evaluate the magnetic-fields,H, one time-step into the future so they are now known (effectively they become past fields).
4. Evaluate the electric-fields, E, one time-step into the future so they are now known (effectively they become past fields).
5. Repeat the previous two steps until the fields have been obtained over the desired duration.

The *Yee algorithm* centres its E and H components in three-dimensional (3D) space so that every E component is surrounded by four circulating H components, and every H component is surrounded by four circulating E components. This provides simple picture of three-dimensional (3-D) space, called a *Yee cell*, illustrated in figure 3.1(a), being filled by an interlinked array of Faraday's Law and Ampere's Law contours.

Whilst a *Yee cell* is necessary for a 3-D space, to describe the workings of the *Yee algorithm* in 1-D space a simpler description may be used. By considering a 1-D space with variations only in the x direction and assuming that the electric field only has a z component, Faraday's law can be written as

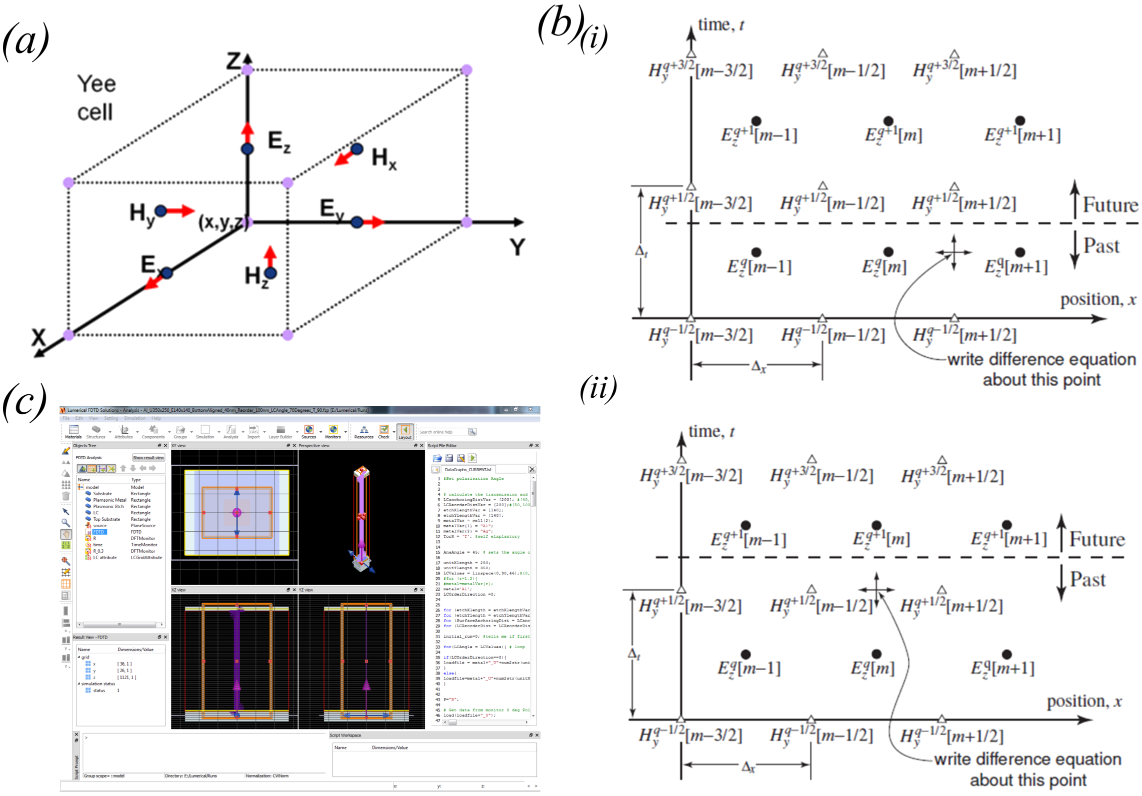

Figure. 3.1 FDTD: Yee Cell, computation and user interface. (a) Graphical representation of a Yee cell, a cartesian computational grid to allow for solving of Maxwell's across a 3D simulation region. Reproduced from [21]. (b,i) The arrangement of E-field and H-field nodes in 1D space and time to obtain an update equation for H_y, reproduced from[98]. (b,ii) Space-time after updating the magnetic field. The dividing line between future and past values has moved forward a half temporal step from (i) and the the difference equation is written to obtain an update equation for E_z, reproduced from[98]. (c) GUI of Lumerical, the commercial-grade simulator based on the finite-difference time-domain method used to solve Maxwell's equations in 3-dimensions for metallic metasurfaces[21].

$$-\mu\frac{\partial \mathbf{H}}{\partial t} = \nabla\times\mathbf{E} = \begin{vmatrix} \hat{\mathbf{a_x}} & \hat{\mathbf{a_y}} & \hat{\mathbf{a_z}} \\ \frac{\partial}{\partial x} & 0 & 0 \\ 0 & 0 & E_z \end{vmatrix} = -\hat{\mathbf{a_y}}\frac{\partial E_z}{\partial x} \tag{3.5}$$

Hence H_y must be the only non-zero component of the magnetic field which is time varying (although there may be static components in the x and z directions). Knowing this we can write Ampere's law as

$$\epsilon\frac{\partial \mathbf{E}}{\partial t} = \nabla\times\mathbf{H} = \begin{vmatrix} \hat{\mathbf{a_x}} & \hat{\mathbf{a_y}} & \hat{\mathbf{a_z}} \\ \frac{\partial}{\partial x} & 0 & 0 \\ 0 & H_y & 0 \end{vmatrix} = -\hat{\mathbf{a_y}}\frac{\partial E_z}{\partial x} \tag{3.6}$$

resulting in two scalar equations

$$\mu\frac{\partial H_y}{\partial t} = \frac{\partial E_z}{\partial x} \tag{3.7a}$$

$$\epsilon\frac{\partial E_z}{\partial t} = \frac{\partial H_y}{\partial x} \tag{3.7b}$$

Equation 3.7a gives the temporal derivative of the magnetic field in terms of the spatial derivative of the electric field. Equation 3.7b gives the temporal derivative of the electric field in terms of the spatial derivative of the magnetic field. Thus equation 3.7a will be used to advance the magnetic field in time while equation 3.7b will be used to advance the electric field, this process will then be repeated, until the entire simulation region and time are covered.

To replace the derivatives in the scalar equations with finite differences, we need to first discretise space and time. Each location in time and space can be represented with the notation

$$E_z(x,t) = E_z(m\Delta_x, q\Delta_t) = E_z^q[m] \tag{3.8a}$$

$$H_y(x,t) = H_y(m\Delta_x, q\Delta_t) = H_y^q[m] \tag{3.8b}$$

Δ_x is the spatial offset and Δ_t the temporal offset between sample points, whilst the index m corresponds to the spatial step and q the temporal step. As we have effectively two dimensions (one spatial, one temporal) we can represent the electric and magnetic field sample points as shown in the figure 3.1(b,i).

The electric field sample points are shown as circles and the magnetic field sample points as triangles, and it is assumed that all the fields below the dashed line are known - they are considered to be in the past - while the fields above the dashed line are future fields and are hence unknown. The FDTD algorithm provides a way to obtain the future fields from the past fields. If we consider Faraday's law at the space-time point $\big((m+\frac{1}{2})\Delta_x, q\Delta_t\big)$

$$\mu \frac{\partial H_y}{\partial t}\bigg|_{(m+\frac{1}{2})\Delta_x, q\Delta_t} = \frac{\partial E_z}{\partial x}\bigg|_{(m+\frac{1}{2})\Delta_x, q\Delta_t} \tag{3.9}$$

The temporal derivative is replaced by a finite difference involving $H_y^{q+\frac{1}{2}}[m+\frac{1}{2}]$ and $H_y^{q-\frac{1}{2}}[m+\frac{1}{2}]$, the magnetic field at one fixed location but two different times. The spatial derivative is replaced by a finite difference involving $E_z^q[m+1]$ and $E_z^q[m]$, the electric field at two different locations but one time. This gives

$$\mu \frac{H_y^{q+\frac{1}{2}}[m+\frac{1}{2}] - H_y^{q-\frac{1}{2}}[m+\frac{1}{2}]}{\Delta_t} = \frac{E_z^q[m+1] - E_z^q[m]}{\Delta_x} \tag{3.10}$$

Solving for $H_y^{q+\frac{1}{2}}[m+\frac{1}{2}]$

$$H_y^{q+\frac{1}{2}}[m+\frac{1}{2}] = H_y^{q-\frac{1}{2}}[m+\frac{1}{2}] + \frac{\Delta_t}{\mu\Delta_x}(E_z^q[m+1] - E_z^q[m]) \tag{3.11}$$

This update equation, specifically for the H_y field, can be applied to any sample point. It shows that the future value of H_y depends only on its past value and the neighbouring electric fields. We can apply this to all the magnetic field sample points and update our space-time grid, moving the future/past dividing line forward one half time step to the position shown in figure 3.1(b,ii).

Now taking Ampere's law applied at the space-time point $\big((m)\Delta_x, (q+\frac{1}{2})\Delta_t\big)$

$$\epsilon \frac{\partial E_z}{\partial t}\bigg|_{m\Delta_x, (q+\frac{1}{2})\Delta_t} = \frac{\partial H_y}{\partial x}\bigg|_{m\Delta_x, (q+\frac{1}{2})\Delta_t} \tag{3.12}$$

By once again replacing the temporal derivative with a finite difference, this time however involving $E_z^{q+1}[m]$ and $E_z^q[m]$, and replacing the spatial derivative with a finite difference this time involving $H_y^{q+\frac{1}{2}}[m+\frac{1}{2}]$ and $H_y^{q+\frac{1}{2}}[m-\frac{1}{2}]$, we get

$$\epsilon\frac{E_z^{q+1}[m]-E_z^q[m]}{\Delta_t}=\frac{H_y^{q+1}[m+\frac{1}{2}]-H_y^{q+1}[m-\frac{1}{2}]}{\Delta_x} \tag{3.13}$$

Solving for $E_z^{q+1}[m]$

$$E_z^{q+1}[m]=E_z^q[m]+\frac{\Delta_t}{\epsilon\Delta_x}(H_y^{q+1}[m+\frac{1}{2}]-H_y^{q+1}[m-\frac{1}{2}]) \tag{3.14}$$

Thus we have an update equation that can be applied to every E_z sample point. Similarly to the update equation for the magnetic field, the update equation for the electric field shows that the future value of E_z depends on only its past value and the neighbouring magnetic fields.

Having solved for all the electric field sample points, the algorithm would move forward another half time step and the process would repeat for the magnetic fields and so on.

By adding in regions of different complex permittivities, sources etc. a model can be set up in 3-D to solve the optical responses of nano-patterned materials. This is all set-up and run within a commercial package[21], the interface of which is shown in figure 3.1(c). By using symmetric/anti-symmetric boundary conditions, the computational power required for modelling large arrays of nano-structures can be reduced significantly, whilst careful control of the size of the Yee cells ($\Delta_{x,y,z}$), the time step (Δt) and the total simulation time can optimise the trade off between total computational time to model accuracy.

The nano-structures utilised in this work are nano-rods and, their inverse, nano-holes. A single nano-structure is modelled with periodic boundary conditions at the periodic unit cell spacing. For metals, complex dispersive material models are used[38]. For liquid crystals (LCs) a diagonal anisotropic refractive index material with n_e and n_o defined as per the specific LC simulated. The orientation of the director of the LC is defined by a 3D rotation matrix. The matrix is designed to incorporate surface anchoring, re-orientation regions and bulk LC re-orientation. The first two are of key importance when modelling any change in plasmonic resonance frequency of a metasurface since, as discussed in 2.1.1, the permittivity of the medium immediately surrounding the metasurface has a direct influence on the plasmonic resonance. The exact size of surface anchoring and re-orientation regions used in the models will be discussed in following chapters.

3.1.2 Computer generated holograms

The principles behind computer generated holograms (CGHs) are discussed in 2.1.2.2, however the practical implementation of CGHs for metasurface devices is presented here.

The CHG, created using code in MATLAB, is a m×n pixel hologram that when illuminated with a coherent source will produce a pre-defined image in the far-field. The pixels of these binary amplitude-holograms can be fabricated using scattering elements designed using FDTD methods. Each pixel in the CGH is defined as a cell of unit size (typically $\sim$ 300nm×300nm), within which a nano-scale scattering element may sit. In the case of a binary amplitude hologram, a scattering element will or will not be present, depending whether the CGH specifies a 1 or a 0 for a specific pixel. The size and shape of the scattering element within the unit cell pixel can be arbitrary, intended to scatter any incoming light, or the element can be, using FDTD modelling, designed to be wavelength and/or polarisation dependent. The specific scattering characteristics of each pixel will determine what coherent light will be transmitted/reflected from each individual pixel, and hence the interference from adjacent pixels to produce the desired far-field diffraction pattern. If a phase hologram were to be designed, each unit cell would contain a nano-structure designed to control the phase as defined in the CGH. However, as these types of holograms are not used in any part of this thesis they will not be discussed further.

Using MATLAB code, the CGH is converted into a pattern file consisting of an m×n array of unit cells, with a distribution of scattering elements as defined by the CGH (see figure 3.2(b)). At this point it is possible, by inserting two or more scattering elements into a unit cell, to convolve two polarisation dependant holograms into one hologram with polarisation sensitive pixels. This hologram would then produce a far-field image dependant on the polarisation of light illuminating the hologram[12]. More complex dependencies may be designed based on the same underlying principles.

The CAD file is then converted into a commercial lithography machine specific pattern file, for use in the physical lithographic process. Using electron beam lithography

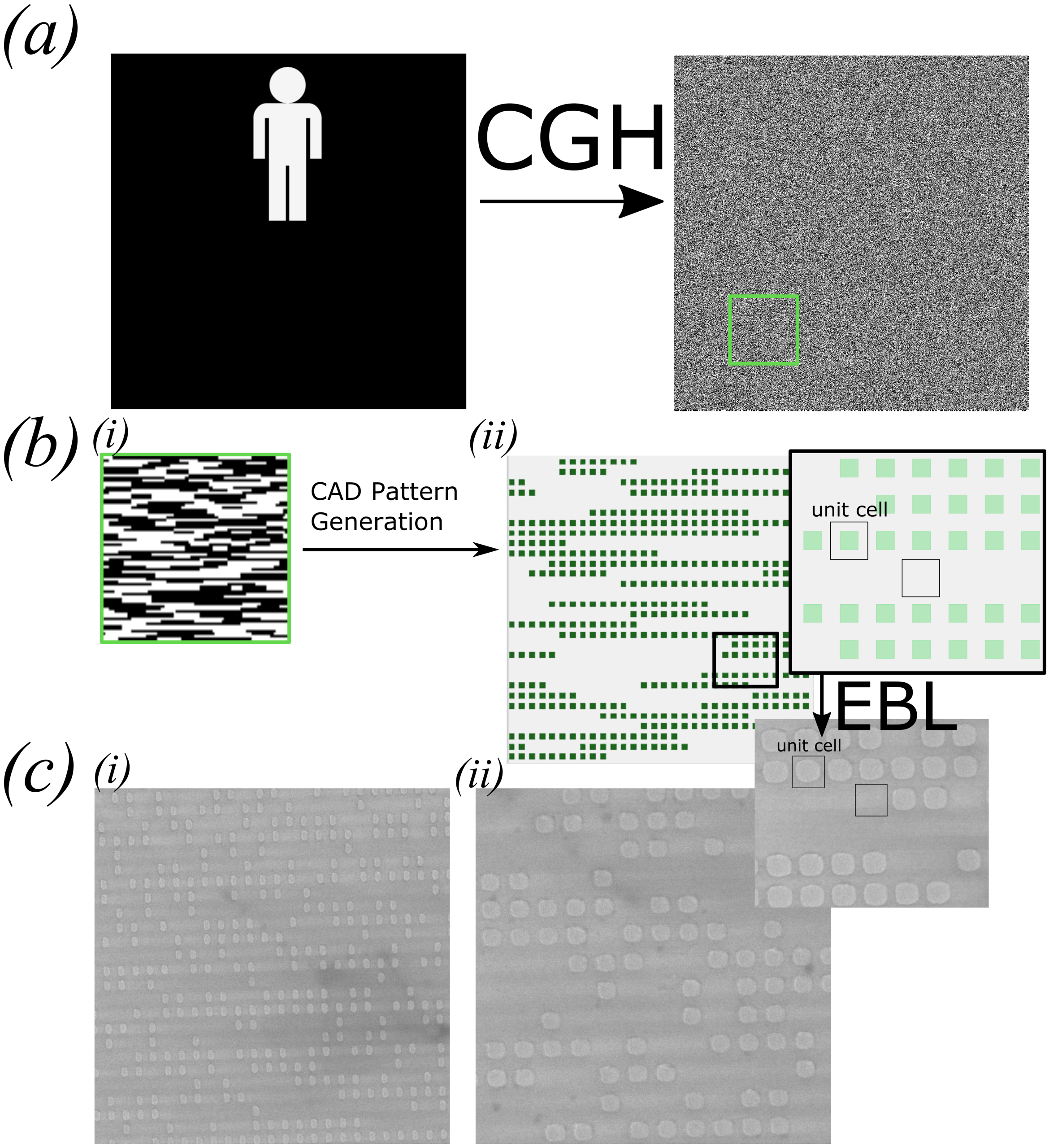

Figure. 3.2 CGH to Pattern Process. (a) Image is converted to a amplitude only hologram via GS algorithm, implemented via MATLAB. (b) The hologram pixels are converted into a pattern file (ii), where a unit cell either contains a scattering element for a value of 1, or does not for a pixel value of 0. (c) via EBL the CAD pattern is converted into metallic scattering elements, which can be (i)anisotropic or (ii) isotropic depending on the desired characteristic of the hologram.

(EBL), and processes to be discussed in the following section of this chapter, the pattern file can be converted into a physical nano-structure that can interact with light to operate as a nano-plasmonic hologram, examples of which are shown in figure 3.2(c).

A hologram, using scattering elements as pixels, could be designed in whole in the FDTD solver. This however would take a huge amount of computing power, and would not be fit for purpose, unlike the multiple step design process discussed here.

3.1.3 Lens design

A flat optical lens can be thought of as a specific hologram, designed, in the case of a lens, to have a singe spot in the centre of the replay field.The basis of the flat optical lenses designed is a Fresnel zone plate[100, 101]. The zone plate has light and dark zones radiating from its centre with the radial distance to the centre of each zone defined by

$$r_n = \sqrt{FLn\lambda + (n\lambda/2)^2} \tag{3.15}$$

and the area of each zone equal to $\pi\lambda FL$, where FL is the focal length of the lens, λ the wavelength of incident light and n is the zone number, increasing from the centre of the lens. Variations on the specific designs will be discussed in later chapters, however the practical implementation remain the same.

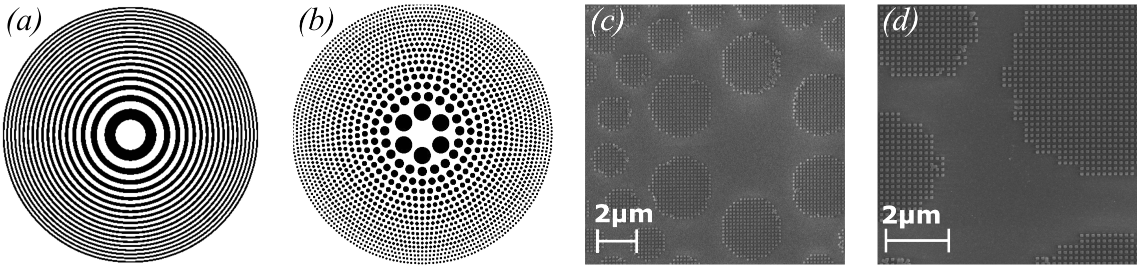

Figure. 3.3 Fresnel Zone Plate (FZP) fabrication. Pattern file of (a) FZP and (b) a photon sieve, a variation of the FZP. (c,d) SEM of photon sieve showing scattering elements for unit cells where dark zones are present

The light and dark zones can be thought of as pixels of an amplitude only hologram with values either 1 (light) or 0 (dark). The physical size of the zones determines the focal length, hence, unlike in the holograms where the total hologram size is defined by the unit cell size and number of pixels in the CGH, in the case of the lens, the total area of the lens is divided into unit cells and the number of pixels is determined by the unit cell and the overall size of the lens.

Using the lenses in transmission, the dark zones contain unit cell pixels with a scattering element present, where as in light zones, the pixels are empty. Figure 3.3(c-d) shows the fabricated elements as scattering pixels in a photon sieve. Again scattering elements can be designed to be wavelength and polarisation dependant, and the process to create the lithography pattern file is the same as used for the holograms.

It is important to note that in both the cases of holograms and flat optical lenses, the commercial FDTD software will calculate the far-field patterns of the metasurfaces, if the surface is inserted into the user interface. The computational time however would be immense, given the scattering elements are of the order of hundreds of nm and the overall size of hologram/lens is hundreds of μm. Therefore by designing the hologram or lens separately and then pixelising the subsequent diffractive optics, the design and compute time can be significantly reduced.

3.2 Cleanroom fabrication

When fabricating plasmonic metasurfaces the feature size is in the order of hundreds of nano-meters, and the processes are susceptible to contamination by larger dust or dirt particles that could ruin a device. As such much of the processing is performed within a cleanroom, where air particulates larger than 0.5μm are all but removed from the environment. The controlled environment removes such issues from the fabrication process, allowing for repeatable processes to be developed to produce consistent and accurate nano-structures.

The fabrication process of a metasurface can be succinctly summarised as follows:

1. Design metasurface using FDTD methods/MATLAB and produce pattern file
2. Pattern resist on substrate using EBL methods
3. Deposit metal on substrate with patterned resist
4. Remove sacrificial resist layer leaving desired metallic pattern on substrate

A schematic of steps 2-4 is shown in figure 3.4 using negative (a) and positive (b) resists.

Having covered step 1, the process of creating pattern files, in section 3.1 the following section covers steps 2-4, the processes involved in electron beam lithography (EBL)

3.2.1 Electron beam lithography

Electron beam lithography is one of several possible techniques available to fabricate nano-sized structures. Other possible techniques include photo-lithography, direct laser writing, nano-imprint lithography and X-ray lithography. The various techniques have differences such as being serial or parallel, mask or maskless/direct-write, top-down or bottom-up, beam or tip-based, resist-based or resist-less methods.

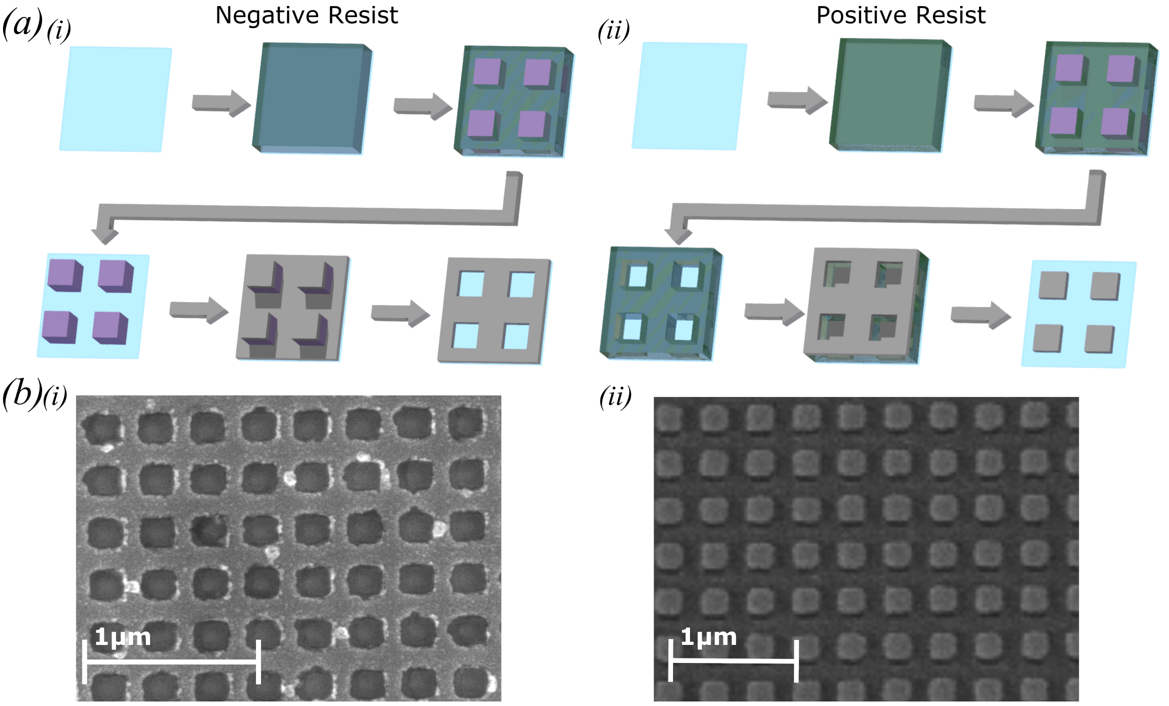

Figure. 3.4 Schematic of the fabrication process for a nano-structured surface. (a) A substrate is covered with resist, which is then patterned using EBL. The resist is developed and the metal deposited. The sacrificial layer of resist is removed leaving the desired pattern of deposited material. Negative resist(i) results in the inverse of the patterned resist being deposited on the substrate. Positive resist(ii) resulting in the pattern patterned onto the resist being deposited on the substrate. (b)SEM image of the same square periodic pattern fabricated using negative(i) and positive(ii) resist.

EBL is most generally used for the fabrication of photolithographic masks or for one-off structures fabricated in the cause of research. This is due to the high accuracy of EBL compared to other techniques. However this ability to pattern smaller features comes with a trade off in processing time. As a comparison photo-lithography uses a mask and a single exposure of photon energy to *expose* the resist, making it a quick process but limited in the size of feature it may produce to the order of hundreds of nm. The mask used will cover the entirety of the substrate and the exposure beam is large enough to illuminate the mask as a whole. The area of resist exposed is determined by the shadow of pattern of mask i.e. the resist that will be exposed is the area not in the shadow of the mask. As such the exposure/patterning time is determined by the amount of energy required to alter the structure of the resist substrate, which will generally be of the order of seconds.

EBL on the other hand is maskless, and instead an electron beam will directly write the resist that it is patterning. This direct write method using a narrow electron beam spot ($<$ 5nm) leads to higher accuracy, however, as the beam needs to be scanned across the whole patterned area, it can be time consuming. In nano-plasmonic research the structures to be patterned vary frequently, and as different optical properties are investigated the patterns are often one-offs. It is not efficient to get many masks made to subsequently pattern by photo-lithography, or to manufacture many masks via EBL that would be subsequently used in photo-lithography, EBL tends to be the technique of choice for research based fabrication. Furthermore, the size of features than can be patterned by photo-lithography is limited by the wavelength of electromagnetic (EM) radiation used to expose the particular resist. Diffraction effects will distort mask patterns at features smaller than the optical diffraction limit. That is not to say that photo-lithography can not be used to produce patterns smaller than the optical diffraction limit, as interference lithography can lead to much smaller feature sizes, however this can be overly complex and difficult depending on the desired patterns. Developing processes to produce these patterns can be timely and more suitable to repetition of the same patterns e.g. in commercial manufacturing, where throughput needs to be high. EBL on the other hand can reliably pattern down to $\sim$ 40nm feature sizes without too much trouble, and has been shown to produce features $<$ 10nm.

A photograph of the EBL machine used and a schematic of a typical EBL machine are shown in figure 3.5(a,b). In the case of the research in this thesis, 80kV electron beam lithography (Nanobeam Ltd. nB1) is used for the high-resolution patterning. An electron source produces electrons that will then be accelerated through a field towards the substrate to be patterned. The beam will then pass through electrostatic and magnetic lenses to focus the beam to a spot size < 5nm. The beam is then deflected to scan the desired pattern. Large beam deflections lead to issues in achieving the desired pattern. To negate the need for large beam deflections the substrate is moved by x-y stage. This process is controlled by a computer which will direct the beam to pattern a pre-defined CAD pattern file uploaded by the user.

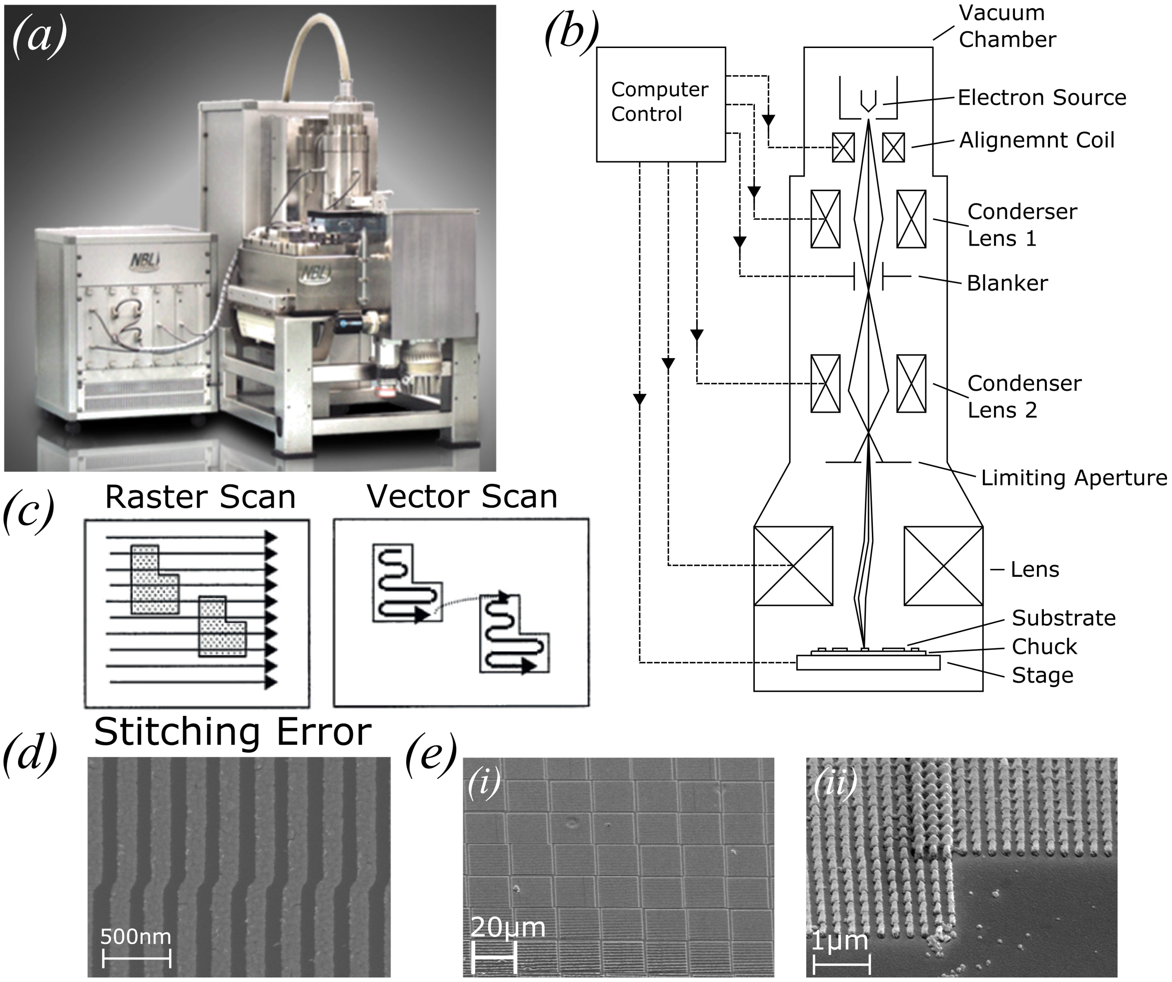

Figure. 3.5 Electron Beam Lithography. (a) Photograph of Nanobeam Ltd. nB1 EBL machine used for patterning in this work. (b) Schematic of the operation of the EBL machine. (c) Graphical representation of two scanning regimes available for EBL Machines. (d) SEM image of pattern error caused by stitching between two main-field patterns. (e) Pattern error caused by beam deflection due to charge build up on insulating substrates.

The substrate that the electron beam is accelerated towards is covered in a thin electron sensitive polymer film known as the *resist*. Electrons in the incident beam lose energy upon entering the resist and will, depending on the type of resist, crosslink or break bonds within the polymer affecting the solubility of the resist in a chemical developer. The interaction of electrons with the polymer resist is known as the *exposure* process.

Following the *exposure* process, the now patterned resist is immersed in a chemical developer solution and the resist is selectively removed leaving behind the desired pattern. This is known as the *development process*.

The dimensions of the features that can be patterned and the quality of those features will depend on resist type (viscosity, film thickness, sensitivity etc.), exposure conditions (beam current, exposure dose) and development conditions (time, developer mixing ratio etc.) The steps taken and the conditions used are summed up in a *recipe* that may be used to create features of chosen size, spacing etc. In the developing the optimum recipe, dose and development tests can be utilised to narrow down the combinations of conditions that may be used.

In the following subsections we will explore the key factors that make up a patterns recipe.

3.2.1.1 Resists

Resists for EBL are electron sensitive polymers. A resist may be *positive* or *negative*. In the case of a positive resist, the energy from the electron beam will break bonds within the polymer, making the resist more susceptible to a chemical developer solution. Hence when the polymer layer is immersed in the chemical developer solution the exposed polymer will be the first to be washed away. When the resist is then covered in whichever desired material for the pattern to be created with, and the sacrificial material removed, the resulting deposited material will be the same as the initial CAD pattern. A negative resist is the opposite. The energy from the electron beam will crosslink bonds within the polymer, making the resist less susceptible to a chemical developer solution. When the resist is then covered in whichever desired material for the pattern to be created with, and the sacrificial material removed, the resulting deposited material will be the inverse of the initial CAD pattern. A graphical representation of this process is shown in figure 3.4. Figure 3.4(a) shows a negative resist resulting in the inverse metallic pattern. Figure 3.4(b) shows the positive resist result with the resulting metallic pattern on the substrate the same as the CAD pattern patterned into the resist. SEM images of an array of squares patterned using both negative and positive resists are shown.

The resist is initially stored in a solvent to allow for it to be spun onto a substrate to form a thin uniform layer that may be patterned. The spinning process involves placing the substrate to be coated on a spinning top, pipetting the resist solution onto the substrate and spinning it at up to 5500rpm for a specified amount of time. The spin speed and spin time used will determine the thickness of a given resist layer, typically shown in the spin curve for a specific resist[102]. A given resist solution can produce thinner or thicker resist layers depending on its viscosity. The thickness of resist is key as it will determine the energy required for patterning. A thicker resist layer will require more energy per unit area, as there more bonds to crosslink or break. The film thickness will also have an effect on the minimum feature size achievable. A larger aspect ratio (height:width) of resist pillars, makes them less mechanically stable, and more likely to fall over during the development process. An SEM image of fallen pillars is shown in figure 3.6(d,ii). The pillars have fallen in random directions that will, following the lift-off process, result in random undesired metallic patterns. Typically the limit is $\approx [5:1]$. Following spinning the substrate will be baked. This process can be not only to drive off the remaining solvent, but in some cases to alter the structure of the resists, e.g. PMMA is heated to 180° to go beyond the polymers glass transition temperature.

There are a myriad of resists that one can chose from. In this work the positive resists used were PMMA and UV111-6, used typically for patterning nano-rods. The negative resist used was ma-N 2405, part of the ma-N 2400 series of resists by *micro resist technology*, typically for nano-holes. The positive resists had better resolution ($<$ 100nm) and of the two the least sensitive resist, PMMA, was the superior. However, PMMA, being less sensitive requires longer exposure times, due to higher electron doses required, hence compromises were made where time was an issue. The negative resist had a resolution limit of around 120nm.

3.2.1.2 Exposure conditions

The minimum feature size achievable using EBL is, unlike photo-lithography, not determined by any diffraction limits, or even the beam spot size, but by the forward scattering of electrons when the patterning electron beam interacts with the resist. The primary electrons in the incident beam lose energy upon entering a material through inelastic scattering or collisions with other electrons. The scattering angle will be smaller for higher energy electrons, hence higher energy electron beams can produce smaller features. There are also issues with thicker resist layers, on top of the aspect ratio limitations mentioned in 3.2.1.1, in that the greater distance for electrons to travel through the resist allows for more scattering events, which can lead to lateral scattering and broader features than desired. Limitations to the minimum feature size achievable is not only determined by the forward scattering of electrons. The pitch resolution of a given pattern is not determined by the forward scattering, but by secondary electrons[103]. Secondary electrons are produced by inelastic collisions of incident electrons, and can have enough energy to break to bonds in the polymer, away from the desired patterned regions. Primary electrons from the incident beam, in addition to producing secondary electrons, if they have sufficient energy to penetrate the resist, can be multiply scattered over large distances from underlying films and/or the substrate. This leads to exposure of areas at a significant distance from the desired exposure location. In cases where primary and secondary electron scattering result one exposure region effects another exposure region it is referred to as the *proximity effect*.

The dose, or amount of exposure during electron beam patterning, is another key parameter. The dose is measured in charge per unit area exposed and typically has units μCcm^{-2}. As previously mentioned different resists have different sensitivities to electron dosage and hence this parameter needs to be carefully controlled. Too high a dose leads to greater scattering and broader features than desired, whilst too low and not enough resist is exposed and the developer will remove the desired pattern of resist. Figure 3.6(a) shows the effect when using a negative resist. Figure 3.6(a,ii) is the pattern using a dose of $200\mu Ccm^{-2}$. When increasing the dose to $250\mu Ccm^{-2}$ but keeping pattern and the development time constant, the square features achieved are larger as shown in figure 3.6(a,iii). The dose also directly affects the write time. The time taken T, is calculated by taking the total exposure area A, multiplying by the dose D, and dividing by the beam current I, $T = AD/I$.

The writing strategy employed by modern EBL systems is *vector scanning* rather than *raster scanning*. The two scanning strategies are shown schematically in figure 3.5(c). In vectoral scanning, the beam in deflected to specific point for a shape and then scanned over the shape, whereas raster scanning is like old dot matrix printers, scanning across the entire substrate, using blankers to turn the beam on and off where exposure is required. Using the vector scanning method, there are limits to how far a beam can be deflected ($\pm 20\mu$m). To write a pattern over a larger area, the pattern is split, or 'fractured', into smaller segments, and the beam or substrate moved from sub-field to sub-field to create the entire pattern. This can cause issues called stitching errors, where a feature spans the edge of a sub-field and the movement of the beam/substrate causes a positioning error. The result can be broken features or kinks in the edge of nano-structures such as that shown in figure 3.5(d).

3.2.1.3 EBL patterning on insulating substrates

The desire for plasmonic meta-surfaces to operate in transmission led to the requirement for the nano-structures to be patterned on a glass substrate. When patterning on glass substrates, photo-lithography is typically used, as opposed to EBL. The primary reason for this is because when electrons are accelerated towards a substrate, being charged particles, they tend to charge the substrate negatively, unless they are able to find a route to ground. The result is the deflection of the patterning electron beam away from its desired location, as well as increased electron scattering and the rounding of patterned structures. The typical substrate of choice for EBL is silicon (Si) that has been doped with holes. When a high-energy beam collides with the Si wafer, almost all of the electrons stop in the wafer and can then follow a path to ground. When a high energy beam collides with a glass substrate, there is no easy path to ground, hence charge accumulation occurs in the substrate. The trapped charge in turn deflects the path of the e-beam and results in distortions of the written pattern[104]. For example the regular array of a $40\mu\text{m}\times40\mu\text{m}$ square pattern shown in figure 3.5(e) no longer has a regular spacing between the squares, but has irregular periodicity and in some cases adjacent square patterns have overlapped as shown in figure 3.5(e,ii).

The issue here is that to pattern features for plasmonic meta-surfaces of the order of 150nm on glass, standard photo-lithography techniques will not suffice. To use EBL the issue of charge accumulation needs to be resolved. Charge accumulation issues may be minimised by incorporating charge dissipation layers above and/or below the resist layer. Often this discharge layer consists of a film of indium-tin-oxide (ITO) between the resist the substrate[105]. The reason ITO is used is the same as the reason it is widely utilised as an electrode in LC display technologies. It is a conductor that is optically transparent. ITO does in fact act as good charge dissipation layer, however it is not possible to remove following the patterning process. How consequential this is depends if one is intending the final structure to be on an insulating substrate. An alternative solution is to use a sacrificial conducting layer on the top of the resist. The layer is present during patterning, but removed prior to development. Conducting polymers, such as PEDOT:PSS have been investigated for such a purpose [106–108], however it was found to be challenging to deposit a thick enough layer on the resist film to provide sufficient charge dissipation, whilst removal following EBL patterning was found nigh on impossible. As an alternative a metallic charge dissipation layer of 40nm Al was used for patterning on glass. To remove the Al charge dissipation layer Decon90 detergent was used. Decon90 contains KOH which reacts with Al, dissolving the layer. Decon90 was used as an alternative to commercial Al etch solutions which were found to attack the underlying resists layer (see figure 3.6(b)), and hence affected the final pattern obtained. When used in conjunction with ma-N negative resists, the charge dissipation layer removal time is key as the resist uses an alkaline developer. Hence too long in the Decon90 solution and the resist starts to develop, with knock on effects to the development time and quality. This issue was not seen with the positive resists.

When patterning < 200nm features, whilst an under layer of ITO was sufficient, a single metallic top charge dissipation layer was not. To ensure nano-structures were on an insulating substrate a 3nm layer of Al was used as charge dissipation layer between the glass substrate and the resists, deposited prior to resist spinning. The Al under layer during patterning acts as a conducting charge dissipation layer, however following pattern processing, the layer will oxidise, and becomes insulating. The layer is too thin to have a significant effect on any plasmonic resonances, yet improves charge dissipation and results in the successful patterning of nano-structures down to dimensions of ≈ 120nm.

3.2.1.4 Development

Following exposure the resist is immersed in a chemical developer solution. The developer will selectively remove exposed or unexposed resist (depending if the resist is negative or positive) to leave the desired pattern of sacrificial polymer. The chemical developers available for a specific resist are numerous. Different developers will dissolve resists at different rates, and each resist and developer datasheet must be studied prior to use to gauge the approximate development time. The development time can subsequently be optimised iteratively. Additionally it is important to note that exposure alters the solubility of a resist in a particular developer rather than affecting whether or not it is soluble in the developer. This means that development time is key, too little and you end up not removing all the exposed resist, but too long and the

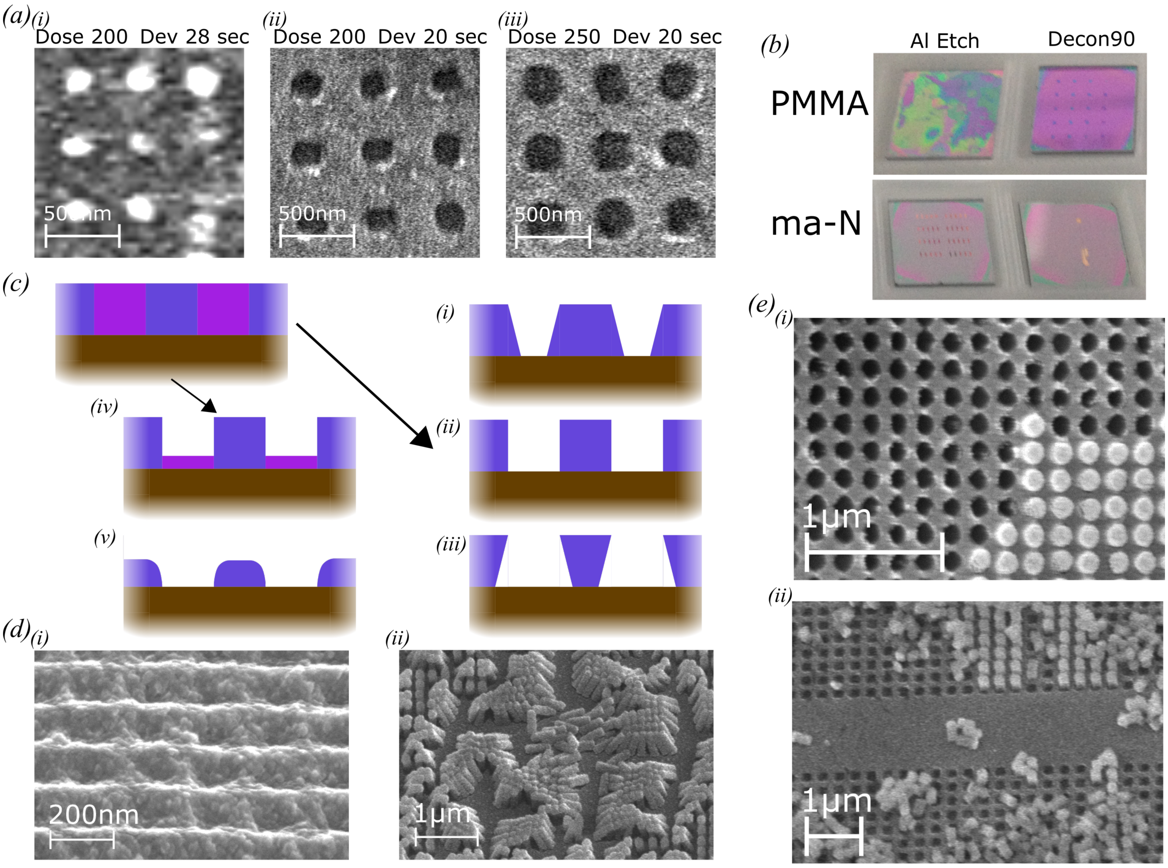

Figure. 3.6 Pattern dependency on resist, electron beam charge dose and development time. (a) Resulting patterns of the same square array achieved by varying dose and development time. Higher does spreads the pattern, where as over-development of pattern results in desired pattern being eroded. (b) Effect on resist of Al etch solution and Decon90. (c) Possible resist structures post development. (i-iii) Resist wall profiles showing (i) over-cut, (ii) vertical walled and (iii) undercut profiles arising from imperfect dose-development time combinations. (iv-v) Resist structure due to under(iv) and over(v) development. (d) SEM images of resulting patterns due to imperfect pattern recipe. (i) undulating metallic layer due to over-development of square nano-pillar pattern. (ii) toppled resists pillars due to too large aspect ratio of nano-structures. (e) Resist lift-off process, showing combinations of fully, partial and remaining patterned polymer pillars.

developer will dissolve the unexposed resist. Over development results in rounding of features shown schematically in figure 3.6(c,v). When metal is subsequently deposited on an overdeveloped pattern, what can occur is that the deposition material makes a continuous film that is undulating where the remnants of the resist appear. An SEM of such an undulating is shown in figure 3.6(d,i). This surface structure is the result of the over-development of the pattern and dose used to create the pattern in figure 3.6(a,iii).

Furthermore the combination of dose and development time can lead to resist sidewall profiles that can be vertical, under-cut, or over-cut (figure 3.6(c,i-iii)). Under-cut resist is ideal for lift-off, but can lose some of the patterns fidelity. Vertical sidewalls result in perfect pattern fidelity but is not as ideal for lift-off. Over-cut features lose pattern fidelity and can result in issues in lift off as there can be a thin layer of deposition material connecting the material on the substrate and on the sacrificial polymer. The result is that the lift-off solvent may not be able to attack the polymer under this layer of material, and if sonication is used to assist the process the whole deposited layer may be removed, destroying parts of the desired pattern.

Development time may also be affected by temperature, with the solubility being reduced by lowering the temperature. By lowering the temperature, the development time is increases and the margin for error is greater. In most cases, however, room temperature will suffice.

In this thesis the developers used are summarised in table 3.1.

Table 3.1 Resists, Developer and Development conditions

Resist	Developer	Typical development time (s)	Developer removal
PMMA A4 950K	MIBK:IPA (1:3)	10	N_2 dry
UV111-6	MF-CD-26	30	DI water rinse
ma-N 2405	AZ-726-MIF	20	DI water rinse

3.2.1.5 Recipe example

Given the parameters that have been touched on so far, there is a huge variable space that can be accessed to fabricated a given nano-structure. The combinations of conditions used are referred to as the *recipe.* Table 3.2 shows a typical recipe used for negative resist patterning and development to fabricate nano-hole arrays for samples used in this thesis. In practice many combinations will be able to create a given pattern of resist which over many iterations will be optimised for a specific pattern.

Table 3.2 Typical Recipe for Negative resist ma-N 2405 EBL

Process	Conditions
Sample Cleaning	Ultrasonic bath: 10 mins acetone, 10 mins IPA, N_2 blow dry
Spin-coating	5000rpm for 60s. Post bake for 3min at 90°, $\sim$ 400nm thickness
EBL	*Exposure*: 80kV, area dose $\sim 2.0\mu C$cm^{-2}. Current $1nAs^{-1}$ *Apertures*: 125μm main-field, 5μm sub-field *Deflection*: $40 - 50$ MHz *Alignment*: (10μm) tungsten alignment marks on substrate
Development	AZ-726-MIF $\sim 20s$, DI water rinse $\sim 60s$, N_2 blow dry
PVD	Thermal evaporator or sputtering $\sim$ 30nm Al
Resist lift-off	Actone soak $\sim 20s$, Actone sonication $\sim 3min$, IPA sonication $\sim 3min$, N_2 blow dry

3.2.2 Metal deposition

Once the polymer resist has been patterned, to realise the desired metallic structure on the substrate, metal must be deposited onto the patterned substrate. The methods used in this thesis can be categorised as *physical vapour deposition* (PVD) techniques. PVD techniques are characterised by processes in which the material is vaporised from a solid state, to be transferred to the desired deposition substrate where it condenses back into a solid state, usually in the form of a thin film.

The two PVD methods used in this thesis are thermal evaporator and plasma sputtering.

Thermal evaporation A schematic of thermal evaporation is shown in figure 3.7(a). The substrate to be deposited onto is secured above the evaporation source material. The substrate must be in line-of-sight of the evaporation source, otherwise the material will deposit on whatever is blocking the way, as the evaporated material will travel in straight lines omni-directionally from the heated material. Due to the extremely low vapour pressure of metals, the evaporation must be performed under high-vacuum ($\sim 2 \times 10^{-6}$)mbar. This has the added benefit of removing oxygen from the evaporation environment, preventing hot metal particles from oxidising prior to reaching the desired

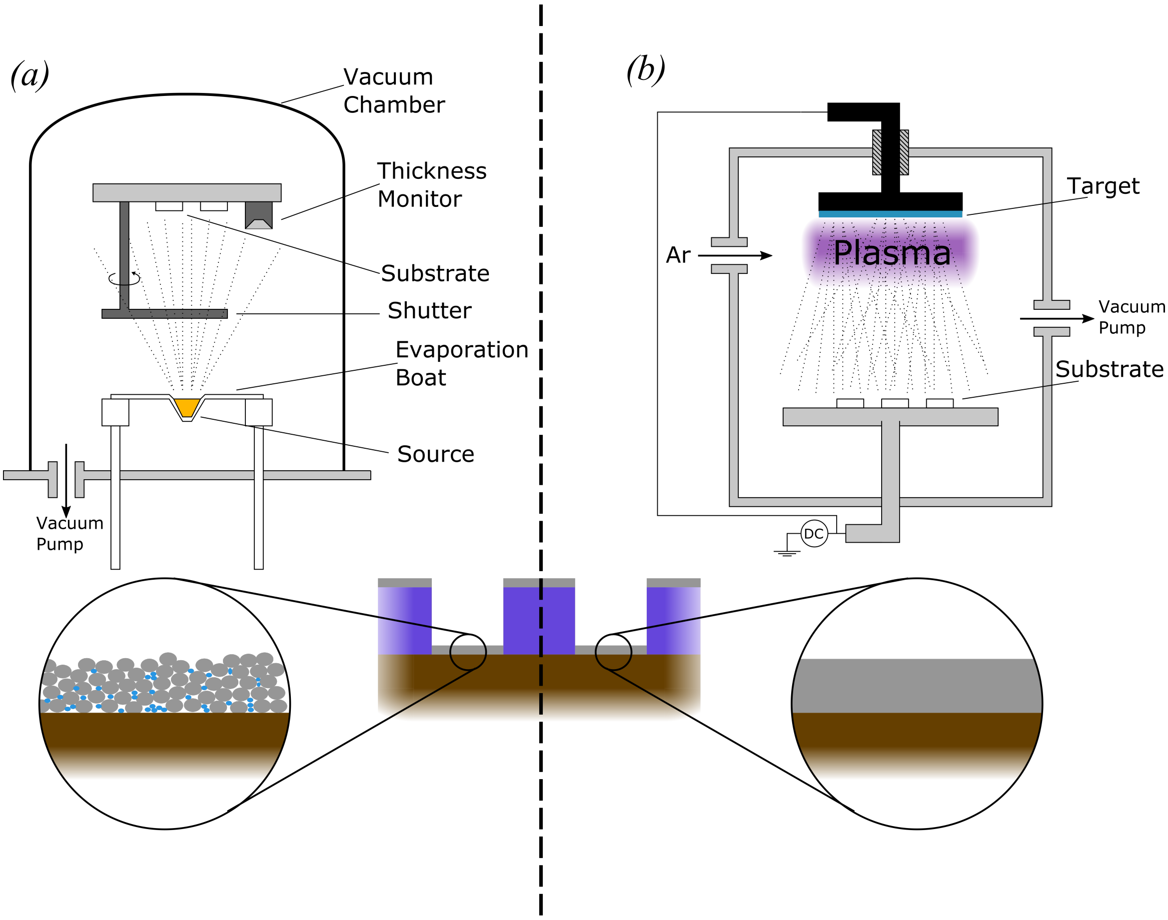

Figure. 3.7 Physical Vapour Deposition techniques. (a) Schematic of Thermal Evaporation of metal. The evaporation boat heats the metal in a vacuum so that the metal vaporises and is deposited, line-of sight, onto the substrate. The deposited metallic layer has a low-density porous structure. (b) Schematic of a DC metal sputterer. A plasma of argon ions are accelerated towards a target of the metal to be deposited. The metal atoms are displaced due to transfer of momentum, and travel towards the substrate where they are deposited. Due to the higher energy of the deposition atoms the metallic layer is uniform and densely packed.

substrate. The material is heated via a ceramic boat, with a wire core, that heats up resistively when a current passes through it. A shutter is used to block the line of sight of the substrate until such a time that it is opened, to allow deposition to begin. This allows contaminants on the metal surface to be evaporated first without affecting the deposition process. Deposition rate and thickness measurements are taken with a quartz piezoelectric crystal monitor. The deposition rate is carefully controlled to be $\sim$ 0.1nm s^{-1} to form a uniform thin layer. The substrate can also be rotated to ensure even covering, however in this work the substrate is simply placed a large enough distance from the metal source to ensure a uniform coating. Evaporation is a relatively low energy process, and, as a result, the thin films it produces are generally porous and of relatively low density. This can have knock on effects as the films can subsequently absorb moisture, which will alter the refractive index of the layer[109]. Low melting point metals (e.g. Al, Ag, Au) are easily evaporated, however high melting point metals are not suitable for this method, as their melting points tend to be higher than that of the metal in the ceramic heating boat and alternative methods must be used.

Plasma sputtering A schematic of a DC sputterer is shown in figure 3.7(b). In this case the substrate to be deposited onto sits below the source material. The source material is attached to an electrode to which an DC signal negative is applied to cause plasma gas ions, in this case Argon (Ar^+), to bombard the surface. The gas ions displace metallic particles from the target and the displaced particles travel towards to the substrate. These high energy atoms are then deposited onto the substrate. Sputtering is a relatively high energy process, resulting in very uniform, low roughness, high density amorphous films, with strong adhesion to the substrate. Unlike thermal evaporation, high melting point metals e.g. W (Tungsten) can be easily deposited. This process, however, in not suitable for the deposition of high quality thin films in the order of $\sim$ 1nm, Fortunately in this work, the only layer required to be of that order is the 3nm Al lower charge dissipation layer for which thermal evaporation may be used.

3.2.3 Resist removal

Having deposited metal onto the substrate, the final step is to remove the sacrificial layer of resist. Once removed all that remains on the substrate is the patterned metallic structures. The removal of the sacrificial resist layer is performed with a solvent, generally acetone. Negative resists are more difficult to remove entirely from a substrate. When this occurs N-Methyl-2-pyrrolidone (NMP) is an appropriate solvent. In both case soaking the polymer covered substrate in a warm solvent bath, followed by sonication for 3 minutes in the solvent, then 3 minutes sonication in acetone (if it was not the solvent used) and lastly 3 minutes sonication in IPA, is typically sufficient to remove all of the sacrificial resist for the purposes of this thesis. Longer time frames may be used when resist removal is more challenging.

Following resist *lift-off* (as this process is called), all that should remain is the desired metasurface.

Figure 3.6(e) shows a pattern part way through the lift-off process. Where the sacrificial resist has been removed there is the desired square nano-hole pattern is present on the substrate surface. In other areas pillars of resist with metal discs, yet to be removed, remain. This was the pattern than covered the substrate prior to lift-off. It is also possible to see part removed pillars. If these are not removed fully they can lead to a dirty surface, which combined with a LC will result in poor alignment and undesired optical properties.

3.3 Device construction

For passive metasurfaces EBL in conjunction with thin film metal deposition would suffice. However in order to convert the metasurfaces into active devices, further processing is required.

To integrate the devices with LCs a LC cell needs to be constructed, to encapsulate the LC on the metasurface and to enable a field to be applied to the LC. In the case of mechanical deformation, the metasurface is required to be transferred to an elastomeric medium.

3.3.1 Liquid crystal cell construction

A typical LC cell used in this thesis is shown in figure 3.8. The LC cell in constructed using the patterned substrate as the bottom encapsulating layer and the bottom electrode. The top layer of the cell is ITO covered glass, with a polyimide alignment

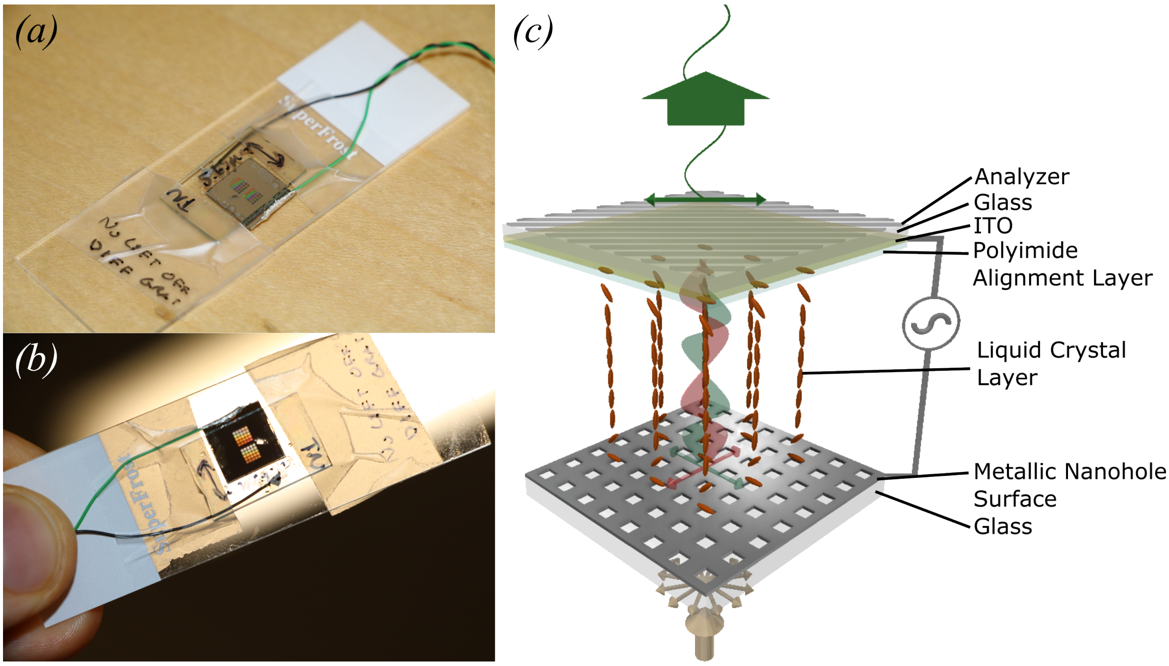

Figure. 3.8 Typical liquid crystal cell fabricated for the work in this thesis. (a) Photography of the cell attached to a glass slide to allow the cell to be viewed in a microscope setup. (b) Photography of the cell illuminated from behind showing patterns (coloured squares) and non-patterned (dark) areas. (c) Schematic of the typical LC cell structure.

layer. The ITO layer on the glass acts as the top electrode of cell, and is widely used in display devices due to its transparency in the visible spectrum. The ITO glass used is purchased from a commercial supplier (Sigma Aldrich: 8-10 Ω/sq, ITO thickness 120-160nm), and cut into rectangles $\sim$ 1cm$\times$1.5cm. The glass is then washed in Decon90 to remove any oil and dirt that may have contaminated the surface during cutting, and sonicated in acetone and IPA to ensure a clean surface. A clean surface is required to ensure an smooth and even alignment layer may be applied. Alignment layers are spin-coated onto the glass, and then baked for 30 min at $\sim$ 220° to drive off all solvent. Following baking, planar alignment layers (LC director parallel to the substrate surface) will be mechanically rubbed using a lint cloth roll ($\sim$ 250rpm). A hard rub will impart grooves into the alignment layer which the LC molecules with preferentially align with, a soft rub will re-align the molecules of the polymer alignment layer that the LC molecules will align to. Homeotropic alignment layers (LC director is perpendicular to substrate surface) do not require rubbing. For the most part hard rubbed LC alignment layers are used. Unlike most LC cells for display application, only one side of the cell has an alignment layer applied to it. This is for various reasons. LCs preferentially align to different metals in different ways[110], for example with Al the preferential alignment is planer, whereas with Ag it is homeotropic. Hence the metallic nano-structures can themselves be used as the lower alignment layer. Furthermore the anisotropic optical properties of LCs are to be used to control the resonances of the metasurfaces, hence the LCs need to be in direct contact with the metallic plasmonic meta-surface.

Once rubbed the ITO glass with alignment layer is glued to the bottom substrate with UV curing glue to create a cell. The glue contains spacer beads to give the cell its desired thickness. The spacer beads can vary in size to give different thicknesses of cells. The two most common spacer bead sizes used in this thesis were 2μm and 5μm. UV curing glue is used as it does not mechanically deform as it sets, hence it is easier to create cells of consistent thickness.

Prior to filling the cell thickness is measured. This is performed using an optical spectrometer connected to a microscope. the reflection spectra from the cell will have Fabry-Perot fringes due to modes associated with the cell thickness, such that

$$m = 2\mathrm{n}t\frac{1}{\lambda_m} - \frac{1}{2} \tag{3.16}$$

where m is the mode number, n is the refractive index of the cell cavity, λ_m is the wavelength of the mode and t is the thickness of the cavity. By plotting $1/\lambda_m$, the inverse of the location of the mode peaks, and taking the gradient you get the thickness of the cell at the point of measurement ($t = grad/2\mathrm{n}$). This is most easily done before filling the cell with the LC as the refractive index of air is 1, where as knowing the average refractive index of the LC in the cell gap is complex given it will depend on knowing its alignment perfectly.

Once the cell thickness is known the cell is filled with LC. The glue used to connect the two substrates is applied to only 2 sides of the cell to allow the cell to be filled with LC. The LC most generally used in the cells constructed for this thesis was BL006 ($\Delta\mathrm{n} = 0.286$), a nematic LC sold by Merck. The LC mixture and cell are heated, on a hot-plate, to the LCs clearing temperature to ensure there is no preferential alignment of the LCs prior to filling. A small volume of LC is applied to the edge of the cell where no glue was placed. Capillary action forces, due to the thinness of the cell, cause the LC to fill through the cell. Once filled the temperature of the cells are cooled slowly ($\sim 1^\circ$/min) to room temperature to ensure uniform alignment through the cell as the LC phase forms. Alignment is checked by placing the cell between crossed-polarisers and rotating about the z-axis. A planar aligned cell, will switch between light and dark states every 90° rotation.

Once filled, wires are connected to each electrode so that an electric field may be applied across the cell. To connect a wire to the metallic nano-structured surface, silver-epoxy resin is used. To connect a wire to the ITO electrode, indium-based solder is used. Where the substrate that ITO is deposited onto is sensitive to heat, the Ag-epoxy is also sufficient to create a contact. To check that the wires are in contact and that the cell is not shorted, the cell is placed between crossed-polarisers and an AC signal ($\sim$ 1kHz, $2V_{p-p}$) applied, if the cell is correctly assembled a planar align cell will switch from a light state to a dark, as the LCs become vertically aligned and no longer show a birefringence, and hence no longer rotate the polarisation of light.

3.3.2 PDMS pattern transfer

Polydimethylsiloxane (PDMS), is one of the most widely used silicon-based organic polymers. It does not absorb visible wavelength EM radiation, it is inert, non-toxic (it is used in foods as an anti-caking agent, E-number:E900), and inflammable. It is also readily available, relatively cheap, easy to mould, and in its solid form, acts as an elastomer. For these reasons, PDMS was the elastomeric compound of choice when considering polymers to use for integration with plasmonic metasurfaces.

It is nigh on impossible to pattern directly onto PDMS. Firstly it is an insulating substrate, which has its issues with e-beam patterning (discussed in section 3.2.1.3). Issues of patterning on non-conducting substrates can be overcome, however, the surface of PDMS is not flat. This can be seen in figure 3.9(e), showing an SEM image of a flat PDMS substrate with $\sim$ 40nm Al layer evaporated onto the surface. As such the charge dissipation strategy used for glass is not suitable for PDMS. Furthermore PDMS is sensitive to chemicals that would be used to remove resist layers, and development and lift-off processes.

The most widely used technique to put nano-structures onto a PDMS surface is pattern transfer [112, 95, 113, 97, 111, 96]. In essence the process is simple. Liquid PDMS is mixed with its cross-linker and poured onto the structure to be transferred. It takes in the order of hours for the mixture to set as a solid PDMS layer, hence there is plenty of time for processing. The PDMS covered structures are placed in vacuum to de-gas the liquid, as air bubbles are mixed into liquid PDMS when mixing with

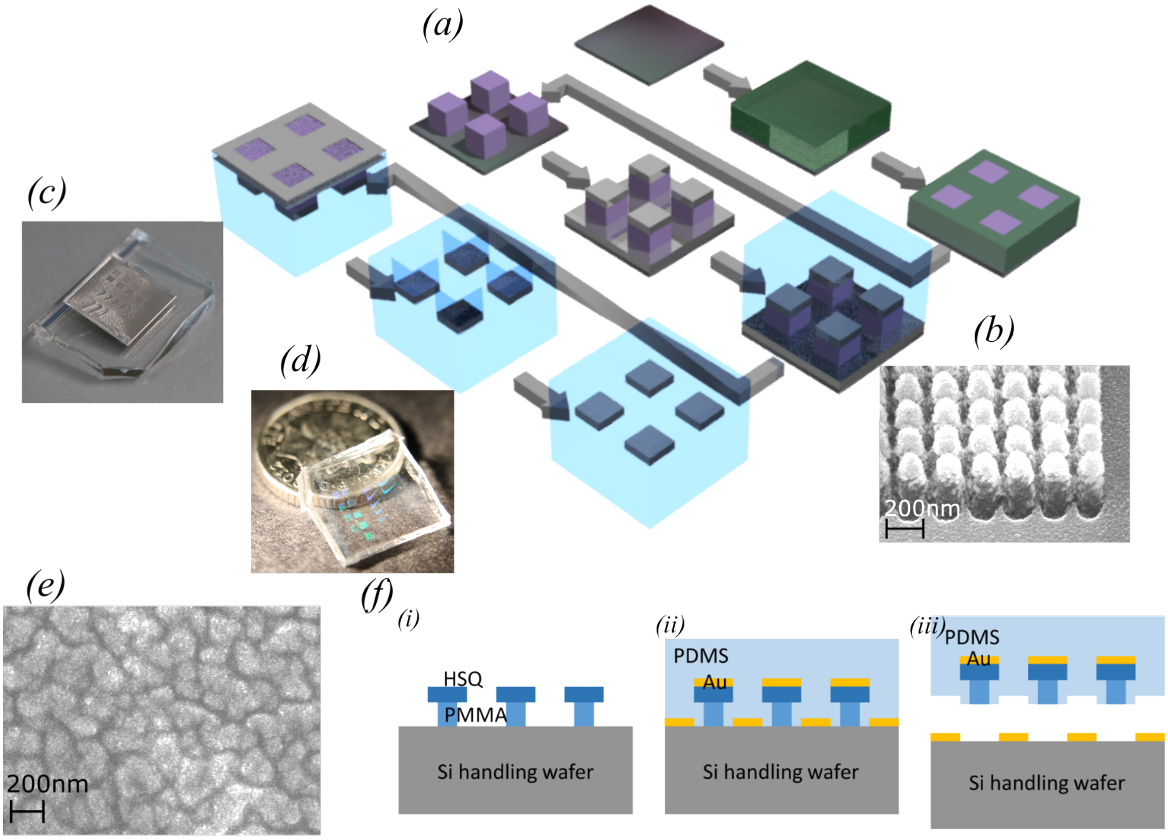

Figure. 3.9 Schematic of the PDMS pattern transfer process. The process is the same as EBL using negative resist, however no lift-off occurs. Instead the substrate is covered in liquid PDMS, which sets due to the action of a crosslinker. The entirety of the metal and resit is removed from the substrate via mechanical peeling. Excess metal transferred is removed leaving the desired pattern embedded in the PDMS. (b) SEM of nano-pillars with metallic nano-rods atop them. (c) PDMS mechanically peeled from a Si substrate, with complete metal film transfer. (d) Photograph of PDMS after excess metal removal. (e) SEM of PDMS surface with ∼ 40nm Al film deposited ontop to allow for SEM imaging. (f) PDMS pattern process proposed by Ee et al. with additional reactive-ion-etch step to allow from PDMS to set all around the nano-structure, images taken from[111].

the crosslinker. As the PDMS sets, it surrounds, shapes to and bonds to the metallic structures. When the PDMS has set solid the PDMS layer is mechanically peeled from the substrate. The metallic layer, along with the metallic structures atop polymer pillars, which preferably bond with the PDMS, is removed with the PDMS and you are left with the desired structure embedded in the PDMS substrate. One of the key factors to this process is the preferable bonding of the metallic layer with PDMS rather than the SiO_2 cap layer of the Si substrate. In this work it was found that preferential bonding was only found between PDMS and the metallic layer when the deposition method was thermal evaporation, as opposed to metal sputtering. Evaporation is widely reported to produce poorer surface adhesion than sputtering, due to the lower energy of particles as they are deposited leading to less dense, more porous films. This process has been shown to work with continuous metallic surfaces with nano-hole and gratings with width down to $\sim$ 100nm[113]. Issues occur when attempting to transfer nano-rods. As shown in figure 3.9(e) the surface of the set PDMS is not flat, with periodicity similar to that of patterns we are attempting to transfer. As such, not all nano-structures are likely to be in contact with the PDMS surface and hence, before any issues of preferential bonding come into play, metallic nano-structures will be left on the substrate. Ee et al. [111] proposed a novel technique to transfer nano-structures of size $\sim$ 100nm. They key part of their pattern transfer process is shown in figure 3.9(f) By using a two layer resist, and using an O_2 plasma to etch underneath the patterns to be transferred, the liquid PDMS is able to form underneath the metallic nano-structures. Hence when the PDMS is mechanically removed from the surface, the nano-rods are removed too.

In the course of this work a simpler technique was developed.

1. Negative resist is spun on a substrate – either glass or Si
2. Resist exposed in desired metallic deposition pattern by EBL
3. Resist developed and unexposed resist removed by developer solution
4. Metal deposited on developed patterned substrate
5. PDMS is mixed with cross linker (10:1 ratio) and poured onto sample
6. PDMS cured and then manually lifted from the sample surface, all resist, metal pattern and excess metal transferred to PDMS as the metal and resist preferably bond with the PDMS

7. Excess metal is removed

8. Nano-structures embedded in PDMS

The process is shown in figure 3.9(a). The idea is to embed nano-rods into the PDMS prior to removal to aid adhesion between the nano-rods and the PDMS. As opposed to patterning with a multi-layer resist and using a plasma etch, a similar structure can be formed by using a single layer of negative resist. By EBL patterning and metal deposition, as described in section 3.2.1, using a negative resist, but overlooking the lift-off process you can achieve nano-rod structure atop resist pillars as shown in figure 3.9(b). Once the patterning and deposition process is complete the desired pattern to be transferred is not on the substrate, but is now on top of resist pillars, that should we be wishing to pattern a nano-hole array would be atop the sacrificial layer of polymer. The result is that when the liquid PDMS is poured onto the substrate, the once discarded polymer pillars with nano-rods atop them are now embedded into the PDMS. When the PDMS sets, these pillars are embedded in the now solid structure and will be removed when the PDMS is mechanically peeled from the substrate surface. During the mechanical peeling, the nano-hole patterned layer will also be removed with the nano-rods. This can be seen in the photo in figure 3.9(c). As we are using Al as our metal of choice, this layer can be removed in a similar fashion to the charge dissipation layer when patterning on non-conducting substrates. A soak in Decon90 removes the residual aluminium nano-hole layer, whilst the desired nano-rods remain as they are protected by a resist pillar. Figure 3.9(d) shows the substrate in figure 3.9(c) following the soak in Decon90. It is possible to see the nano-structured patterns that remain in the resist.

The result is that an array of nano-rods can be embedded into an elastomeric PDMS surface, with high spatial precision, that may then be mechanically deformed. The rods may be protected further by covering the surface in an encapsulating PDMS layer.

3.4 Characterisation

Various techniques were used to characterise the devices fabricated for this thesis. The fabricated metallic nano-structures can be observed directly using *scanning electron*

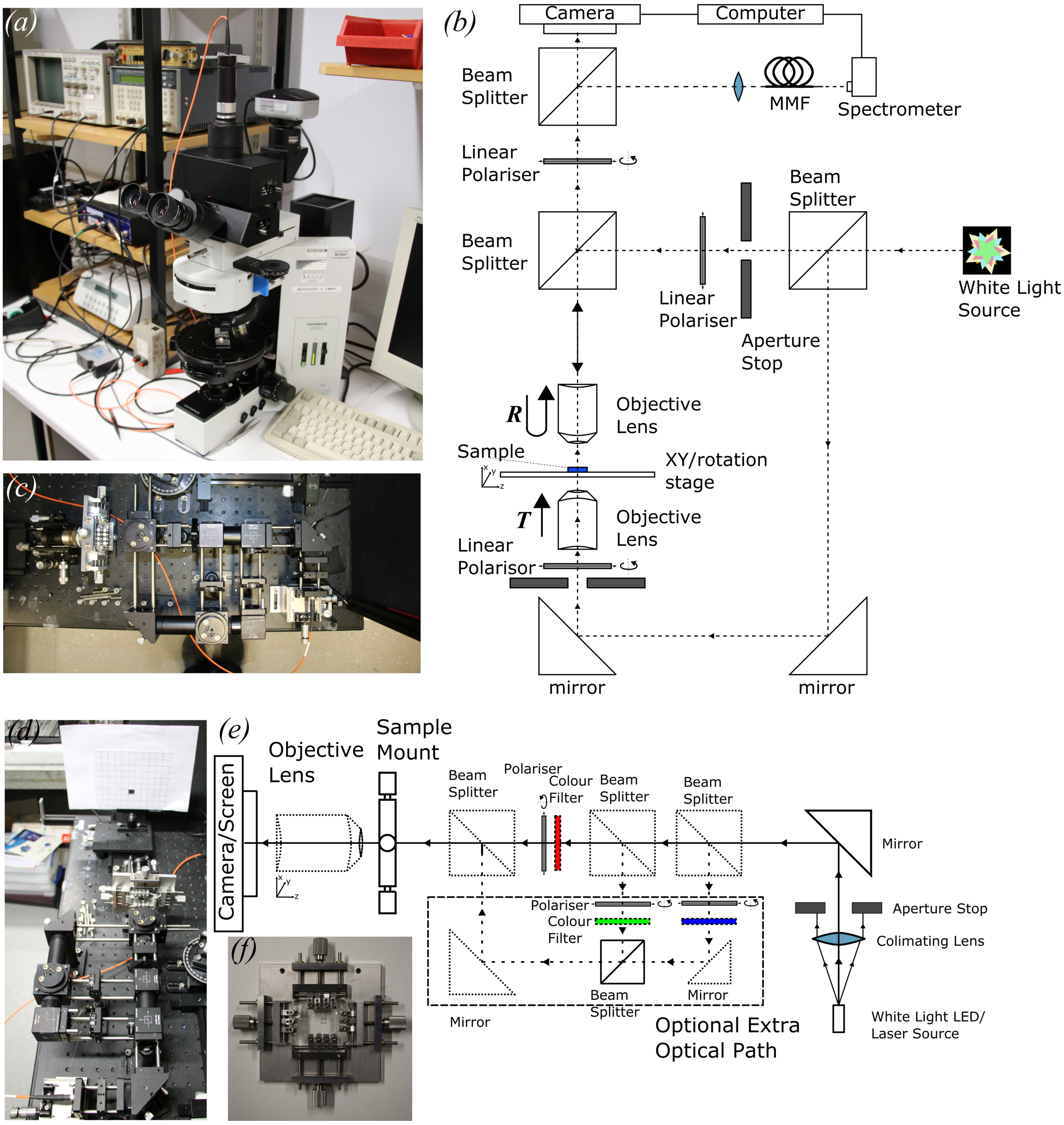

Figure. 3.10 Optical characterisation setups. (a) Photograph of Olympus BX-51 polarising optical microscope in laboratory setup. The microscope has attached to it a camera and spectrometer which are subsequently connected to a computer for data logging. The setup sits next to a signal generator to allow signals to be applied to the LC cells and data recorded. (b) Schematic of the polarising optical microscope setup. (c,d) Photograph of custom optical bench setup. (e) Schematic of the custom optical setup, showing optional extra components (dashed lines). When white-light source used, the objective lens is required and a camera records the image of the mounted sample. When a laser source is used, the objective is removed and camera replaced my a diffuse screen to display far-field pattern of the mounted samples. (f) Custom mount to enable stretching of elastomeric samples. Lateral stretches are achieved by turning the 4 screws. Each arm is attached to the sample via sliding clamps to minimise localised strain effects.

microscopy (SEM). Through SEM imaging it is possible to view the features to nano-scale detail. The SEM machine used was a commercial machine, operated with a standard operating procedure and as such will not be described any further. The optical performance of fabricated devices was observed using polarising optical microscope setup, incorporating a spectrometer and DSLR camera connected to a PC. In addition a custom optical-bench setup to allow for custom made apparatus to be used, as well as enabling far-field images of holograms to be recorded. These techniques are detailed in this section

3.4.1 Polarising optical microscope

A photography of the polarising optical microscope setup used is shown in figure 3.10(a), whilst a schematic of the setup is shown in figure 3.10(b). The microscope was an Olympus BX-51 polarising optical microscope. Connected to the microscope was a spectrometer (Ocean Optics HR2000+) and a DSLR camera, both connected to a PC which was able to capture and store the data. The illumination source of the microscope was a halogen white light source (with IR filters removed), and could illuminate the sample from above and below, allowing for both transmission and reflection data to be taken. The microscope had the ability to insert rotatable linear polarisers into the illumination and collection path. A range of objectives, from 4×-100× were used.

3.4.2 Custom optical bench setup

Photographs of the custom optical bench setup for hologram illumination and non-holographic device illumination are shown in figure 3.10(c,d) and a schematic is shown in figure 3.10(e). The main difference between the two setups is that for the hologram illumination a diffuse screen, with size grid, is used to view the image in the far-field, where as when setup for non-holographic devices the screen in replaced with a DSLR camera and an objective lens may be added. The coherent source used for hologram illumination an RGB laser diode (three laser diodes, optically combined; PM-RGB100:$\lambda = 450\text{nm}(100mW); 532\text{nm}(50mW); 650\text{nm}(100\text{mW})$) module. For non-holographic devices an incoherent 'cool-white' light diode source (ThorLabs) was used, coupled into the optics using an multi mode fibre (MMF), followed by a collimating lens. After the source there are optional beam splitters in whose paths are polarisers and colour filters to illuminate the desired sample with selectively polarised colours.

The samples are mounted in a custom holder detailed in figure 3.10(f). The mount is designed to allow the mechanical deformation of the sample in the x- and y-direction. Following the sample mount there is a removable objective to be able to view micron-sized features in the samples. The objective has an extra long working distance to allow for high magnification into the middle of relatively thick PDMS samples.

3.5 Summary

In this chapter the various simulation, fabrication and characterisation techniques used in this work have been outlined. Simulation of nano-structures is performed using a commercial-grade simulator based on the finite-difference time-domain method. Wider simulation of their applications (e.g. CGH) is performed using code written in MATLAB. Metallic nano-structures are fabricated using electron beam lithography (EBL) and physical vapour deposition (PVD). Devices were fabricated on optical transparent substrates (e.g. glass) to operate in transmission, and where necessary constructed into cells filled with liquid crystals (LCs). When constructed into a LC cell, the metallic pattern surface acts as the bottom electrode, whilst ITO covered glass forms the top electrode to allow a field to be applied across the cell. An alignment layer is used on the ITO glass layer to give alignment from the top of cell, whereas alignment at the bottom of the cell is determined by the metallic nano-structure. The nano-structures may be embedded into an elastomeric polymer layer allowing for mechanical deformation of the metallic nano-structure. The facile technique to embed nano-structures into a polymer layer is unique and developed by the author specifically for work presented in thesis.

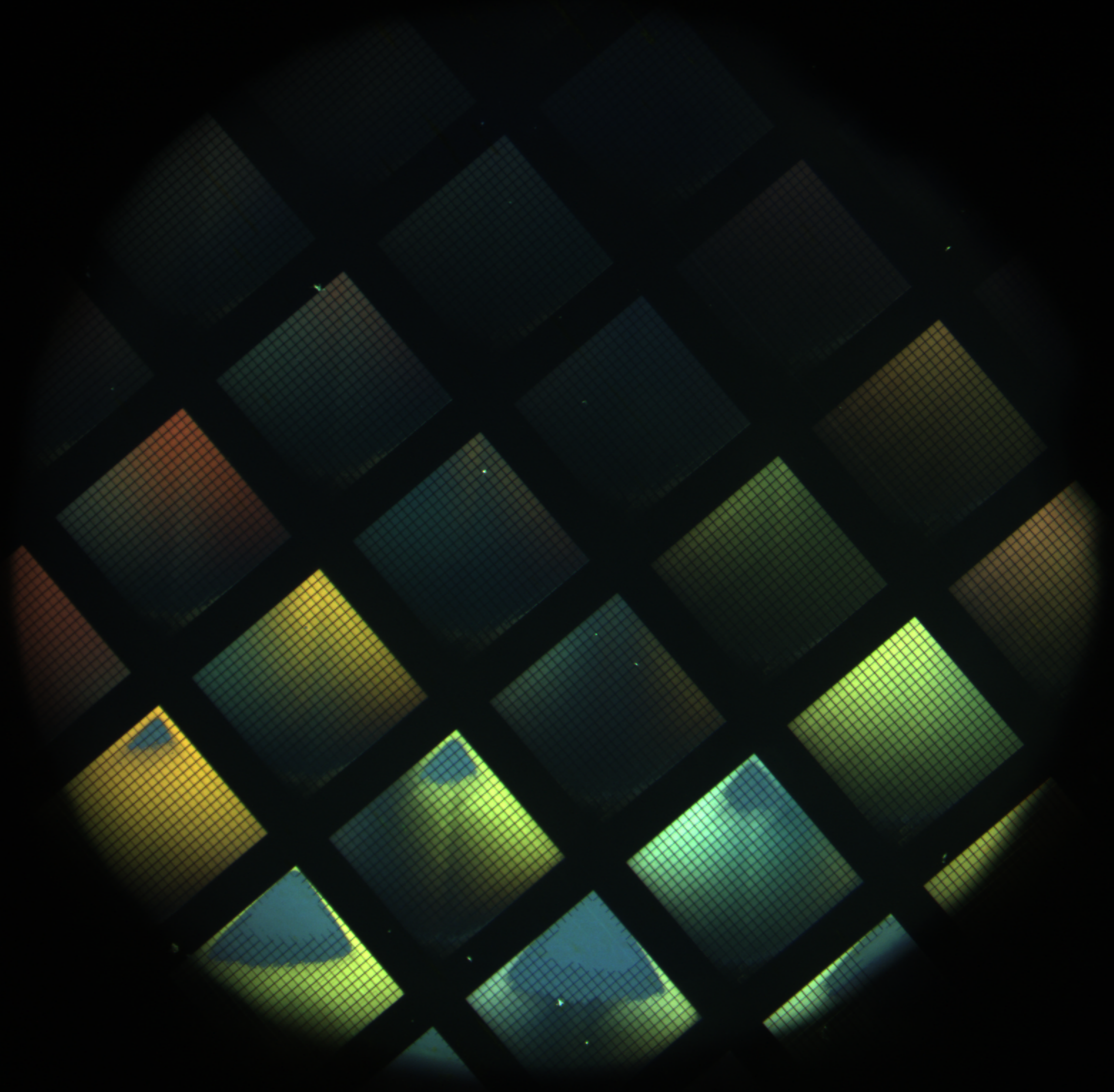

Chapter 4

Plasmonic nano-hole electrodes for active colour pixels

Introduction

Structural colour from nano-structured metallic surfaces has be used to create static pixels that can span the visible wavelength spectrum. As such they have the potential to replace colour pigments in modern display technologies and act as high resolution colour filters, polarisers, electrodes and even alignment layers. In this chapter, dynamic plasmonic pixels are presented which look to incorporate all of these properties. The colour of these structures is determined by the optical properties of the materials used and the physical dimensions of the structures themselves. The physical dimensions of the nano-structures may not be actively altered, that is to say post-fabrication these dimensions are constant, severely restricting its potential applications. It is possible, however to dynamically alter the optical properties of the medium surrounding the nano-structures. In this chapter, the structural colour generated from varying both the physical dimensions of the nano-structures and the permittivity of surrounding medium is presented. This information is then used in the design and fabrication of active devices, that have the potential to dynamically tune the transmission spectra of light passing through.

The devices in the chapter, for the most part, look to utilise the anisotropy and reconfigurability of liquid crystals (LCs). By changing the dielectric constant surrounding the metallic nano-structure, thereby shifting the plasmon resonance spectral location, the first device presented looks to build on previously demonstrated examples which currently either operate in the infrared or terahertz frequencies[114] or operate in the visible regime but only operate in reflection[93]. Secondly, LCs are used to modulate the polarisation state of light as it propagates through the device, followed by a linear polariser acting to selectively filter the transmission. Using this principal, we show voltage controlled plasmonic colour from single pixels[1]. Thirdly combining the metallic nano-structures with nematic LCs in a twisted nematic cell configuration, the LCs rotate the polarisation of light between crossed polarisers. When an E-field is applied to the device the LCs no longer rotate the polarisation of light and no light is transmitted, thus we show a plasmonic colour pixel with electronically controlled transmission intensity. Last, a device using an electro-optic substrate is presented, which, rather than altering the dielectric constant surrounding the metallic nano-structure, looks to electrically alter the refractive index of the substrate on which they are patterned.

4.1 Making nano-hole arrays active

Nano-plasmonics offers a pathway for creating a new class of ultrathin display pixels, which exhibit highly tunable optical properties using tailored arrays of sub-wavelength metallic nano-structures[17, 58, 93]. Pigment based colour filters currently have size limitations to the order of tens of microns for pixel size and microns in terms of the colour filter thickness, both of which may be surpassed by nano-plasmonic pixels. Compared with pigment based colours, nano-plasmonic pixels usually appear brighter under sunlight and are immune to photo-bleaching[115, 116]. Furthermore due to the reduction in material and chemical usage, metallic nano-plasmonic pixels offer an environmentally friendly alternative.

Metallic nano-hole arrays can be used to excite surface plasmon polaritons (SPPs), leading to wavelength dependent enhanced optical transmission in optically thick metallic layers[117]. The optical properties of the nano-hole layer are dependant on the geometry of the nano-hole and the material of the metallic layer. Through design, SPP excitation can be utilised to create a myraid of plasmonic based pixels operating across the visible spectrum[74, 93, 61, 118, 76, 119]. These include multi-colour polarisation dependent filtering, in which output colour is controlled via linear polariser

---

[1] This is published in Optics Letters Jul '17, "Plasmonic nanohole electrodes for active color tunable liquid crystal transmissive pixels"

rotation[120, 60], and complex wavefront shaping, based on arrays of spatially variant metallic nano-structures[121, 94]. Towards the goal of thinner, higher resolution and multi-functional electro-optic display pixels, these plasmonic pixels offer an innovative solution[58].

However, challenges to incorporate wideband tunable optical properties remain[17, 58], and generally, to induce a shift in plasmonic resonance, the manipulation of surrounding materials' refractive index is utilised[114, 92, 93]. Liquid crystals are optically anisotropic, and, possessing permanent dipole moments, will re-orientate under an applied electric field, providing an electro-optically tunable medium. Widely used as a fundamental building block for modern displays, LCs are a promising candidate for integration with metallic nano-structures for highly tunable plasmonic pixels[122, 93, 123].

4.1.1 Design

4.1.1.1 Surface structure; holes or rods?

When designing a surface for structural colour generation one has, initially, a choice between utilising a nano-rod, or its inverse, a nano-hole surface. Nano-hole surfaces produce colour due to a combination of surface plasmon polaritons (SPP) and localised surface plasmon resonances (LSPR) whilst a nano-rod array generates colour via LSPR and non-plasmonic resonances. A regular array of nano-hole or nano-rods may be thought of as a two-dimensional (2-D) metallic grating. A metallic grating is a useful structure to exploit in the process of producing structural colour. To excite a SPP resonance in a metallic surface, as discussed in section 2.1.1.1, extra momentum is required due to the binding of the resonant mode to metallic surface. This extra momentum may be provided by scattering from a topological defect or an undulation of the metallic surface. The metallic grating structure is able to provide the extra momentum required to generate surface plasmon polaritons. When light is diffracted by a grating structure it may be coupled into the surface plasmon mode parallel to the metallic surface. The periodic structure provides an in-plane wavevector increase by a factor $m\frac{2\pi}{\Gamma}$, where m is an integer and Γ is the grating pitch.

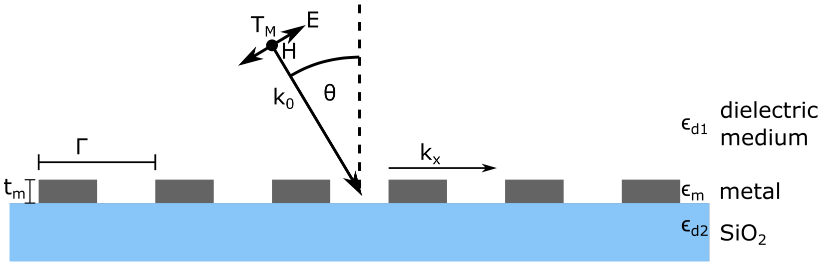

Figure. 4.1 Schematic of metallic grating upon SiO_2 substrate illuminated by a T_M polarised light wave

The coupling between SPPs, the incident light wave and the grating structure occur when the following condition is met when

$$k_{SPP} = k_x + k_{grat} \tag{4.1a}$$

$$\begin{aligned} k_{SPP} &= k_0\sqrt{\frac{\epsilon_m \epsilon_d}{\epsilon_m + \epsilon_d}} \quad ; \qquad k_x = k_0 \sin\theta \\ k_{grat} &= 2\pi\sqrt{\frac{m^2}{\Gamma_x^2} + \frac{n^2}{\Gamma_y^2}} \quad ; \quad m, n = 1, 2.....N \end{aligned} \tag{4.1b}$$

Fundamentally the spectra from a nano-hole or nano-rod structures are very similar. Modelled transmission and reflection spectra from a nano-rod and nano-hole with identical dimensions in an optically thin aluminium surface are shown in figure 4.2. The plots show how the spectra changes as the period of the grating structure increases (equally in the x- and y-directions).

Common to the two structures are LSPRs; responsible for the reflection dips in nano-hole surfaces, reflection peaks in nano-rod arrays and vice versa. The continuous nature of a nano-hole surface however, allows for the excitation of SPPs, whereas the nano-rod surface does not. The commonality of the LSPRs in the structures results in the spectra from each surface structure, like the structures themselves, being similar to the inverse of each other, i.e. the transmission spectra through a nano-hole surface is similar to the reflection spectra from a nano-rod surface, bar where SPPs of the nano-hole layer result in a deviation.

In the end though, the choice between utilising nano-rods or nano-holes comes down to a practical choice for integrating the plasmonic metasurface into a liquid crystal (LC) device.

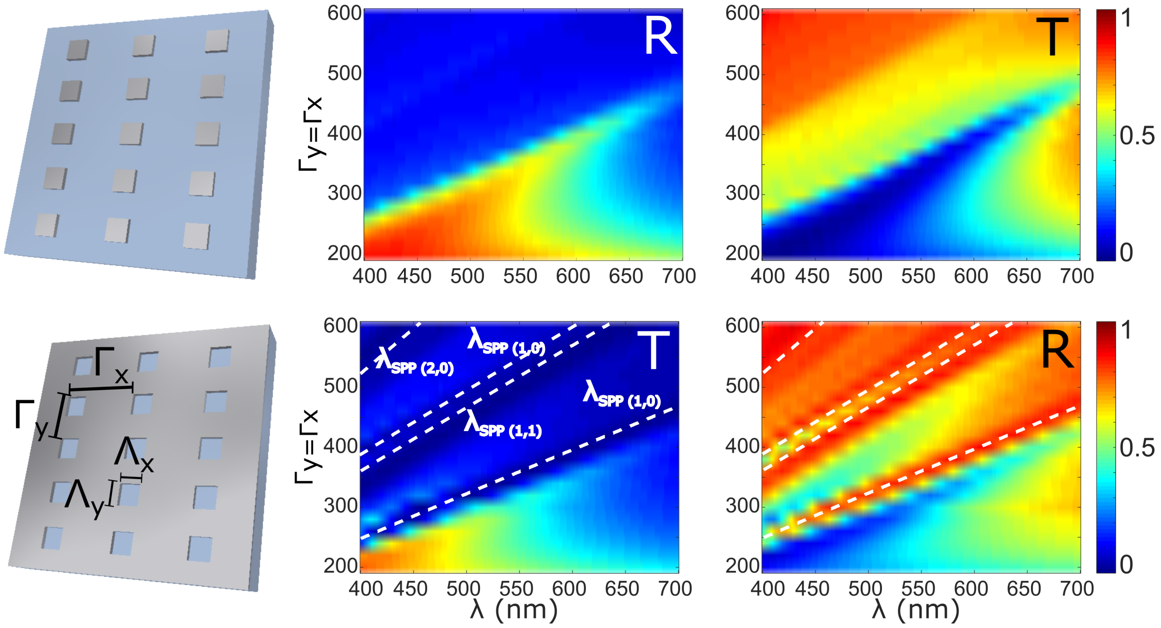

Figure. 4.2 FDTD simulated transmission and reflection spectra of a square nano-rod and nano-hole Aluminium (Al) surfaces with varying pitch, $\Gamma_{x=y}$. The metallic layer thickness $t_m = 30$nm and nano-structure size $\Lambda_{x,y} = 140$nm. Schematic of the nano-rod and hole surfaces are shown. Trend lines plotted show λ_{SPP} for an Al-grating on an SiO_2 substrate in air.

To exploit the optical birefringence of the LCs to create an active plasmonic device it is necessary to be able to re-orientate the LC molecule. This can be achieved by applying an E-field across the LC. Due to the polar nature of LC molecules, the molecule will align to the electric field that is applied. To apply an E-field across a LC layer, it is sandwiched in between two electrodes, which in most optical devices are two layers of ITO covered glass since ITO is optically transparent and is conductive. The integration of a plasmonic metasurface into such a cell involves replacing one of the ITO covered glass electrodes with the plasmonic metasurface. As such the choice of nano-holes is made, as the perforated metallic layer may act as an electrode layer. Nano-rods, being isolated metallic particles, either need to be patterned on a conducting substrate, or covered in an optically transparent conducting layer. Patterning nano-rods on a conducting substrate will alter the plasmonic resonances of the surface, whilst covering in an optically transparent conducting layer will bring the nano-structures out of contact with the LC, and hence removing the potential to exploit the birefringence of the LC to tune the plasmonic resonances of the surface. As such a nano-hole surface was chosen for the plasmonic nano-structures.

4.1.1.2 Nano-structure thickness

The coupling of light into the grating excites surface plasmons at the interface between the metal and the dielectric medium, and between the metal the substrate. The evanescent wave of the SPP modes perpendicular to the direction of propagation (z-direction) has a decay length in the surrounding dielectric medium of $\sim \lambda/2$ and in the metal approximately its skin depth (δ_d). At a sufficient thickness of metal (t_m) the two surface modes are independent of each other. When the thickness of metal is of the order of δ_d, or thinner, there is significant coupling between the two surface modes.

The coupling between the modes can be found by solving Maxwell's equations with the appropriate boundary conditions giving[124]

$$\tanh(S_2 t_m) = -\frac{\epsilon_m S_2(\epsilon_{d1} S_3 + \epsilon_{d2} S_1)}{\epsilon_{d1}\epsilon_{d2} S_2^2 + \epsilon_m^2 S_1 S_3} \tag{4.2}$$

S_1, S_2 and S_3 are defined as

$$S_1^2 = k_x^2 - \epsilon_{d1} k_0^2 \tag{4.3a}$$

$$S_2^2 = k_x^2 - \epsilon_m k_0^2 \tag{4.3b}$$

$$S_3^2 = k_x^2 - \epsilon_{d2} k_0^2 \tag{4.3c}$$

The FDTD simulated transmission spectra of a square nano-hole surface, with hole size 140nm×140nm and pitch 300nm×300nm, for Al, Ag and Au, in air, with varying thickness of the metallic layer are shown in figure 4.3. Overlaid on the spectra plots are the solutions to equation 4.1a and equation 4.2 for each metal ($m\!=\!1, n\!=\!0$). The solutions to equation 4.1a shows the resonant wavelength of the SPP modes at each interface with no coupling. The resonant wavelength for the metal-air interface is in the UV-wavelength range for the metals and hence is not shown in the figure.

Solutions to equation 4.2 are the resonant wavelength of the coupled modes. As the thickness of the metal increases, so it becomes possible to excite the resonant SPP modes at the metallic interfaces. The coupling of the two interface modes results in a lengthening of the resonant wavelength at the metal-air interface$\lambda_{SPP(1,0)}$. As the thickness of the metal reaches and passes through the skin depth of the metals, the resonant wavelength reaches, and moves through the visible spectrum, converging to the resonant wavelength of an isolated metal-substrate surface mode$\lambda_{SPP(metal-glass)}$.

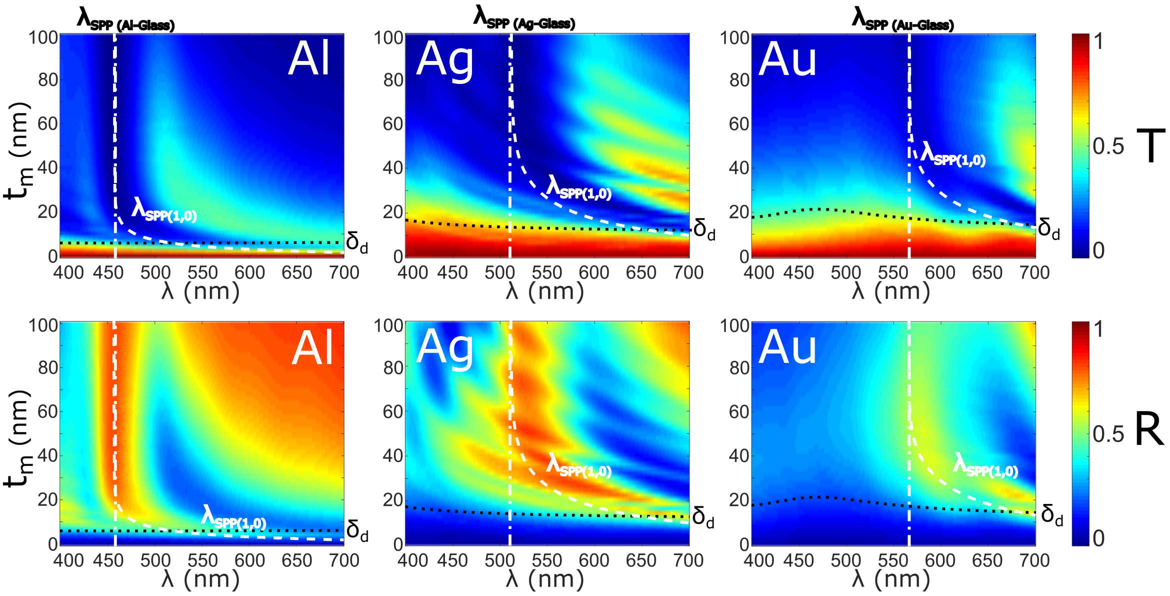

Figure. 4.3 FDTD simulated transmission and reflection spectra of a square nano-hole metallic surface varying layer thickness for Aluminium (Al), Silver (Ag) and Gold(Au). A schematic of the nano-hole surface is shown. The simulated surface has square nano-holes of size $\Lambda_{x,y} = 140$nm and periodicity $\Gamma_{x,y} = 300$nm. Trend lines plotted show $\lambda_{SPP(1,0)}$. The skin depth (δ_d) of the metals, calculated using the metals κ, is plotted.

The reflection spectra is in theory the inverse of the transmission spectra however there are optical losses to be taken into account which cannot be avoided. For Au these occur towards the shorter wavelengths of the optical spectrum. Looking at figure 4.3 neither reflectance or transmission is significant below $\lambda_{SPP(Au-glass)}$. The consequence is that should we be wishing to fabricate a nano-plasmonic device that has the potential to operate over the entire visible spectrum, Au is not a feasible option. As such, it is discounted from the rest of this work.

The surface plasmon polariton mode at the interface between the metal and the substrate, with resonant wavelength $\lambda_{SPP(metal-glass)}$, takes on an extra significance in the design of active devices. To make an active plasmonic metasurface device, the premise of the majority of designs is to modify the permittivity of the medium in which the metasurface sits. That is to say by modifying ϵ_d in equation 4.1a the resonant wavelength of the SPP mode may be altered. However the nano-structure needs to be fabricated somehow, typically using electron beam lithography (EBL). This process involves patterning on a substrate, typically Si or, in the case of devices designed to operate in transmission, glass. Neither of these substrates have the ability to modify their permittivities, hence there will always be a SPP mode that once the device is fabricated, may not be modified. In the case of a nano-hole surface in transmission this will cause a dip in the transmission spectra at $\lambda_{SPP(metal-glass)}$, that will need to be incorporated into the design of the device.

The thickness of devices to be fabricated was chosen to be $\sim$ 30nm. This thickness of metal provides a starting point for an active device that operates in the visible range. Considering figure 4.3, for Al this is an appropriate thickness as the transmission peak is in the visible range, whilst the transmission dip due to $\lambda_{SPP(Al-glass)}$ may be shifted out of the visible wavelength range by reducing the periodicity of the two dimensional grating. In the case of Ag, whilst the transmission dip due to the $\lambda_{SPP(Al-glass)}$ mode is in the middle of the visible wavelength regime, the thickness of metal is thin enough that the two SPP surface modes couple and the transmission dip is due to a combination of the SPP on both interfaces of the metal layer, resulting in the value of $\lambda_{SPP(coupled)}$ changing by modifying the resonance of $\lambda_{SPP(Ag-glass)}$ or $\lambda_{SPP(Al-dielectricmedium)}$.

4.1.1.3 Nano-structure geometry

Having determined the nano-structure type and the thickness of the metallic layer, the dimensions of the nano-hole layer need to be considered.

Various shapes of nano-structures have been considered over years for plasmonic applications. Bow-tie nano-structures have in particular been used for high field enhancement applications, whilst in structural colour applications regular shapes, typically circular or rectangular, and variations thereof, have been used. The use of regular shapes has additional ease of fabrication benefits.

When a rectangular nano-hole structure is illuminated with un-polarised light, two orthogonal resonant modes will be excited along the x- and y-axis of the shape, as illustrated in figure 4.4. By increasing the number of edges to the nano-hole aperture, one can increase the number of polarised modes. As the number of polarised modes increases, so does the cross-talk between the modes. For example when the square aperture is illuminated, un-polarised light will excite two distinct SPP modes polarised in the x and y directions, that is to say no component of the x-polarised modes affect the y-polarised mode. When the number of sides to the shape of the nano-structure are

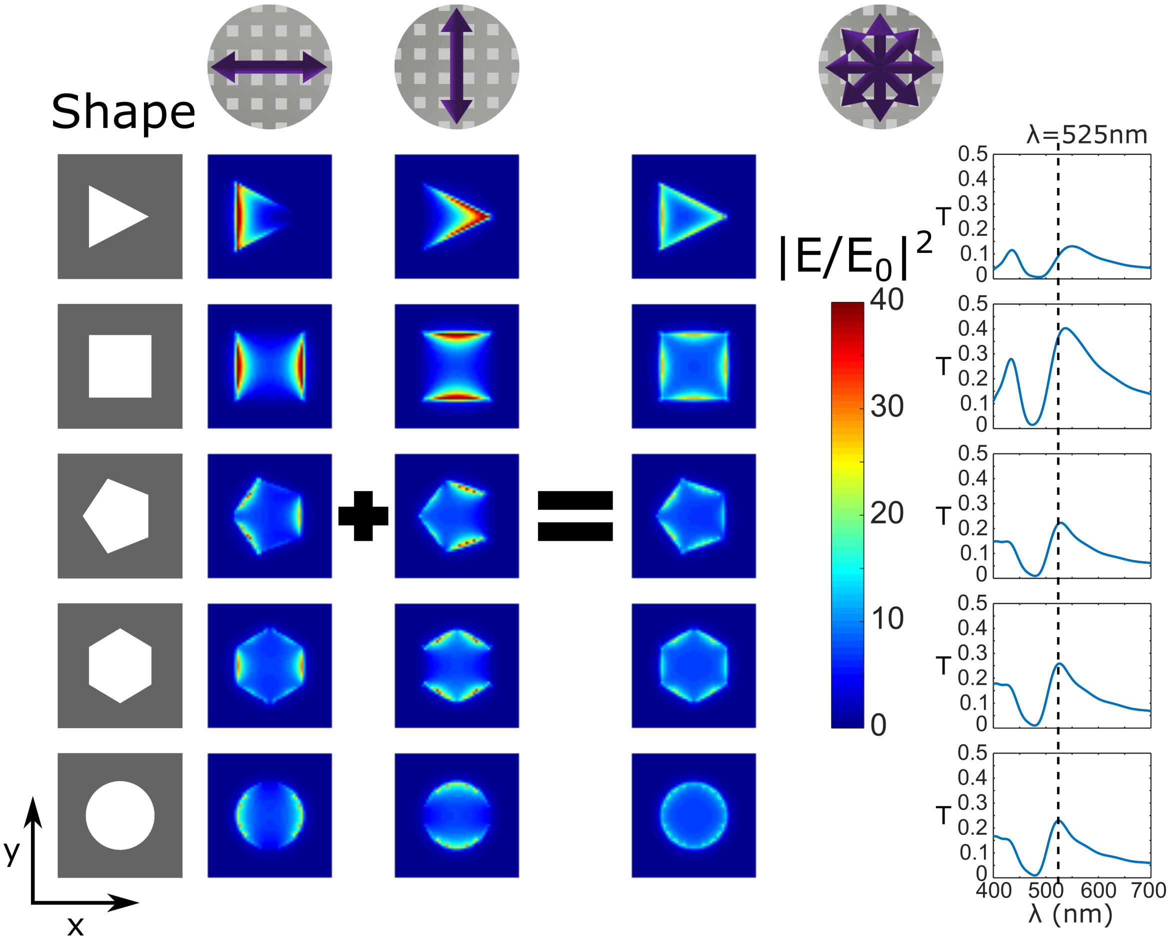

Figure. 4.4 Electric field intensity for nano-hole with varying geometry under x- and y-polarised illumination and un-polarised illumination. The shapes have increasing number of vertices $n_v = 3, ..., 6, \infty$. Transmission spectra for the varies nano-hole geometries with a pitch $\Gamma_{x,y} = 300$nm are shown.

increased, further modes are excited. The nano-holes are fabricated in a 2-D plane, and therefore only 2 axes exist which are totally independent of the other. The consequence is that unlike the rectangular apertures, in other shapes it is not possible to excite a single mode with a singular polarisation of light, hence there is cross talk between the different resonant modes of the nano-hole apertures. Furthermore should the apertures not have central symmetry, there will be a complex spectra from the aperture. This is shown clearly in the electric field enhancement plots shown in figure 4.4. Each aperture has the same periodicity and similar size, hence the transmission spectra for each individual shape is very similar. The highest transmission comes from the rectangular aperture, which combined with the fact that rectangular apertures possess two distinct orthogonal modes with no cross talk and are the simplest structure to fabricate, it is for these reasons the nano-hole surfaces designed and fabricated in this thesis will have a rectangular aperture.

4.1.1.4 Nano-structure dimensions

A schematic of a rectangular nano-hole surface is shown in figure 4.5. The dimensions that we may modify are the pitch, $\Gamma_{x,y}$, of the arrays of nano-hole in the x- and y-directions and the size, $\Lambda_{x,y}$, of the x- and y-dimensions of the rectangular nano-holes.

According to the solution to equation 4.1a the position of the dip in the transmission spectra due to SPPs is dependent on the grating period, $\Gamma_{x,y}$. When the grating period is equal in the x and y directions, $\Gamma_x = \Gamma_y$, and assuming the nano-hole is also symmetric, $\Lambda_x = \Lambda_y$, the resulting spectra is polarisation independent. This is because the polarised transmission from a rectangular aperture depends on the two orthogonal SPP modes by[17]

$$T_\theta = T_x \sin^2\theta + T_y \cos^2\theta \tag{4.4}$$

As θ varies, should the periodicity and aperture size and shape be consistent in the x and y directions $T_x = T_y$ and hence T_θ will be constant. However, should the pitch no longer be equal in the x and y direction, $\Gamma_x \neq \Gamma_y$, $T_x \neq T_y$ and the transmission spectra will no longer be polarisation independent.

The grating period of the nano-hole array has a significant influence on the transmission spectra through a nano-hole array. By varying the grating pitch, $\Gamma_{x,y}$, the resonant frequency of the plasmonic modes is altered.

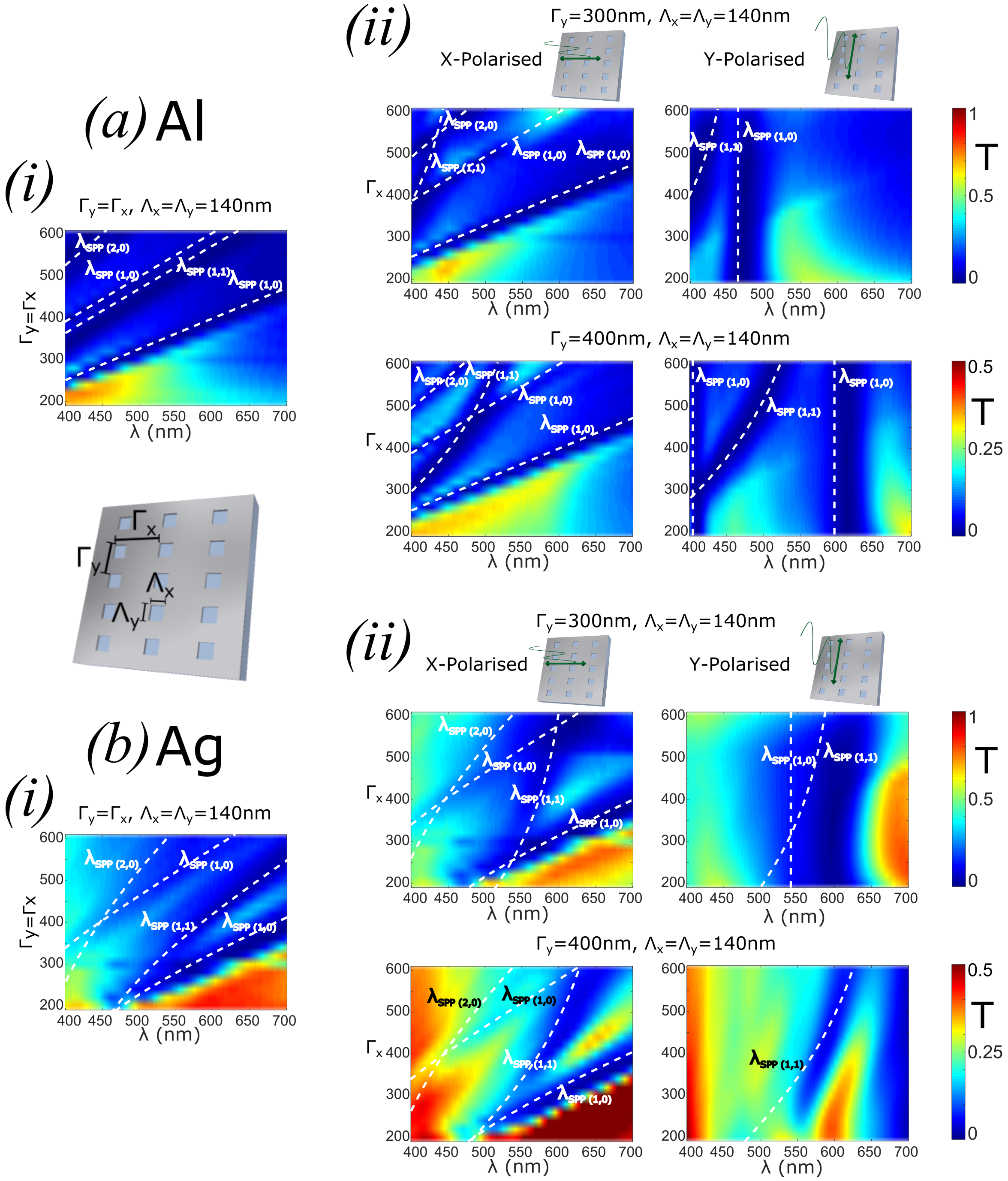

Figure. 4.5 Simulated transmission spectra varying rectangular nano-hole periodicity for (a) Al and (b) Ag metallic nano-hole layers. (i) Transmission spectra varying nano-hole periodicity equally ($\Gamma_{x=y}$). (ii) Tranmission spectra for nano-hole arrays varying Γ_x whilst keeping Γ_y constant. Spectra are shown for light polarised along the x and y axis. The dimensions of the rectangular nano-holes are $\Lambda_{x,y} = 140$nm.

Figure 4.6(a,i) shows the transmission spectra for an array of rectangular nano-holes, with dimensions $\Lambda_x = \Lambda_y = 140$nm, in a 30nm thick aluminium layer, varying the periodicity, Γ, evenly in the x- and y- direction from 200nm to 600nm. The resonant wavelengths, $\lambda_{SPP(m,n)}$, of the various SPP modes are plotted. When $(m = 1, n = 0)$ the solutions to equation 4.2 corresponding to the metal-air and metal-dielectric interfaces pass through the visible spectrum, albeit not necessarily for the same value of Γ. At certain values of $\Gamma_{x,y}$ there are more than one λ_{SPP} dips in the transmission spectra, which may be exploited to narrow the transmission spectral peaks.

By asymmetrically varying the pitch of the nano-hole arrays it is possible to manipulate the transmission spectra further, as well as realising a polarisation dependent response from the surface. Figure 4.6(a,ii) shows the FDTD simulated transmission spectra of an aluminium nano-hole array varying Γ_x and holding Γ_y constant at 300nm, under x- and y-polarised illumination. Looking at the separate orthogonal polarisation results, varying the periodicity of the array in the same direction as the polarisation of the incoming light, similar trends in the resonant wavelength of the SPP modes are seen as when varying Γ_x and Γ_y equally. When illuminated with x-polarised light, no $\lambda_{SPP(0,1)}$ mode exists, hence the variation of Γ_x is the critical dimension for Al. This is supported by the simulated transmission spectra, when varying Γ_x and illuminating the array with y-polarised light. The position of $\lambda_{SPP(1,0)}$ does not vary. The higher order mode, $\lambda_{SPP(1,1)}$, will vary with either polarisation of illumination, however, for aluminium the resonance is generally away from the visible spectrum.

As one might expect, keeping the size of the nano-holes constant while increasing the pitch of the array, there is a drop in the overall intensity of transmission, as the area through which may be transmitted becomes less per unit area of the nano-hole surface.

Still varying Γ_x but keeping Γ_y constant at the larger periodicity of 400nm, shows the dependency on the Al nano-hole array periodicity in the same direction as the illumination polarisation. The location of the resonant SPP modes, when the nano-hole array is illuminated with x-polarised light, are the same as when $\Gamma_y = 300$nm, with the exception of $\lambda_{SPP(1,1)}$, which has a dependency on Γ_y. Under y-polarised illumination the transmission dips due to the $\lambda_{SPP(1,0)}$ modes have been moved to longer wavelengths.

Like aluminium, nano-hole arrays in silver, with periodicity, Γ, varying from 200nm to 600nm have their SPP resonant modes in the visible wavelength regime. Due to the different permittivity of Ag to Al, the location of the SPP resonances vary, and in fact, with Ag, higher order modes are more prominent. Figure 4.6(b,i) shows the equivalent plot for Ag, varying the periodicity, Γ, evenly in the x- and y- direction. Similar trends as those seen for Al are shown, however the $\lambda_{SPP(1,1)}$ mode is more prominent, occuring at a wavelength in between that of the two $\lambda_{SPP(1,0)}$ surface mode resonances.

When varying varying Γ_x but keeping Γ_y constant for a nano-hole array in Ag, the $SPP_{(1,1)}$ mode plays a significant role. Figure 4.6(b,ii) shows the FDTD modelled transmission spectra varying Γ_x but keeping Γ_y constant at 300nm, $\lambda_{SPP(1,1)}$ occurs in the middle of the visible wavelength, a fact that is not changed by increasing Γ_y to 400nm. This will be a hindrance that needs to be accounted for in the design of green structural colour, if using a silver metallic layer.

Overall what figure 4.6 shows us is that by varying the periodicity of a nano-hole array it is possible to manipulate the resonant wavelength of the various SPP modes of the nano-hole surface to generate colour across the visible wavelength spectrum. The dips in transmission spectra are shown to be due to the SPP modes of the metallic nano-hole structures, however the overall transmission is reduced by increasing the periodicity, $\Gamma_{x,y}$, but not the size of the nano-hole, $\Lambda_{x,y}$, as the overall area through which light may be funnelled is reduced. As we see this issue may be overcome by varying the dimensions of the rectangular nano-holes

The last remaining geometric parameter which may be varied are the dimensions of the nano-holes themselves, $\Lambda_{x,y}$. The size of the nano-hole influences the transmission spectra by means of localised surface plasmon resonances (LSPR) and their interactions with the propagating SPP modes. The influence of these LSPRs gets smaller as the periodicity of the nano-holes increases. Figure 4.6(i) shows the effect of varying the size of the nano-holes in an Al and Ag layer with periodicity of $\Gamma_{x,y} = 300$nm. Looking initially at a nano-hole array in aluminium, when varying the x- and y-dimensions of the rectangular nano-hole equally, $\Lambda_x = \Lambda_y$, there is a transmission dip whose spectral location does not change and corresponds to the resonant wavelength of $\lambda_{SPP(1,0)}$. The location of the SPP resonant modes, as per equation 4.2, depends on the periodicity of the nano-hole layer, not the dimensions of the nano-hole itself. As the size of the nano-structure increases, however, the magnitude of the transmission peak increases and the wavelength shortens. The increase in the magnitude of the transmission peak is expected as there is a larger area for the light to be funnelled through. The shortening of the wavelength of the transmission peak is due to localised effects.

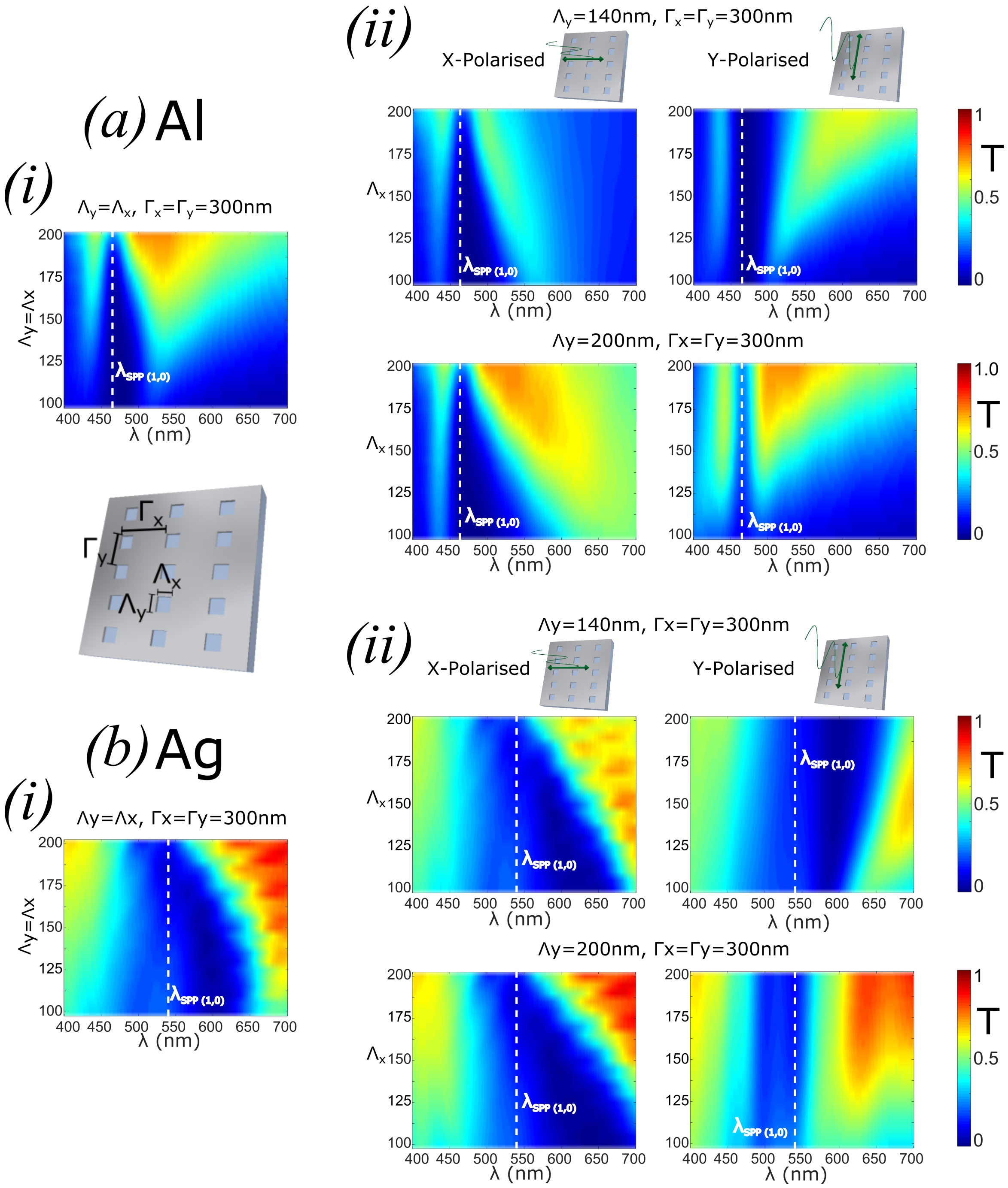

Figure. 4.6 Simulated transmission spectra varying rectangular nano-hole dimensions for (a) Al and (b) Ag metallic nano-hole layers. (i) Transmission spectra varying nano-hole dimensions equally ($\Lambda_{x=y}$). (ii) Transmission spectra for nano-hole arrays varying Λ_x whilst keeping Λ_y constant. Spectra are shown for light polarised along the x and y axis. The periodicity of the rectangular nano-hole arrays is $\Gamma_{x,y} = 300$nm.

When varying Λ_x and Λ_y independently, the effects of varying the x- and y-dimensions are unique to each axis and are shown in figure 4.6(a,ii). If the size of the nano-hole is increased in the same direction as the polarisation of incoming light (i.e. varying Λ_x and keeping Λ_y constant whilst illuminating with x-polarised light) the wavelength of the transmission peak shortens. However when the size of the nano-hole is increased orthogonal to the polarisation of the incoming light (i.e. varying Λ_x and keeping Λ_y constant whilst illuminating with y-polarised light), the wavelength of the transmission peak increases. In both cases there is still the immovable transmission dip due to $\lambda_{SPP(1,0)}$. Adjusting the size of the dimension held previously held constant, Λ_y, simply shifts the starting points for the two plots, with the same trends seen.

Changing to a different metal, does not alter the trends seen. Figure 4.6(b), presents the same plots for Ag as those discussed for Al. The location of the $\lambda_{SPP(1,0)}$ is now in the centre of the visible spectrum due to ϵ_{Ag}, however, how the spectrum varies around this mode is similar. When varying Λ_x and Λ_y equally the magnitude of the transmission peak increases, whilst the wavelength of the transmission peak (λ_{pk}) shortens. When altered individually, when the dimensions in the same direction as the polarisation (i.e Γ_x with x-polarised light) is increased λ_{pk} shortens, whereas when the dimension orthogonal to the polarisation is increased (i.e Γ_x with y-polarised light) λ_{pk} increases. The fact that when both Λ_x and Λ_y are increased λ_{pk} decreases shows that the dimension parallel to the incoming polarisation of light has the greatest effect on the peak transmission wavelength.

The two mechanisms that influence the spectra maxima and minima can be best illustrated by the electric field plots shows in figure 4.7. The transmission spectra of a nano-hole with dimensions $\Lambda_{x,y} = 140$nm on glass and in a dielectric medium of n=1.53, in array with $\Gamma_{x,y} = 300$nm and as an isolated nano-hole, are shown. The spectra of the nano-hole array has a transmission maxima due to LSPRs and a minima due to SPPs. If the nano-hole is not in an array, but is simply an isolated nano-hole, SPPs may not be supported, and the only mechanism available to alter the spectra are LSPRs. The LSPR mode supported in the individual nano-hole is broadband, enhancing transmission across the visible spectrum.

The presence of SPPs in the nano-hole array is indicated in the electric field plots for the nano-hole array. At λ_{SPP} the electric field plot of an individual nano-hole in the array shows a high E-field across the surface of the unit cell. This is due to the propagating SPPs. At λ_{LSPR} the E-field is highest within the nano-hole and the

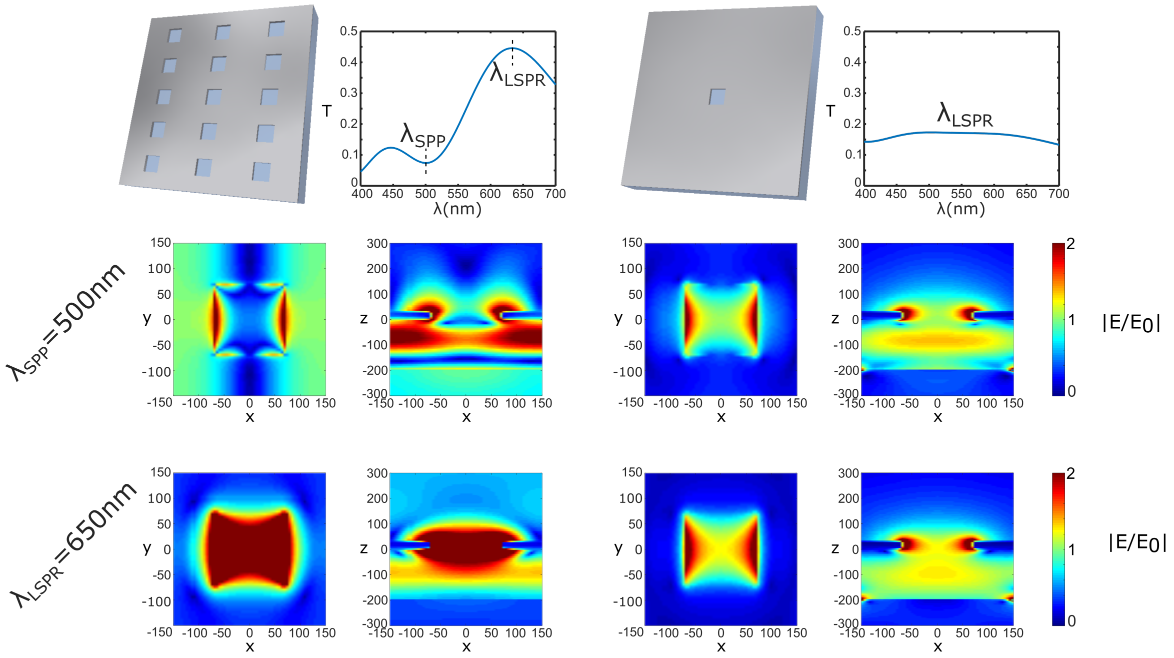

Figure. 4.7 Comparison of nano-hole array and isolated nano-hole plasmonic resonances. Transmission spectra showing location of SPP and LSPR resonances. E-field plots at z and x normal planes of both a nano-hole in an array and an isolated nano-hole at the SPP and LSPR resonant wavelengths of the nano-hole array

resonances are localised to the nano-hole, decaying to edge of the unit cell. The result is at λ_{SPP} the optical energy is reflected and at λ_{LSPR} transmitted. This is once again shown in the E-field plots, with the E-field at the z_{min} and z_{max} boundaries (note that the source is positioned at z=−200nm). The best comparison for the array data comes from observing the isolated nano-hole. The reason for this is because a singular nano-hole is unable to support SPPs. Hence any field enhancement would be due to LSPR as opposed to SPPs. At both λ_{SPP} and λ_{LSPR} of the periodic nano-hole array, the E-field enhancement of the isolated nano-hole is within the nano-hole and decays to the edge of the unit cell. This is directly comparable to the E-field plot of the nano-hole array at λ_{LSPR} confirming the mechanism for maxima in the transmission spectra.

4.1.1.5 Design Summary

The effect of altering the physical dimensions of the rectangular nano-hole structure on the peak transmission wavelength (λ_{LSPR}) and the minimum transmission wavelength (λ_{SPP}) are summarised succinctly in figure 4.8. This clearly shows how the size of

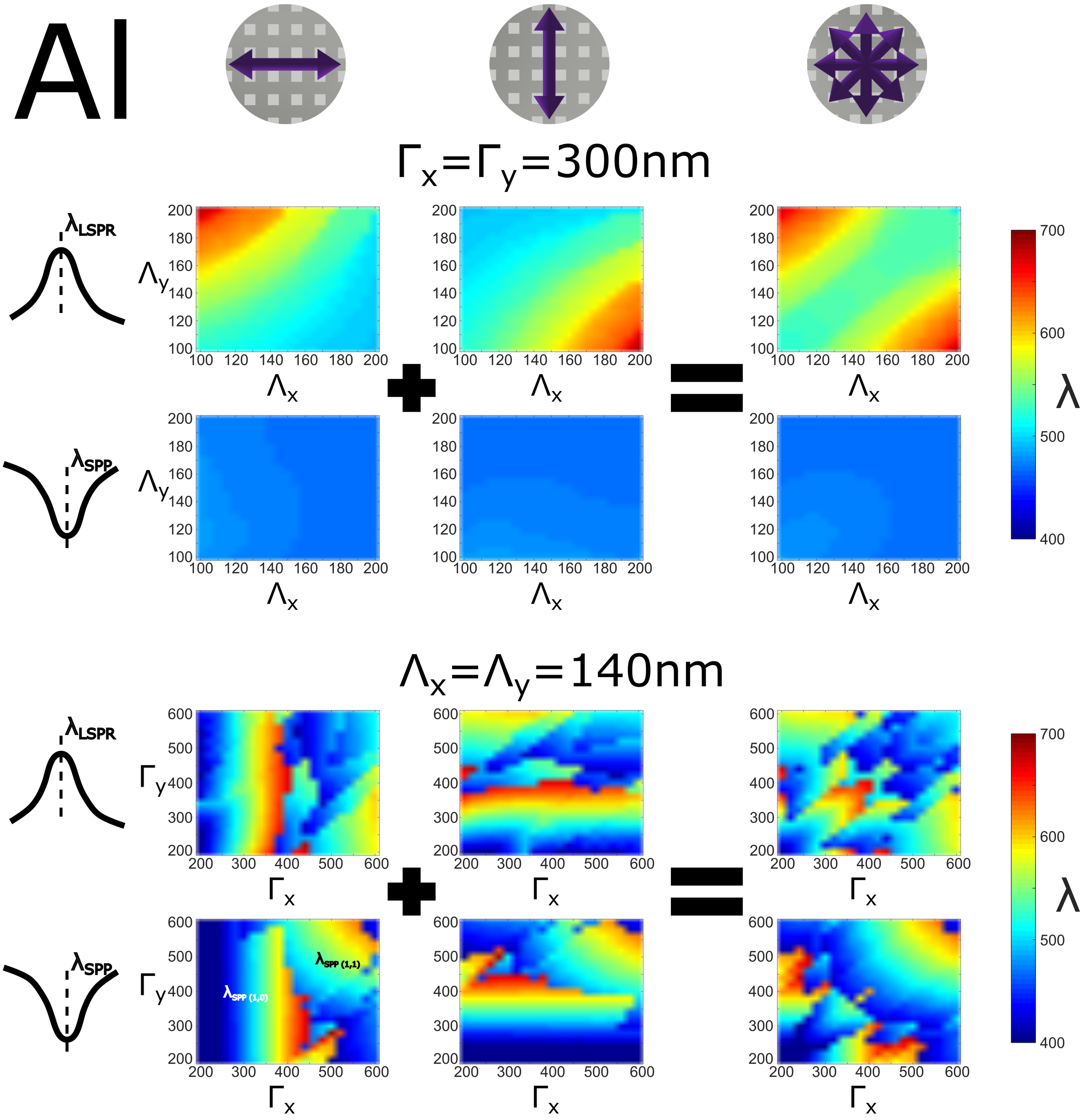

Figure. 4.8 Location of maximum (λ_{LSPR}) and minimum (λ_{SPP}) simulated transmission wavelengths for rectangular nano-hole array, varying the dimensions of the array under x,y and un-polarised illumination. (i) Maximum and minimum transmission wavelengths keeping $\Gamma_{x,y} = 300$nm and varying $\Lambda_{x,y}$. (ii) Maximum and minimum transmission wavelengths keeping $\Lambda_{x,y} = 140$nm and varying $\Gamma_{x,y}$

nano-hole and pitch of nano-holes affects the transmission spectra. What this does not show is the width of the peaks and troughs and thus only gives an indication of the eventual colour that will be seen from such a fabricated metasurface.

4.1.1.6 Fabricated nano-hole arrays

The structural colour produced by metallic nano-hole arrays is best demonstrated by a fabricated device. Figure 4.9 shows a nano-hole array in a 30nm thick aluminium surface in transmission and reflection, illuminated with x-polarised, y-polarised and un-polarised light. The nano-hole surface is split into a 6x6 large grid pattern. Each grid is 400μm$\times$400μm in size. The bottom left grid has a periodicity $\Gamma=200$nm. As you move from grid to grid in the x- and y-directions the periodicity increases by 50nm in the x and y directions respectively. Thus the grid in the top right corner has a periodicity of $\Gamma_x=\Gamma_y = 450$nm. Each large grid is split into 20x20, 20μm$\times$20μm, sub-grids. Each sub-grid has nano-holes of different dimensions. In the bottom left corner of each sub-grid the dimensions of the rectangular nano-holes are 100nm $\times$ 100nm. As you move from sub-grid to sub-grid in the x- and y-directions the size of the nano-hole increases by 5nm in the x- and y-directions respectively. Thus the sub-grid in the top right corner of each large grid has nano-hole dimensions of $\Lambda_x=\Lambda_y=200$nm.

Looking at the nano-hole surface in transmission it is clear to see the influence of λ_{SPP}. Under x-polarised light, as Γ_x increases the location of λ_{SPP} increases and the colour of each gird square changes from red/yellow at $\Gamma_x = 300$nm, to red at $\Gamma_x = 350$nm and green at $\Gamma_x = 400$nm. As predicted by the FDTD modelled spectra an increase of Γ_y under x-polarised light does not shift the position of λ_{SPP}, but does reduce the magnitude of transmission. What does happen as the size of $\Gamma_{x,y}$ are reduced is that the influence of the size of the nano-hole increases. This can be seen by observing the colour change across individual constant periodic grids. For example, under x-polarised illumination, when $\Gamma_x = 350nm, \Gamma_y = 450$nm there is less variation in colour across the grid as $\Lambda_{x,y}$ change, whereas when $\Gamma_x = 350nm, \Gamma_y = 200$nm there is clear colour shift from purple/blue in the top right to red in the bottom left. The colour shift across grid is most pronounced for $\Gamma_x = 300$nm, with variations in Γ_y having limited variation of the colour shift between grids. Similar trends can be seen looking at the nano-hole surface in reflection, however a greater variety of colours may be seen. For example, under x-polarised illumination, when $\Gamma_x = 350$nm, as Γ_y varies

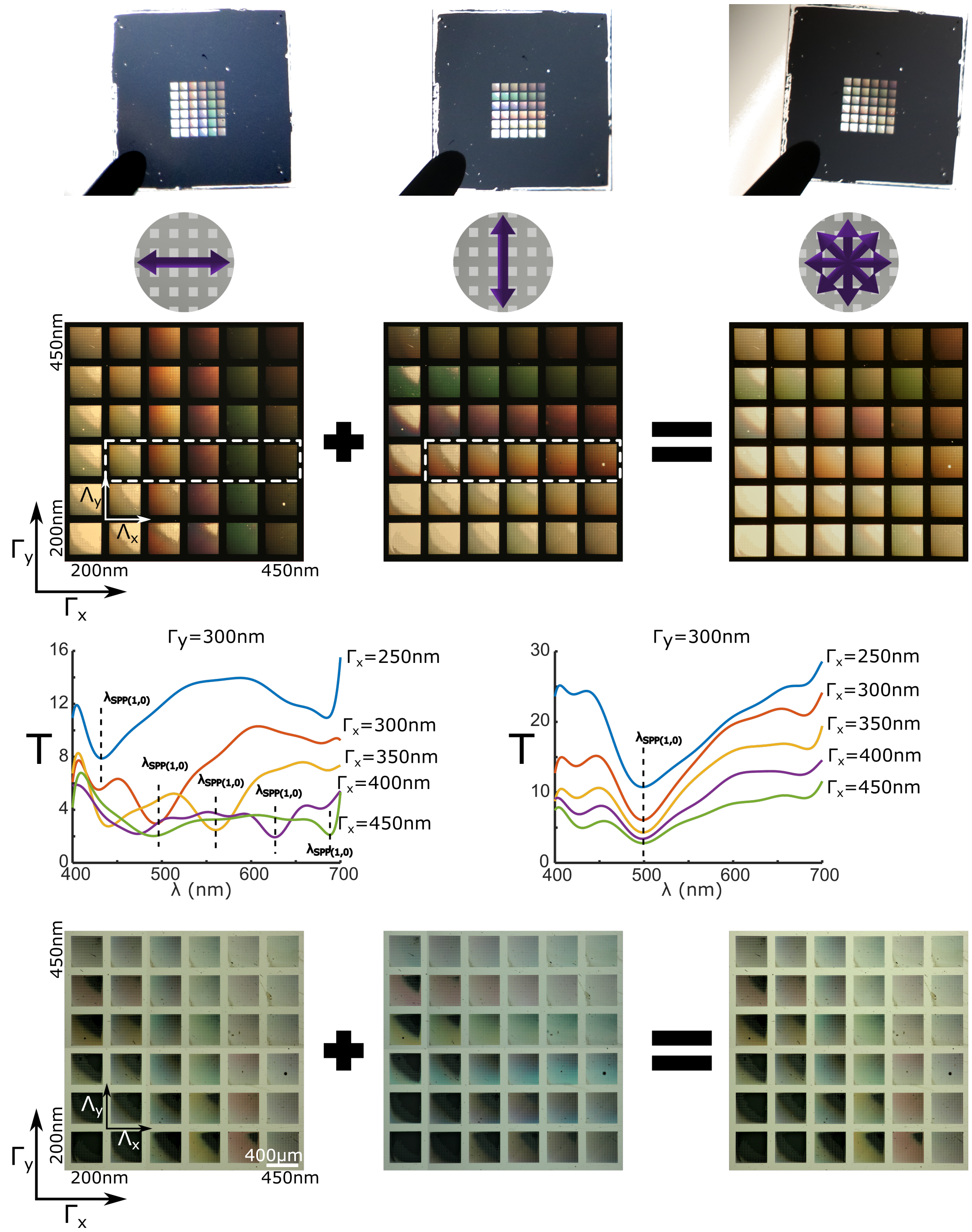

Figure. 4.9 Photos and measured spectra of Al nano-hole array under x,y and un-polarised illumination and measured transmission spectra varying $\Gamma_{x,y}$. (a)DSLR camera photo of nano-hole layer on a 1cm x 1cm glass chip, illuminated from behind by fluorescent tube lighting. x and y polarisation was provided by linear polariser on the camera lens. (b)Photos of Al nano-hole layer in polarising optical microscope setup, in transmission, under x-, y- and un-polarised illumination. Large grids vary $\Gamma_{x,y}$ by 50nm each grid step in corresponding direction. Large grids are divided into 20 × 20 small grids varying $\Lambda_{x,y}$ by 5nm per step in x and y direction. (c)Transmission spectra of nano-hole large grids, highlighted by dashed box in (b). Plots show $\lambda_{SPP(1,0)}$ position for various different pitch (Γ_x) of nano-hole, under x- and y-polarised illumination. (d) Photos of Al nano-hole layer in polarising optical microscope setup, in reflection.

from $200 - 450$nm there is a clear shift in the colour reflected from yellow to green to blue.

The colours seen in transmission and reflection under x-polarised light are the same under y-polarised light but effectively the image has been rotated by 90°. This is because the patterned surface is symmetric about a diagonal axis.

The experimentally measured transmission spectra of nano-hole arrays with $\Gamma_y =$ 300nm and $\Gamma_x = 250 - 450$nm, under x- and y-polarised illumination is also shown in 4.9. The location of $\lambda_{SPP(1,0)}$ is indicated on each spectra measurement. The measured spectra fit well with the modelled spectra and back up the observations made regarding the colour seen in the camera images. As the periodicity is increased parallel to the polarisation of illumination, the transmission dip due to the $SPP_{1,0}$ mode increases, whilst when the illumination is perpendicular to the increase in periodicity there is no movement in the SPP mode resonant wavelength, $\lambda_{SPP(1,0)}$. Furthermore as the periodicity increases, the intensity of the transmission dips due to the lower proportion of surface area available for transmitting light.

The figure shows the range of colours that may be accessed by such a nano-structured surface. However, this provides only a starting point for an active plasmonic metasurface. Whilst altering the dimensions of a nano-hole metasurface may generate colours across the visible spectrum, the dimensions of a metallic nano-hole surface may not be actively tuned. That is once the surface is fabricated, the dimensions may not be altered.

4.1.2 Varying the refractive index of the surrounding media

Looking at the components to equations 4.1a and 4.2, we have discussed how we can modify t_m or $\Gamma_{x,y}$ to influence the spectral response of a metallic nano-hole surface. Neither t_m, nor $\Gamma_{x,y}$, however, may be altered dynamically. We have also seen how varying the dimensions of the rectangular nano-holes, $\Lambda_{x,y}$, may alter the transmission spectra, however once again active modulation is not possible. If we wish to alter the SPP resonant wavelength, we now have the possibility of modulating ϵ_{d1}, ϵ_{d2} or ϵ_m. It has been shown that the value of ϵ_m may be altered using electro-chromic switching[90, 91], however in this work we are assuming that the permittivity of the metal may only be altered by switching the metal used in the deposition process, hence ϵ_m may not be actively tuned. Thus ϵ_{d1} and ϵ_{d2} remain as possible variables to

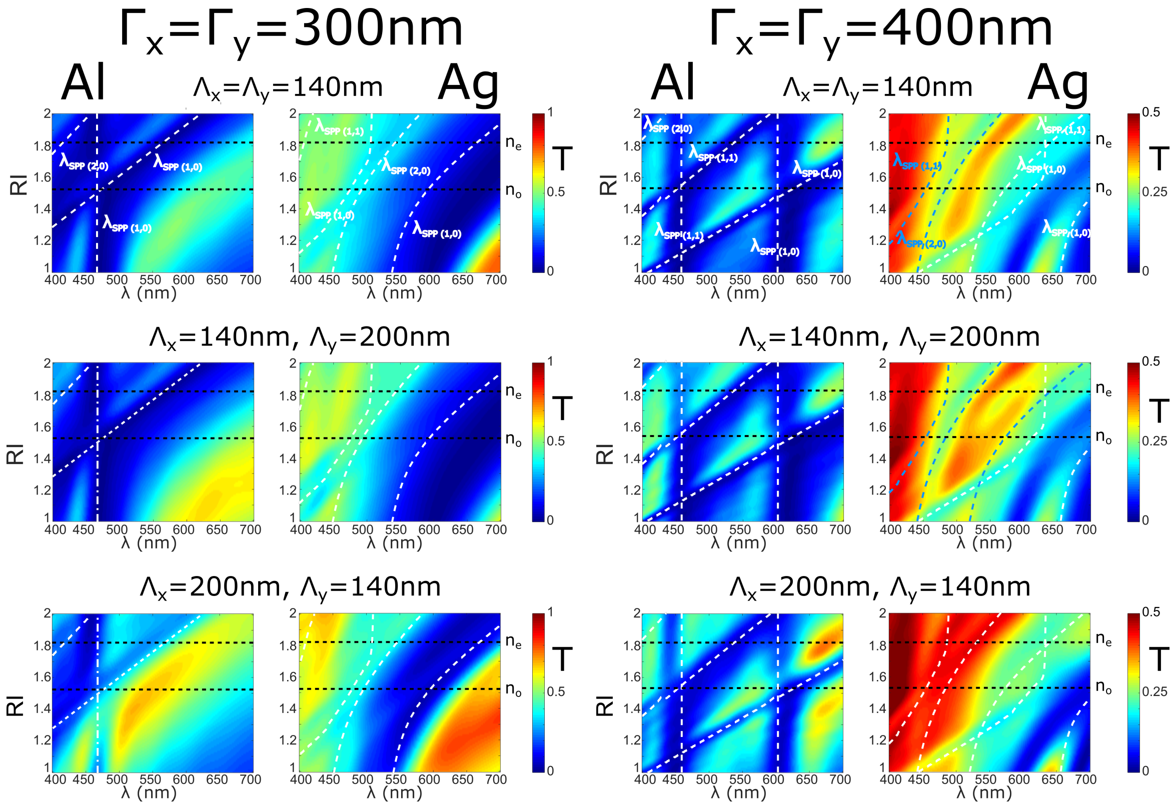

Figure. 4.10 Transmission spectra of nano-hole arrays of various dimensions in aluminium and silver metallic layers varying the surrounding refractive index (RI)

dynamically alter. The substrate that the nano-structures are patterned on in this work is generally glass. There are substrates, that are transparent in the visible wavelength range, whose refractive index may be electro-optically switched, however we shall come back to this later. At this point we shall assume that the substrate onto which the nano-structure is fabricated has a permittivity which may not be altered, and hence that ϵ_{d2} is constant. This leaves one final variable that may investigate for dynamic modification, ϵ_{d1}, the dielectric medium which surrounds the nano-structure.

Liquid crystals (LCs) are optically anisotropic, and, possessing permanent dipole moments, will re-orientate under an applied electric field, providing an electro-optically tunable medium. Widely used as a fundamental building block for modern displays, LCs are a promising candidate for integration with metallic nano-structures for highly tunable plasmonic pixels[122, 93, 123]. By varying the permittivity of the dielectric medium that surrounds the nano-structures, it is possible to modify the resonant wavelength of the SPP modes of the plasmonic metasurface. Figure 4.10 shows the transmission spectra for Al and Ag nano-hole structures, varying the refractive index (RI) of the surrounding dielectric medium. The nano-hole surfaces simulated have $\Gamma_x = \Gamma_y = 300$nm, and three combinations of rectangular nano-hole dimensions of $\Lambda_{x,y} = 140/140\text{nm}, 140/200\text{nm}, 200/140\text{nm}$. The RI of the surrounding medium is modelled to increase from 1 (air/vacuum) to 2. Marked on the plots are the refractive indices of the ordinary, $\mathrm{n_o}$, and extraordinary, $\mathrm{n_e}$, axes for nematic LC BL006 (Merck). BL006 is a LC with a relatively large birefringence, $\Delta\mathrm{n} = 0.286$, whilst still being colourless and is the LC of choice in this thesis. The region between $\mathrm{n_o}$ and $\mathrm{n_e}$ shows the change in transmission spectra that could be achievable with full re-orientation of the LC BL006. The plots show that as the refractive index, and thus permittivity, of the surrounding medium increases, λ_{SPP} increases. By choosing $\Lambda_{x,y}$ appropriately, it is possible to vary the peak transmission wavelength by $\sim$ 75nm. The structure that works best in this configuration is one where $\Lambda_{x,y}$ are chosen such that λ_{SPP} is similar to λ_{pk}, thus the peak wavelength will change linearly with λ_{SPP}. This is the case shown in figure 4.10, with $\Lambda_x = 200nm, \Lambda_y = 140$nm.

Thus, in theory by combining passive nano-hole surface with a LC, by re-orientating the LC it should be possible to create an active device that will have the resonant wavelengths of its SPP modes electronically tuned.

4.1.3 Liquid crystal - nano-hole device fabrication

The liquid crystal - nano-hole (LC-NH) devices are formed when a metallic nano-hole layer is used as one side of a typical liquid crystal cell. A schematic of the cells are shown in figure 4.11(a). The nano-hole layer is fabricated using the cleanroom fabrication techniques described in section 3.2 of this thesis. The substrate chosen for these devices was double-side polished borosilicate glass (thickness 500 μm), primarily so that the nano-hole layer may be illuminated in transmission as well as reflection. The nano-hole pattern is created using electron-beam lithography (EBL) with ma-N 2405 negative tone photoresist. To overcome the issue of charge accumulation associated with EBL patterning on insulating substrates[105], two charge dissipation layers (2nm Al prior to spin-coating the resist; the second, on-top of the resist, a 35nm Al layer) are used. Resist development was in AZ-726-MIF developer solution for $\sim 22s$. Deposition of Al ($\sim$30nm) was performed using a thermal evaporator. Resist lift-off was carried out in acetone. Following lift-off of the sacrificial polymer resist layer, the desired metallic nano-hole patterned layer remains on the substrate. An SEM image of such a metallic nano-hole layer is shown in figure 4.11(b). The fidelity of the rectangular nano-holes is not perfect, with rounding at the corners and edges. This fact should not result in significant changes of the transmission spectra of the nano-hole surface, as the spectra is primarily a result of the periodicity of the grating, $\Gamma_{x,y}$. Furthermore, as shown in figure 4.4, the shape of pixel has a limited effect on the peak transmission wavelength. The imperfect rectangular shape may result in more polarisations of SPP modes, and not only two orthogonally-polarised modes, however, adverse effects were not experimentally observed.

The transmissive cell is formed with the nano-hole layer (bottom electrode) and indium-tin-oxide (ITO) covered glass (top electrode), with nematic LCs sandwiched in between. A polyimide alignment layer is used on the ITO-glass side only, aligned parallel to the square holes; with LCs re-orientating perpendicular to the nano-hole surface with applied voltage. The preferential alignment of the polyimide layer is given by mechanically rubbing of the layer. Nematic LCs preferentially align planar to the Al surface, with bulk LC rotation induced through the top-electrode alignment layer[110].

The preferential alignment of Ag with a LC is homeotropic. As such to use BL006, to re-orientate the LC, one would need to apply a planar electric field across the cell. The devices are fabricated such that a field is applied between the bottom electrode, the nano-hole surface, and an electrode at the top of the cell, resulting in a vertical field

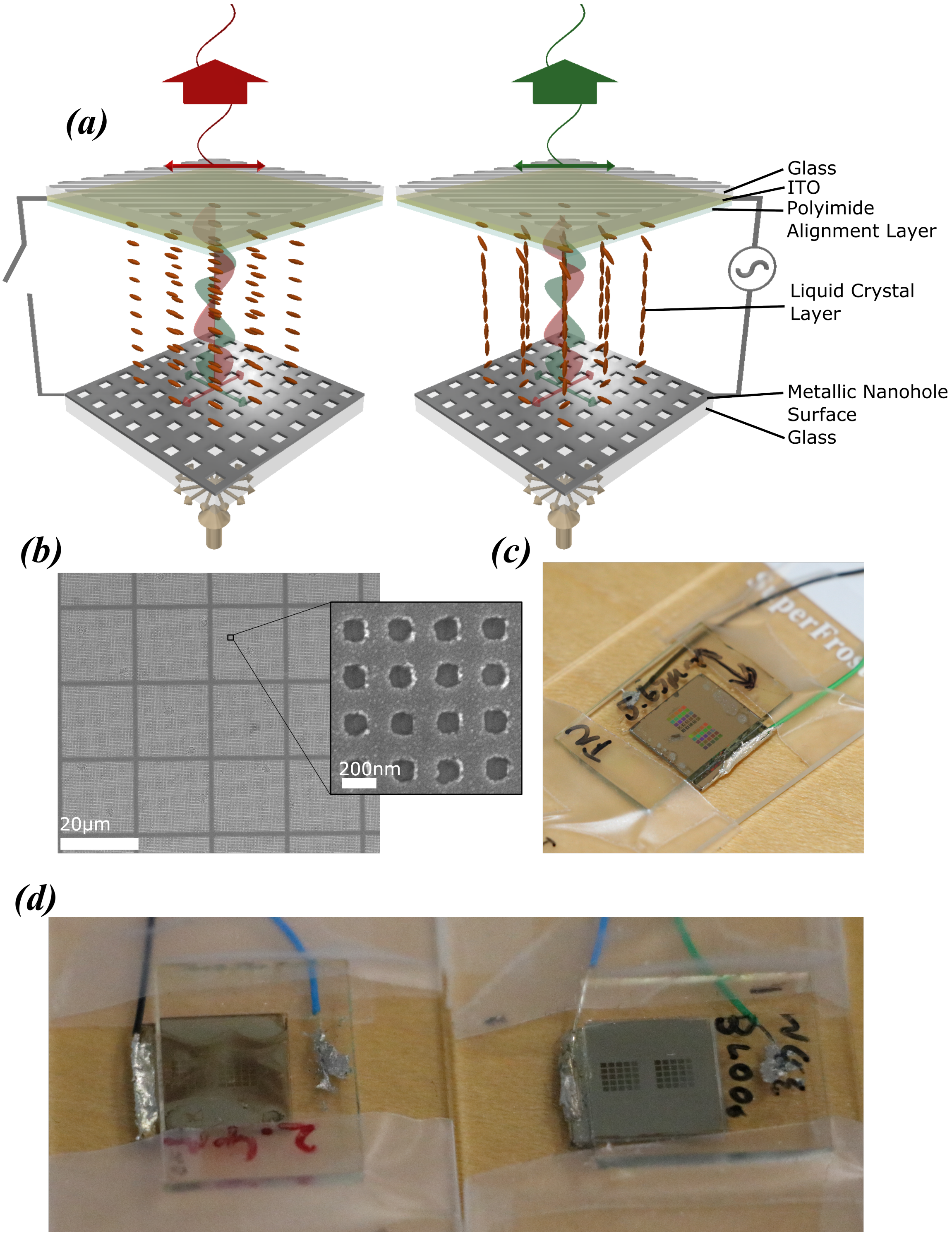

Figure. 4.11 Schematic and images of LC-NH device. (a) Schematic of the LC-NH device operation: with and without applied voltage. (b) SEM of metallic nano-hole layer. (c) Photo of fabricated LC-NH device, with electrodes attached and mounted on glass slide of ease of handling. (d) Photos of Ag (left) and Al (right), 3 months after construction, showing tarnishing of Ag device and unaffected Al device.

perpendicular to the nano-hole surface. There is no way, in the current construction to apply a field parallel to the nano-hole surface, particularly as the nano-surface is earthed. Even putting an electrode at the side of the device, the field will not penetrate across the device as it will travel to ground at the earliest opportunity. As an alternative one could use a LC with a negative dielectric anisotropy. Such a LC will align perpendicular to the field lines of an applied E-field. Hence, using an Ag nano-hole layer and a homeotropic alignment layer at the top of the LC, the now vertically aligned LCs, under application of an electric field across the cell, will switch from homeotropic to planar. There are however further issues that arise using homeotropic to planar switching. Negative dielectric anisotropy LCs with large enough birefringence are not common and the lifetime of devices constructed using Ag is limited due to the sulfidation of the metallic surface. An image of two LC-NH devices constructed with Ag (left) and Al (right) are shown in figure 4.11(d). The devices at the point of photographing are three months old. There is clear tarnishing of the Ag metal, which has then permeated the LC, rendering the device unusable. The Al device however shows no sign of such issues and remains operable over 12 months following fabrication. For these reasons it was determined that the LC-NH devices would be constructed using Al as opposed to Ag.

The cell is constructed using UV-cured glue containing $2\,\mu$m glass spacer beads resulting in a cell thickness of 2.5–3.3 μm. Wires are connected to the metallic nano-hole layer and the ITO with silver epoxy resin and indium solder respectively. A 1 kHz sinusoidal AC signal is then applied to the electrodes to create a field across the cell, to which the LCs will re-align. For ease of handling the cell is attached to a glass slide.

4.2 LC-Nanohole switching devices- shifting the plasmonic resonance

When an electric field is applied across the LC-NH cell, the liquid crystal molecules will re-align to the E-field, and the permittivity, due to the anistotropic nature of the LC molecules will be modulated. Thus, in theory, when a nano-hole surface is immersed in a LC layer, the re-alignment of the LC molecules will determine the plasmonic resonance of the surface.

The LC-NH device was constructed such that when the LC is aligned planar to the nano-hole surface (i.e when no field is applied) the director is aligned with the y-axis and can be described as being in line with the nano-hole lattice. A schematic of this alignment is shown in figure 4.12(a). In this configuration, with no E-field applied across the cell, light from the nano-hole surface polarised along the x-axis of the device will experience the ordinary refractive index of the LC ($\mathrm{n_o}$), while light polarised along the y-axis of the LC-NH device will see the extraordinary axis of the LC and thus will experience the refractive index $\mathrm{n_e}$. The refractive index however that has the determining factor on the position of λ_{SPP} is the refractive index in the direction perpendicular to the nano-hole surface. It is the permittivity experienced by the evanescent field of the SP modes that influences the location of λ_{SPP}. In the planar alignment configuration this is $\mathrm{n_o}$. As an electric field is applied across the cell, the liquid crystal molecules will start to re-orientate, and align to the E-field lines which run vertically down the cell between the two electrodes, until the magnitude of the E-field is large enough such that the LC director aligns with the electric field. As the LC molecules reorientate, light polarised along the x-axis, despite the re-orientation of the LC will always only see an ordinary axis of the LC molecule. Light polarised in the y-direction will transition between *seeing* the extraordinary axis to an ordinary axis of the LC, and the evanescent field of the SP modes will transition between *seeing* $\mathrm{n_o}$ and $\mathrm{n_e}$.

The refractive index that the evanescent field will experience, when the LC molecules are aligned at an angle of θ to the nano-hole surface, will be

$$\mathrm{n}(\theta) = \frac{\mathrm{n}_e \mathrm{n}_o}{\sqrt{\mathrm{n}_e^2 \cos^2\theta + \mathrm{n}_o^2 \sin^2\theta}} \tag{4.5}$$

As the permittivity of the media surrounding a metallic nano-structure increases, the resonant wavelength red-shifts. As such, as the LC molecules re-align to the E-field, the resonant wavelengths of both the SPP and LSPR mode of the nano-hole will increase. This effect is polarisation independent as SP resonances excited by either x- or y-polarised light see the same value of permittivity in the z-direction ϵ_z.

The fabricated LC-NH device was placed into a polarising microscope optical setup, and illuminated, from beneath, with a halogen light-source. To the microscope was attached a spectrometer and a DSLR camera to record the spectra and to take images of the device respectively. A 1 kHz sinusoidal AC signal was applied to cell, with the $\mathrm{V_{p\text{-}p}}$ varying from 0-10 V ($\Delta V = 0.25$). Images and spectra were recorded for un-polarised and x- and y-polarised illumination.

The experimentally observed results, for a nano-hole surface with dimensions $\Gamma_{x,y} = 300\text{nm}, \Lambda_{x,y} = 140\text{nm}$ are shown in figure 4.12(b-d). The DSLR images shown in 4.12(b) show little observable difference in the colour of the pixel as the E-field is increased for the three polarisation states. The spectra shown in (c,d) tell a similar story. The position of $\lambda_{SPP(1,0)}$, corresponding to the dip in the transmission spectra does not appear to shift at all for each of the polarisation states. Line plots in figure 4.12(d) provides a clearer picture. For x-polarised light, there appears to be very little movement in $\lambda_{SPP(1,0)}$, in contrast to what one would expect should the LC molecules be re-orientating at the nano-hole surface. When illuminated with y-polarised light there is potentially an observable increase in the value of $\lambda_{SPP(1,0)}$, however its location in the plot is ambiguous, and if there is an increase of its value it is an order of magnitude smaller that what would have been expected for the given change in refractive index with full re-orientation of the LC shown in figure 4.10. The plots for un-polarised illumination in (c,d) show no change at all in the position of $\lambda_{SPP(1,0)}$, suggesting that changes in the spectra for the x- and y-polarised illuminations are due to un-wanted polarising effects within the components of the optical set-up and there is in fact no change in the permittivity surrounding the metallic nano-hole surface.

The reason for the lack of movement in the position of $\lambda_{SPP(1,0)}$, is due to surface anchoring of the liquid crystal molecules[122, 92, 125] to the metallic nano-hole surface. The alignment of LC molecules to the surface depends on the chemical and geometrical structure of the surface. The interaction between LC molecules and the metallic nano-hole layer is strongest at the surface, but decays with the distance from the surface. The surface anchoring distance may be defined as the distance from the surface that the orientation of the molecules does not alter from the surface orientation when under influence from an externally applied electric field. It can be approximated as[122]

$$\xi_d = \frac{d}{\pi}\frac{V_{th}}{V} \tag{4.6}$$

where d is the thickness of the LC cell, V_{th} is the *Freedericksz's threshold voltage* of the LC and V the voltage applied to the cell. For BL006 $V_{th} = 2.42$, hence with an applied voltage of $10V$, $\xi_d \sim 250\text{nm}$.

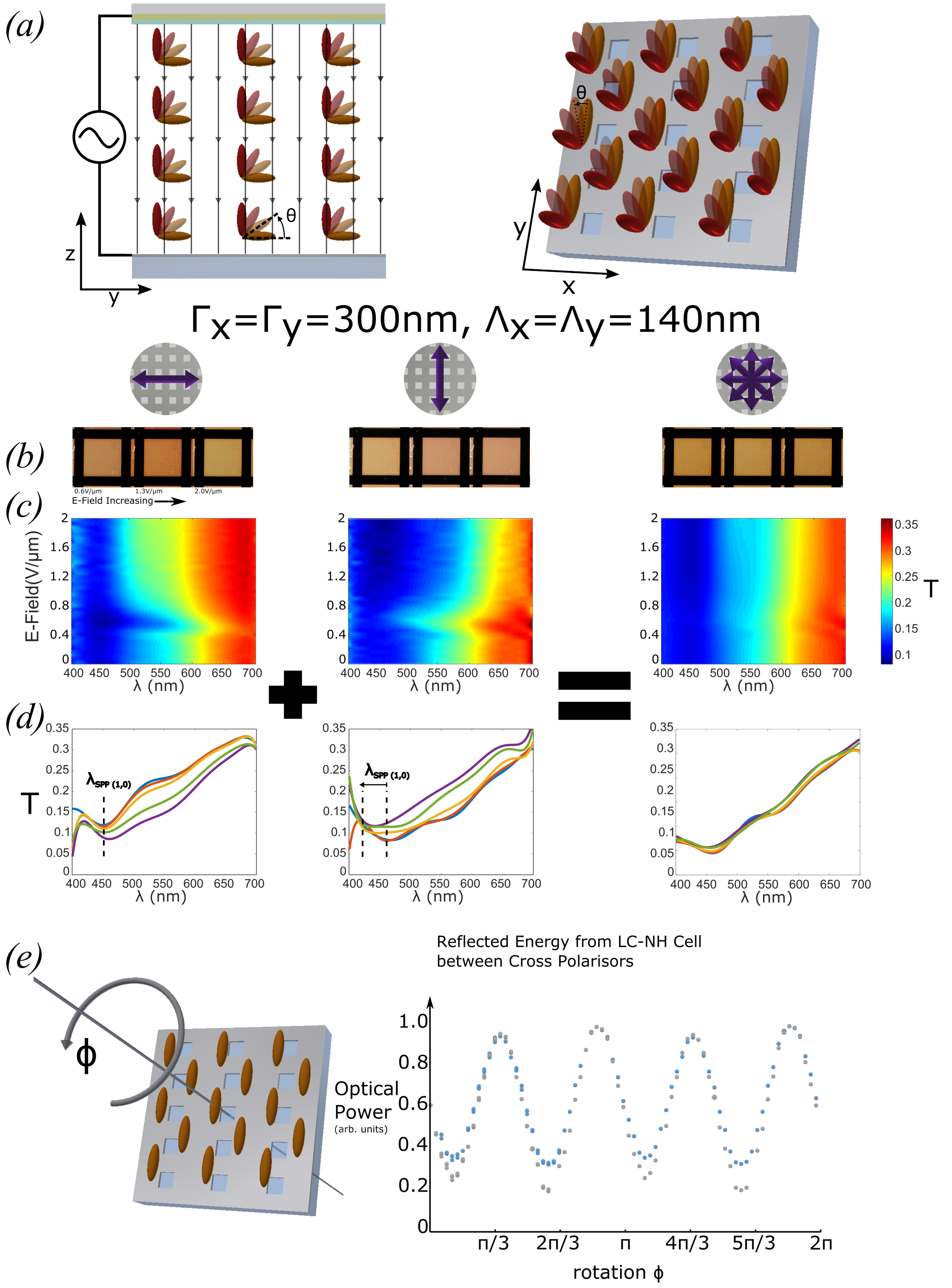

Figure. 4.12 Operation and experimental results of LC-NH device with no analyser in optical configuration. (a) Visualisation of the alignment and re-orientation of LC molecules in a LC-NH device under and applied electric field (b) Photo of LC-NH device under x-, y- and un-polarised illumination, varying E-field across the cell. (c) Transmission spectra of LC-NH device under x-, y- and un-polarised illumination, varying E-field across the cell. (d) Line plot of transmission spectra varying E-field, showing location of λ_{SPP}. (e) Schematic of and optical power transmitted through LC-NH device when placed between crossed polarisers and rotated about its z-axis

The distance the SPP mode perpendicular evanescent wave penetrates into the liquid crystal is of the order $\sim \lambda/2$. For visible light, this is similar to ξ_d, hence there is some weak interaction of the SPP mode with the re-orientating LCs, hence the small shift in λ_{SPP} when a voltage is applied to the LC-NH cell. However the potential of liquid crystals to actively tune SP resonances is severely hindered by the significant surface anchoring forces they encounter, preventing full re-orientation of the liquid crystal and hence limiting the birefringence that can be utilised in such devices.

Using an FDTD model, figure 4.13 shows the simulated spectral change when varying the anchoring distance, t_{anch}, for a LC in contact with a nano-hole surface when under an E-field such that the bulk LC orientation is aligned perpendicular to the nano-hole surface. It is assumed that the re-orientation of the LC from the surface anchored orientation, to the fully homeotropically aligned orientation occurs over a negligibly small distance. When $t_{anch} = 0$ the refractive index experienced by the SP modes is $\mathrm{n_e}$. Within the surface anchored layer the refractive index perpendicular to the surface is equal to $\mathrm{n_o}$. As t_{anch} increases, SP modes experience a larger region where the refractive index perpendicular to the nano-hole layer, $\mathrm{n_z}$, is equal to the lower value of $\mathrm{n_o}$. As such the values of λ_{SP} decrease until t_m has reached a value such that there is no interaction between the evanescent field of the SP modes and the homeotropically aligned LC. Figure 4.13(b) shows the modelled spectra from a nano-hole surface as t_{anch} increases. The transmission dip at around $\lambda = 440$nm is constant and is due to the Al-glass substrate SPP mode. The λ_{SPP} mode due to the Al-LC interface initially descends, until plateauing out, in a similar trend to that of the peak transmission wavelength attributable to λ_{LSPR}. Figure 4.13(c,d) plots the location of $\lambda_{SPP/LSPR}$ versus t_{anch}. The evanescent wave of λ_{SPP} appears to have a greater penetration depth into the LC than that of λ_{LSPR}, as its value becomes relatively constant at $t_{anch} \approx 220$nm whereas the value of λ_{LSPR} becomes constant at $t_{anch} \approx 150$nm. Both these values are similar or less than the value of ξ_d previously calculated. Thus the effect of the liquid crystal surface anchoring must then be taken into account in the model for the LC-NH cell. The orientation of the LC is modelled using a 3D matrix rotation of the LC director. The alignment of the LC is modelled with a surface anchoring layer at each surface of the cell, where the director is aligned planar to the top and bottom electrode surfaces, re-orientation layers, where the director rotates sinusoidal to match the bulk alignment, and a bulk alignment layer.

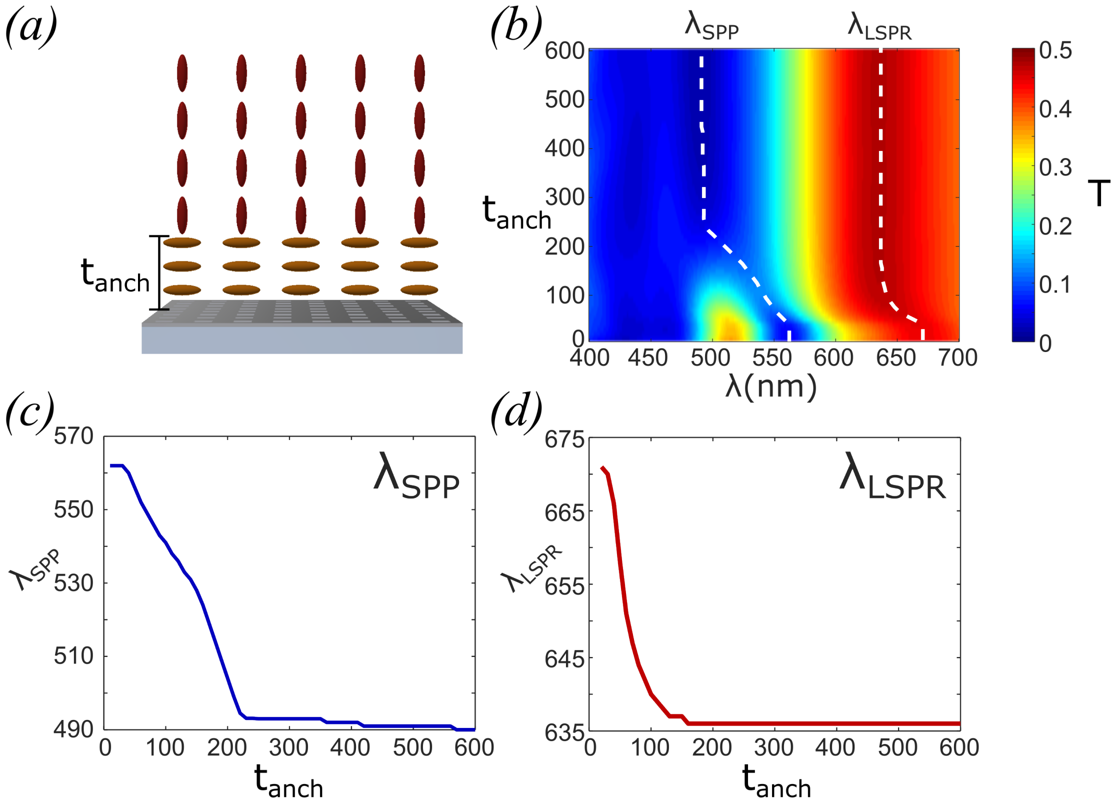

Figure. 4.13 Simulated transmission spectra of a nano-hole array in a hometropic aligned LC, varying the thickness (t_{anch}) of planar aligned surface anchored LC layer. (a) Schematic of nano-hole layer in homeotropic aligned LC, (b) Transmission spectra and (c,d) location of SPP and LSPR transmission minima and maxima, varying planar aligned surface anchored layer thickness.

In the transmission spectra versus applied field surface plots in figure 4.12(c), there are dips in the magnitude of the transmission between an applied field of $0.4 - 1V/\mu$m, in the x- and y-polarised spectra. The modification of the amplitude of the transmission appears to be polarisation dependent as the change in spectra is not seen in the un-polarised plot. The dips occur due to the modification of the polarisation light transmitted from the nano-hole surface which is then filtered due to the imperfect nature of the optics in the polarising optical microscope i.e. the optics in the microscope act mildly as polarisers/analysers. Should the LC be aligned to the nano-hole lattice, the effects seen here should not be able to occur, as the polarised light from the resonant modes of the nano-hole arrays would see no birefringence and hence no modulation of it polarisation state. It can thus be deduced that the LC planar alignment is at an angle to the nano-hole lattice. This is confirmed by the experimental optical power measurements in figure 4.12(e). The plot shows the optical power transmitted when the LC cell is placed in between a pair of crossed polarisers and then the cell is rotated about the z-axis. When the LC director is aligned with the polarisation of either of the polarisers, there will be low optical transmission. When the LC director is not aligned, the light passing through the cell, sees the optical birefringence of the LC, and the polarisation is rotated, and optical power is transmitted through the cross polarisers. Maximum birefringence will be seen when the LC director is aligned at 45° to the lattice. The results shown in figure 4.12(e), show that when the crossed polarisers are aligned to the nano-hole lattice, it is not at a optical power transmitted minima. The minima occurs at approx 15° indicating that the LC director is aligned at 15° to the nano-hole lattice.

These results do however suggest there may be a way to create active electro-optic colour devices using a LC-NH using birefringent and polarisation effects.

4.3 LC-Nanohole continuously tunable devices

The Al nano-hole arrays are designed to exhibit plasmonic resonance at a specific wavelength and in effect act to polarise and filter the light. Through integration of nematic LCs with an Al nano-hole array on glass, an applied voltage across the LC-NH pixel results in variable colour output. The colour tuning capability is made possible by the introduction of an analyser at 45° to the nano-hole lattice acting to filter the transmission. The result is an active colour tunable LC-NH transmissive pixel device operating in the visible spectrum with un-polarised input light.

The LCs are used to modulate the polarisation state of light as it propagates through the device, whilst the linear polarised analyser acts to selectively filter the transmission. Using this principal, it is possible to create voltage controlled plasmonic colour from single pixels. The devices shown are attractive for display applications and may help to reduce the dependency on RGB pigment-based filters, shrink pixel technology and offer additional optical functionality from a single pixel.

The rectangular nano-holes in this work, under un-polarised light illumination, exhibit two orthogonal modes, shown with finite-difference time-domain (FDTD) simulations[21] in figure 4.14, aligned x-polarised (0°) and y-polarised (90°) to the nano-hole lattice. The two resonant modes, in an isotropic refractive index ($n_o = n_e$), at any given wavelength, are in phase and of equal intensity. Hence the transmitted

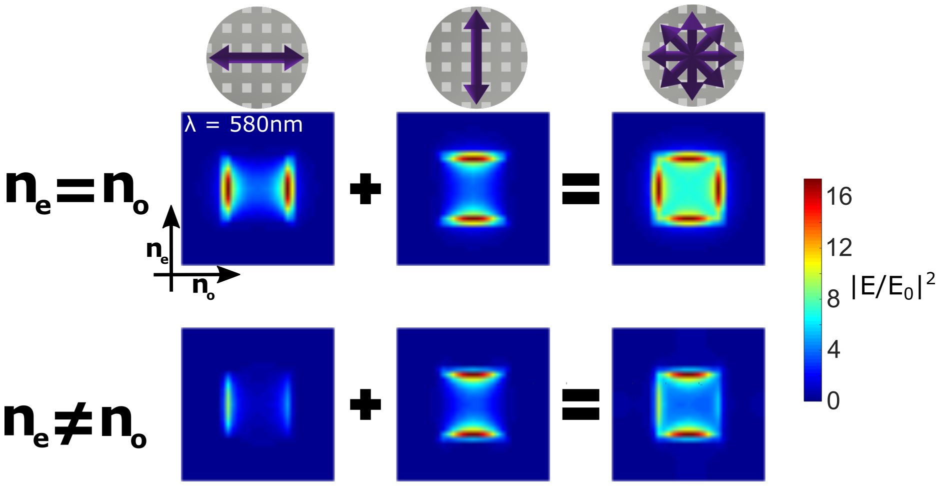

Figure. 4.14 FDTD simulations of the Al nano-hole layer ($\Lambda_{x,y} = 140$nm and $\Gamma_{x,y} = 300$nm) illuminated with un-polarised light. The two orthogonal SP-modes are exhibited shown through the normalised E-field enhancement maps at $\lambda = 580$nm. These modes determine the spectra and polarisation of light transmitted through the nano-hole layer and into the device. When $\mathrm{n_o}$=$\mathrm{n_e}$ both modes are equal and the light is linearly-polarised at 45° to the nano-hole lattice.

light from the nano-hole surface has a linearly-polarised output (at 45°). With LC integration, the surrounding anisotropic index ($\mathrm{n_o} \neq \mathrm{n_e}$) leads to two distinct modes, as now the surrounding index is dependent due to the orientation of the LC.

The LC birefringence ($\Delta\mathrm{n} = \mathrm{n}_{||} - \mathrm{n}_{\perp}$) causes the propagating transmitted light from the two nano-hole modes to travel through the device at different velocities, altering the phase ($\phi_{x,y}$) between the two components. This phase difference, $\gamma = \phi_x - \phi_y$, at a given wavelength λ, is dependant on the Δn and thickness (t) of the LC layer such that

$$\gamma = \frac{2\pi\Delta\mathrm{n}t}{\lambda} \tag{4.7}$$

Δn between the two modes is dependant on the LC orientation, which is dependent on applied voltage. With no applied field, the LC is planar aligned, whereby $\mathrm{n}_{||} = \mathrm{n}_e$ and $\mathrm{n}_{\perp} = \mathrm{n}_o$, thus $\Delta\mathrm{n} = \mathrm{n}_e - \mathrm{n}_o$. Whereas, with an applied voltage (AC signal) sufficiently large enough for homeotropic alignment, $\mathrm{n}_{||} = \mathrm{n}_{\perp} = \mathrm{n}_o$ and $\Delta\mathrm{n} = 0$. In the intermediary situation, $\mathrm{n}_{||}$ is a function of applied voltage, between the two LC indices. This operation is demonstrated through FDTD simulations[21], shown in figure 4.15. The square nano-hole array exhibits an optical response dependent on geometry and LC state. As this light propagates through the LC layer, depending on propagation distance, the polarisation state oscillates between linearly ($\gamma = 0, \pm\pi$) and circularly

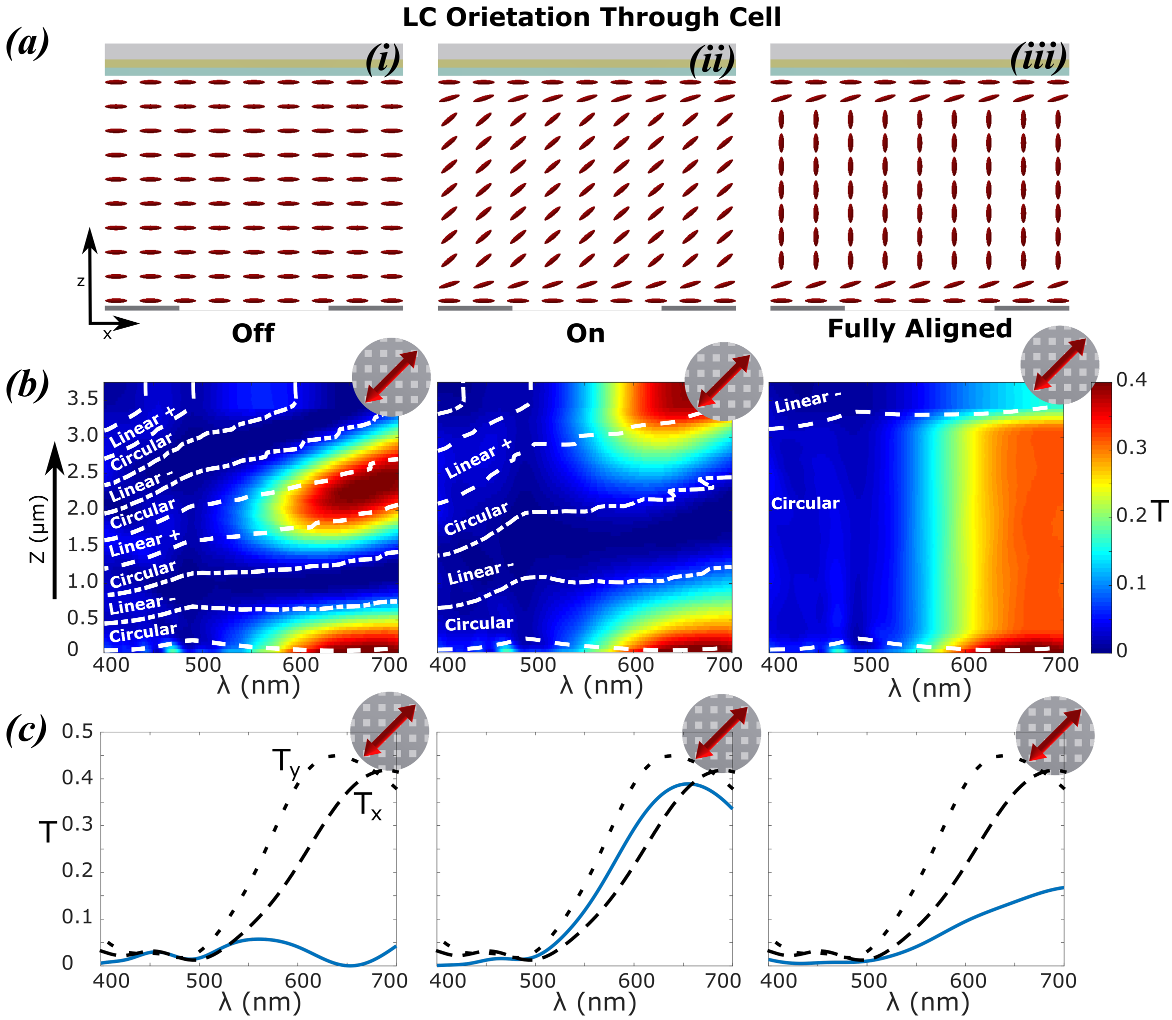

Figure. 4.15 FDTD simulations of the LC-NH device: $\Lambda_{x,y} = 140$nm and $\Gamma_{x,y} = 300$nm. (a) LC orientation (x-z plane) in the Off, On and (fully aligned) states. (b) The transmission spectra, polarised at 45° (shown with red arrow) to the nano-hole lattice of the LC-NH device, as light propagates through the device. (c) Transmission spectra, with output anaylzer at 45°, for the chosen cell thickness of $\sim 3.3\mu$m. The dashed lines are the unfiltered nano-hole response of the two orthogonal SP-modes and solid line post-LC interaction.

($\gamma = \pm\pi/2$) polarised. Thus by varying the amplitude of the applied voltage between the nano-hole and ITO layers, the phase difference between propagating orthogonal field components, and the spectra from the LC-NH device, can be controlled.

Generally, depending on voltage, the pixel can operate in On/Off mode or variable colour output mode. Moreover, an output analyser aligned 45° to the lattice means equal contributions from the orthogonal nano-hole modes. The result is an electro-optic device which has an output from a combination of the nano-hole array spectra, shown in figure 4.15(c), the optical retardance from the LCs, and output analyser selected to be polarised at 45° to the nano-hole lattice.

Figure 4.16 shows the experimental optical transmission results for the LC-NH pixels, for varying nano-hole geometries. The device is illuminated with un-polarised light and an output analyser aligned 45° to the lattice is captured with both a DSLR (a) and polarising optical microscope (b). The device is shown in On/Off (0/4V) states, and colour switching from red to green is visually observed. The total pixel widths are chosen to be large enough ($400\,\mu$m) in order to be easily visible to the naked eye. Figure 4.16(b) shows optical microscopy imagery of the LC-NH pixel arrays in the same On/Off states. The pixels contain nano-hole arrays with $\Gamma_{x,y} = 300$nm and $\Lambda_{x,y}$ ranging from $110 - 170$nm. The colour variation in the pixels is due to the size variation of the rectangular nano-hole geometry.

A single pixel is now selected for investigation into finer control of colour, shown in figure 4.16(d). The pixel has fixed nano-hole grid geometry: $\Lambda_x =$155nm, $\Lambda_y = 140$nm and $\Gamma_{x,y} = 300$nm. The applied voltage is varied in incremental steps of 0.5 V. The four rows show images of the selected pixel, with un-polarised illumination, for four output analyser states: (1) no output analyser; (2) analyser orientated at 0° to the lattice; (3) at 135°; and (4) at 45°. For the un-polarised state, there is no significant change in output colour, due to limited re-alignment of LCs around the nano-hole surface, resulting in a small shift in plasmonic resonance of the nano-hole modes. For an analyser at 0°, again there is little shift in output colour. This analyser state selects a single orthogonal SP-mode (with reference to figure 4.14), and as this mode passes through the LC layer, regardless of optical retardance, the polarisation of the single SP-mode is unaltered. Hence the spectra, filtered by the output analyser, is unaltered.

For the 45°/135° state, a combination of the modes can be selected by the output analyser. The resulting spectra from the two orthogonal analyser states is such that $T_{\lambda,\,noA} = T_{\lambda,\,A:\,45^\circ} + T_{\lambda,\,A:\,135^\circ}$. The LC layer, through voltage controlled retardance,

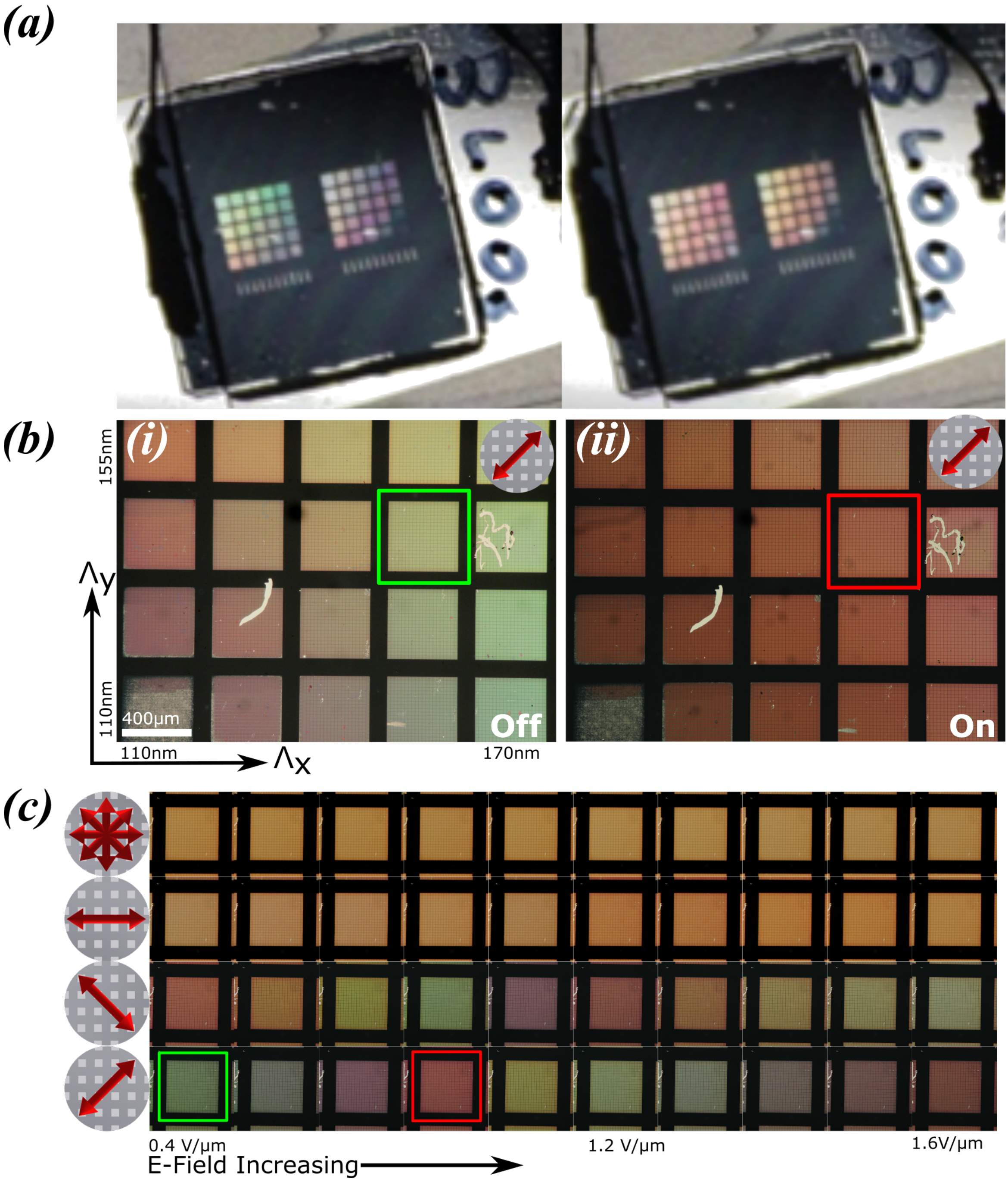

Figure. 4.16 Experimental optical transmission. (a) Schematic of nano-hole surface, indicating width ($\Lambda_{x,y}$) and pitch ($\Gamma_{x,y}$). (b) Photos of LC-NH device in Off (left) and On state containing a range of pixels, with $\Gamma_{x,y} = 300$nm and varying $\Lambda_{x,y}$. Under an optical microscope, the same devices are shown in (c), with analyser at 45° — the iterated dimensions are indicated on the sub-plot. A single pixel is selected (indicated by coloured box) from (c) and the applied voltage is now iterated in smaller increments: results shown in (d). The dimensions are $\Lambda_x = 155$nm, $\Lambda_y = 140$nm and $\Gamma_{x,y} = 300$nm. The results are shown with: no output analyser (top row); output analyser aligned orthogonal to nano-hole lattice; 135°; and 45° (bottom row).

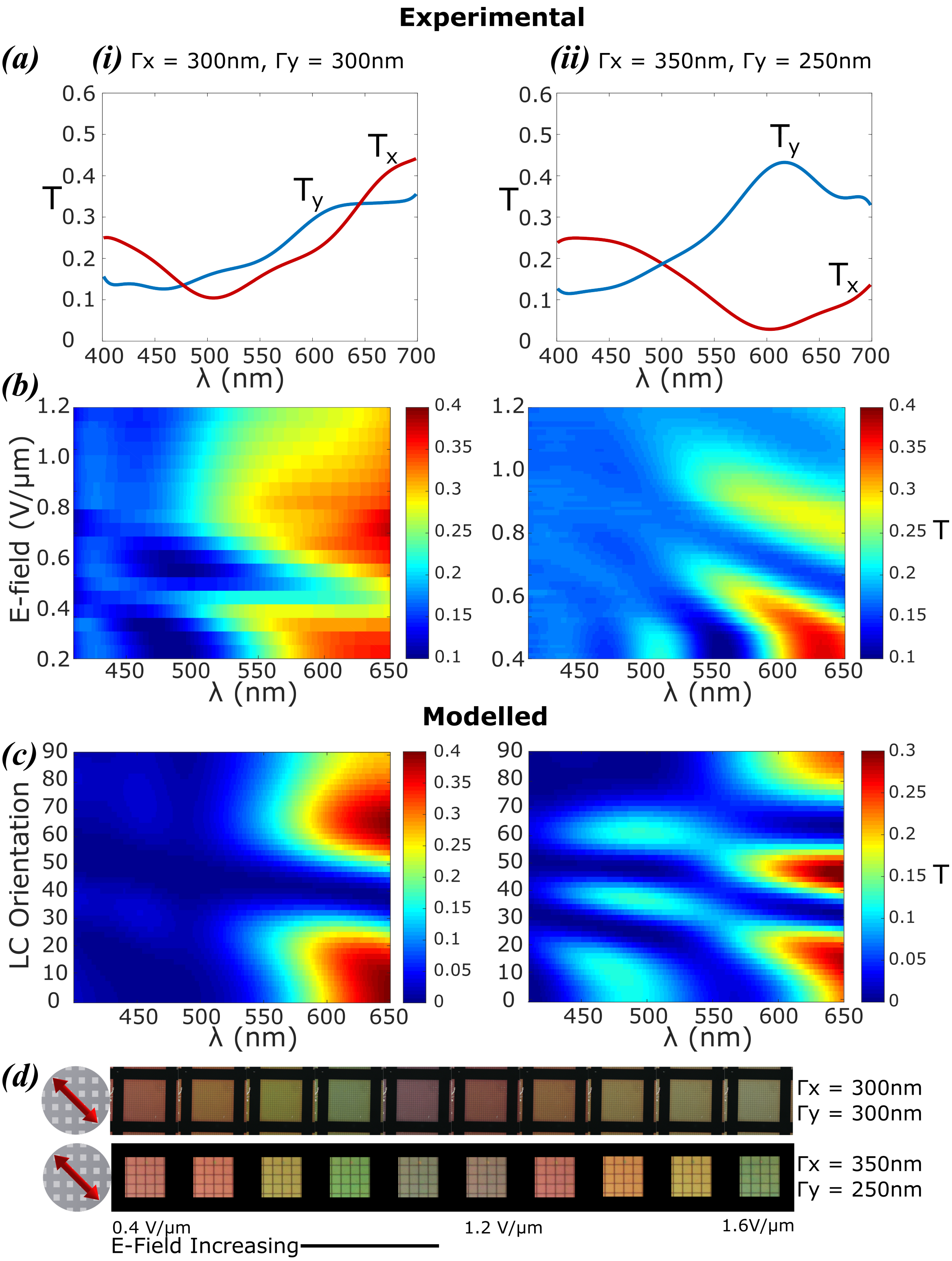

Figure. 4.17 Experimental and simulated transmission spectra for two LC-NH pixel geometries: (i)$\Gamma_{x=y} = 300$nm and (ii) $\Gamma_{x\neq y} = 250/350$nm, with constant $\Lambda_{x,y} = 140$nm. Pixels are illuminated with un-polarised light and output analyser at 135° to the lattice. (a) Experimental transmission spectra from orthogonal nano-hole SP modes. (b) Experimental and simulated (c) transmission spectra as a function of voltage. (d) Shows the pixels' colour under optical microscope for varying applied voltages.

acts to mix the relative contributions of the two modes and more specifically acts as a tunable band pass filter. This effect is indicated by the field dependent colour shift, shown in figure 4.16(d), and supported through the simulation results in figure 4.15(c).

Figure 4.17 shows pixel operation with output analyser at 135° in further detail. Two pixel geometries are investigated: $\Gamma_{x,y} = 300$nm and $\Gamma_{x,y} = 250/350$nm, for constant nano-hole widths; $\Lambda_{x,y} = 140$nm. The experimental transmission spectra for the two LC-NH pixels is shown in figure 4.17(a), whereby two SP modes are observed for orthogonal output states. The pixel in which $\Gamma_{x \neq y}$ results in much greater spectral distinction between orthogonal modes due the variation in orthogonal grating vectors, and hence SPPs. Figure 4.17(b) and figure 4.17(c) show the experimental and simulated transmission spectra respectively for the two LC-NH pixel geometries under varying applied voltages. Figure 4.17(d) shows optical microscope images of the respective pixels. Initially the spectra of light is toward the red part of the spectrum. As the electric field increases, the retardance of the LC layer is modulated, and the output transmission peak blue shifts. As the phase difference between the two propagating SP modes cycles between $\gamma = 0$ and $\gamma = \pi$ the spectra shifts back and forth from 650nm (red) to 550nm (green). In the case where $\Gamma_{x,y} = 300$nm, both orthogonal SP-modes have their resonance towards the red part of the spectrum, hence red dominated output transmission spectra. At sufficient voltage induced retardance, for which the red part of the spectrum is filtered, the remaining colour spectra (in the green part of the spectrum) is broad and weak. Two similar SP-modes are present, with variation in spectral position due in part to the orientation of the LC (anisotropic index) surrounding the nano-holes. Hence the combined output is a broadened red peak. In contrast, for the pixel in which $\Gamma_{x \neq y}$, the more spectrally distinct SP-modes, which are more readily resolvable, results in both narrower transmission spectra and a wider colour palette over the full tunable range. The two respective pixel outputs are shown in figure 4.17(d) under the same exposure conditions, and in combination with figure 4.17(b-c), demonstrate greater colour vividness based on the narrower output peaks.

4.4 LC twisted nematic cell with plasmonic grating

Whilst the aforementioned LC-NH device seeks to circumvent the issue of strong surface alignment between LCs and an aluminium surface, it is also possible to exploit this surface alignment in other ways.

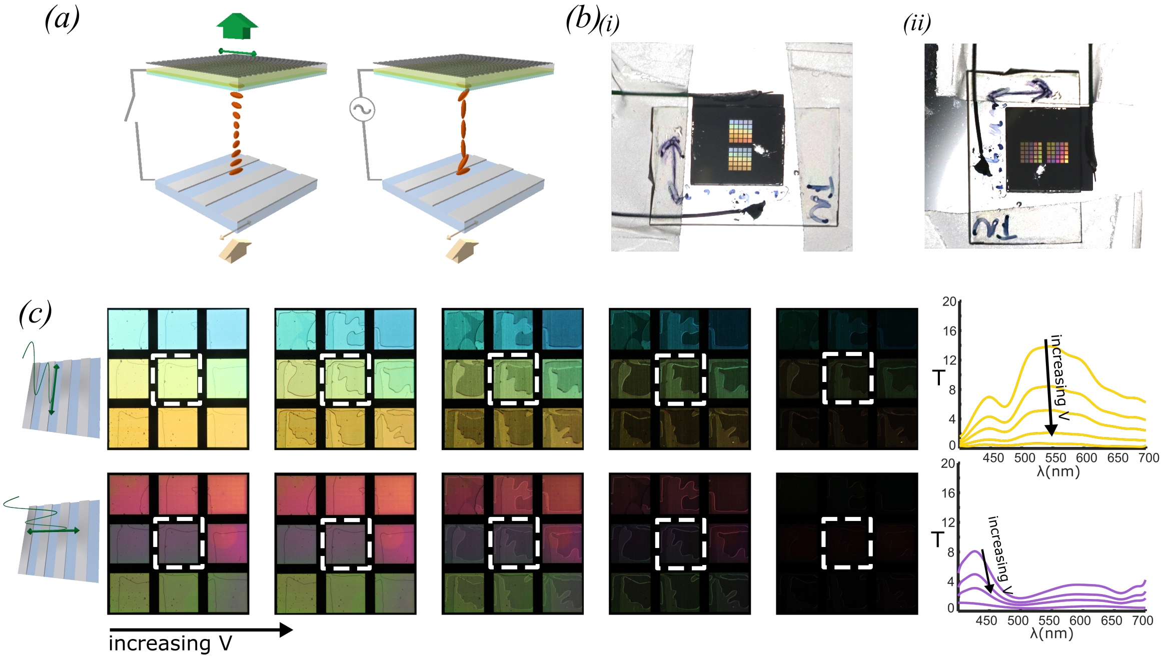

Figure. 4.18 Twisted nematic nano-grating (TN-NG) device under applied E-field. (a) Schematic of TN-NG device between crossed polarisers without (transmission on) and with (transmission off) signal applied. (b) DSLR image of TN-NG device with single polariser aligned parallel (i) and perpendicular (ii) to the grating grooves. (c) Polarising optical microscope images of TN-NG device between crossed polarisers with increasing voltage applied across the cell. Images and corresponding transmission spectra shown for input polariser aligned parallel and perpendicular to grating grooves.

A typical twisted nematic (TN) cell used in modern commercial LCD technology consists of a liquid crystal cell where the planar aligned director of the LC rotates by 90° around the propagation axis of cell. The result is that the polarisation state of light is rotated by 90° as the light passes through the cell. Thus, if the cell is placed between two orthogonally aligned polarisers (crossed polarisers), the polarisation of light passing through the initial polariser will be rotated by 90° and will be able to pass through the second polariser orientated at 90° to the initial polariser. By applying an electric field across the cell, the LC alignment becomes homeotropic. Now, as the light passes through the cell, its polarisation state is not rotated, and when placed between two crossed polarisers, the light from the initial polariser is not rotated and is unable to pass through the second orthogonally orientated polariser and hence no light is transmitted through the device. In this way an electro-optic switch is constructed that switches between the light and dark states. By incorporating pigment based colour filters one is able to create colour pixels, and is the basis for commercial LCD displays. The field across the cell is created by using ITO covered glass, and the alignment of the LCs is created by the rubbing direction of the alignment layer at the top and at the bottom of the cell being orthogonal to each other.

An aluminium grating, due to the strong surface anchoring forces between LC molecules and the metal, has previously been shown to be a very good alignment layer[126, 127]. By exploiting the structural colour of the Al grating, it should be possible to manipulate the grating structure such that not only may the grating act as the alignment layer for the TN-LC cell, but also the colour filter creating a twisted nematic nano-grating (TN-NG) device.

A TN cell, using an Al grating as alignment layer an colour filter is schematically shown in figure 4.18(a). The cell operates as a typical TN cells described previously, however, as opposed to ITO glass with a polyimide alignment layer, the Al grating acting as the bottom electrode and alignment layer combined. Figure 4.18(a) shows the device in both on and off state. When no electrical signal is applied, the polarised white light incident upon the grating is filtered, has its polarisation rotated, and is transmitted through the top analyser. When a signal is applied the polarisation of light is rotated and the now colour filtered light is not transmitted through the device. This can be seen experimentally in figure 4.18(c). As the voltage of the signal applied across the cell the magnitude of the transmission decreases until there is no transmission.

In the previous section it was shown how an Al nano-hole layer was able to act as a combined alignment layer, polariser and colour filter in a new type of pixel (a LC-NH pixel). The pixels in the LC-NH device have the ability to selectively transmit light across the visible spectrum. By using a plasmonic grating in a TN cell structure, tuning the spectral output across the optical spectrum is no longer possible. However the device structure offers alternative benefits to the LC-NH device, such as direct substitution in modern display technologies and a true dark state, along with the benefits of combining the colour filter and electrode seen in the LC-NH device.

When the grating is illuminated with light polarised orthogonal to the grating slits, SPP modes are excited. The SPP modes of an aluminium grating may be described by equation 4.1a, with the difference from the nano-hole layer that there is no grating term for the y-direction, as the periodicity in the y-direction is now infinite. The result is that when an aluminium grating, with the grating periodicity in the x-direction, is illuminated by light polarised in the x-direction (TM polarised light), the SPP mode will create a dip in the transmission spectra that can be tuned by varying the periodicity of the grating, and thus creating structural colour. When the grating is illuminated by light polarised along the grating slits (TE polarised light), no plasmonic modes may be excited. However via other mechanisms, structural colour may be produced, allowing for an alternative structural colour to be produced. The exact mechanisms to produce structural colour under TE polarisation are beyond the scope of this thesis, however in the following sections possible mechanisms are suggested to explain how the colours are experimentally achieved.

An example of the different colours generated for the two polarisation states are shown in figure 4.18(b,c). Figure 4.18(b,i) shows a DSLR camera image of a grating structure TN device illuminated with TE polarised light while (ii) shows the same device with TM polarised light. Polarising optical microscope images of the devices are shown in (c), illuminated with light polarised parallel and perpendicular to the grating grooves. The images in (c) show how when the device is placed between crossed polarisers, when a voltage is applied the intensity of the transmission is reduced until the LC is homeotropically aligned, there is no rotation of the polarisation of the propagating light, and there is no transmission through the crossed polarisers.

Given the device may produce two distinct spectra responses, under TM and TE illumination, it is also possible to use the device as a binary switch. Illuminating the device with un-polarised light, and only using an output analyser aligned orthogonally to the grating slits, when no E-field is applied across the device the TM mode response of the grating, whilst initially aligned to the output analyser, will be rotated by 90°, and will not transmit through the analyser. On the other hand the TE mode response of the grating, initially-polarised orthogonal to the analyser, will be rotated by 90° and will be transmitted through the analyser. When an E-field is applied across the cell, the LC molecules will align to the applied field, and the LC layer will no longer rotate the polarisation of light passing through it. Hence the TM mode will be transmitted through the output analyser and the TE mode will not. In this way the device may act as a binary colour switch.

4.4.1 Fabrication

The fabrication of the devices is similar to that described for the LC-NH cell. The grating is fabricated, using EBL techniques, on glass. The direction of rubbing of the top alignment layer is orthogonal to the grooves of the grating. When the constructed cell is filled with a LC, the LC molecules at the bottom of the cell will align with their director parallel to the grooves of the Al grating, whilst at the top of the cell the LC molecules will align to the direction of rubbing of the polyimide alignment layer. In the bulk of the cell the LC molecules orientation will transition between the orthogonal top and bottom alignment states creating the twisted nematic cell.

4.4.2 Design

The parameters that may be utilised to design structural colour in a grating structure are less than can be utilised for a nano-hole structure simply due to the fact that one of the x- or y-dimensions must be effectively infinite for the structure to be a grating. In this case the y-dimension of the nano-hole has been made infinite ($\Gamma_y \approx \infty$).

The structural colour may be altered by varying the duty cycle (DC=Λ_x/Γ_x) of the grating, however to simplify the design process, the DC of the grating was set to be 0.5. The thickness of the metal layer of the grating is chosen to be the same as that of the nano-hole structure, 30nm. FDTD simulated transmission spectra of an Al grating, varying the pitch of the grating, Γ_x, are shown in figure 4.19(a,b). The simulated grating structures are on a glass substrate. The transmission spectra are shown for the grating in (a) air, and (b) immersed in a LC medium. The LC chosen is once again BL006 ($\mathrm{n}_o = 1.53, \Delta\mathrm{n} = 0.286$). The transmission spectra are shown for the devices under TE and TM polarised illumination.

Under TM polarisation, the simulated results show a clear dip in transmission where there are SPP resonances as described by equation 4.2. In (a) where the grating is in air, there are two clear $\lambda_{SPP(1,0)}$ modes associated with the metal-glass and metal-air interface. In (b), when the grating is simulated in a LC, there is a singular transmission dip, as glass has a similar refractive index to the LC, and hence the SPP modes of the two interfaces have similar resonances.

When illuminated under TE polarisation, the transmission spectra are similar to the inverse of the TM illumination. This is despite the fact that under this illumination

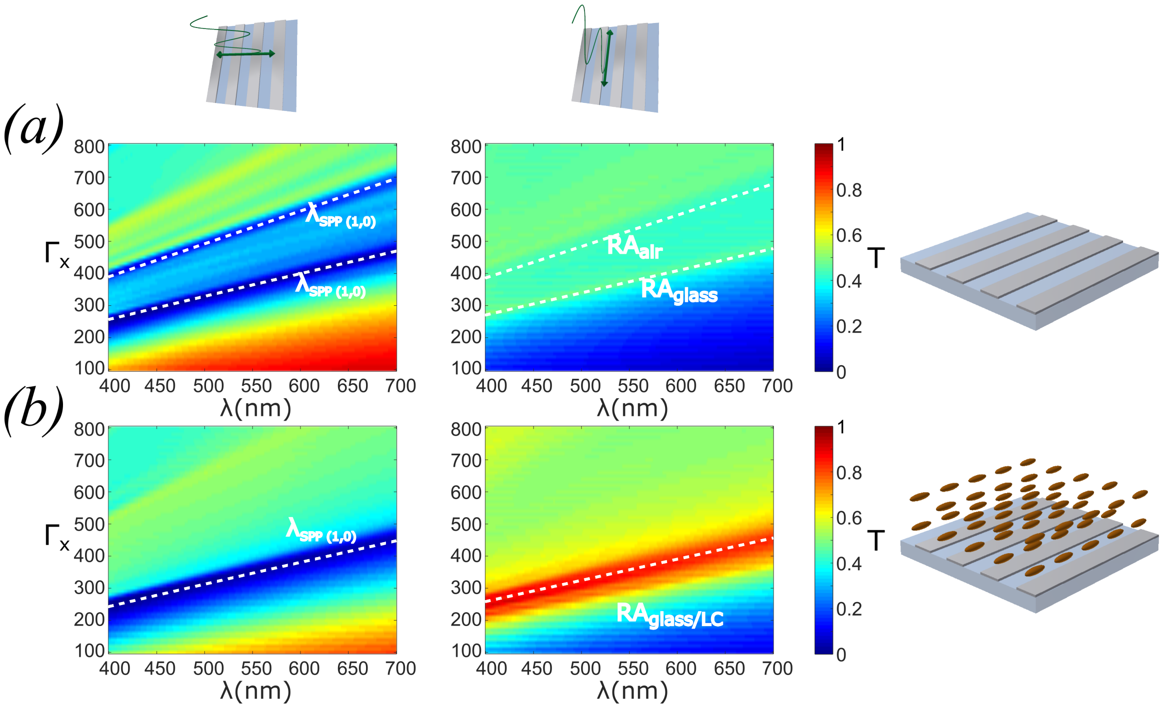

Figure. 4.19 FDTD modelled transmission spectra of nano-grating with duty cycle = 0.5, varying periodicity (Γ_x) of grating. The grating is illuminated with polariser aligned parallel and perpendicular to the grating grooves, in air (a) and in a LC medium (b)

plasmon modes may not be excited. The transmission peaks appear to be when light is coupled into the grating

$$k_x + k_{grat} = k_0\sqrt{\epsilon_d} \tag{4.8}$$

and is particularly strong for the case where the grating is in the LC medium, where the refractive index surrounding the grating is constant. One possible explanation of this enhanced transmission is the Wood-Rayleigh anomaly (RA)[128–130], where light can not be diffracted back towards the source, and hence is redirected into allowed modes forward.

The result is that for a metallic grating on a glass substrate in a LC medium, under TM polarised illumination the modelled results show a transmission dip proportional to the grating periodicity, Γ_x, and under TE polarised illumination there is a transmission peak proportional to the grating periodicity, both of which could result in distinct structural colour from a fabricated grating.

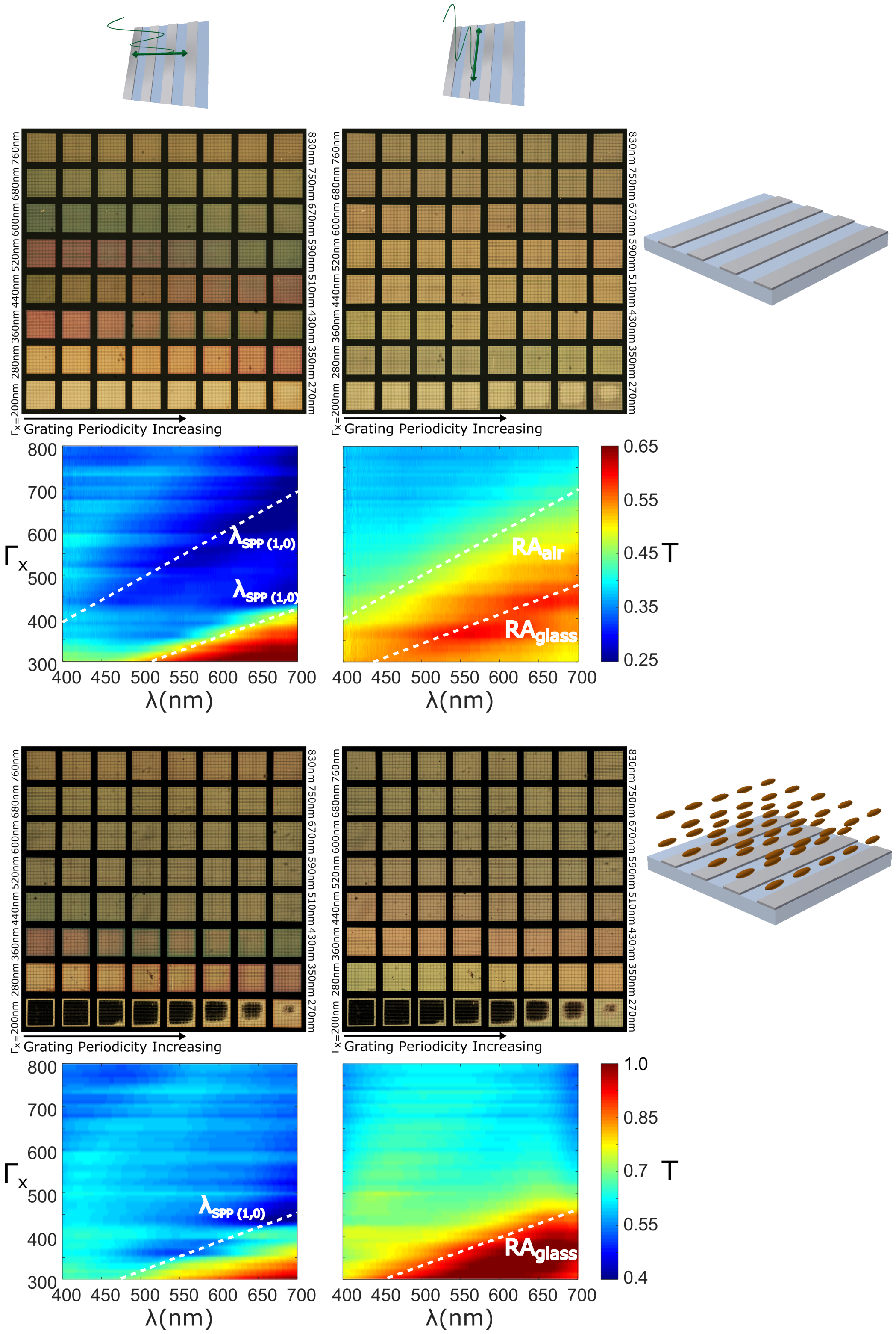

Figure. 4.20 DSLR images and transmission spectra of aluminium nano-grating on a glass substrate with duty cycle =0.5. Periodicity of grating varies from 200 to 830nm. The grating is illuminated with light polarised parallel and perpendicular to the nano-grating grooves. The results are shown for a nano-grating in air and in a twisted nematic LC nano-grating device.

4.4.3 Experimental results

Aluminium gratings on a glass substrate were fabricated with varying grating periodicity, $\Gamma_x = 200 - 830$nm. DSLR camera images of the gratings and the measured spectra, in both air and a LC medium, under TM and TE polarised illumination, are shown in figure 4.20. The images and spectra when the grating is part of the TN-LC device are taken when no signal is applied to the cell. Should a signal be applied to the cell the transmission would be near zero and the images would be dark.

Looking initially at the experimental results recorded for the grating structures in air, the DSLR images show a greater colour variation in the structural colour from the grating under TM polarisation than TE polarisation. The images under TE polarisation are generally mustard in colour, with more variation seen at the short pitched gratings. This observation is supported by the experimentally recorded spectra. Under TE polarisation the transmission is high across the visible wavelength range, with an enhancement in transmission following the solution to equation 5.3 at the glass interface. The grating structures in air, but under TM polarisation, show a greater variation in colour. The DSLR images clearly show the transmitted colour varying from yellow, to orange, to red, to green as the periodicity of the gratings increase. The experimentally measured spectra show the two transmission dips due to SPP excitation, which are the main drivers of the structural colour seen in the camera images.

Comparing to the FDTD modelled spectra show in figure 4.19(a) the measured spectra fit reasonably well. It is possible to see the two $\lambda_{SPP(1,0)}$ modes under TM polarisation. The transmission minima are however less distinct and there is less of an obvious transmission peak between the $\lambda_{SPP(1,0)}$ minima. Under TE polarisation, there is a larger disparity between the magnitude of the peaks that follow the two RA trend lines defined by equation 5.3 than predicted in the modelled data, with the line associated with air lower than that of glass. This may suggest that the mechanism is not due to the RA, however there is a strong correlation between the transmission peak and the solution to equation 5.3 for glass.

When the grating structures are placed into a LC cell it is clear from the DSLR images in figure 4.20 that the grating under TM illumination loses the variation in colour, and under TE polarisation it increases. This may be expected as the LC medium has a similar refractive index to glass, under TM polarisation the SPP modes from the upper and lower interfaces of the metallic gratings converge, and hence there is a singular transmission dip that creates the structural colour, and under TE polarisation the RA scattering converges to one singular transmission peak, which will become more pronounced and will be able to create more observable colours.

For both TE and TM illumination, the shortest periodicity of grating is black. This is because during the lift off process the grating has been damaged due to the limitation of the fabrication techniques, and as such there is no alignment of the LC in these areas, hence the light through the device is not rotated and cannot pass through the crossed polarisers. Also under both TE and TM illumination, placing the grating structure in a LC medium increases the overall transmission intensity of the device, as shown in the colour scales of the experimentally measured spectra. The measured spectra from the devices again fits with the modelled results. For TM illumination there is a transmission dip corresponding to the SPP mode, and under TE there is a transmission peak according to the solution to equation 5.3.

What the experimental results show us is that a metallic grating may act as a combined alignment layer, colour filter and electrode in a twisted nematic device. The device may produce structure colour via plasmonic resonances under TM illumination, and, via other mechanism beyond the scope of this thesis, under TE illumination. The device provides an alternative to the LC-NH device previously discussed to create an active plasmonic metasurface in the visible spectrum. The TN device has advantages over the LC-NH device, such as the ability to switch between light and dark state, but lacks the colour tunability and the lower vividness of colours are compromises that have to be made.

4.4.4 Improving the colour of TN-NG device

Whilst the vividness of colour of a TN-NG device is not as great as that of the LC-NH devices, it is possible for it to be improved by altering the structure of the nano-grating.

During the fabrication of the metallic grating for the TN-NG device, it was observed that prior to the lift-off process, there was a greater breadth of colours produced by the nano-grating structure. This new structure consists of a nano-grating on the glass substrate as before, however, there is now a second grating atop the previously sacrificed polymer resist layer.

The removal of the lift-off step in the fabrication process of nano-structured devices has been used previously to produce structural colour. The metal-insulator-metal

(MIM) structure has been used with sub-wavelength metallic hole arrays[73–76]. The insulator layer in these structures is of the order $\sim$ 100nm and exploits the coupling of plasmonic resonances between the nano-structures on the substrate and atop the resist pillars to create their structural colour. In the case of the nano-grating MIM structure proposed in this thesis, the resist layer between the two gratings is of the order $\sim$ 400nm, and the coupling between plasmonic modes of the gratings, under TM illumination, is minimal. The structure is more similar to that produced by Zeng et al.[62] and Raj Shrestha et al.[118], where a plasmonic grating is coated in a defined thickness layer of dielectric. In addition to the SPP excitation, the structure gives rise to non-plasmonic phenomena, such as the guided-wave resonance (GMR)[131]. GMR can guide light into the region between the two gratings, thus creating a transmission dip at the resonant wavelengths.

The resonant condition for GMR is given by[118]

$$k_0 H_d = \frac{1}{\sqrt{\epsilon_{d1} - k_{grat}/k_0}} \left\{ \tan^{-1}\sqrt{\frac{k_{grat}/k_0 - \epsilon_{d2}}{\epsilon_{d1} - k_{grat}/k_0}} + \tan^{-1}\sqrt{\frac{k_{grat}/k_0 - \epsilon_m}{\epsilon_{d1} - k_{grat}/k_0}} + m\pi \right\} \quad (4.9)$$

where H_d is the dielectric layer thickness, ϵ_{d1} is the permittivity of ma-N 2405 and ϵ_{d2} is the permittivity of the propagation interface, either air or LC.

Figure 4.21 shows a schematic of the structure in air (a) and in a LC medium (b). The FDTD modelled transmission spectra of the grating-insulator-grating (GIG) structure under TM and TE illumination is also shown. The structure is now much more complex than the simple grating structure and as such the modelled transmission spectra increases in complexity. The thickness of the insulator layer in the model is 400nm as per the spin curves for ma-N 2405, confirmed by SEM imaging.

Observing the GIG structure in air, under TM polarisation first, the transmission spectra shown in figure 4.21(a). As the grating periodicity increases there are numerous transmission minima due to the various resonance mechanism. Plotted are the trend lines for the SPP modes due to the metal-substrate and metal-air interface. The SPP resonance at the metal-glass and the metal-resist are similar and hence only one line is plotted. Where the resonance occurs there are significant transmission dips.

Also plotted is the GMR resonant modes associated with the GIG structure with the air interface. Equation 4.9 has been derived for a singular grating in a dielectric medium with a the spacing between the grating and the air-dielectric interface as

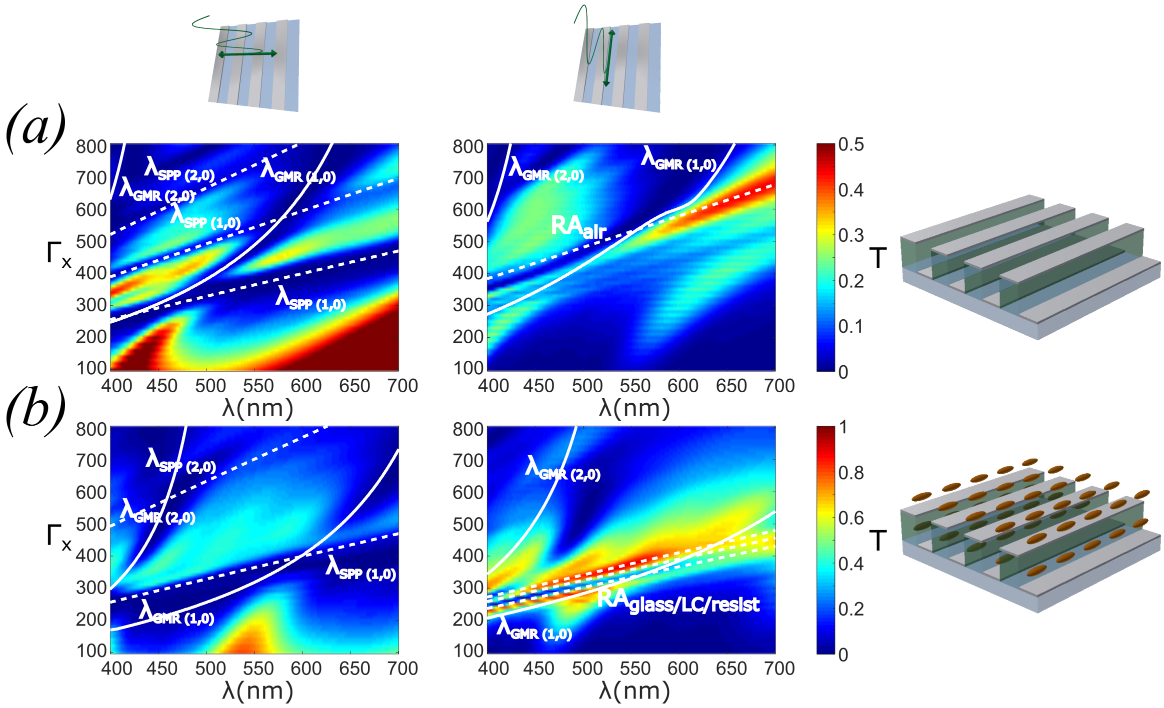

Figure. 4.21 FDTD modelled transmission spectra of GIG structure with duty cycle = 0.5, varying periodicity (Γ_x) of grating. The grating is illuminated with polariser aligned parallel and perpendicular to the grating grooves, in air (a) and in a LC medium (b)

the dielectric layer thickness. The structure used here is much more complex. The substrate, whilst having a similar permittivity to ma-N 2405, they are not the same. The propagating interface from the second grating is air, but in between the layer comprises 50% air & 50% resist. Hence the use of equation 4.9 has been altered in each scenario to discover the best fit and gain some insight into the resonant mechanisms of the structure. The trend line for TM illumination for the GIG structure in air has been calculated using $\epsilon_{d1} = \epsilon_{glass}$ and $\epsilon_{d2} = (\epsilon_{air} + \epsilon_{ma-N})/2$. The resulting trend line shows a good correlation with the modelled transmission dip.

Under TE polarisation, there are no longer transmission dips due to SPP resonances as SPP modes may not be excited in this configuration. However there are transmission dips similar to the those predicted by the GMR modes. The transmission dips above a periodicity of 600nm fit well with that shown under TM illumination, however beneath this pitch the FDTD modelled spectra does not follow the trend predicted by equation 4.9. If $\epsilon_{d1} = \epsilon_{glass}$ and $\epsilon_{d2} = \epsilon_{air}$, as plotted in figure 4.21(a), the fit of the GMR trend line below $\Gamma_x \sim 600$nm improves but worsens above this periodicity. Given a single grating structure shows a transmission peak that follows the solution to equation 5.3, one would expect a double grating to have a similar transmission peak. Plotting the RA line on the surface plot, there is a good agreement about $\Gamma_x \sim 500$nm, but not below. This may be due to the GMR effect negating the RA enhancement effect.

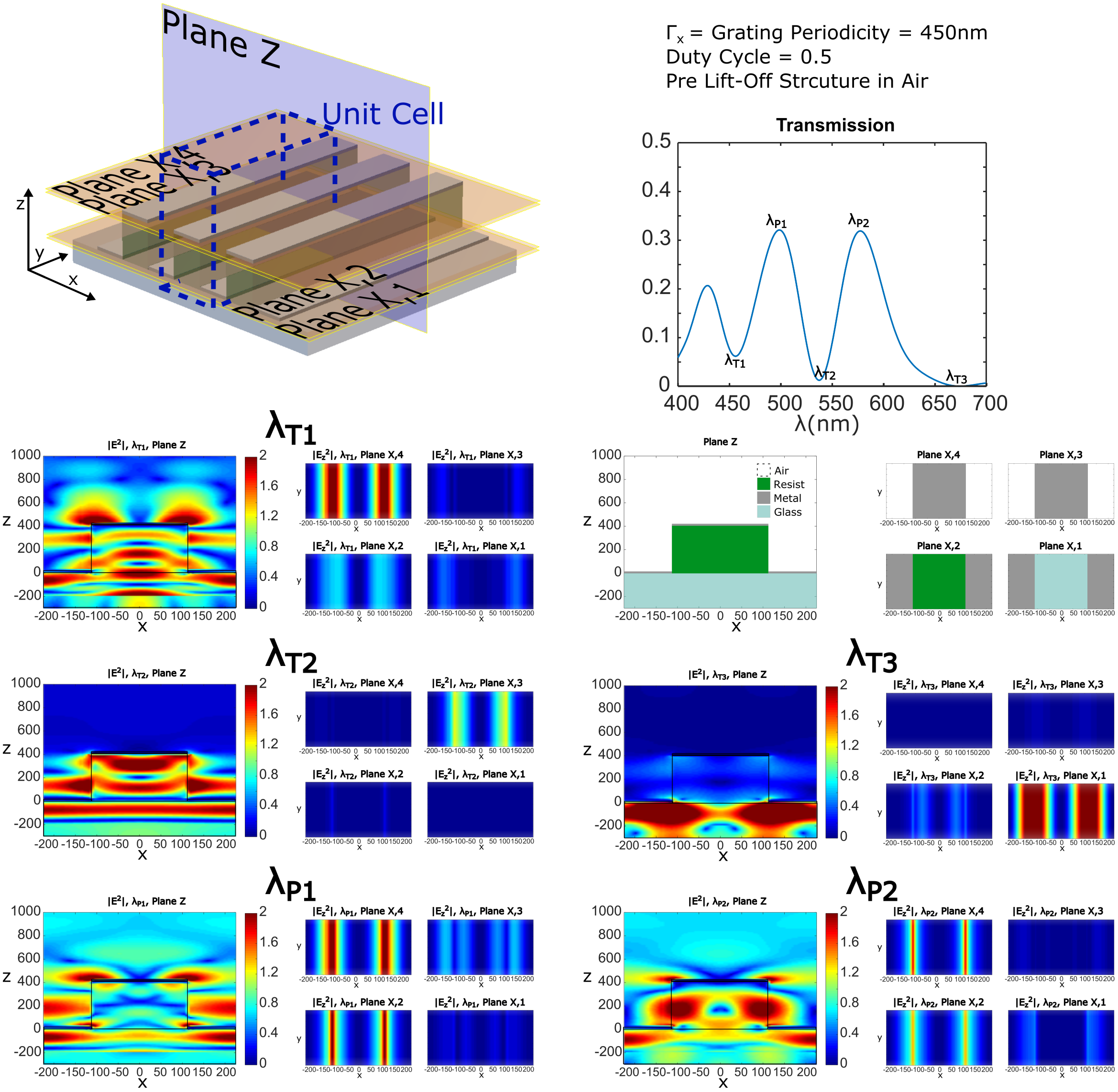

Figure. 4.22 E-field profiles of GIG structure in air with $\Gamma_x = 450$nm, duty cycle = 0.5, at transmission maxima and minima with schematic of GIG structure showing location of E-field planes

To further investigate and clarify the causes of the transmission peaks and dips the E-field profiles of the structure are observed for a grating with periodicity $\Gamma_x = 450$nm and DC=0.5 under TM illumination in figure 4.22. The figure shows a schematic of the grating structure and the location of the planes where the E-field intensity is observed. The z-plane gives a cross sectional view of the structure whilst the x-plane cuts observe the z-component of the E-field at the four metallic interfaces, to show if any plasmonic resonances are occurring. The illumination of the device is from underneath at $z = -200$nm. The transmission spectra plot shows the location of the three transmission troughs and two transmission peaks. Looking at the initial transmission dip at λ_{T1} the E-field plots show significant field enhancement at the metal-air interface at the top of the GIG structure. This transmission dip is predicted to be due to the SPP resonance at the air-metal interface (as shown in figure 4.21), due to the SPP mode interfering deconstructively with the propagating light. The $\mathrm{E_z}$ field plot at the X,4 interface confirms the presence of an SPP mode, and thus it can be concluded that the transmission dip is due to the $\lambda_{SPP(1,0)}$ mode at the metal-air interface.

The second transmission dip, λ_{T2}, is predicted to be from the first GMR mode ($\lambda_{GMR(1,0)}$) associated with the GIG-air structure. The E-field enhancement plot for the z-plane clearly shows the minimum in transmission and the coupling into the insulator cavity. The x-plane plots show some SPP E-field enhancement at the metal-resist interface. It however does not look significant enough to be the cause of the transmission dip and is likely only a contributing factor, and is associated with the second order SPP mode of the metal-resist interface.

The third transmission trough, λ_{T3}, is predicted to be from the first SPP mode ($\lambda_{SPP(1,0)}$) associated with the metal-glass interface. This is confirmed by the z-plane plot showing low E-field beyond the initial metal surface, and significant $\mathrm{E_z}$ enhancement at the X,1 interface.

The transmission peak plots are more difficult to decipher. In the LC-NH devices the transmission peaks were due to LSPR, which is most likely the case here, however this is difficult to confirm with the x-plane $\mathrm{E_z}$ plots as a plasmonic resonance localised to the edge of a grating looking much the same as a plasmonic mode propagating along a grating edge, as both have E-field enhancement along the entire edge of the metallic grating structures. What is shown is that for transmission peaks there is significant E-field enhancement at the upper metallic surface of both the lower and higher grating.

Here an attempt has been made to shed some light on the mechanisms behind the transmission maxima and minima in the GIG structure. Whilst some possible solutions have been presented, more work is needed to decipher the nano-plasmonic resonances in the structure, which are beyond the scope of this thesis.

When the GIG grating structure is placed into a LC medium the modelled transmission spectra, shown in figure 4.21(b) are much simplified. This is due to the removal of the air interface, which has been replaced by a medium with similar refractive index to both the resist and glass substrate. Under TM illumination the transmission dips appear to be due to the first two modes of both SPP and GMR resonances, and the FDTD calculated transmission dips correlate well with the SPP and GMR resonances predicted by equations 4.2 & 4.9. The GMR resonance wavelengths have been calculated in this case with $\epsilon_{d1} = \epsilon_{ma-N}$ and $\epsilon_{d2} = \epsilon_{LC}$. This suggests the resonances in this instance are due to the upper part of the GIG structure.

Under TE illumination there is the transmission enhancement predicted by equation 5.3, potentially due to the RA, negated by the GMR mode. The GMR resonance wavelengths have been calculated in this case with $\epsilon_{d1} = \epsilon_{glass}$ and $\epsilon_{d2} = (\epsilon_{LC}+\epsilon_{ma-N})/2$. As with the structure in air, for TE polarised illumination, even with careful choice of the dielectric constants, the GMR transmission dip predicted by the FDTD model is shifted from that predicted by equation 4.9.

Despite the deviations from solutions suggested from equation 4.9, figure 4.21(b) shows that the GIG structure in an TN LC device, should be able to create a colour pixel with a relatively narrow spectral peak, whose transmission can be switched off with application of an E-field across the device.

4.4.4.1 Fabricated GIG cells

The GIG TN cell was fabricated in the same manner as the TN-NG device, however skipping the lift-off process during the EBL fabrication process. The experimental results obtained for such a GIG-LC device are shown in figure 4.23.

What is most apparent is the greater variation of colour of the GIG structure, in the DSLR images, as opposed to the simple grating structure. This however comes at a cost to the intensity of the transmission through the GIG structure. Considering the GIG structure under TM polarisation in air, the DSLR images show a strong green colour, however as the colour shifts away the intensity drops and the colours are difficult to decipher. This is backed up by the measured spectra. Transmission dips due to SPP modes can be seen, however those due to GMR resonances are less clear, or potentially have a lower influence than predicted by the FDTD model. The same structure, under TE illumination, shows a larger intensity of transmission and

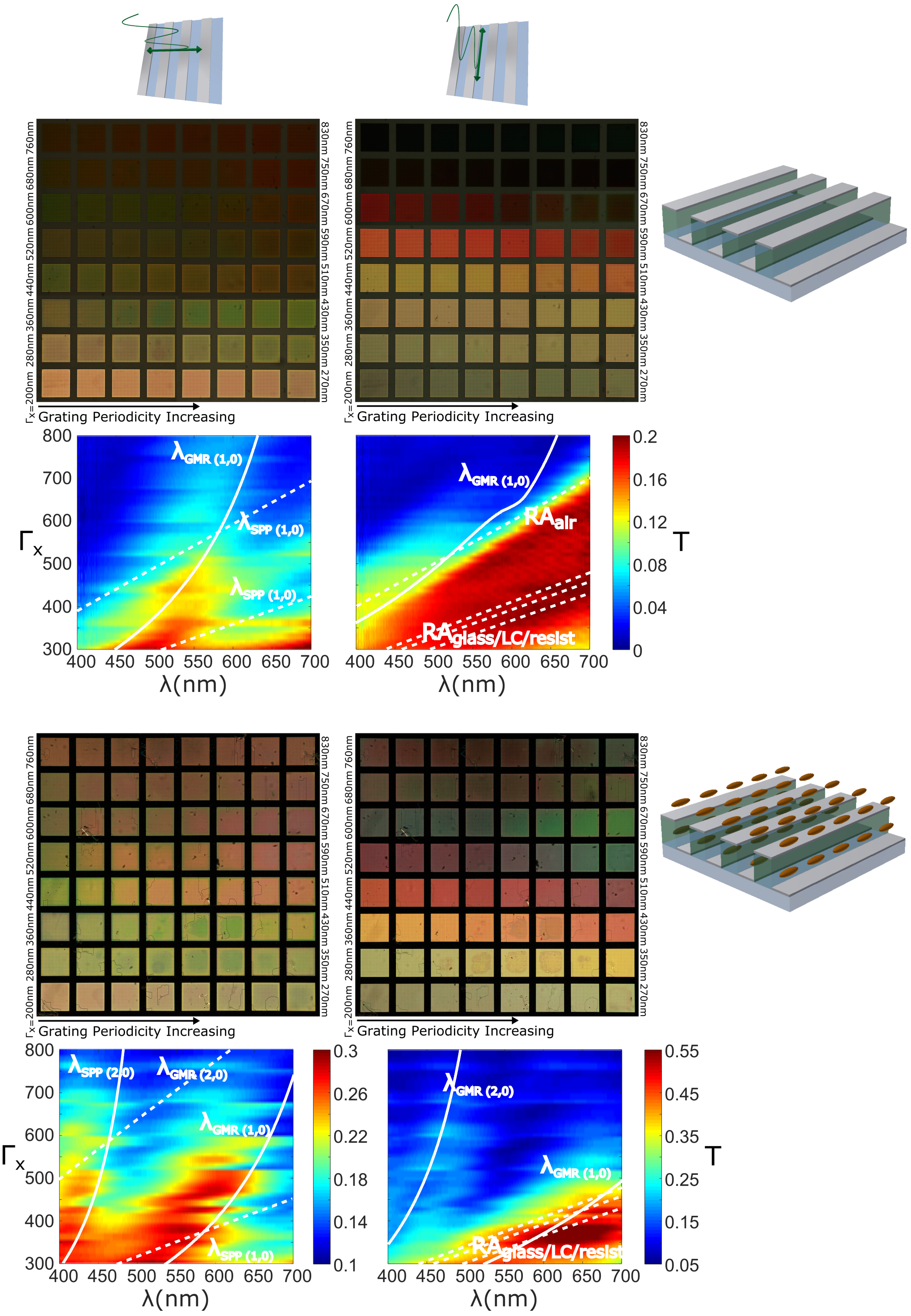

Figure. 4.23 DSLR images and transmission spectra of aluminium GIG structure on a glass substrate with duty cycle =0.5. Periodicity of grating varies from 200 to 830nm. The grating is illuminated with light polarised parallel and perpendicular to the nano-grating grooves. The results are shown for a GIG structure in air and in a twisted nematic LC GIG device.

a broader range of colours. The DSLR images show a good progression from yellow to red, however no colours in the shorter end of the visible spectra. The transmission intensity is once again, however, higher than under TM illumination. The measure spectra show a broad transmission peak, possibly due to the RA effect in air, glass and the resist combined, which are all similar but differ enough be resolvable.

When the GIG structure is constructed into a TN cell, gains are seen in transmission intensity and in the structural colours achievable, as shown in the DSLR images of the device. Under TM illumination, the measured spectra clearly show the transmission dips due to the first two SPP modes. Less clear is the effect of the GMR resonance which, whilst pronounced in the FDTD modelled spectra, the transmission dips are less clear in the experimental results.

Under TE illumination, the DSLR image shows a broad range of colours, with transmission intensity up to $\sim$ 50% in some cases. The experimentally measure transmission spectra show a peak corresponding to the RA equation, however, as with the TM illumination the effect of the GMR is less clear. What is interesting to note is the transmission dip, under TE illumination, is shifted from the solution to equation 4.9, in the experimentally measured results, by a similar amount to that observed when comparing solution to equation 4.9 to the FDTD modelled transmission spectra.

4.5 $LiNbO_3$ substrates

The devices mentioned so far in this chapter have created dynamic structural colour by altering the refractive index of the medium surrounding the grating. It was previously mentioned that the substrate for the nano-structure was glass, which would result in a SPP resonance at the glass-metal interface which could only be modified by altering the dimensions of the nano-hole surface.

There are however substrates, that are transparent in the visible wavelength range, whose refractive index may be electro-optically switched. One such material is lithium niobate ($LiNbO_3$)[132]. By applying a very high electric field across $LiNbO_3$ it is possible to alter its permittivity, and hence incorporating with a plasmonic metasurface, it should be possible to alter λ_{SPP} electronically.

If an electric field, E, is applied in the z direction the change in n_z is[133]

$$\Delta \mathrm{n}_z = -\frac{1}{2}\mathrm{n}_o^3 r_{33} E \tag{4.10}$$

where n$_o$ is the refractive index of the ordinary axis and r_{33} is an electro-optic coefficient obtained by experimental measurement (which in the case of Lithium Niobate is approx 30×10^{-12}m$/V$).

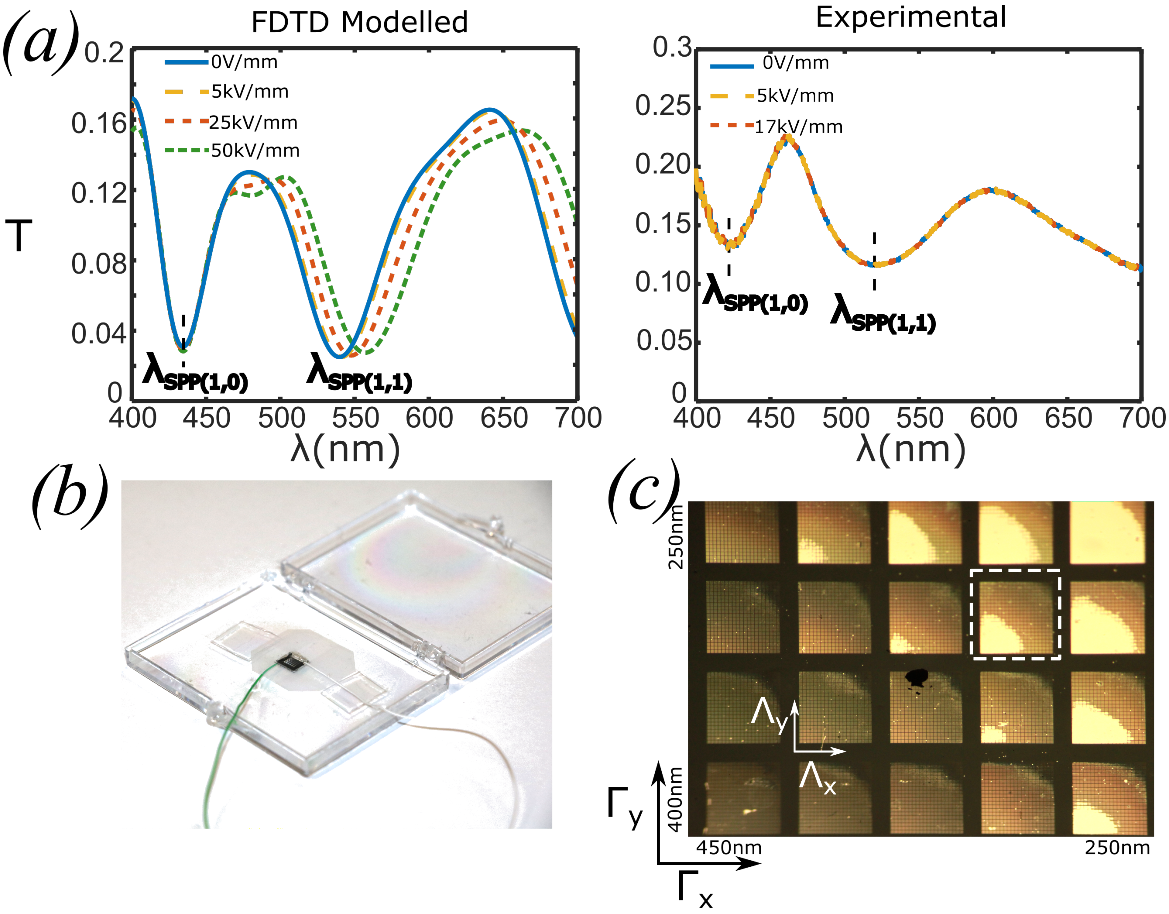

Figure. 4.24 (a)FDTD modelled and experimentally measured transmission spectra of aluminium metallic nano-hole layer $\Gamma_{x,y} = 300$nm, $\Lambda_{x,y} = 140$nm, on a LiNbO$_3$ substrate, varying electric field across the electro-optic substrate. (b) Photo of LiNbO$_3$-NH device. (c) Image of nano-hole layer on LiNbO$_3$ substrate illuminated with un-polarised light in transmission in a polarising optical microscope setup

Using equation 4.10 to model the refractive index of the LiNbO$_3$ substrate, the transmission spectra of an aluminium nano-hole surface, with $\Gamma_{x,y} = 300$nm and $\Lambda_{x,y} = 140$nm was modelled using a commercial FDTD simulator. The simulated spectra, increasing E-field applied across the substrate, are shown in figure 4.24(a).

The modelled transmission spectra show that it is potentially possible to shift the location of the SPP resonance of a nano-hole surface using an electro-optic substrate. The transmission spectra has a transmission dip at $\sim$ 430nm which corresponds to the SPP mode between the metal and the surrounding medium (n= 1.4). This transmission dip does not move with the application of an E-field as the surrounding medium is not an electro-optic material. The transmission dip at $\sim$ 550nm is associated with the $\lambda_{SPP(1,1)}$ mode of the metal-LiNbO$_3$ interface. As the field increases, so the wavelength of the SPP resonant dip increases in the transmission spectra. The E-field to create a shift of $\sim$ 20nm in the resonant dip is, however, extremely high at 50kV/mm. To apply a field of this magnitude across a substrate of 0.5mm thickness, a V_{rms} of 25kV would be needed. The voltage required can be reduced significantly by reducing the thickness of the substrate. However there is a limit to how thin the wafer may before issues start to occurring in the fabrication processes. Furthermore when a signal of that magnitude is applied, the spacing between the top and bottom electrodes needs to be taken into account, as if they are only separated by the wafer thickness at the edge of the sample, if the sample is in air, dielectric breakdown and arcing will occur. To overcome some of these issues, a LiNbO$_3$ substrate thickness of 200μm was used. The electrode layers on the top and bottom surfaces of the substrate were deposited away from the edge of the substrate. Lastly, after wires were connected to the electrode, the whole device was encased in PDMS, to prevent dielectric breakdown of the surrounding medium.

The nano-hole pattern was fabricated on the LiNbO$_3$ substrate using EBL techniques previously described, ensuring charge dissipation layers were used to overcome the issues that arise with EBL patterning on insulating substrates. As with the LC-NH device, the nano-hole layer acted as the top electrode. To apply an E-field across the substrate a $\sim$ 50nm ITO electrode layer was sputtered on the underside of the substrate. Under the application of heat, the LiNbO$_3$ substrate will fracture, hence to connect wires to the top and bottom electrodes, soldering is not feasible. As an alternative silver-epoxy resin was used. Once the electrodes were attached, the device was encased in a polymer (PDMS), to protect the substrate, and prevent arcing under application of a high voltage.

A DSLR photograph of the constructed device is shown in figure 4.10(b) and in a polarising optical microscope set up in (b). The adhesion of the Al metal nano-hole layer appeared to be lower than that of a glass substrate, as there was lower fidelity of the nano-hole pattern following the lift off process during fabrication as shown in figure 4.10(c).

The device was placed into a polarising optical microscope setup and a AC signal was applied with V_{p-p} increasing up to 5kV. The experimentally measured transmission spectra for increasing V are shown in figure 4.24(b). Unfortunately there was no observed movement in the location of the $\lambda_{SPP(1,1)}$ transmission dip. One possible reason for this may be the limitation of the lab equipment to apply a high enough electric field. The apparatus was limited by V_{p-p}=5kV, V_{rms}=3.5kV equivalent to an E-field of 17kV/mm. This field strength however should have been able to create a shift in $\lambda_{SPP(1,1)}$. The use of the nano-hole surface as the electrode may have had an effect as it is not a continuous electrode layer. The tolerance of the thickness of the $LiNbO_3$ substrate from the manufacturer is $\pm 25\mu$m, which could reduce the applied field.

4.6 Summary

In this chapter various devices for the control of the transmission spectra through a plasmonic metasurface have been discussed.

The devices use plasmonic resonances to create structural colour, which may be filtered to create active plasmonic pixels. The initial structural colour of a device is a function of the physical dimensions of the nano-hole surface and the permittivities of the surrounding media and the metallic layer itself. The nano-hole layers were fabricated on glass to allow the devices to operate in transmission, and were fabricated using an optically thin ($\sim$ 30nm) metallic layer. The metallic layer has the added advantage that it may act as an electrode to enable control of the pixel via application of an electric field to modulate the refractive index of the media surrounding the nano-structured layer.

To activate the plasmonic pixel liquid crystals are used to modulate the refractive index of the medium surrounding the nano-hole surface. The liquid crystals are placed between the metallic nano-hole layer, acting as a bottom electrode, and ITO covered glass, acting as a top electrode. By applying an electric signal between the nano-hole layer and ITO layer, an E-field is applied across the LC layer, to which the LC molecules will align. In theory the re-orientation of the LC molecules could shift the resonant wavelengths of the nano-hole plasmonic modes, however due to strong surface anchoring effects between the liquid crystal and the metallic surface re-orientation of the LC molecules does not occur close to the metallic surface. Hence the surface anchoring forces between the liquid crystal molecules and the metallic surface prevent tuning of the surface plasmon resonances as a means to modify the spectra transmitted through the electro-optic devices.

By using an analyser, orientated at 45° to the nano-hole lattice, to filter the orthogonally-polarised plasmonic modes from a nano-hole layer, a liquid crystal nano-hole (LC-NH) device was created whose spectral output spanned the visible spectrum, circumventing the surface anchoring issue.

The strong surface anchoring effects may be exploited by using a metallic grating as a combined colour filter, electrode and alignment layer. Using a nano-scale metallic grating as one half of a twisted nematic liquid crystal cell, it is possible to construct a plasmonic pixel which may switch between light and dark states when placed between crossed polarisers. The vividity of the colour achieved with a nano-scale grating was lower than desired, but may be improved by creating a two layer grating structure with the two gratings separated by a polymer layer. This structure did improve the colour by introducing further non-plasmonic resonant mechanisms into the structure. In fact the strongest colours were achieved when the grating was illuminated with light polarised parallel to the grating grooves, when no plasmonic resonances are able to be excited.

Lastly the potential of using a metallic nano-hole layer on an electro-optic substrate, whose refractive index may be modified with application of an electric field, was discussed. The substrate used was lithium niobate, and despite positive simulation results, the experimental results showed no change in the transmission spectra of the devices.

Chapter 5

Plasmonic nano-structures in elastomeric Polymers

Introduction

The scattering from metallic nano-rods, shown to be due to LSPR resonances within the nano-particles, demonstrate near-field properties such as wavelength and polarisation dependence. Through careful design, one can design nano-rod structures and surfaces to optimise the scattering efficiency at particular polarisations and wavelengths.

The scattering from metallic nano-rods may be utilised for numerous applications such as flat optics, hologram pixel and structural colour. The applications all have properties which depend upon the geometry of the overall structure. For example in flat optics, the focal length of a Fresnel zone plate (FZP) depends on the area and separation of concentric circular zones. In holography the size of the replay field is determined in part by the pitch of pixels in the physical hologram, and in a nano-rod array the LSPR resonant wavelength is dependent on the periodicity of the nano-rods.

Nano-rods are typically fabricated using EBL fabrication techniques. Once fabricated the geometry of these optical elements are fixed. With a static nano-rod surface, the anisotropic nature of the nano-rods has been utilised to create active devices that can switch between far-field images depending on the polarisation of the incident light[94]. The devices are however limited to two far field images, one for each orthogonal polarisation state

Whilst the dimensions of individual nano-rods may not be altered post fabrication, the ability to vary the dimensions of a metasurface consisting of the optical scattering elements post fabrication opens up a new genre of dynamic optic devices. By fabricating the hologram on a stretchable substrate the physical dimensions may be altered so as to multiplex between two or more holographic images[134]. Furthermore, arrays of Fresnel zone plates fabricated using silicon nano-wires on PDMS have been shown that under strain to point along various angles in order to capture images, offering an exceptionally wide field of view and axial focus scanning[135], whilst the ability to actively control the perceived colour of objects, desirable for a variety of applications such as camouflage, sensing, and displays, has been shown to be achievable using Si grating embedded in PDMS[97].

In this chapter a new facile pattern transfer technique has been developed for the transfer of EBL fabricated nano-rods into a PDMS substrate. The transfer process has several advantages over those previously demonstrated[113, 111]. Notably there is no need for any plasma treatment prior to transfer or bilayer resists, simplifying the transfer process. Furthermore the technique has been shown to transfer nano-particles down to $\sim$ 100nm in size. The process does, however, suffer from certain limitations, including issues with transferring grating structures, and only being suitable for aluminium.

After detailing the pattern transfer process, various potential applications are presented. All the devices presented utilise the mechanical deformation of the PDMS substrate to dynamically alter the properties of the various structures.

First, dynamic colour from the mechanical deformation of plasmonic nano-rod arrays is investigated. The structural colour from such an array depends on the metal of choice of the scattering element, the size of the scattering element, and the periodicity of the array. By stretching the PDMS substrate, the periodicity of the array may be actively altered.

Next flat lenses fabricated from nano-rods embedded in PDMS are discussed and the design and fabrication presented. By stretching these lenses it is possible to actively tune the focal length of the lens. Such lenses have been shown using CNTs as an absorbent medium for the opaque zones of a Fresnel zone plate[96], however, the use of nano-rods opens up the possibility of creating a tunable micros lens with polarisation and wavelength selectivity.

Finally, stretchable holograms utilising the scattering property of nano-rods to act as holographic pixels are demonstrated. The advantages of using nano-rod scatters include the sub-wavelength dimensions of the structure and their wavelength and polarisation properties. By fabricating the hologram in PDMS the physical dimensions of the hologram may be altered, changing the size of the replay field. In addition opportunities are opened up to design holograms whose wavelength dependencies alter with mechanical deformation.

5.1 Plasmonic nano-rods as scattering elements

The basis for plasmonic nano-structures in an elastomeric polymer are metallic nano-rods. Unlike when patterning on a rigid substrate, a continuous nano-hole layer is not feasible as the structure will be damaged in the mechanical deformation process.

The LSPR condition of a spherical nano-particle is defined in equation 2.1. The efficiency with which a nano-rod will scatter and absorb light can be summarised by the scattering and absorption cross-sections that may be written as[24]

$$\begin{aligned}\sigma_{scat} &= \frac{8\pi}{3}k^4r^6\left|\frac{\epsilon-\epsilon_{env}}{\epsilon+2\epsilon_{env}}\right| \\ \sigma_{abs} &= 4\pi kr^3\,\mathrm{Im}\left[\frac{\epsilon-\epsilon_{env}}{\epsilon+2\epsilon_{env}}\right]\end{aligned} \tag{5.1}$$

where r is the radius of the spherical particle, $k = \frac{2\pi}{\lambda}$ is the wave-number of the incident radiation and ϵ/ϵ_{env} is the permittivity of the metallic particle and surrounding environment respectively. When $r \ll \lambda$ absorption dominates scattering, whilst scattering is more significant than absorption for larger particles.

The ability of nano-rods to have a scattering area larger than the physical dimensions of the nano-structure mean that an individual element may act as, for example a pixel in a hologram, or an array of nano-rods that may replace continuous structures (e.g. for the zones of a FZP). The dipole-like resonances in a metallic nano-rod, mean the structure can be considered as optical antenna. In antenna theory, the ideal length of the antenna is $\lambda/2$. At optical frequencies this relation breaks down, as the incident radiation is not perfectly reflected, but penetrates into the metal, exciting plasmon resonances. Novotny et al. showed at optical frequencies an antenna no longer responds to the external wavelength but to shorter effective wavelength λ_{eff} where[136]

$$\lambda_{eff} = n_1 + n_2[\lambda/\lambda_p] \tag{5.2}$$

where λ_p is the plasma wavelength and n_1, n_2 are coefficients with dimensions of length that depend on antenna geometry and static dielectric properties. Hence the nano-structures will be able to show scattering that has wavelength dependency and polarisability leading to potential applications such as polarisation and wavelength sensitive holograms[12, 94]. Moreover, due to Bragg's law, as the scattering elements get smaller in size, the diffraction angle increases, hence with nano-scale scatterers there will be a large angular intensity distribution, attractive for wide-angle holography applications.

The FDTD modelled scattering cross-section of an isolated aluminium and silver nano-rod, measured in reflection, is plotted in figure 5.1. The nano-rod was illuminated with light polarised along the x-axis whilst varying the x- and y-dimensions ($\Lambda_{x,y}$) of the nano-rod. Figure 5.1(c,i) shows how the scattering cross section, σ_{scat} across the visible range varies, keeping Λ_y constant and varying Λ_x. The plots for Al and Ag both show as the rod lengthens so does the peak scattering wavelength of the rod. Al has a broader spectral response than Ag does, however both will scatter light in the visible range. Keeping Λ_x constant but varying Λ_y shows that the peak scattering wavelength of an individual nano-rod depends on which dimension is parallel to the polarisation of illumination. As Λ_y increases the relative scattering increases, as one might expect from a larger nano-particles, however the peak wavelength remains relatively consistent. Figure 5.1(d) shows the wavelength of peak scattering varying the dimensions, $\Lambda_{x,y}$, of the Al or Ag nano-rod under x-polarised illumination. The plot clearly shows the dependency on of the peak scattering wavelength on Λ_x. Both have peak scattering wavelengths in the visible regime, with this arising for Ag at smaller nano-rod dimensions that that of Al. This suggests that Ag is more suitable for applications requiring higher resolution, however the Al dimensions for visible wavelength scattering are more easily fabricated.

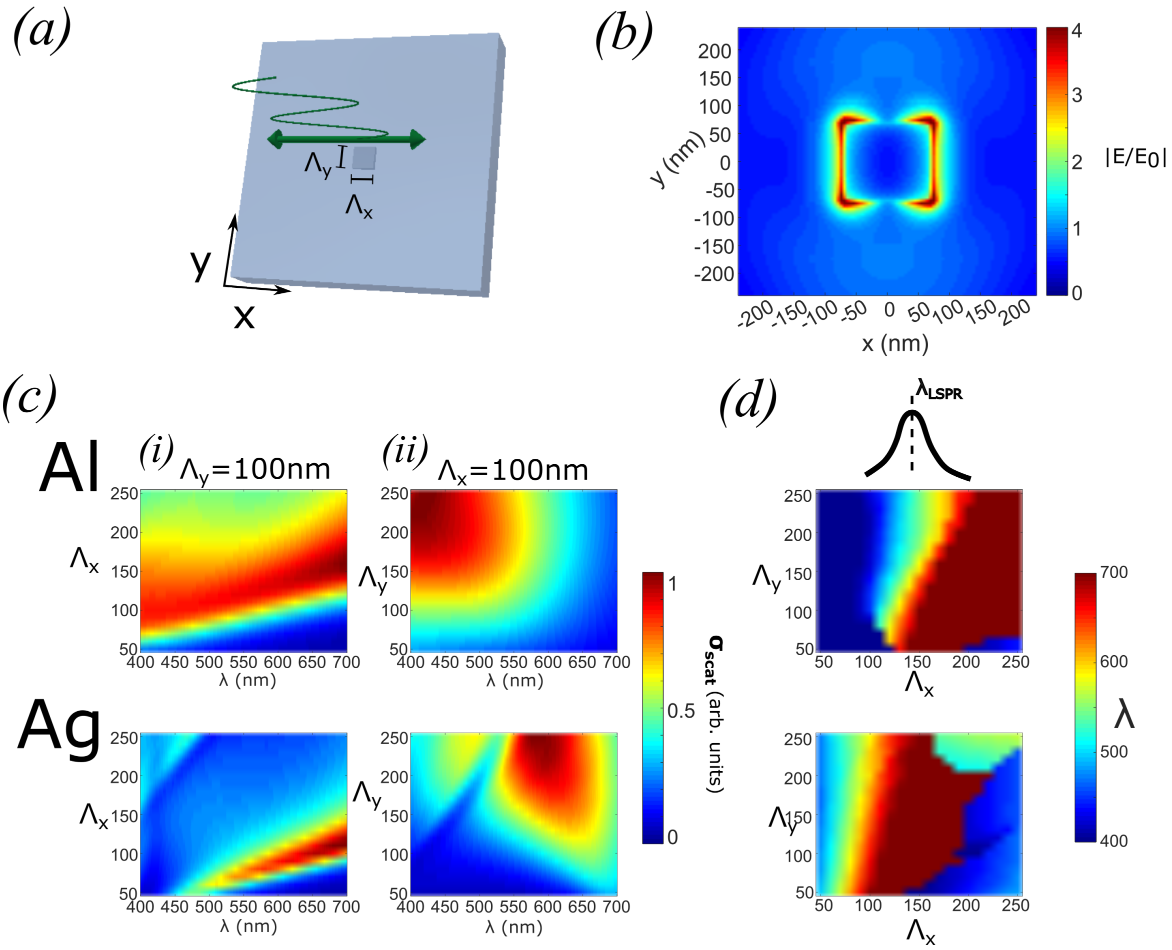

Figure. 5.1 Scattering from an isolated nano-rod. (a) Schematic of isolated nano-rod illuminated with x-polarised light. (b) Electric field profile of nano-rod at LSPR resonance under x-polarised illumination. (c) Scattering cross section of Al and Ag isolated nano-rods, measured in reflection, varying the (i) x dimension (Λ_x) of the nano-rod whilst keeping the y dimension (Λ_y) illuminated with x-polarised light, (i) keeping Λ_y constant at 100nm and (ii) varying Λ_y keeping $\Lambda_x = 100$nm. (d) Peak scattering wavelength in the visible wavelength range of the Al and Ag nano-rods varying $\Lambda_{x,y}$.

5.2 Fabrication

The fabrication of nano-structures on, or embedded in, an elastomeric polymer is not straightforward. One approach that could be taken would be to pattern directly onto the elastomer itself; to replace the patterning substrate used in the EBL processes with the desired polymer.

The polymer in question is polydimethylsiloxane (PDMS). PDMS is a transparent, viscous, liquid which will solidify when mixed with a cross-linker. It is a widely used polymer. Due to its inert and non-toxic nature it is used in medical and biological applications, as well as a shampoo and a food additive. It has a wide operating temperature range (-50 to 200°C), low absorption in the visible wavelength range. Combined with its low Young's modulus (7.5×10^{-4}GPa) and highly elastic nature (it may be stretched up to 120% before mechanical failure) PDMS is a suitable substrate for flexible, mechanically tunable metamaterials[137]. As a result it has been used widely in the fabrication of flexible electronic and optics[95, 113, 111, 138].

There are however issues with using PDMS substrates in EBL processes. Firstly there are issues with the de-lamination of a sacrificial resist layer due to the poor adhesion between resist material and the PDMS[113]. Secondly, PDMS is a non-conducting polymer, and as such, steps taken previously, described in section 3.2.1.3, to overcome charge accumulation issues would need to be repeated. This is an issue as, not only will a charge dissipation layer be difficult to deposit on top of a resist layer that de-laminates from the substrate, but the surface of PDMS is not flat, meaning that a continuous charge dissipation layer underneath the resist layer will be extremely challenging to deposit. The best demonstration of this is shown in figure 5.2(a). The photo shows a PDMS substrate with (i) a 100nm Al sputtered onto the surface and with (iii) a 30nm Al evaporated onto the surface, compared to (ii)a 30nm Al layer evaporated onto a glass substrate. The glass substrate has a smooth polished surface, which when Al evaporated is onto the surface, creates a thin continuous layer, shown by its reflective nature. The PDMS surfaces however are not smooth, and hence do not create the thin reflective layer. When sputtered, the Al creates a matte finish, whilst when evaporated, the thin layer does not reflect at all, but creates a dull area. SEM images of the surfaces are shown in (b) corresponding to the surfaces in (a). (b,ii) shows a smooth surface with nano-pillars, pre-pattern transfer. The metallic surface is smooth. In both (b,i) and (b,iii) it is possible to see surface texture. The surface in (b,i) looks to have been distorted by the exposure to the plasma in the metal sputterer. The left side of the image has imprinted nano-structures which would not be able to be fabricated on the ridges of the PDMS surface as they appear in the image. (b,ii) shows the surface with the 30nm Al layer deposited by evaporation. The surface is not smooth, but is flat enough to show imprinted nano-structures on the right of the image. Being a soft pliable polymer, the PDMS surface may not be polished smooth.

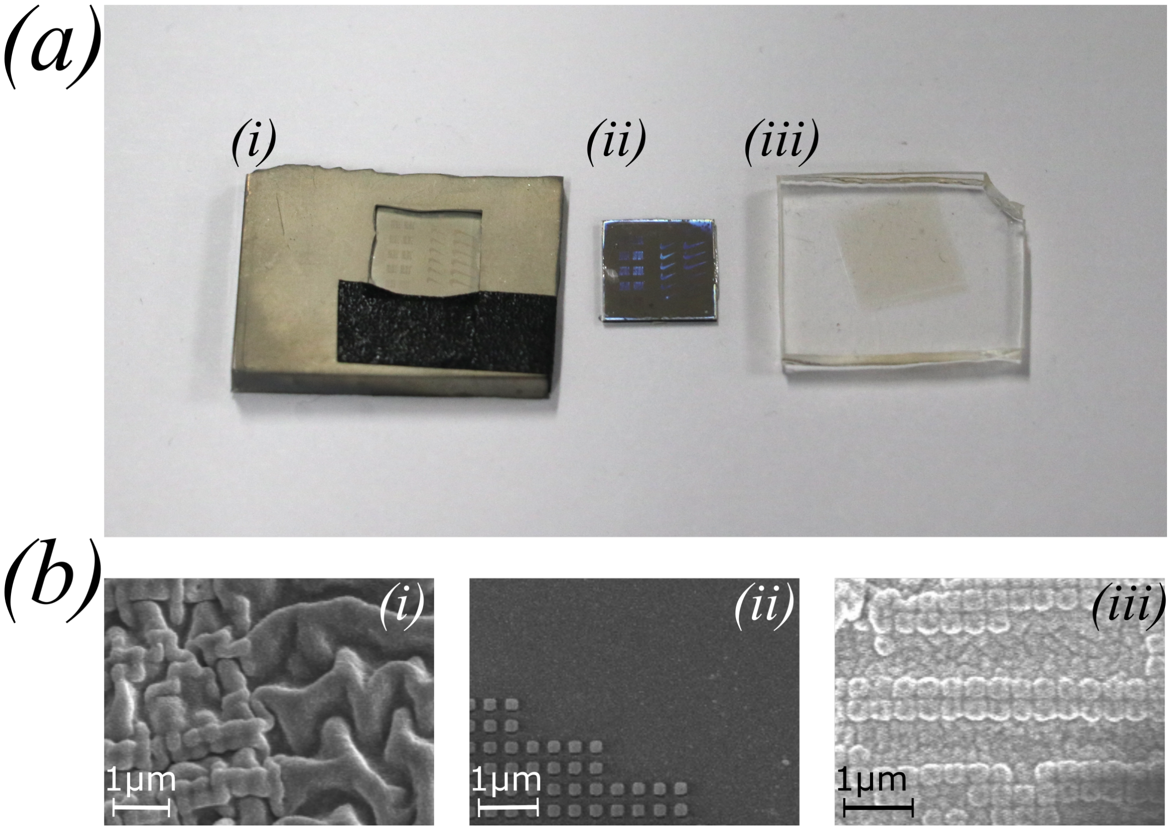

Figure. 5.2 Surface topology of imprinted PDMS and patterned Si substrates with Al deposited onto surface. (a) Camera photos of substrates with metallic layer deposited onto surface to allow for SEM imaging and (b) corresponding SEM images of the substrate surfaces. (i) PDMS with 100nm Al sputtered onto surface, after hologram surface imprinting, (ii) patterned resist on Si chip with 30nm Al evaporated onto surface and (iii) PDMS after hologram imprinting with 30nm Al evaporated onto surface. When sputtered onto PDMS, the Al creates a matte finish, whilst when evaporated, the thin layer does not reflect at all, but creates a dull area. When deposited onto a polished glass/Si surface a continuous smooth reflective layer of Al is created.

The lack of a flat PDMS surface also has consequences for other potential fabrication methods. Most prevalently, should we wish to use a master mould to stamp the PDMS, and then deposit metal onto the nano-structured PDMS surface, as the PDMS surface will not be level and smooth it is difficult to ensure the nano-scale pattern is firstly transferred accurately to the PDMS surface and secondly that the metal deposited is then deposited in the desired pattern. This method was not pursued.

Due to patterning directly onto a PDMS substrate not being possible, in the course of the work for this thesis, a simple pattern transfer process has been developed that builds on previously demonstrated processes used for large metallic structures[113] and simplifies those already used for the transfer of nano-particles for optics applications[111]. What makes this procedure unique is that previously used pattern transfer techniques for nano-structures use a bilayer resist to create the structures to be transferred. Following patterning an etch into the lower resist layer is performed, so that the liquid PDMS may form round the particle as the liquid PDMS cures, enabling the particle to be lifted off as the PDMS is mechanically peeled from the substrate. The technique developed in this thesis does not require the etch step. The pattern is created using a single layer of negative tone resist. If the negative tone resist does not undergo the lift-off process, the desired nano-rod pattern sits atop resist pillars. Immersing the pillars in PDMS results in the PDMS forming around the nano-structures atop the resist pillars as they are raised from the substrate by the thickness of the resist layer.

Prior to pattern transfer the nano-structures must be fabricated with EBL techniques. As we are transferring the pattern from the substrate, there is no need for it to be transparent. Hence silicon may be used, which is semi-conducting, as opposed to glass, which is an insulator, and steps taken to introduce charge dissipation layers used in Chapter 4 are not required. A single-side polished silicon wafer (thickness 525μm with a 300nm oxide layer), is diced to 1cm×1cm samples, cleaned in an ultrasonic bath of acetone, followed by isopropyl-alcohol (IPA), then blow-dried with compressed N_2. 80kV electron beam lithography (EBL) (Nanobeam Ltd. nB1) is used for the high-resolution patterning of the nano-structures. ma-N 2405 negative tone photoresist is spin-coated on top of the sample at 5,000 rpm for 60s to form a ~400 nm thick layer, then baked at 90°C for 3 min to remove the solvent. An EBL exposure dose of 200 μC cm^{-2}, 2 nAs^{-1} current and main-field aperture 50 μm were used. Resist development was in AZ-726-MIF developer solution for maN-2405 for ~ 20s, followed by a 60s rinse in DI water and a N_2 blow dry. Deposition of Al (~30nm) is performed using a thermal evaporator (base pressure 1x10^{-6} mbar); rate of ~0.1 nm s^{-1}.

Initially the transfer process was attempted using patterns fabricated with positive tone resists. The results of this process will also be discussed.

The initial pattern transfer process adopted was outlined by Du et al.[113] and is shown in figure 5.3(i). The process is used for large scale transfer of nano-scale patterns in continuous metal films. The process as shown works well for nano-structures down to ∼ 325nm in periodicity. The process was replicated here for the alternative purpose of transferring isolated nano-structures, (to act as individual scattering elements in a plasmonic metasurface), from the fabrication substrate onto an elastomer substrate.

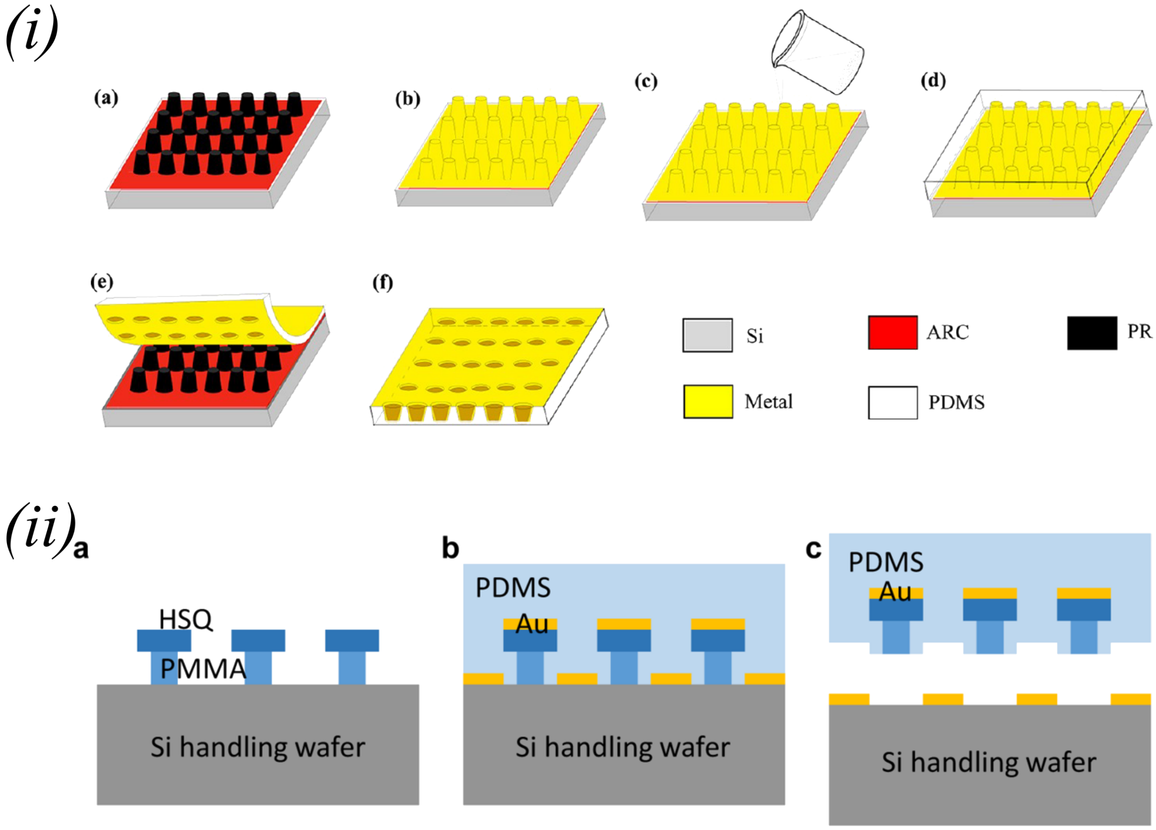

Figure. 5.3 (i)Schematic of a pattern transfer process of metal nano-structures onto a PDMS substrate by Du et al.[113]. (a) Photoresist (PR) nano-patterns fabricated by using laser interference lithography. (b) Metal deposited by evaporation and (c) moulding of PDMS elastomer onto the metal layer. (d) Curing and (e) detachment of the PDMS/metal layer to form a (f) planar substrate with metal nano-structures. (ii) Schematic of a pattern transfer process of metal nano-structures onto a PDMS substrate by Ee et al.[111] (a) HSQ/PMMA bilayer e-beam lithography and O_2 plasma etching. (b) Au deposition by evaporation followed by pouring and curing PDMS. (c) Stripping of the PDMS with embedded nano-structures. Figures re-worked from references.

The PDMS was prepared using a commercially available Sylgard 184 Silicone elastomer kit purchased from Dow Corning, USA. The PDMS to cross linker mixing ratio used was 10:1. Alternative mixing ratios were investigated. When the ratio was increased the pattern transfer fidelity decreased until at a ratio of >1:20 the PDMS did not fully cure. At mixing ratios of 1:5 the PDMS fully cures however the fidelity of the patterns transferred noticeably decreased.

Following mixing, the mixture degassed in a low vacuum to remove air bubbles before being poured onto the chip with the nano-structures to be transferred on its surface. The PDMS covered chip was then placed in a vacuum (base pressure $\sim 1 \times 10^{-5}$mbar) to ensure the PDMS formed around tight arrays of nano-structures, enabling air bubbles trapped in a tight nano-array to escape. The fidelity of the pattern transfer of periodic arrays with sub-300nm spacing is significantly increased when reducing the pressure of this step from $\sim 1 \times 10^{-3}$mbar to $\sim 1 \times 10^{-5}$mbar. After degassing the PDMS coated chip was baked at 40°C for 2 hours to quicken the curing process.

The PDMS is removed from the Si chip by mechanically peeling the two substrates apart. The evaporated metallic layer preferably bonds to the PDMS over the Si and hence the Al in contact with the Si chip and the Al on top of resist pillars are removed in its totality. The metallic layer will only be removed if the Al layer has been evaporated as opposed to being sputtered. The structure of the Al metallic layer, shown schematically figure 5.4, is very different under the two deposition methods[109]. Sputtering is a high energy process, hence metallic atoms from the sputter target arrive at the substrate with significant momentum. This results in extremely uniform, high density, amorphous films with excellent adhesion to the substrate. Thermal evaporation on the other hand is a low energy method. The metal to be deposited is heated in a ceramic boat, under high vacuum so that the metal vaporises and this vapour stream re-condenses on the substrate in line of sight of the metal in the boat. As the metal re-condenses it creates a porous, relatively low density structure. This porous structure will have less surface contact with the silicon substrate and higher surface contact with the PDMS. Bonding energies determined by Gajasinghe et al.[139] suggest that the Al will preferably bond to the Si substrate, however due to the deposition method the bonding energies change allowing a simple transfer process to exist.

Figure 5.4, (b) shows a patterned Si chip, which has has a metallic layer sputtered onto the surface, after the PDMS transfer step. The PDMS substrate is also shown. It is clear to see that the metal has not been removed and nothing has been transferred to the PDMS substrate. Figure 5.4 (c) shows a PDMS substrate post PDMS pattern

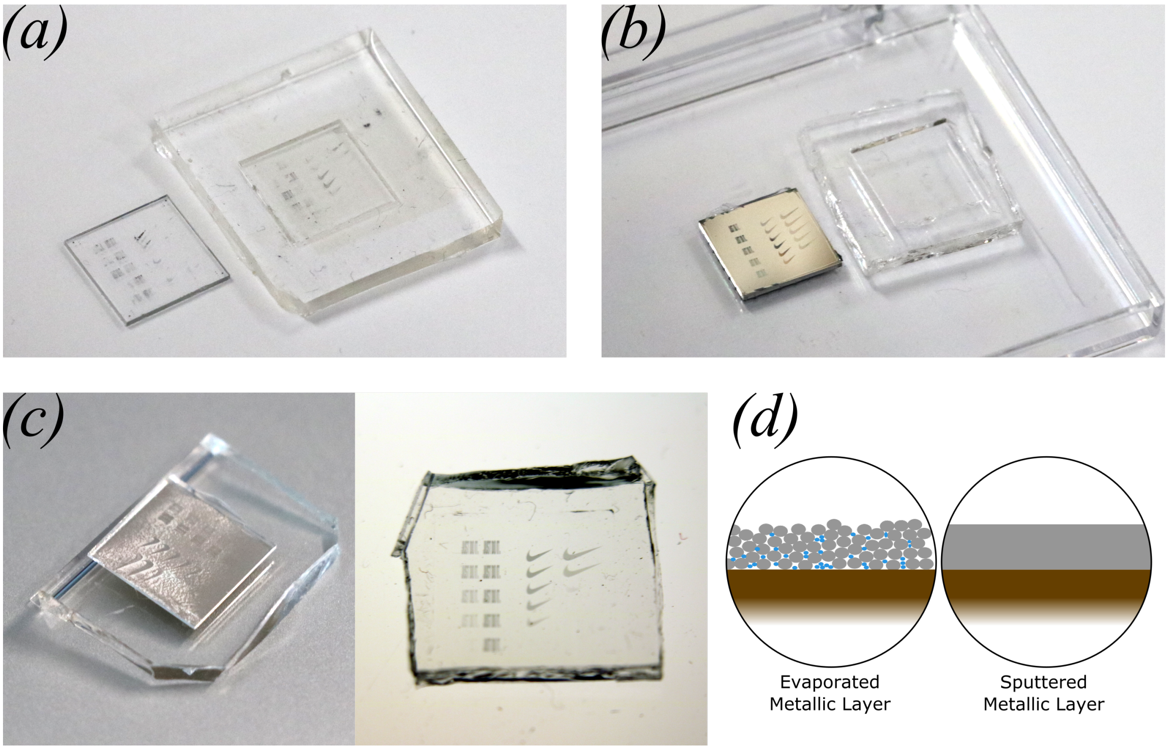

Figure. 5.4 Examples of PDMS pattern transfer. (a) Pattern transfer of nano-structures patterned onto glass substrate and then transferred to PDMS. Both glass patterned substrate and PDMS substrate shown after transfer. Nano-structures are imperfectly transferred, both being transferred to the PDMS and remaining on the glass substrate. Metal deposited via evaporation. (b) Pattern transfer of sputtered metallic surface. Sputtered metallic surface remains on Si chip, with no metal transferred to the PDMS substrate. (c) Pattern transfer of evaporated metallic surface on developed negative tone resist. The metallic layer is transferred in its entirety. Once excess Al removed, nano-structures, transferred on top of resist pillars are embedded into the PDMS substrate. (d) Schematic of metallic layer structure under different deposition methods. The evaporated metallic layer has a low-density porous structure. Due to the higher energy of the deposition atoms the sputtered metallic layer is uniform and densely packed.

transfer, for a patterned Si chip which has had a metallic layer evaporated onto the chip and patterned resist structure. The metal has been transferred in its entirety and once the excess Al layer has been removed, all that remains is the transferred nano-structures embedded in the PDMS substrate (also shown in (c)).

When using a positive tone resist, following the fabrication process, the metallic pattern that is desired to be transferred to the PDMS is on the Si substrate surface. When this structure undergoes the aforementioned transfer process not all the nano-structures are transferred. Figure 5.4(a) shows a partial transfer of hologram patterns. Both the glass substrate used for patterning and the PDMS substrate to which the nano-rods are to be transferred show remnants of the initial pattern. One reason for this lack of transfer may be that the PDMS surface does not create a contact with all the nano-structures. Figure 5.2(b,iii) shows the PMDS surface has an undulating surface with periodicity of $\sim$ 300nm, similar to that of periodicity of the nano-structures to be transferred. Since the thickness of the metallic layer is only $\sim$ 30nm, only a small curvature of the PDMS surface may come into contact with the nano-structures which could result in the non-transfer of nano-particles. What is more, in this setup the transfer fidelity is not consistent, with a low yield.

The fact that the entire pattern is not transferred, whilst a challenge for colour pixels, is less of an issue for holographic applications. The information for the replay field of a hologram is stored over the entire region. Hence should not all the pixels be transferred across, a significant amount of information may still be transferred to the elastomer substrate. This may be helped by the fact that the transfer of metallic scattering elements is not necessary for holographic PDMS applications. By stamping the pattern of the hologram into the PDMS surface, flexible holograms are still achievable (see section 5.6 in this chapter). Stamping a periodic structure into the surface of PDMS was not compatible with structural colour applications.

To make the process suitable for the high fidelity transfer of individual nano-particles a negative tone resist is used. When using a negative tone resist, the pattern that would be achieved on the substrate using EBL methods by the positive tone resist is present, separated from the substrate, atop the sacrificial resist layer, prior to lift-off. This has a number of advantages. When liquid PDMS is poured onto the pattern, the desired nano-structures to be transferred are not on the surface of the PDMS, but embedded into the liquid. When the PDMS is removed the metallic nano-structures are protected by the PDMS surrounding them, preventing the damage to the pattern and meaning that under stretching and contracting the relative locations of the individual nano-structures remains consistent. This process is shown in figure 5.5.

When this process is used, the entirety of the pattern is removed from the patterned substrate to the PDMS. As shown experimentally in figure 5.3(c) and schematically in 5.5, not only does the desired embedded nano-structured pattern transfer across but so does the metal in contact with the Si substrate when patterning. This continuous layer must be removed to leave the embedded pattern only. When using Al this excess layer of metal may be removed using Decon90. The Al reacts with the KOH in the Decon90, whilst the PDMS is unaffected. The ma-N resist is sensitive to the alkali

Decon90 solution, however it is more resistant than Al, and hence will protect the Al nano-structures embedded in the PDMS, leaving the desired pattern in the PDMS structure. The process has high fidelity, down to structures with periodicity of 250nm. When depositing Ag this process is unsuitable. This is because Ag will not be dissolved using Decon90. Ag does dissolve in nitric acid, however when using a dilute nitric acid solution, the excess Ag layer and the nano-structures are dissolved. Hence the process developed is, in its current form, only suitable for Al.

The process is summarised in table 5.1 and is schematically shown in figure 5.5

Table 5.1 PDMS pattern transfer process

1. Negative tone resist ma-N 2405 is spun on a Si substrate @ 5000 rpm and baked at 90° for 180s.
2. Resist exposed in desired metallic deposition pattern by EBL, dose 200 μCcm^{-2}, 2 nAs^{-1} current
3. Resist developed in AZ-726-MIF developer solution $\sim$ 20s removing unexposed resist.
4. 30nm Al metallic layer deposited on patterned resist on substrate by thermal evaporation.
5. PDMS is mixed with cross linker (10:1 ratio) and poured onto sample. Sample is placed in vacuum ($\sim 1 \times 10^{-5}$mbar) for $\sim$ 1hr.
6. Sample baked @40° for $\sim$ 2hrs to cure PDMS. Cured PDMS manually lifted from the sample surface. Metal pattern, resist and excess metal transferred to PDMS .
7. Excess Al metal is removed in Decon90 bath.
8. Nano-structures embedded in PDMS and sealed with second PDMS layer.

Finally a further layer of PDMS may be used to encase the nano-structures in PDMS. Any residual resist has little effect on the optical properties of the nano-structures as the resist has a similar permittivity to PDMS.

Ee et al.[111] have developed a similar process for Au, instead using a hydrogen silsesquioxane/poly(methyl methacrylate) (HSQ/PMMA, $\sim$ 90/180nm thickness) bi-layer mask followed by O_2 plasma etch the structure shown in figure 5.3(ii). The O_2 plasma etch results in the a layer of resist below the desired pattern to be transferred

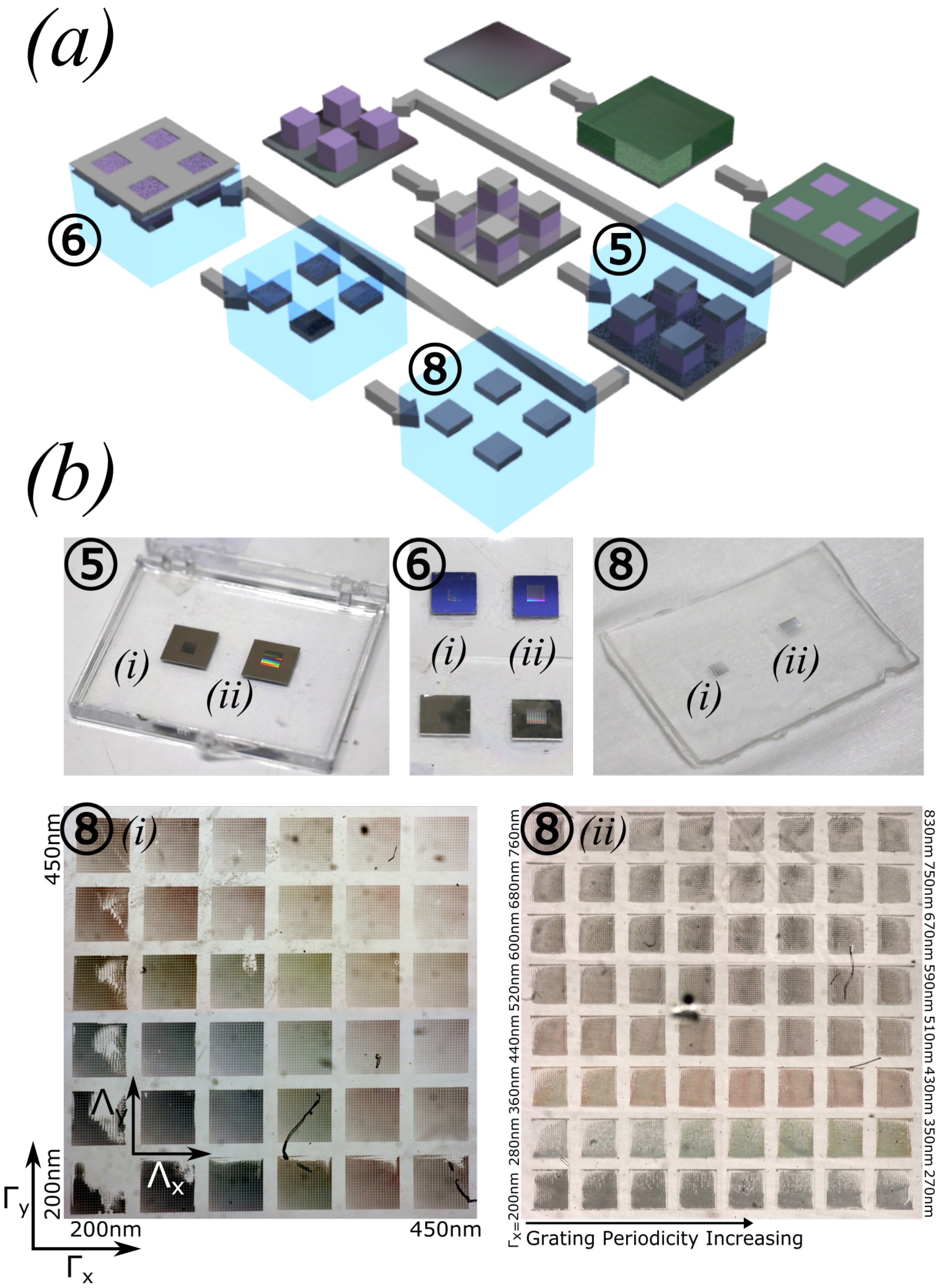

Figure. 5.5 PDMS pattern transfer process. (a)Schematic of PDMS pattern transfer process as described in table 5.1. (b) Photos of transfer substrates at various points during the pattern transfer process, with substrate (i) patterned with nano-rods to be transferred and substrate (ii) with a nano-grating to be transferred. *Step 5* Si substrate with Al layer on top of patterned negative tone resist after PDMS has been poured on and cured. *Step 6* Si and PDMS substrates after mechanical peeling. The grating pattern (ii) is shown to be incompletely transferred whereas the nano-rods structures (i) has transferred more completely. *Step 8* Nano-structures embedded in PDMS. Optical microscope photographs show the higher fidelity of nano-rods (i) as opposed to the nano-grating (ii). Images of PDMS sample A.

to be undercut, so that when the uncured PDMS is poured onto the substrate it forms around the nano-structures, and hence they are removed when the PDMS is peeled from the substrate surface. The process is similar to that developed in this thesis however it is more complex, using bilayer resist mask and an additional O_2 plasma etch. The presence of an overhang may be a useful addition to aid in the transfer of smaller metallic nano-particles however is not necessary for the work in this thesis, and the benefits of a bi-layer resist structure has not been investigated in this thesis.

The effectiveness of this process can be best demonstrated by the optical microscope image in figure 5.5 and the SEM images in figure 5.6. The optical microscope shows the transferred pattern, illuminated in transmission, of (i) a nano-rod array of varying dimensions and (ii) a nano-grating pattern of increasing periodicity. The periodicity ($\Gamma_{x,y}$) of the nano-rods in the array vary from 200nm to 450nm. The transfer of the nano-rods appears to be near 100% down to $\Gamma_{x,y} = 250$nm. When either the x- or y-periodicity of the nano-rod array is 250nm or greater the part of the patterns that have not been transferred appear to be issues with the patterning process, not a fundamental flaw in the pattern transfer process. When $\Gamma_{x,y} = 200$nm the transfer process of nano-rods from the Si chip to the PDMS shows lower fidelity. The reasons are not obvious as when either the x- or y-periodicity is kept constant the fidelity is not equal, that is to say if there was a consistent reason for the pattern transfer process not to work the far left column of nano-rod array in figure 5.5 Step 8(i) would look the same as the bottom row in the same image. Needless to say the lowest fidelity comes from the transfer of the pattern where $\Gamma_{x=y} = 200$nm. SEM images in figure 5.6 confirm what has already been deduced from figure 5.5. The figure shows the SEM images of either the Si chip (i) pre-transfer or (ii) post transfer for (a) a hologram structure with $\Gamma_{x=y} = 360$nm or (b) nano-rod array, with differing values of $\Gamma_{x,y}$. (i) clearly show the nano-rods on top of polymer pillars ready for transfer into the PDMS. (ii) shows the clean Si surface when there has been complete transfer of the nano-rods atop the resist pillars and the excess metal on the Si chip surface. When this occurs there is a residue of polymer on the Si chip that can be seen as the shadows of the nano-rods transferred to the PDMS. (iii) shows the incomplete transfers. In the case of the hologram (a,iii) the rods and resist pillars have been transferred across, but not all the surface metal has been removed. As this layer is to be removed in a Decon90 bath anyway and has no effect on the fidelity of the transferred pattern it is of no consequence to the pattern transfer process. (b,iii-iv) however shows not only surface metal that has not been transferred, but also nano-rods atop resist pillars. What is

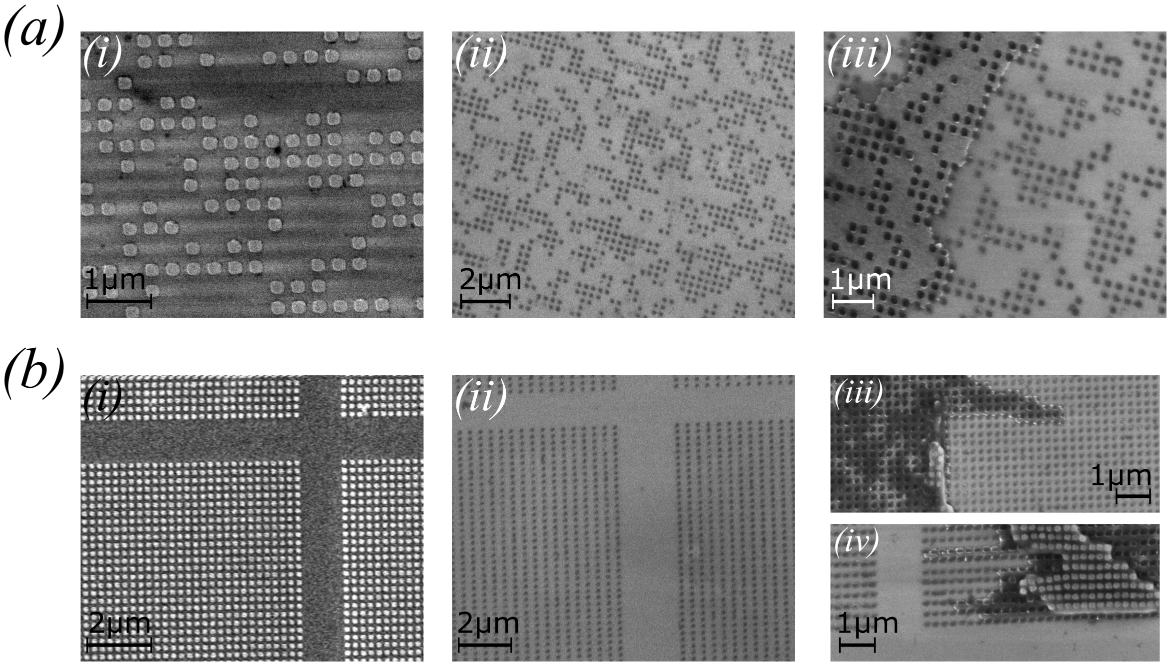

Figure. 5.6 SEM of patterned Si substrate prior to and after pattern transfer to PDMS. (a) Transfer of nano-rods for hologram. (i) Nano-rods atop resist pillars prior to pattern transfer. (ii) Si substrate post pattern transfer, shadows are at location of nano-pillars. (iii) Si substrate post pattern transfer, showing surface metal residue, however nano-rods and resist pillars transferred. (b) Transfer of nano-rods array for structural colour. (i) Nano-rods atop resist pillars prior to pattern transfer. (ii) Si substrate post pattern transfer, shadows are at location of nano-pillars. (iii,iv) (iii) Si substrate post pattern transfer, showing surface metal residue and PDMS residue with nano-rods and resist pillars on Si surface.

interesting to see is that the remaining pillars appear to be encased in residual PDMS. This could mean that due to the greater density of pillars the polymer does not wish to break/detach and instead the PDMS surface breaks. This may also mean that the PDMS is not properly mixed and a different crosslinker:PDMS mixing ratio occurs in small regions at the surface, creating a different region of bond strength in the cured PDMS. It does however suggest that should the resist pillars be weakened, greater pattern transfer fidelity may be achieved for the lower periodicities of arrays. This could be achieved using an ultrasonic step prior to mechanical peeling to weaken the resist pillars.

The effectiveness of the pattern transfer process for a grating structure is lower than that for the nano-rod arrays. Looking at figure 5.5 Step 6(ii) even up to the larger periodicities there are issues with the transfer. The transfer is good enough in parts to still create structural colour, however on the whole is it non-ideal. The reason is likely to be that due to the larger amount of resist to remove from the Si chip surface, as seen with the higher density nano-rod arrays, the resist does not break, and will instead stay fully intact with the Si chip surface and remain with the grating. Different directions of mechanical peeling have different effects on fidelity, however none come close to a 100% pattern transfer fidelity. Hence the process will need to be adjusted to become appropriate for such structures.

5.3 Mechanical deformation

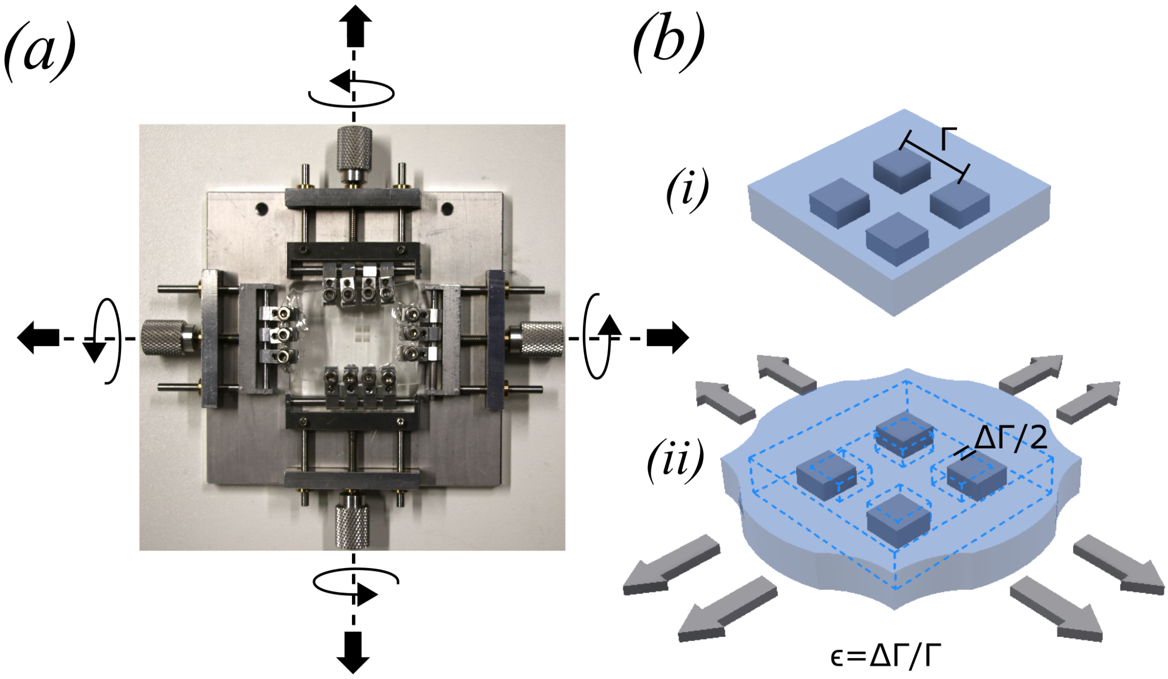

Figure. 5.7 Mechanical deformation. (a) Custom mount for mechanical deformation of PDMS substrate. PDMS sample is fixed by clamps that can move in x- and y-directions. Stretch induced by tightening screws at x- and y-extremities. (b) Schematic of PDMS stretch. (i) Nano-rods in PDMS substrate un-stretched. (ii) Nano-rods in PDMS substrate with strain, ϵ, applied

To stretch the PDMS the substrate was connected to a specially constructed mount shown in figure 5.7(a). The edges of the PDMS substrate are cut such that screws can be threaded through the edge of the substrate as well being gripped by clamps with teeth that will grip, but not damage, the substrate. The clamps are designed such that those creating the y-strain are free to move in the x-direction and the clamps providing the x-strain may move in the y-direction so that strain is not localised to the clamp and will be even across the substrate. The substrate is clamped in both x- and y- directions to reduce any deformation in the direction perpendicular to the direction of applied strain due to the Poisson effect Strain is applied by tightening screws shown in figure 5.7(a). The strain on the PDMS is shown schematically in figure 5.7(b).

5.4 Dynamic plasmonic colour pixels by mechanical deformation

5.4.1 Design

In section 4.1.1 the design of structural colour in an ultra thin metallic nano-hole surface was covered. However, a metallic nano-hole surface is not suitable for mechanical deformation, as a strain applied to the surface will result in damage to the continuous metallic layer. Whilst a continuous metallic layer was desirable in active devices using LCs due to the possibility of using the layer as an electrode, this constraint is not applicable when the dynamic modulation of the nano-structured surface is by means of mechanically applying a strain to the nano-structure arrays. Hence it is possible to use arrays of nano-rods as opposed to arrays of nano-holes.

The mechanisms for structural colour in both structures are dominated by surface plasmon resonances, however the main mechanism of a nano-hole surface is surface plasmon polaritons (SPPs) where as the dominant mechanism in a nano-rod surface is localised surface plasmon resonances (LSPRs), in both cases creating dips in the transmission spectra of the two structures.

The thickness of the metallic nano-rods was chosen to be $\sim$ 30nm, the same as the optically thin layer chosen for the nano-hole surface utilised in Chapter 4. The effect of varying the thickness of the nano-rods is shown in figure 5.8. As the metallic nano-rods, in a nano-rod array, increase in thickness, the LSPR resonant wavelength shortens. This trend is apparent for both Al and Ag. The peak wavelength remains constant at around $\sim$ 430nm, for both the Al and Ag array, however it is more pronounced for Al nano-rods, until overlap with the LSPR occurs, in which case, as the LSPR is the dominant resonant mechanism, the peak seen at $\sim$ 430nm is modulated.

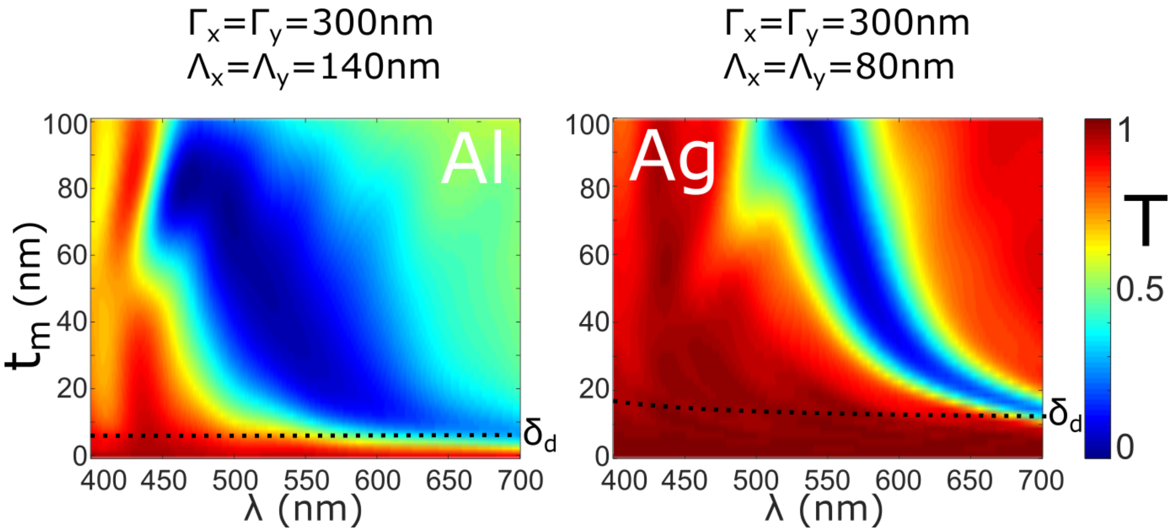

Figure. 5.8 Transmission spectra of metallic nano-rod array varying nano-rod thickness for Al and Ag nano-rods. The skin depth (δ_d) is plotted for each metal.

Figure 5.9 shows the transmission spectra for an array of aluminium nano-rods varying (a) the periodicity, $\Gamma_{x,y}$, of the nano-rod array and (b) varying the size, $\Lambda_{x,y}$, of the nano-rods, under x- and y-polarised illumination.

First we will consider a nano-rod array, in PDMS (n = 1.41)[116], with a square nano-rod of size $\Lambda_{x=y}$ = 140nm, varying the periodicity of the array equally, ($\Gamma_{x=y}$). The results shown in figure 5.9(a,i) show a linear relationship between transmission dip and peak and the increase in periodicity of the array. The transmission peak in fact follows the equation for light coupled into the grating

$$k_x + k_{grat} = k_0\sqrt{\epsilon_d} \tag{5.3}$$

a similar result to that seen in section 4.4 of this thesis when considering a plasmonic grating on a glass substrate.

It can be shown that the transmission peak in the visible wavelength spectrum is associated with a non-plasmonic resonance, where as the transmission dips are due to LSPRs by considering the electric field profile of a singular nano-rod in an array. Figure 5.10 shows z-normal x-plane and x-normal z-plane cuts of a nano-rod of size $\Lambda_{x=y}$ = 140nm, in an array $\Gamma_{x=y}$ = 350nm and isolated, in PDMS. Shown is the E-field enhancement and the z-component of the E-field enhancement. The reason for this is that the z-component of the E-field will be due to plasmonic resonances. The E-field plots are taken at the transmission minima and maxima of a nano-rod

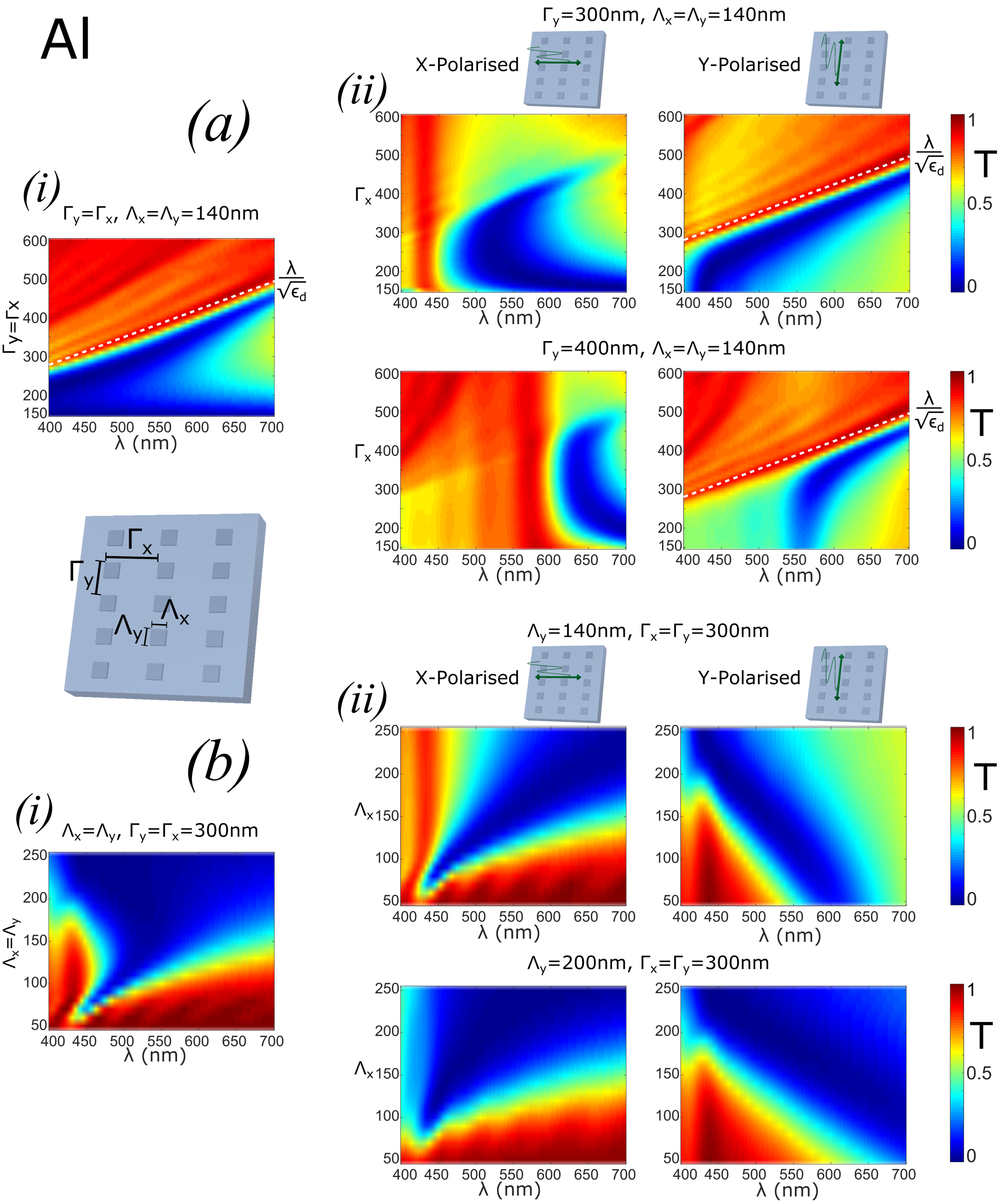

Figure. 5.9 Simulated transmission spectra varying (a) array periodicity and (b) nano-rod geometry for Al nano-rod arrays in PDMS. (a,i)Transmission spectra varying nano-rod periodicity equally ($\Gamma_{x=y}$) and (a,ii)for nano-rod arrays varying Γ_x whilst keeping Γ_y constant. Spectra are shown for light polarised along the x- and y-axis. The dimensions of the rectangular nano-rods are $\Lambda_{x,y} = 140$nm. (b,i)Transmission spectra varying nano-rod dimensions equally ($\Lambda_{x=y}$) and (b,ii) varying Λ_x whilst keeping Λ_y constant. Spectra are shown for light polarised along the x- and y-axis. The periodicity of the rectangular nano-hole arrays is $\Gamma_{x,y} = 300$nm.

arrays. The E-field plots of an isolated nano-hole in PDMS at the two wavelengths are similar. It was shown in figure 5.1 that an Al nano-rod has a broad wavelength scattering response and this is shown in the plot of scattering cross-section of the isolated nano-rod. At both wavelengths there is significant field enhancement around the nano-rod and a significant z-component of that field. When the nano-rod is arrayed there is a significant difference. At the transmission minima there is the same field enhancement around the nano-rod as seen with the isolated nano-hole, though with a narrower LSPR resonance as opposed to broad scattering of an individual nano-hole. This allows a transmission peak at $\sim$ 500nm. E-field enhancement occurs away from edges of the nano-rod, however, when considering a nano-hole in a metallic film this is due to surface plasmon polaritons, SPPs may not be supported in a PDMS medium and the field enhancement is due to a different non-plasmonic resonance. This confirmed by the lack of field enhancement in the z-component of the E-field.

Referring back to the nano-rod arrays in figure 5.9(a), below a periodicity of $\sim$ 270nm the LSPR is dominant and there is low transmission across the visible spectrum. It should be noted that as the size of the nano-rod is not significantly smaller than the wavelength of light, scattering, and not absorption, by the nano-rods is the dominant mechanism in play. Hence the reflection and transmission spectra of such a surface are the inverse of one another.

By keeping Γ_y of the nano-rod array constant and varying Γ_x under x- and y-polarised illumination, we may gain greater insight into the colour generation from the surface. The simulated transmission spectra is shown in in figure 5.9(a,ii) and we will first consider where $\Gamma_y = 300$nm. Under x-polarised illumination, varying Γ_x is to vary the periodicity parallel to the polarisation of the illumination. When this occurs the transmission peak of the nano-rod array remains unchanged. Even more remarkable is that the location of the LSPR resonance shortens between $\Gamma_x = 150 - 250$nm, then lengthens up to $\Gamma_x = 450$nm with its effect on the transmission spectra diminishing as the periodicity is increased further. There is indeed a point where one would expect the effect of scattering from small particles to reduce when the periodicity reaches a certain size. Due to the field enhancement extending beyond the physical dimensions of a nano-rod at resonance, the effective scattering cross section is larger than the physical dimensions of the rod. However, at a certain point this effective cross section will be significantly smaller than the periodicity of the array. At this point despite the high scattering, due to the fact an increasingly smaller proportion of the propagation area

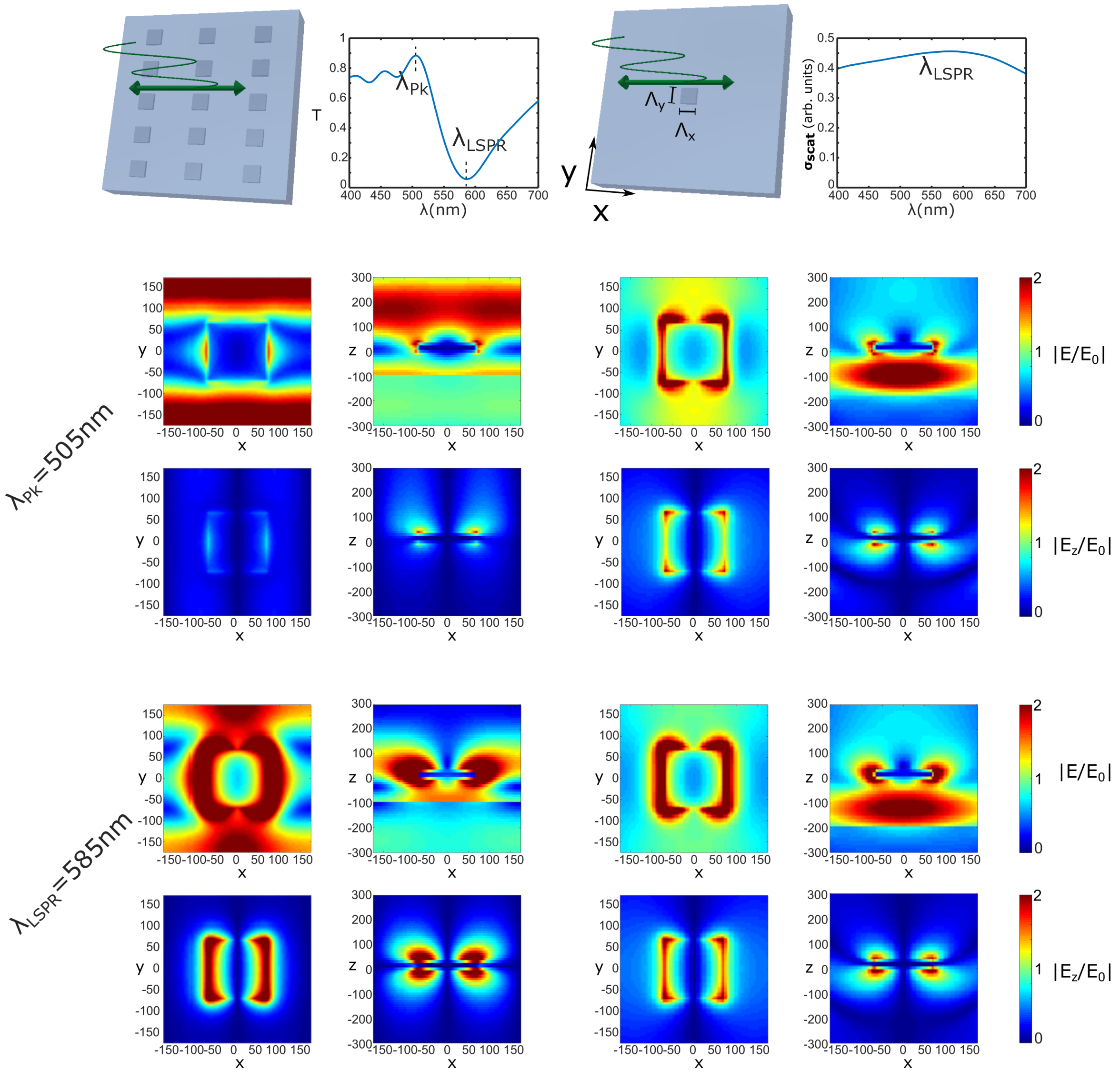

Figure. 5.10 Comparison of nano-rod array and isolated nano-rod resonances under x-polarised illumination. Transmission spectra of a nano-rod array showing location of transmission maxima and LSPR resonance and scattering cross-section of an isolated nano-rod. E-field plots at z and x normal planes along with plots of the z-component of the E-field in the x-normal plane of both a nano-rod in an array and an isolated nano-rod at the peak transmission and LSPR resonant wavelength of the nano-rod array are shown

will be effectively scattering, the effect of the plasmonic scatterers will be diminished. Under y-polarised illumination, varying Γ_x is to vary the periodicity perpendicular to the polarisation of the illumination. As Γ_x increases so does the location of the transmission peak, following equation 5.3, and the LSPR transmission dip. The LSPR transmission dip is linear above a periodicity of $\sim$ 250nm, however the transmission dip stays constant at a wavelength of $\sim$ 430nm at lower periodicities. By varying Γ_x but keeping Γ_y constant at 400nm similar trends are observed. Under x-polarised illumination the position of the transmission peak has now shifted higher to $\sim$ 580nm and the LSPR transmission dip has also moved higher. As Γ_x increases, the LSPR resonant wavelength shortens but by a proportionally smaller amount, and its effect diminishes around the same periodicity as that for $\Gamma_y = 300$nm. There is a similar theme under y-polarised illumination, with the LSPR transmission dip moved towards the red part of the visible spectrum, however, the transmission peaks are in fact identical to that seen when $\Gamma_y = 300$nm. Hence one can say that the location of the transmission peak is determined by the periodicity perpendicular to the polarisation of illumination. The transmission dip may be determined by the periodicity perpendicular to the polarisation of illumination, however there is a minimum cut off set by the periodicity parallel to the polarisation of illumination.

It is interesting to note comparing figure 5.9(a) to figure 4.5 in Chapter 4, which represents the same plots but for a nano-hole rather than a nano-rod structure, that the plots are the inverse, with x- and y-polarisations swapped. Whilst this may be expected since the transmission maxima of a nano-hole structure and the transmission minima of the nano-rod array both due to LSPRs, the transmission minima of the nano-hole structures, which corresponded very closely to the transmission maxima of the nano-rod array, are due to SPP resonance which may not be supported in a nano-rod array structure. The mechanism for transmission maxima for the transverse electric (TE) illumination of a grating structure, which was postulated in section 4.4 to be due to the Rayleigh anomaly, is most likely at play again here.

The same plots but for an Ag nano-rod array are shown in figure 5.11. The location of the LSPR resonance is further towards to the red end of the visible spectrum. This is expected given an isolated Ag nano-rod that scatters light in the visible spectrum is smaller than the corresponding Al nano-rod. Once again, when varying the pitch of the nano-rod array, it is the dimension perpendicular to the polarisation of illumination that has the greater determining factor on the location of the LSPR of the nano-hole

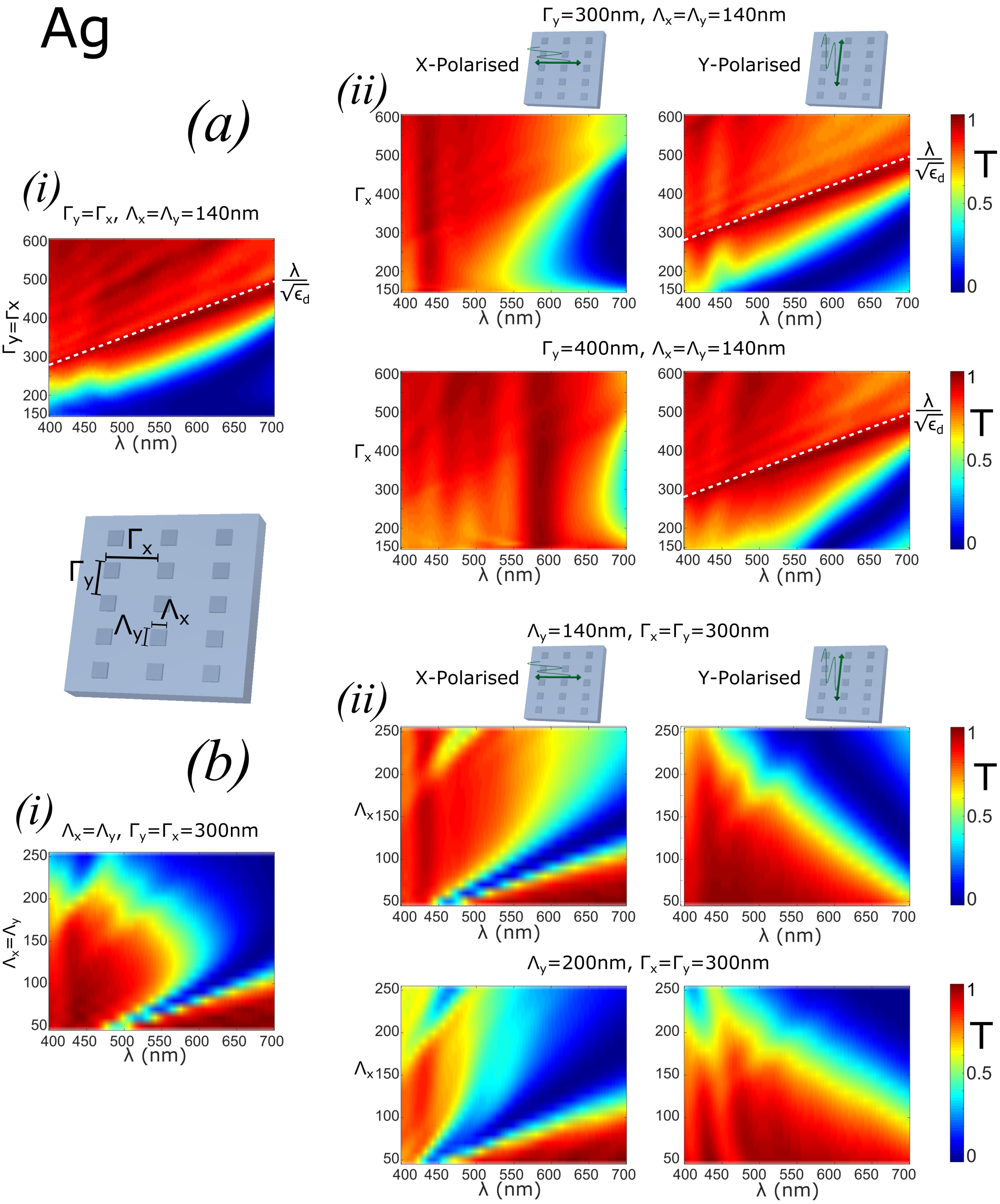

Figure. 5.11 Simulated transmission spectra varying (a)array periodicity and (b) nano-rod geometry for Ag nano-rod arrays in PDMS. (a,i) Transmission spectra varying nano-rod periodicity equally ($\Gamma_{x=y}$) and for (a,ii) nano-rod arrays varying Γ_x whilst keeping Γ_y constant. Spectra are shown for light polarised along the x- and y-axis. The dimensions of the rectangular nano-rods are $\Lambda_{x,y} = 140$nm. (b,i) Transmission spectra varying nano-rod dimensions equally ($\Lambda_{x=y}$) and (b,ii) varying Λ_x whilst keeping Λ_y constant. Spectra are shown for light polarised along the x- and y-axis. The periodicity of the rectangular nano-hole arrays is $\Gamma_{x,y} = 300$nm.

array. What is interesting is that the transmission peak, whilst less prominent, is in the same location as with the Al nano-rod array. This suggests it is the structure of the array that creates the transmission maxima. Due to the close proximity of the transmission peak and LSPR transmission minima in an Al array, the transmission peak is more prominent and will potentially create more vivid structural colour than a corresponding Ag array in transmission.

Now, by keeping the periodicity of the grating constant at $\Gamma_{x,y} = 300$nm, and varying the size of the nano-rod itself, $\Lambda_{x,y}$, it is possible to alter the location of the LSPR transmission minima. Like the transmission minima in a nano-hole surface, the transmission maxima location is not moved by varying the size of the nano-rod, however, as the LSPRs are the dominant mechanism, where the LSPR overlaps with the transmission maxima, the maxima disappears. When the x- and y-dimensions of the nano-rod are modified equally ($\Lambda_x = \Lambda_y$), there is initially a linear relationship with transmission minima and size of the nano-rod, however as the size of the nano-rod becomes larger, eventually no transmission is seen across the visible spectrum. This is potentially not only due the LSPR resonance of the Ag nano-rod but also due to proportion of transmission area covered by the metal. By varying the x dimension of the nano-rods, Λ_x, but holding the y dimension of the nano-rod constant at $\Lambda_y = 140$nm, whilst illuminating with x- and y-polarised light further insight into the optical response of the Ag nano-rod arrays may be given. When varying Λ_x and illuminating the nano-rod array with x-polarised light, the location of the transmission dip is proportional to Λ_x. This is expected as the resonant wavelength of an individual isolated nano-rod is proportional to the length of the nano-rod. The inverse occurs when illuminated with y-polarised light, that is to say as Λ_x increases the resonant wavelength decreases.

When holding the periodicity of an Ag nano-array constant and varying the size of the nano-rod, we see once again that the LSPR resonance is dependent on the aspect ratio of the rod. The significant difference between the Ag and Al modelled results here are that the transmission dips for the Al array are wider than those of a similar Ag nano-rod array. Given what we have seen with regards to the wavelength response of the scattering cross-section of isolated nano-rods this is expected and suggests a greater tunable range of an Ag nano-rod array.

The impact of the altering the physical dimensions of an Al nano-rod array are summarised in figure 5.12. The figure plots the location of the transmission minima and maxima when varying $\Lambda_{x,y}$ whilst keeping $\Gamma_{x,y}$ constant at 300nm, and the transmission

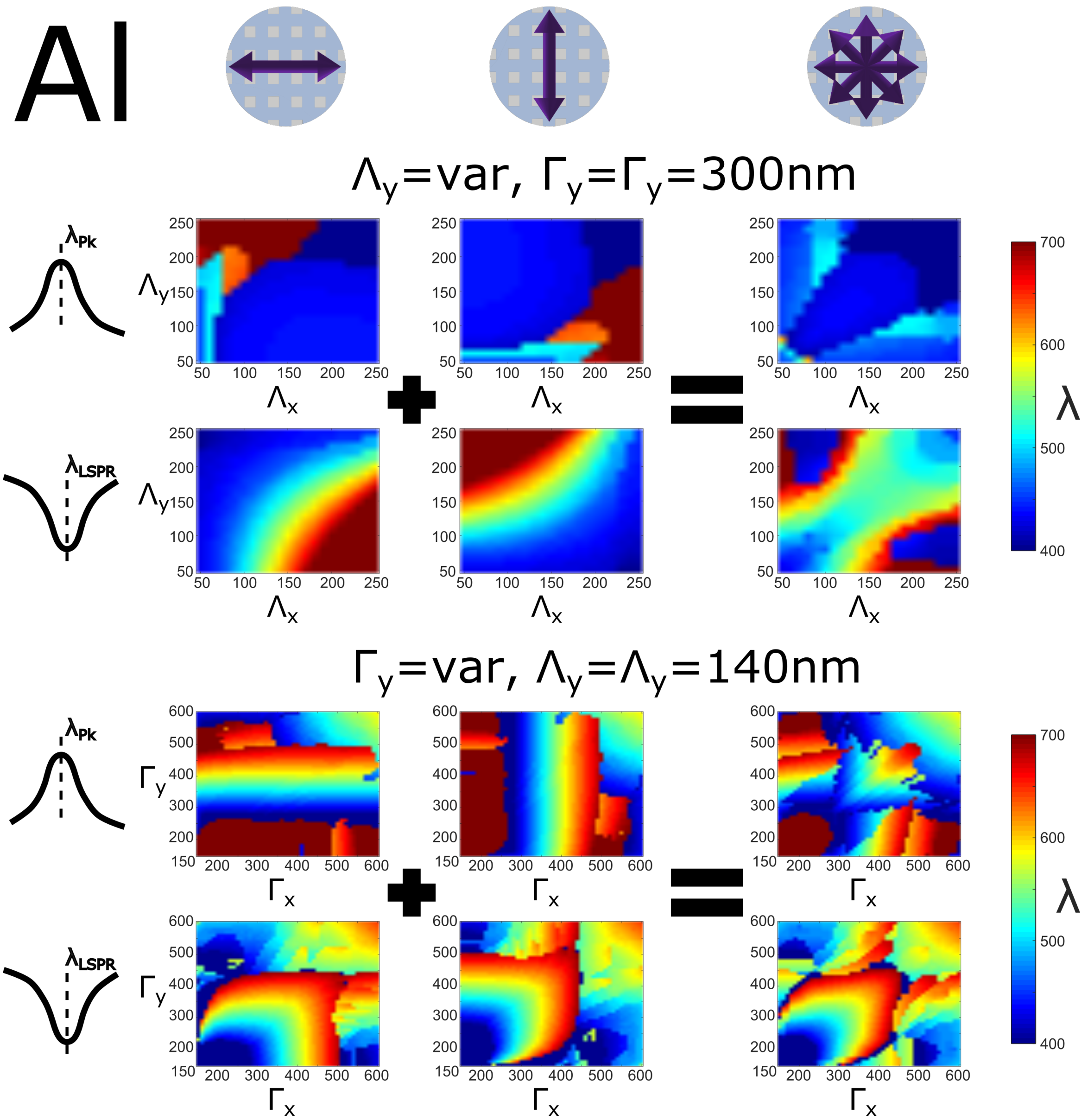

Figure. 5.12 Location of maximum (λ_{pk}) and minimum (λ_{LSPR}) transmission wavelength for rectangular nano-rod array within the visible wavelength range, in PDMS, varying the dimensions of the array under x,y and un-polarised illumination. Maximum and minimum transmission wavelengths keeping $\Gamma_{x,y} = 300$nm and varying $\Lambda_{x,y}$. Maximum and minimum transmission wavelengths keeping $\Lambda_{x,y} = 140$nm and varying $\Gamma_{x,y}$

minima and maxima when varying $\Gamma_{x,y}$ whilst keeping $\Lambda_{x,y}$ constant at 140nm. When varying the size of the nano-rods in an array there is little movement in the peak transmission wavelength, but the transmission minima is varied across the entirety of the visible spectrum. When varying the periodicity, however, there is significant movement of both the transmission minima and maxima, demonstrating a greater tunable range of the dimension. This is very useful as when embedded in PDMS it is possible to mechanically deform the PDMS and alter the periodicity of the array after the array has been fabricated, whereas this is not possible with the size of the nano-rods.

5.4.2 Fabricated nanorod arrays in PDMS

Al nano-rod arrays in PDMS were fabricated as described in section 5.2 and the results are shown in figure 5.13. The array fabricated consists of a 6×6 grid of $400\mu\text{m}\times400\mu\text{m}$ nano-hole arrays with each array split into 20×20 sub grids. The large grids vary their x- and y-periodicity, $\Gamma_{x,y}$, from grid to grid in the x- and y-direction, whilst the larger grids are split into smaller sub grids where the size of the nano-rods themselves vary spatially each sub-grid step. 5.13 (a) shows photos taken with a DSLR camera of the fabricated arrays will x-, y- and un-polarised light. The same images taken with the device in a polarising optical microscope setup are shown in (b). In both (a) and (b) it is possible to see the expected colour variation from the FDTD modelled spectra. There is some but not significant colour variation when varying the size of the nano-rods from $\Lambda_{x,y} = 100 - 200$nm. When illuminated with x-polarised light, there is clear colour disparity between each row, from red ($\Gamma_y = 400$nm) to green ($\Gamma_y = 350$nm) to blue ($\Gamma_y = 300$nm), that is to say there is a shift in the transmission peak as the periodicity is varied perpendicular to the polarisation of illumination, in line with the modelled spectra. When illuminated with y-polarised light the colour variation comes with the variation of Γ_x, and the colour of the grids under un-polarised illumination is a combination of the two.

The experimentally measured transmission spectra shown in (c) shows the expected transmission peak and fits well with the FDTD modelled spectra. There is however no clear transmission dip at the LSPR resonant frequency. The lack of a clear dip is not enough to suggest that a LSPR resonance is not present. The experimental spectra were taken using a spectrometer whose collection area covers an area which includes a reasonably broad range of size of nano-rod. The effect fo this will broaden the LSPR

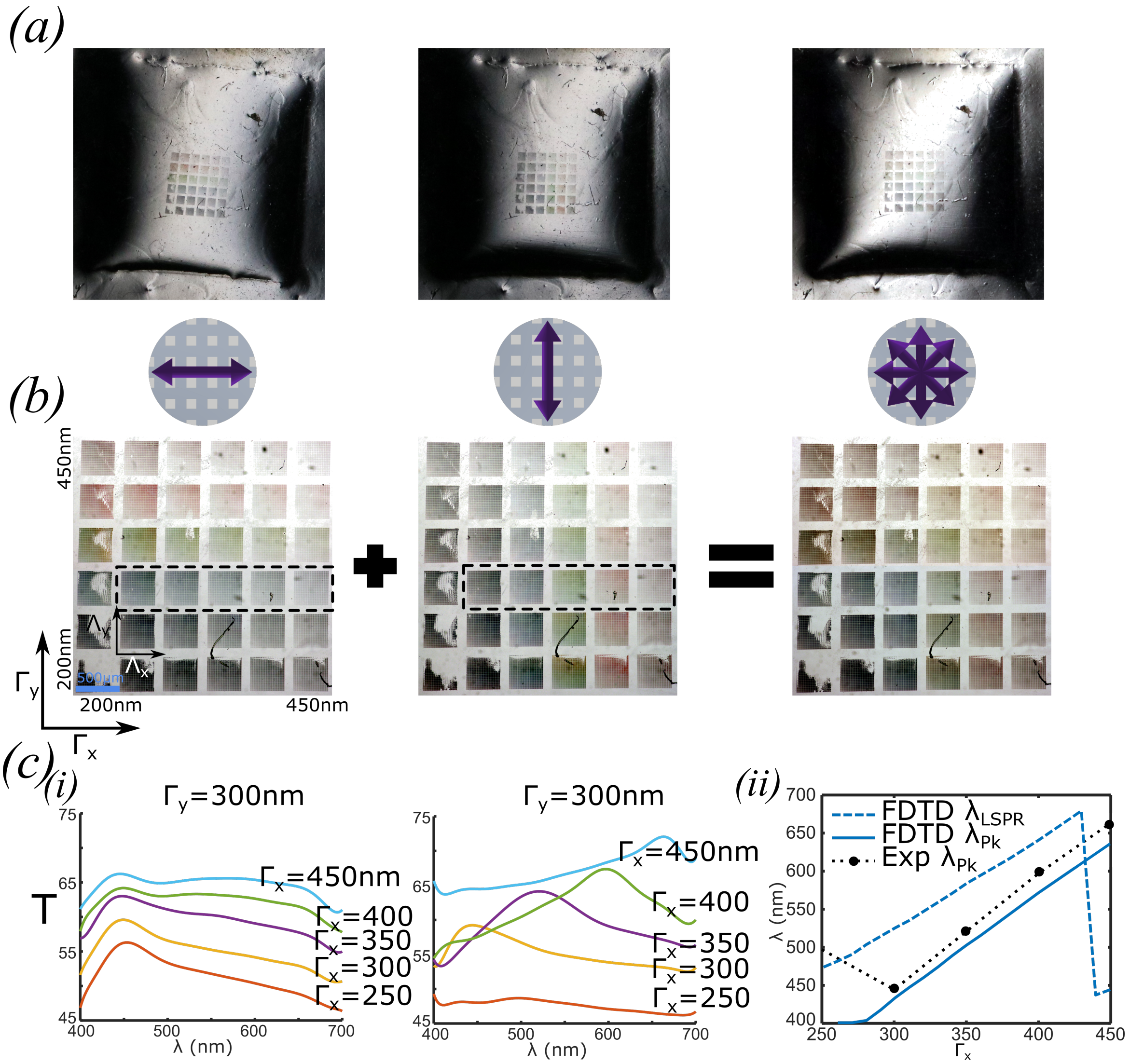

Figure. 5.13 Photos and measured spectra of Al nano-rod array in PDMS under x,y and un-polarised illumination and measured transmission spectra varying $\Gamma_{x,y}$. (a) DSLR camera photo of nano-rod array in PDMS, illuminated from behind by fluorescent tube lighting. x- and y-polarisation was provided by linear polariser on the camera lens. (b) Photos of Al nano-rod array in PDMS in polarising optical microscope setup, in transmission, under x-, y- and un-polarised illumination. Large grids vary $\Gamma_{x,y}$ by 50nm each grid step in corresponding direction. Large grids are divided into 20×20 small grids varying $\Lambda_{x,y}$ by 5nm per step in x- and y-direction. (c)(i) Transmission spectra of nano-rod array in PDMS large grids, highlighted by dashed box in (b) under x- and y-polarised illumination. (ii)Plot of peak transmission wavelength for FDTD modelled and experimentally measured spectra versus array periodicity in x-direction. Sample A used for images and data.

dip seen. Furthermore the illumination beam not being a perfect plane wave, as well as the surface roughness of the metallic nano-rods and the PDMS through which the light must travel may also act to broaden the LSPR resonance dip. A good indicator the LSPRs are occurring are the colour variation across the large grids of nano-rods in figure 5.9 within which the periodicity of the nano-rod arrays are consistent but the size of the nano-rods is varying.

5.4.3 Mechanical deformation of fabricated nan-rod arrays in PDMS

Fixing the PDMS substrate into the custom made mount described in section 5.3 the nano-hole array was mechanically deformed. Figure 5.14 shows the fabricated Al nano-rod array under x and y-polarised illuminated, under no strain, $\epsilon = 0\%$, and under an applied strain of $\epsilon = 15\%$ in the y-direction. First considering the substrate when the strain is applied perpendicular to the axis of polarisation of the illuminating light the FDTD modelled results suggest we would expect to see a significant shift of colours of the nano-rod array. This is in fact what occurs. When $\epsilon = 0\%$ and under x-polarised illumination the rows of large grid with colour are $\Gamma_y = 300$nm (blue), $\Gamma_y = 350$nm (green) and $\Gamma_y = 400$nm (blue). Under a strain of 15%, these approximate periodicities shift down a row of the image, and with the change of periodicity the colour shifts with it.

When the strain is applied in the same direction as the polarisation of illumination, the FDTD modelled results suggest that no colour change should occur. Looking at figure 5.14 for y-polarised illumination this is in fact the case. As a strain is applied in the y-direction there is no change in the colour of the nano-rod grids.

Figure 5.15 looks at the change in colour in more detail. The figure shows the normalised spectra of three Al nano-rod arrays, as strain is applied to the PDMS substrate. The nano-rod array is illuminated with y-polarised light, with the strain applied along the x-axis. The spectra is normalised such that the peak transmission under each level of strain is comparable. As the PDMS substrate is placed under strain the periodicity of the nano-rod array increases. The normalised spectra is annotated with its corresponding periodicity, and colour coded to correspond with their initial periodicities. As the strain is increased perpendicular to the direction of polarisation of illumination the transmission peak increases and the colour of the nano-rod array

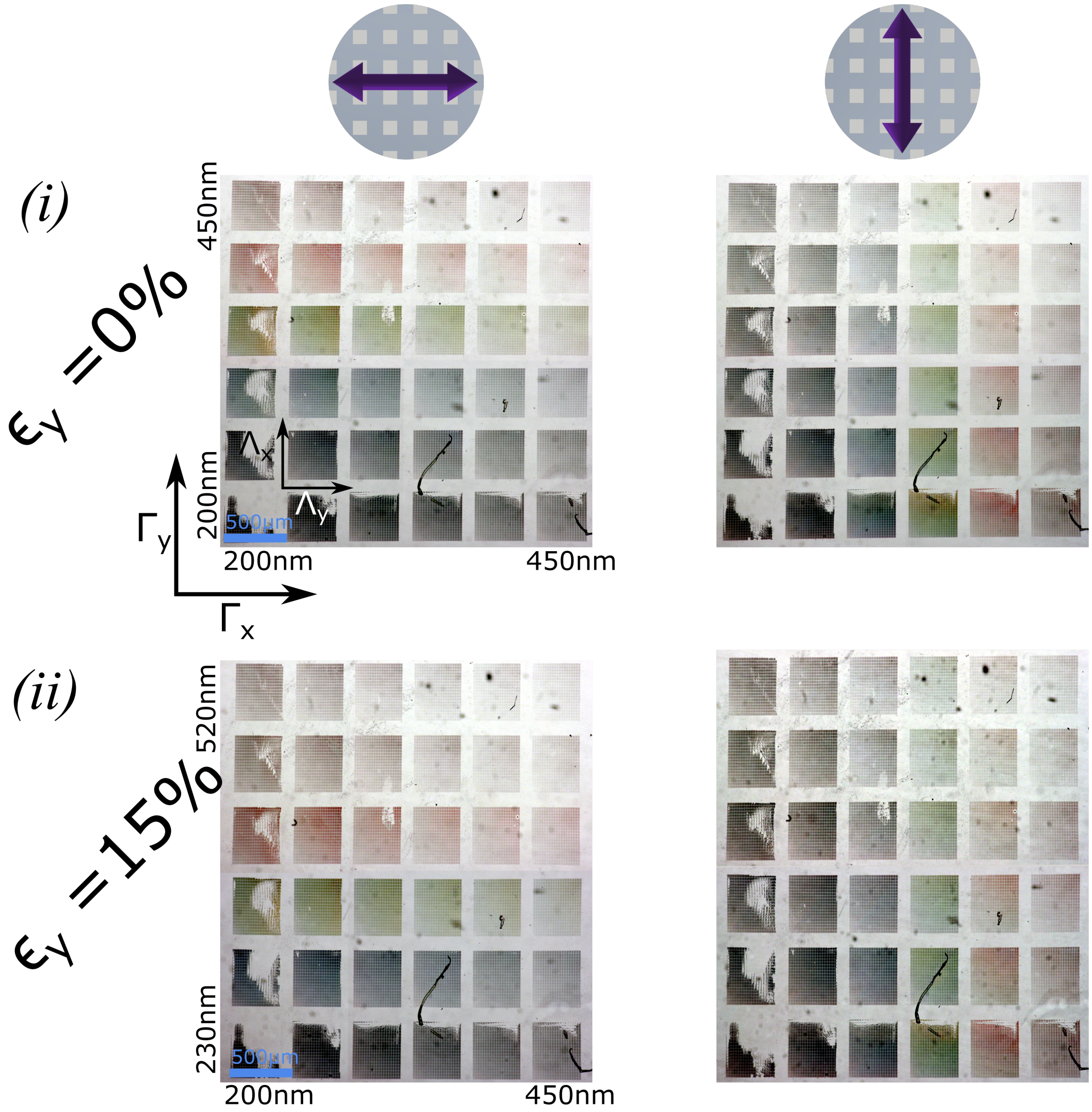

Figure. 5.14 Photos of un-stretched and stretched Al nano-rod array in PDMS illuminated with x- and y-polarised light in transmission with strain applied in the y-direction of (i) $\epsilon_y = 0\%$ and (ii) $\epsilon_y = 15\%$. Under x-polarised illumination the strain is applied perpendicular to the polarisation of illumination and the colour of the grids shifts. Under y-polarised illumination the strain is applied parallel to the polarisation of illumination and, in agreement with FDTD modelled results, there is no shift in colour of the nano-rod arrays. Sample A used for images and data.

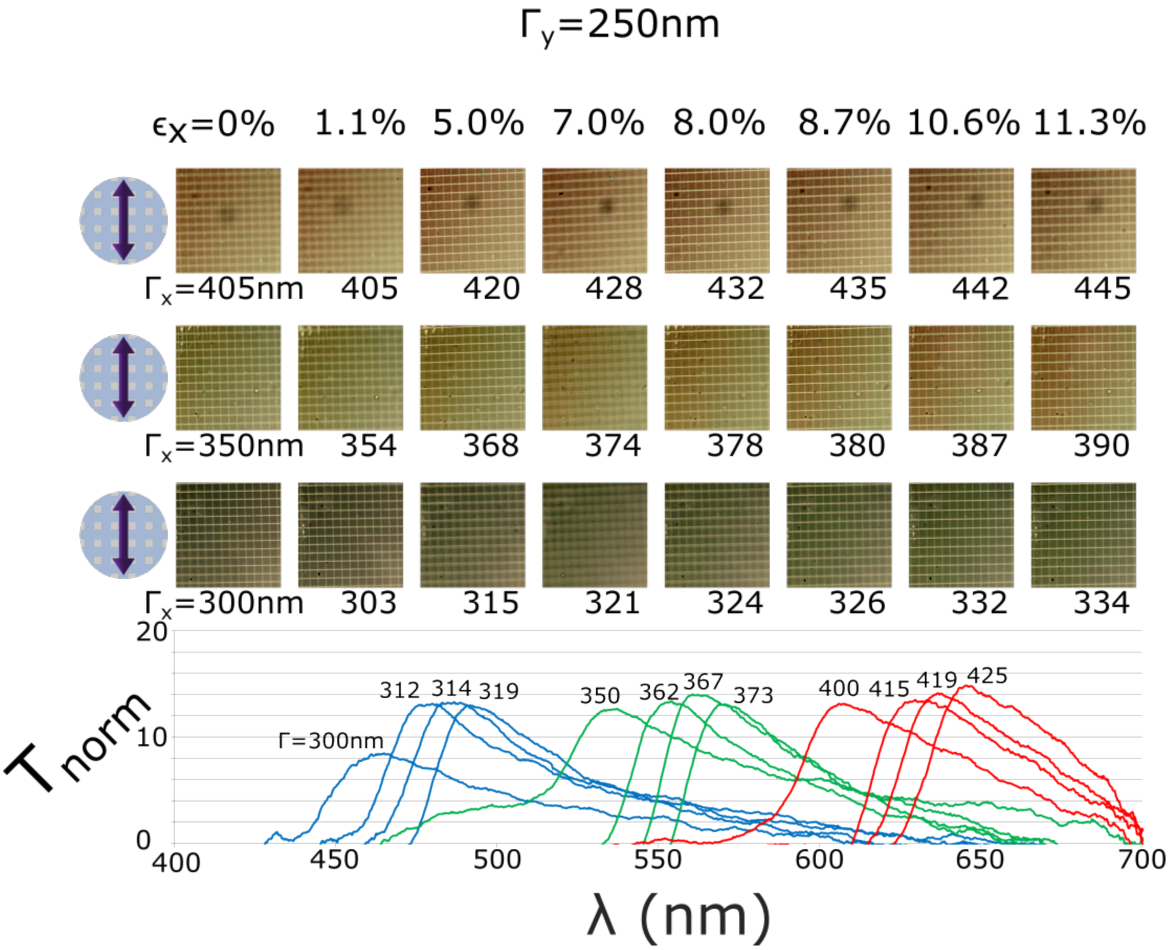

Figure. 5.15 Photos and corresponding normalised spectra of Al nano-rod array in PDMS under varying strain. Illumination is y-polarised whilst strain is applied in the x-direction. Transmission spectra is normalised so that peaks have similar magnitudes. Transmission spectra and array images are labelled with new periodicity of the nano-rod arrays under the applied strain.

is modulated with blue gradually turning to green, green to red, and red staying red until the transmission peak moves beyond the visible range.

The PDMS substrates with nano-rod arrays may also be viewed in reflection. The FDTD simulated reflection spectra of a nano-rod array in PDMS, illuminated with un-polarised light, varying the periodicity in the y-direction, is shown in figure 5.16(a). The reflection spectra is essentially the inverse of the transmission spectra, suggesting the absorptions from the nano-rods in the visible is small. Photos of the nano-rod array in reflection, with and without a strain applied are shown in figure 5.16(b). There is reasonable reflection from the surface of the PDMS substrate making it difficult to image the nano-rod array, whilst also where the transmission was particularly high (e.g.

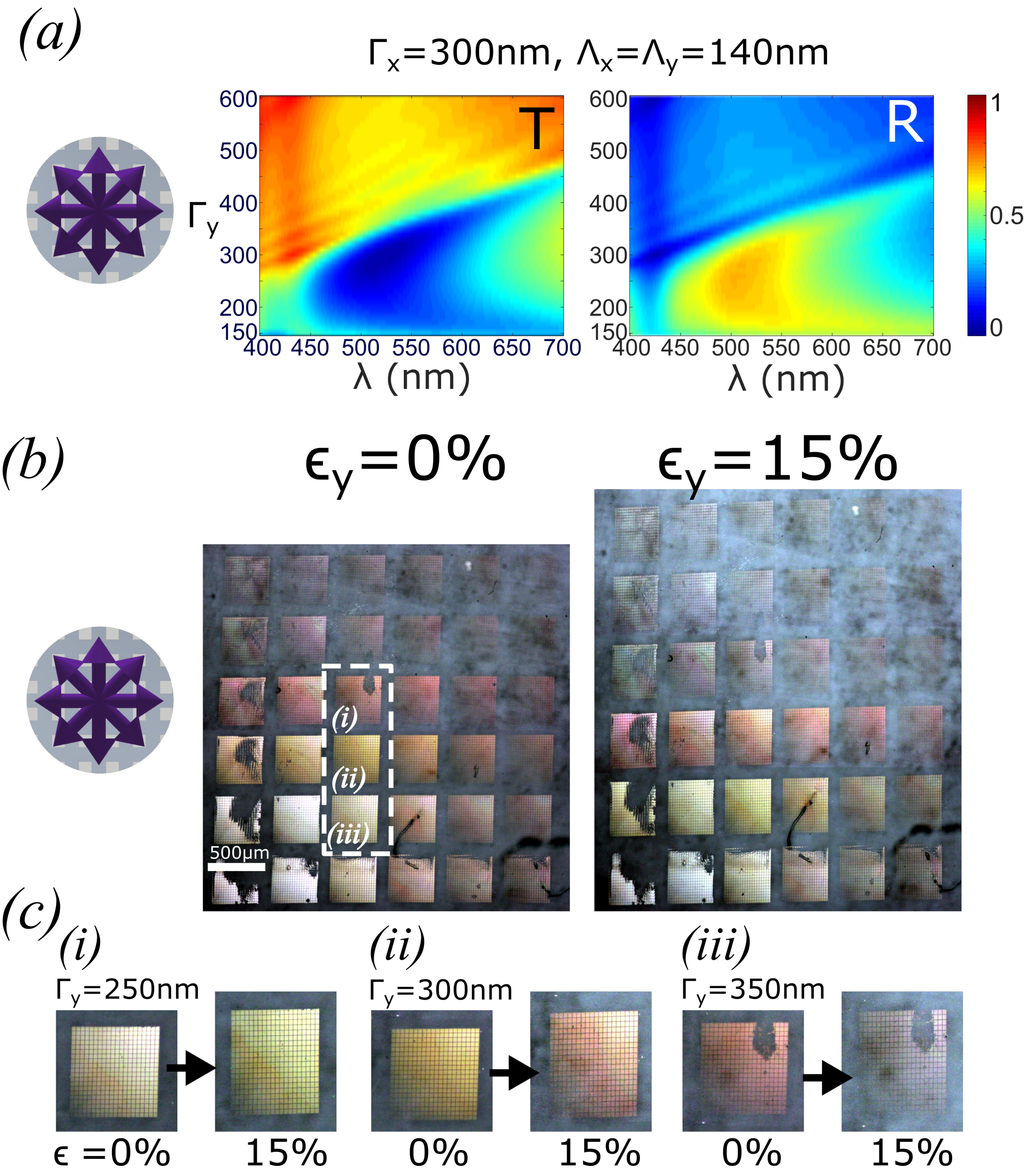

Figure. 5.16 (a) FDTD simulated transmission and corresponding reflection spectra of nano-rod array in PDMS. (b) Photos of un-stretched and stretched Al nano-rod array in PDMS illuminated with x- and y-polarised light in reflection with strain of $\epsilon_y = 0\%$ and $\epsilon_y = 15\%$. (c) Enlarged images of selected nano-rod arrays to highlight colour change upon applied strain. Sample B used for images and data.

at the largest periodicities), the reflection is extremely low. At $\Gamma_y = 300$nm there is a clear yellow colour, whereas in transmission it was blue and at $\Gamma_y = 350$nm where in transmission the colour was green, in reflection there is a deep red. When the PDMS array is stretched, as with the array in transmission the colours shift with the change in periodicities.

5.5 Dynamic plasmonic lens

Various methods have been used to create lenses with actively controlled focal lengths at a micron-scale including elastomer-based tunable liquid-filled micro-lens arrays[140], electro-capillarity in order to control the shape of a transparent drop edge [141] and a variable focal length binary Fresnel zone plate, constructed from carbon nano-tubes (CNTs) embedded in an elastomeric medium[96].

When attempting to miniaturise lenses, flat optics have numerous advantages over the traditional curved surface lenses. Shrinking traditional lenses may lead to undesirable optical properties such as small numerical apertures, spherical aberrations and fabrication complications at micron scales. Diffractive flat optics on the other hand are flat, thin and can achieve high numerical-aperture (NA) focusing without spherical aberration[83, 20].

A binary amplitude Fresnel zone plate (FZP), with alternating opaque and transparent zones, uses structured patterns to spatially modulate the intensity distribution of the light passing through, focusing incident light to a single spot via diffraction. FZPs on PDMS have been shown to achieve a wide field of view while maintaining control of the imaging depth, by fabricating a micro-lens array on a flexible substrate so that they can be dynamically reconfigured into different forms[135].

Using plasmonic nano-rods as scattering elements it is possible to fabricate a FZP with nano-rods occupying the opaque zones of the lens. Given the effective scattering area of a nano-rod is larger than its physical dimensions, it is possible to construct the opaque zones of a FZP with nano-antenna with dead space between the physical structures whilst the incident radiation sees a continuous surface. Furthermore, when the FZP, fabricated from nano-rods is embedded in an elastomeric medium such as PDMS, is stretched, despite the increase in dead space between scattering elements the incident radiation will still see a continuous opaque zone.

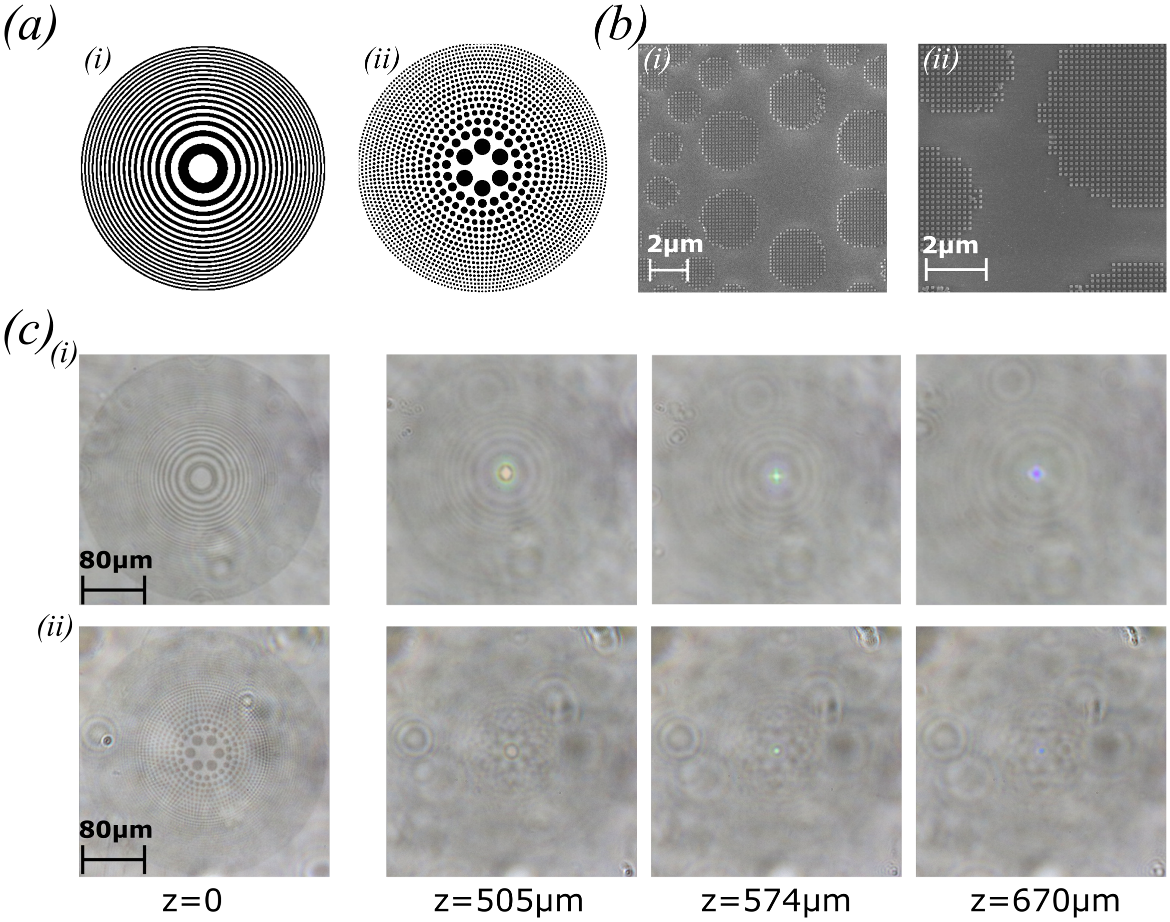

Figure. 5.17 Fresnel zone plate (FZP) and photon sieve (PS) design and fabrication. (a) FZP (i) and PS (ii) patterns generated via MATLAB. (b) SEM images of EBL fabrication of PS on Si chip prior to PDMS transfer. Dark zones are pixelated with nano-rods. (c) Optical microscope images of (i) FZP and (ii) PS in transmission post transfer to PDMS. Images are taken with the focal plane of the microscope setup at the plane of the lenses and at the red, green, and blue focal lengths of the lenses.

5.5.1 Design

The flat lenses utilised in this work are traditional FZPs and photon sieves. A photon sieve (PS) is essentially a FZP in which the rings have been broken up into isolated circles. Both FZPs and PSs can be thought of as unique holograms with a singular spot in centre of the replay field. The patterns of a FZP and PS are shown in figure 5.17(a)

For an infinite conjugate, binary FZP of focal length f at wavelength λ, the radial distance to the centre of the nth bright zone is given by[101]

$$r_n^2 = 2nf\lambda + n^2\lambda^2 \tag{5.4}$$

with the area covered by each zone totalling $\pi\lambda f$. To convert the FZP into a PS, the continuous zone is replaced by a set of circles, whose centres lie evenly spaced on circle with radius r_n and whose total area equals $\pi\lambda f$, so that the area covered by a zone of either a FZP and PS are equal.

When a strain, ϵ, is applied to the lens so that it is increased in size by a factor $s = (1+\epsilon)$ such that $r'_n = sr_n$ the new focal length, f_1, is related to the original focal length, f_0, by

$$f_1 \approx s^2 f_0 \tag{5.5}$$

Hence should a lens be fabricated using nano-rod scatterers for the opaque zones, in a pliable medium, it should be able to actively tune the focal length of the lens by mechanically deforming its dimensions

5.5.2 Fabrication

To fabricate such a lens first a pattern file is required. To generate the zoned pattern MATLAB is used following equation 5.4. An example of the pattern files generated are shown in figure 5.17(a). The pattern is then split into pixels. Again using MATLAB code, each pixel has a nano-rod placed at its centre and an EBL pattern file is generated. The pattern file is used for EBL following methods outlined in section 3.2.1. Following EBL, nano-rod structures in either a FZP or PS pattern are now on a Si chip ready to be transferred. An example of the nano-rods on top of resist pillars ready to be transferred to form a PS are shown in figure 5.17(b). The SEM images show how the opaque zones of the PS has been split into pixels with a nano-rod scattering element in the centre of each pixel. The nano-rods are then transferred into the PDMS following methods outlined in section 5.2. The result is a flat lens, whose size may be mechanically altered to dynamically change the focal length of the lens. DSLR camera images of both a FZP and a PS are shown in figure 5.17(c). The images show the structure of the lens at $z = 0$, and images of the focal points at the red, green and blue focal lengths.

5.5.3 Dynamic focal length by mechanical deformation

The tunable lenses having been fabricated in a PDMS substrate, the substrate was mounted in the custom mount describe in section 5.3. The mount was placed into the custom optical setup described in section 3.4.2. The setup allows the DSLR camera to focus at different focal planes along the direction of propagation (z axis). Photos were taken at regular intervals along the z axis, and then processed to provide a 3D image of the propagation of light energy. The red, green and blue components of light were determined using the RGB sensors in the detection array of the DSLR camera. Photos were taken at strains of $\epsilon = 0\%$ and $\epsilon = 12\%$. The results are shown in figure 5.18. The figure shows a 3D plot for each colour component of light, and an accompanying slice at in the lens plane and z-slice showing the optical power as light propagates through the lens to the focal point. As expected the red component, having the longest wavelength has the shortest focal length, followed by the green and then blue component of light. The plots for the strained and un-strained lens show a significant shift in focal length. According to equation 5.5, for a strain of $\epsilon = 12\%$, you would expect a shift of $\sim 25\%$ in the focal length. The red focal point shifts from 505μm to 625μm ($\sim 24\%$), green from 575μm to 710μm ($\sim 24\%$) and blue from 670μm to 840μm ($\sim 25\%$), all in line with expectations, given experimental error.

Table 5.2 Strain (ϵ) v Focal Length (FL) of FZP v Expected change in FL (ϵ^2)

Strain, ϵ (%)	FL(μm)	ΔFL (μm)	ΔFL (%)	ϵ^2
0.0	505	0	0	0
2.0	521	15	3.0	4.0
6.3	574	69	13.6	13.0
9.3	605	99	19.6	19.4

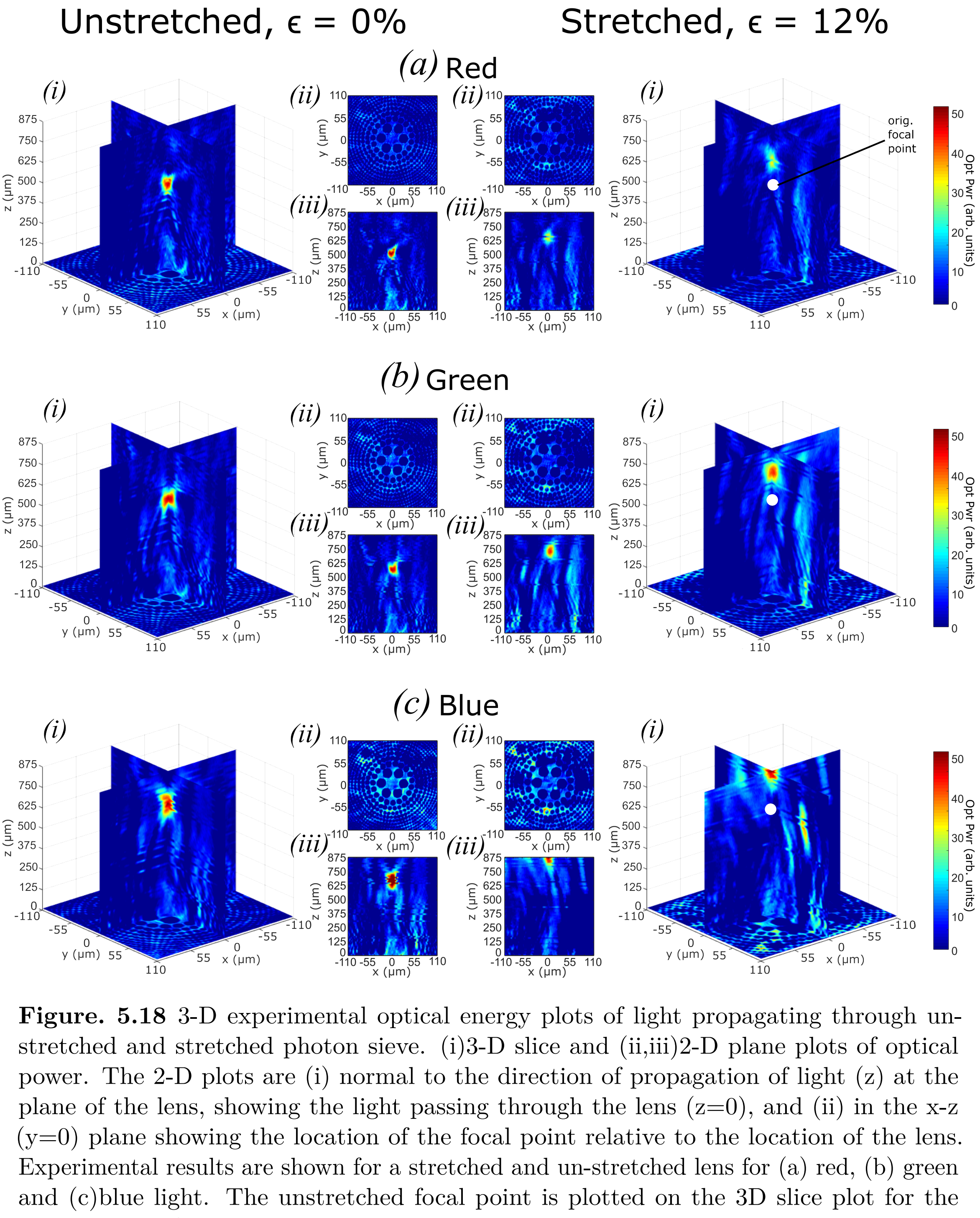

Figure. 5.18 3-D experimental optical energy plots of light propagating through unstretched and stretched photon sieve. (i)3-D slice and (ii,iii)2-D plane plots of optical power. The 2-D plots are (i) normal to the direction of propagation of light (z) at the plane of the lens, showing the light passing through the lens (z=0), and (ii) in the x-z (y=0) plane showing the location of the focal point relative to the location of the lens. Experimental results are shown for a stretched and un-stretched lens for (a) red, (b) green and (c)blue light. The unstretched focal point is plotted on the 3D slice plot for the stretched lens for comparison.

To provide further experimental rigour the table 5.2 shows how the focal length of a PS changes for different value of strain, with the results following the trend predicted by equation 5.5.

5.6 Stretchable Holograms

By utilising the optical scattering properties of plasmonic nano-rods it is possible to create holograms using metallic nano-rods as the fundamental unit of the holograms pixels. The advantages of using nano-rod scatters for holographic applications include the sub-wavelength dimensions of the structure allowing for extremely high pixel densities, and wavelength and polarisation dependency of the scattering from a nano-rod opens up possibilities for wavelength and polarisation sensitive pixels[12]. Whilst the wavelength sensitivity of an isolated nano-rod is dependant on it dimensions, when placed in close proximity to other nano-rods, such as in an array, the wavelength dependency of the scattering becomes a function of the proximity between nano-rods. Thus if one could alter the spacing between nano-rods within a hologram pixel, it could be possible to alter the wavelength sensitivity of the pixel, altering its scattering cross section, with the ultimate aim to be able to switch a pixel on or off. Hence it could be possible to design a hologram with such pixels that, upon mechanical deformation, the replay field of the hologram changes.

The first challenge to overcome however, is to fabricate a plasmonic hologram whose dimensions may be altered post fabrication.

According to scalar diffraction theory the pixel pitch of a hologram, α, is related to the pixel pitch of the replay field, Δ, by[49]

$$\alpha = \frac{D\lambda}{\Delta} \tag{5.6}$$

where D is the distance from the hologram pixel to the replay field pixel. Thus the size of the replay field pixels are inversely proportional to the size of the hologram pixels. If a hologram can be created in an elastomeric medium, stretching the hologram will result in shrinking of the replay field.

5.6.1 Design and fabrication

To create a stretchable hologram on an elastomeric medium, plasmonic scattering elements are not in fact required. By nano-imprinting the surface of PDMS, the pattern surface structure will scatter light due to the change in refractive index. The surface structure is shown schematically in figure 5.19(a). An SEM image of the surface covered with a thin layer of metal to allow for imaging is also shown in figure 5.2.

The holograms are designed using the algorithm outlined in section 2.1.2.2. The binary hologram is converted into a nano-imprint pattern using MATLAB to place a scattering element at the centre of each pixel with a value of 1, and no scattering element for pixels with a value of 0.

Phase only PDMS hologram To create holograms with a structured PDMS surface only, the hologram pattern is fabricated via EBL methods using a positive tone resist. The patterned resist, which if we were fabricating nano-rods on a Si chip would have metal deposited on it and then sacrificed, is instead coated in liquid PDMS which is then cured. The PDMS does not bond to the polymer, but does mould to the surface structure, resulting in the hologram pattern being imprinted on the surface topology of the PDMS. Figure 5.19(a,i) shows a microscope light field image of the surface. As the scattering structures are sub-wavelength they may not be viewed with an optical microscope, but due to the scattering nature, the patterned area appears darker than the surrounding relatively smooth surface. The scattering effect of the structures can be shown by viewing the structured PDMS surface in the dark-field, shown in figure 5.19(a,iii). Under dark field illumination, the un-scattered light beam is excluded from the image, hence scattering elements appear light. Unlike plasmonic scattering elements, the structured dielectric surface has no polarisation dependency, hence under cross polarisers no light will be transmitted. The PDMS only hologram works by altering the phase of the incoming light. Where there is a PDMS structure patterned on the surface the light has a further distance through the PDMS, hence its phase is retarded compared to the light which does not travel through a patterned PDMS structure. The light of different phases then interferes to create the far field pattern. The hologram is designed using binary phase, which may also act as a binary amplitude hologram, hence the singular hologram design can be used for a structured PDMS surface hologram and one consisting of nano-rod scattering elements.

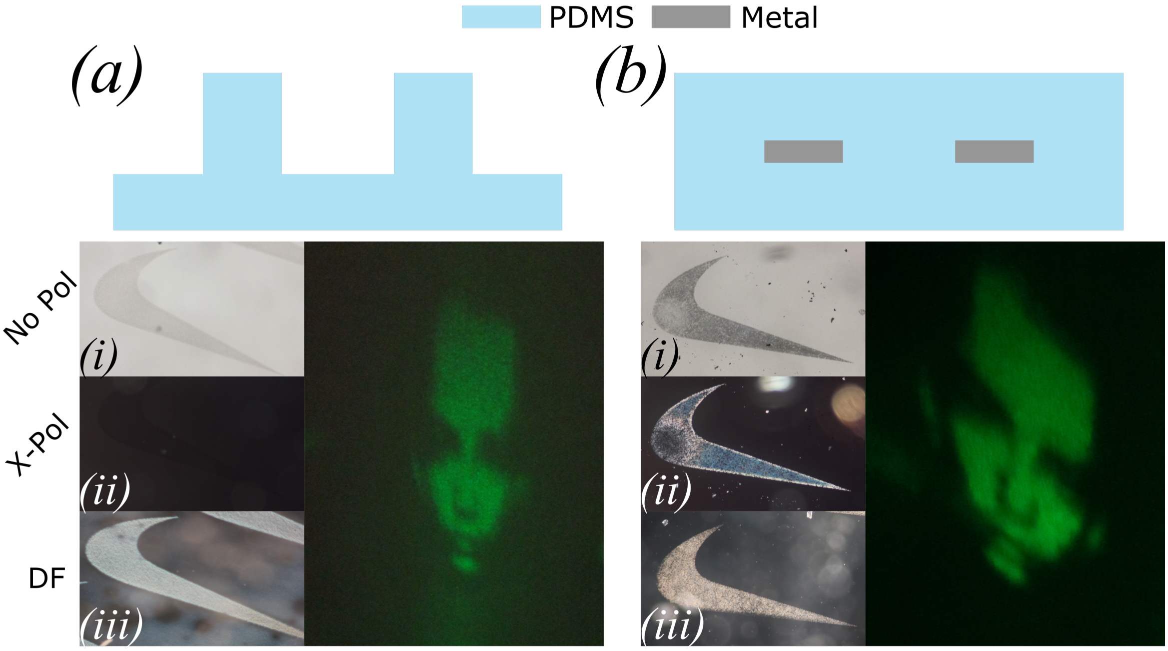

Figure. 5.19 Holograms via dielectric and metallic scatterers. Schematic of imprinted PDMS surface (b) and metallic scatterers embedded within PDMS (b). Polarising optical microscope images of hologram fabricated via imprinting of PDMS surface and metallic scatterers embedded in PDMS in transmission viewed in (i) light field with no polarising optics, (ii) light field between crossed polarisers and (ii) in dark field. Replay field of respective holograms are also shown under illumination with green laser pointer.

Amplitude only nano-rod in PDMS hologram To create a stretchable hologram, using plasmonic scattering elements as the pixels of an amplitude only hologram, in PDMS the methods outlined in section 5.2 are used. The pattern to be transferred is created using CGH techniques, and then patterned using EBL methods using a negative tone resist on a Si chip. The developed pattern has metal evaporated onto the structure which is then transferred to the PDMS substrate and encapsulated. A schematic of the embedded nano-rods is shown in figure 5.19(b). Light and dark field images of the hologram are shown in 5.19(b,i,iii). The nano-rods' scattering elements were $\Lambda_{x=y} = 150$nm in size. The scattering elements were not designed to have any particular wavelength dependency, hence under white light illumination in an optical microscope setup the nano-rod arrays appear as a dark area. The scattering from the nano-rods is greater than from the structured dielectric surface, as shown by the dark patterned area in the light field images and the lighter patterned area in the dark field image. Whilst the nano-rods were not designed to have any particular polarisation dependency, the rectangular shape of the nano-rods will mean that light is scattered polarised along the nano-rods axes, hence when the hologram is placed between crossed polarisers with the elements orientated away from the polarisers polarisation axes, the scattered light may be seen, as shown in figure 5.19(b,ii)

The replay field of the two holograms is also shown in figure 5.19. The dielectric hologram has a lower efficiency than the plasmonic hologram, as demonstrated by the sharper image and lower background colour of the images shown.

5.6.2 Dynamic replay field by mechanical deformation

To mechanically deform the holograms the PDMS substrate with hologram pattern embedded was mounted in the custom mount described in section 5.3. A visibly clear way to show the effect of altering the pitch of holograms is shown in figure 5.20(a). The replay field is an image of a person. When the hologram is stretched vertically, the height of the person decreases. The decrease in height can be quite significant. The grid shown in the images are 3cm×3cm and there is a decrease in height of the image of $\sim 30\%$ upon vertical deformation of the hologram.

The same process was repeated for a replay field of 11×11 dots shown in figure 5.20(b). The change in size of replay field is less visibly obvious however measurements of the change of size of replay field for a change in size of hologram pixel pitch is shown in figure 5.20(b). The trend follows that expected from equation 5.6. The stretch of the hologram pixels was measured using the movement of the clamps of the custom mount. The actual strain of the hologram will be proportional to these values as the strain will not act evenly through the PDMS. Experimental error bars plotted in figure 5.20(b) are quantified using the error in measurement of the distance between dots in the replay field using processed images of the replay field.

5.6.2.1 Dynamic composite scattering elements

Having established that a hologram comprising of nano-rod scattering elements may be fabricated in an elastomeric substrate and mechanically deformed, the next task is to design a hologram whose replay field not only changes in size but whose image also changes.

One way that has previously been utilised is to design a a hologram with a 3D replay field. The 3D replay field consists of different images at different focal planes.

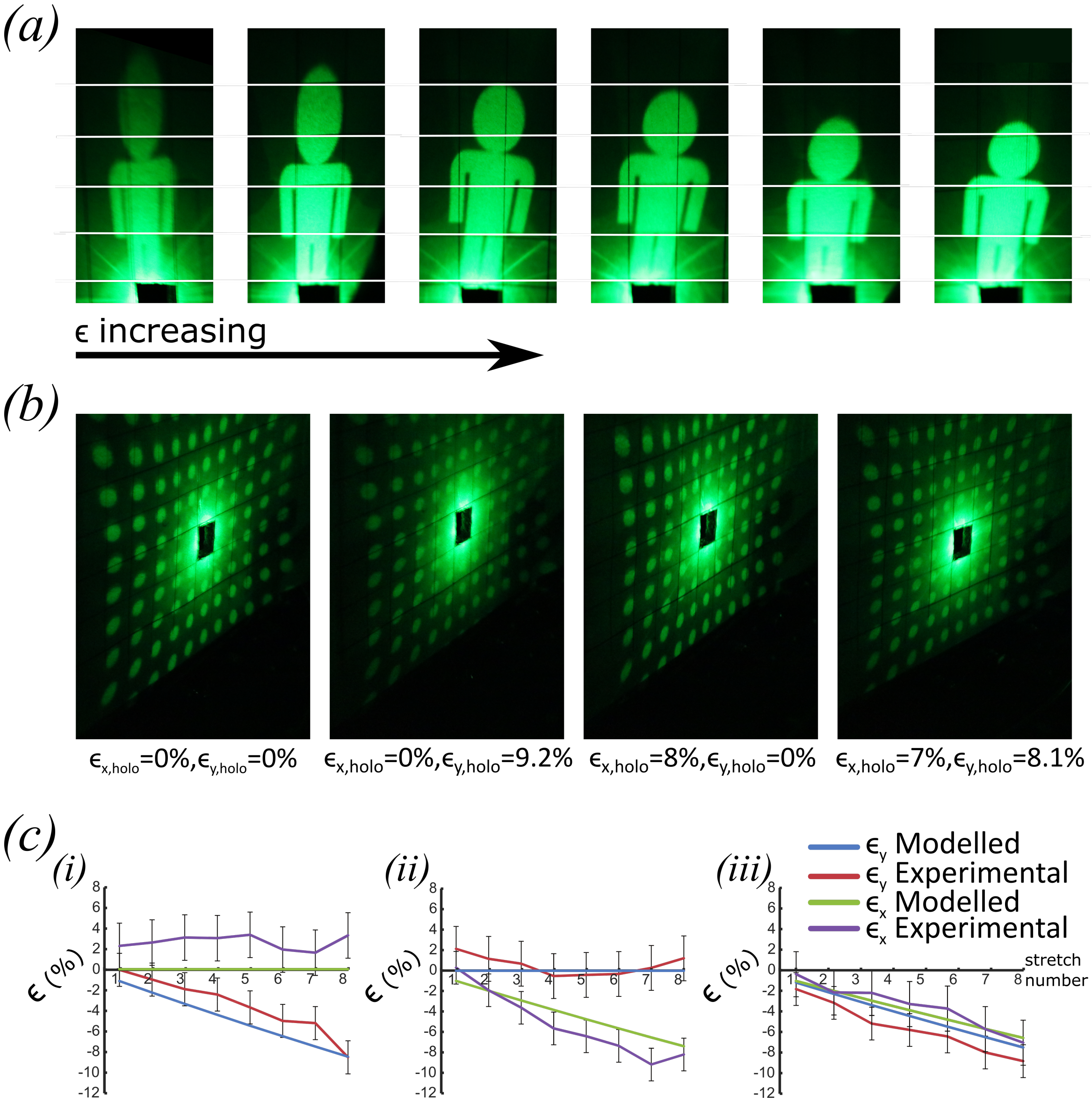

Figure. 5.20 Stretching plasmonic holograms. (a) replay field of hologram fabricated using metallic scattering elements embedded in PDMS, showing an image of a man. An increasing strain is applied to the physical hologram resulting in modification of the replay field and a shrinking of the man. (b)replay field of hologram fabricated using metallic scattering elements embedded in PDMS, showing a uniform array of dots. Strain is applied to the physical hologram in x-, y- and both x- and y-directions simultaneously altering the dimensions of the replay field. (c) Experimentally measured versus expected change in size of replay field, ϵ, for strain applied to the physical hologram, in x- , y- and both x- and y-directions simultaneously. Graphs shows change in respective strain for 8 different strains applied to the physical holograms.

By placing a camera a set distance away, and altering the size of the physical hologram, the plane of the replay field that is at the camera plane is altered and the replay field image changes[134].

Here we present a new plasmonic scattering pixel. The pixel is shown schematically in figure 5.21(a). Comprising of 4 individual scattering elements in a rectangular arrangement. The nano-rods are equally sized with x- and y-dimensions of $\Lambda_{x,y}$. Whilst the individual nano-rods have their own resonant wavelengths, when brought into close proximity the interaction between the E-fields of each individual nano-rods creates a different composite pixel resonance. This scattering resonance depends on the spacing between the nano-rods in the x- and y-directions ($\Psi_{x,y}$). Thus when embedded in an elastomeric medium such as PDMS, when the substrate is stretched, the spacing between the 4 nano-rods is altered and the resonant wavelength of the composite pixel is altered.

The FDTD simulated scattering from a pixel with $\Lambda_x = 60$nm, $\Lambda_y = 100$nm and $\Psi_y = 80$nm, whilst varying Ψ_x is shown in figure 5.21(a). The composite pixel consists of Al nano-rods as this is the material that is currently compatible with the PDMS patten transfer process developed. The dimensions of the individual nano-rods is chosen such that under x-polarised illumination there is minimal scattering whilst under y-polarised illumination there is scattering in the visible wavelength. The dimensions were chosen as such so that the pixels will operate under un-polarised illumination. As there will only be a y-polarised resonance there will be no cross-talk from an x-polarised resonant mode.

By varying the spacing in the x-direction, by applying a strain to the PDMS substrate, the resonant wavelength in the visible spectrum will be modified. If the hologram is illuminated with a green laser of wavelength, $\lambda \sim 530$nm, by fabricating a pixel with $\Psi_x = 80$nm, under no application of strain the pixel will have low scattering. Applying a strain of $\sim 100\%$, the spacing of of the nano-rods within the composite pixels become $\Psi_x = 160$nm, where the scattering at $\lambda = 530$nm is high. Likewise, we can fabricate a pixel whose spacing $\Psi_x = 160$nm under no application of strain, and hence has high scattering at $\lambda = 530$nm. When a strain of $\sim 100\%$ is applied, the x spacing becomes $\Psi_x = 320$nm and the scattering of the composite pixel at $\lambda = 530$nm becomes low. In this way pixels whose scattering may be switched under strain have been created. To include in a hologram, single non-composite scattering elements with high and low scattering may be used for non-variable pixels. Hence two holograms may

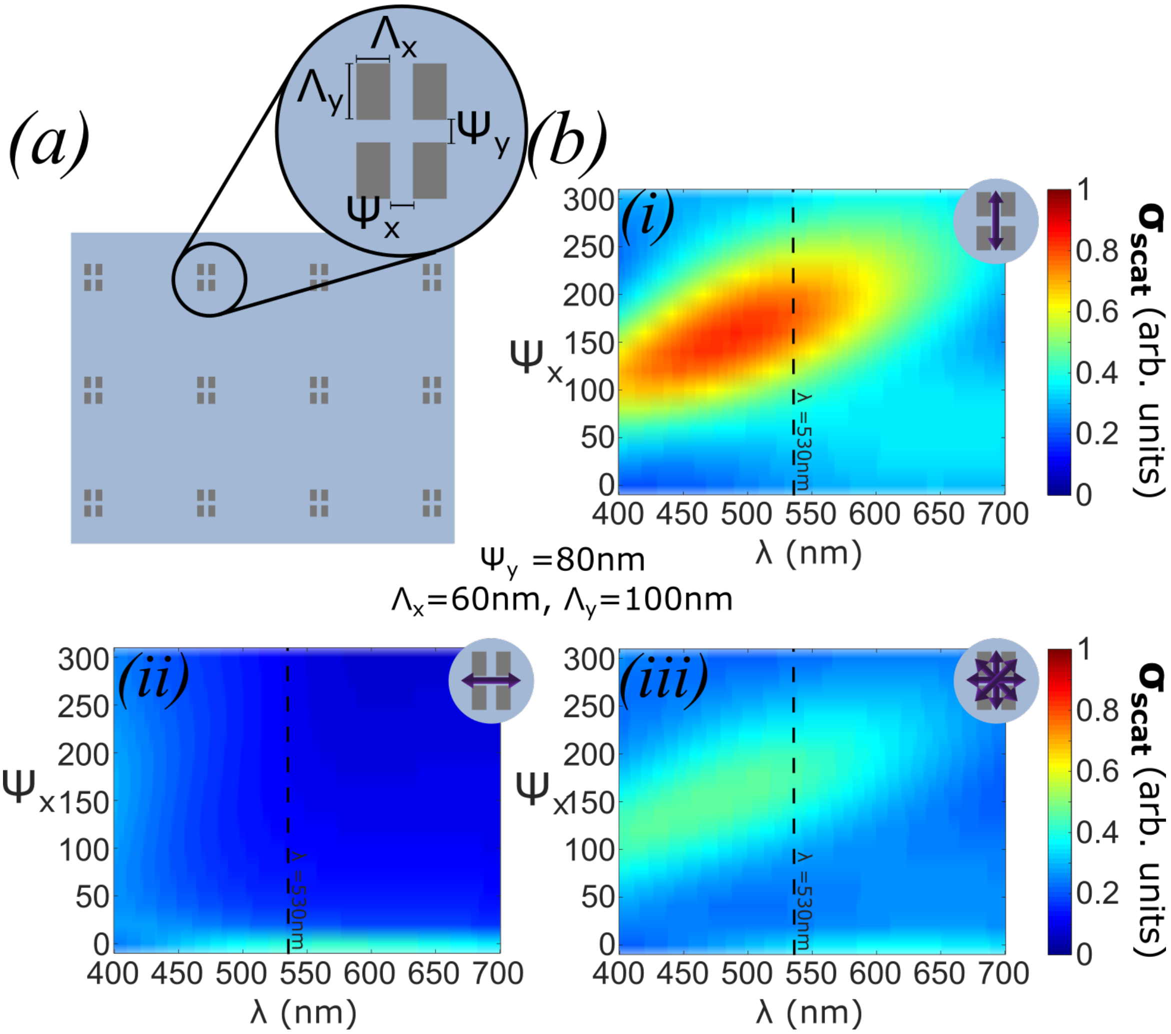

Figure. 5.21 Composite scattering elements for dynamic holographic pixels. (a) Schematic for composite scattering pixels in PDMS. Each individual composite scattering pixel is comprised of four nano-rods of szie $\Lambda_{x,y}$, in a grid arrangements with spacing of $\Psi_{x,y}$. (b) Spectra for composite pixel under (i) y-, (ii) x- and (iii)un-polarised illumination, with nano-rods of size $\Lambda_x = 60$nm, $\Lambda_y = 100$nm and spacing $\Psi_y = 80$nm. The size of the x-spacing (Ψ_x) is varied whilst holding all other dimensions constant. The vertical line indicated the wavelength of a typical green laser ($\lambda = 530$nm).

be multiplexed into a hologram whose scattering pattern change under application of a strain, and hence the replay field will be altered.

The design so far has not taken into account size limitations of the fabrication process. Currently scattering elements of size $\Lambda_x = 60$nm, $\Lambda_y = 100$nm are not achievable with ma-N 2405 negative tone resist being used in the fabrication process. As such before the composite pixels may be fabricated and tested, more work is needed to develop the pattern transfer process to enable even smaller nano-rods to be embedded into an elastomeric substrate. Furthermore due to the smaller scattering element size of Ag nano-rod, smaller pitch of composite pixels, with narrower spectra scattering peaks, may be achieved, however once again more work is needed to adapt the pattern transfer process to alternative metals.

5.7 Summary

In this chapter a process for fabricating aluminium nano-rod structures embedded in PDMS was presented. The process is similar to previously developed processes for the transfer of metallic nano-structures to PDMS, but is simpler for the fact that no plasma treatment step is needed. The process can transfer nano-particles down to 100nm in size with a pitch as low as 200nm. The size limitation found in the work is the same as the feature size limitation of the patterning recipe and may not be due to limitations of the transfer process itself, but of the resist used in the EBL fabrication process. The process is currently only suitable for aluminium due to excess metal that is transferred during the process. This may easily be removed with a soak in a Decon90 bath, which dissolves the excess metal, leaving the PDMS and embedded nano-rods unharmed. The process may transfer other metals but a suitable bath needs to be found to dissolve the excess transferred metals before the process is suitable.

The process is used to create nano-rod structures whose optical properties may be altered by mechanically deforming. Those highlighted in this chapter are structural colour from nano-rod arrays, a tunable focus flat lens and plasmonic holograms. The mechanical deformation is performed using a custom sample mount fabricated for this work.

The design of structural colour using nano-rods embedded in PDMS is summarised and compared to that created by nano-hole layers in Chapter 4. The nano-rod arrays were fabricated in PDMS and characterised using a polarising optical microscope setup, with and without a strain applied. The patterns showed a significant shift in colour due to mechanical deformation that fitted well with the FDTD simulated spectra.

The flat lenses utilised were a Fresnel zone plate and a photon sieve. The lenses focus light using transparent and opaque zones to diffract light to a single point at the focal length. The transparent and opaque zones are circular, and it is the physical size and spacing of the zones that determine the focal length. Using plasmonic nano-rod scatters as the fundamental elements of pixels comprising the opaque zones, flat optical lenses were fabricated in PDMS. The focal length and optical power along the axis of light propagation were recorded using a custom optical setup, with and without strain applied to the lens. The change in focal length due to mechanical deformation was proportional to the square of the strain applied as theory predicts.

Lastly the fabrication process was used to create holograms embedded in PDMS that may be mechanically deformed. Aluminium nano-rods act as the fundamental scattering element of the hologram pixels. As the pitch of the holograms pixels is altered, so the size of the pixels in the replay field changes with an inversely proportional relationship. The ability to fabricate plasmonic holograms in an elastomeric medium opens up a myriad of opportunities to develop holograms whose replay field may change when the hologram is physically stretched, due to the wavelength, polarisation and proximity dependence of the plasmonic resonance of the nano-rods.

A new composite nano-rod pixel whose scattering resonance may be altered under mechanical deformation was presented. Whilst FDTD modelling shows promising results for the application of dynamic plasmonic holograms by the application of mechanical strain, the size of nano-rods required is smaller than that currently achievable using the pattern transfer process in its current form.

Chapter 6

Conclusions

6.1 Summary of findings

As visual display technologies strive to shrink pixel sizes, towards the ultimate goal of a *true* three-dimension (3D) displays, hardware innovations will need to keep pace. The work in this thesis aims to provide a means to contribute to the solutions of the challenges that remain. For example, in liquid crystal display pixel technologies, traditional pigment based colour filters are currently over an order of magnitude greater than the fundamental diffraction limit of visual displays. Structural colour, generated due to plasmonic resonances, offers a solution to this issue. The current state of the art plasmonic colour pixels are, however, static. That is to say, once fabricated their colour properties may not be altered. This work strives to design and fabricate dynamic plasmonic pixels. Specifically it looks at plasmonic pixels whose colour properties may be dynamically tuned to span the entire visible spectrum, or whose colour may be efficiently switched On/Off.

Furthermore, as pixels look to shrink beneath the diffraction limit, new pixel elements will need to be designed to meet the task. Electro-holographic displays require dense, highly functional and reconfigurable pixels. Plasmonic nano-structures have been demonstrated to provide a possible solution to the fabrication of this class of pixel, however, like plasmonic colour, current state of the art metasurfaces suffer from their static nature. This thesis looks at way to activate the plasmonic pixels. Specifically it identifies the potential of mechanical deformation, and endeavours to discover a means to fabricate plasmonic metasurface in a medium which may be mechanically modified. Such a process was developed to embedded plasmonic nano-structures into a elastomeric substrate with high spatial accuracy. Having developed this process its viability was determined by fabricating various flat optical devices, whose optical properties may be altered with mechanical deformation.

The following is a summary of the main conclusions from this work:

LC-Nanohole continuously tunable devices. Plasmonic resonances in metallic nano-structures may be used to create structural colour. One such set of nano-structures are arrays of rectangular nano-holes. Utilising surface plasmon polaritons (SPPs) excited by the grating structure of the nano-hole array and localised surface plasmon resonances (LSPRs) excited by the nano-holes themselves to tune the transmission minima and maxima respectively, the colour of a nano-hole array may be designated across the visible spectrum. The plasmonic modes excited by the nano-hole structure have the added benefit of polarising un-polarised illumination. In chapter *4* a plasmonic pixel whose colour may be tuned across the entire visible spectrum is designed and fabricated. By integrating the nano-hole structure with a liquid crystal layer and an output analyser orientated at 45° to the nano-hole lattice, a liquid crystal nano-hole (LC-NH) device was created whose spectral output spanned the visible spectrum. The LC retardance, modulated by the voltage applied across the cell, actively filters the light passing through the pixel in combination with an output analyser at 45° to the nano-hole lattice. The pixel design combines electrode, polariser and colour filter into a single ultrathin (< 40nm) Al nano-hole surface, reducing the dependency on separate sub-pixel components, such as pigment based-filters, for commercial display devices. In this way a dynamic plasmonic pixel whose colour, determined through an applied voltage between a nano-hole surface and ITO-glass electrodes, has been created.

LC twisted nematic cell with plasmonic grating. The colour of a plasmonic metasurface depends not only on the material and dimensions of the nano-structures, but also on the refractive index of the medium in which the nano-structures sit. Attempts to tune the refractive index medium around aluminium nano-structures using liquid crystals in ***chapter 4*** proved to be unsuccessful due to strong surface anchoring forces. However the strong surface anchoring forces that prevented the re-alignment of liquid crystal molecules close to the metal interface were instead exploited to use a metallic grating as a combined alignment layer, electrode and colour filter in a liquid crystal twisted nematic cell. Using a nano-scale metallic grating as one half of the twisted nematic liquid crystal cell, it is possible to construct a plasmonic pixel which may switch between light and dark states when placed between crossed polarisers. The vividity of the colour achieved with a nano-scale grating was lower than desired, but was improved by utilising a novel structure, fabricating two gratings, separated by a polymer layer. This structure improved the colour of the pixels by introducing further non-plasmonic resonant mechanisms into the structure. In fact the strongest colours were achieved when the grating was illuminated with light polarised parallel to the grating grooves, when no plasmonic resonances are able to be excited. Furthermore this pixel structure is directly comparable to modern liquid crystal display technologies, reducing the effort required for integration into a commercial device.

Nano-hole arrays on electro-optic substrates. Where liquid crystals were shown to be unsuccessful at tuning the plasmonic resonance of a nano-hole surface, an alternative avenue of utilising an electro-optic substrate, whose refractive index may be altered upon application of an electric field, was pursued. In ***chapter 4*** the potential of lithium niobate ($LiNbO_3$), one such substrate, was investigated using FDTD modelling. Following encouraging simulation results, a metallic nano-hole array on a $LiNbO_3$ substrate device was fabricated. Unfortunately no change in transmission spectra of the pixel was observed. The electric fields required to produce a refractive index change great enough to induce a colour shift in the nano-hole surface was prohibitively high, with safety and dielectric breakdown issues arising. The modelled result show that an electro-optic substrate is a feasible route for dynamic plasmonic colour pixels, however, an electro-optic material with a higher electro-optic coefficient is needed for practical use.

Dynamic nano-rod surface fabrication. Metallic nano-rods generate surface plasmon resonance behaviour which is geometry, material and surrounding index dependent. This resonant behaviour produces large scattering cross-sections (many times greater than the actual physical area of the nano-rods) that are wavelength and polarisation dependent. Such nano-strucutres have been shown to have many potential applications, not only structural colour[17, 13, 58], but also flat optics [20, 57] and even holograms [12]. However, like the structural colour generated by plasmonic nano-holes, the ability of nano-rods to alter the phase and amplitude of incoming radiation suffers from the fact that the metasurfaces are static, and their optical properties may not be altered post fabrication. To dynamically alter the optical properties, mechanical deformation of the surface was chosen as a potential avenue. For this to be possible the substrate, upon which the nano-structures are patterned onto, would need to be pliable. Given its previous use in electric and optic applications, PDMS was chosen as the elastomeric substrate. It has a wide operating temperature range, low absorption in the visible wavelength range and has a highly elastic nature. In ***chapter 5*** a new facile process for fabricating aluminium nano-rod structures embedded in PDMS was presented. The process was found to be simpler and transfer smaller nano-particles than similar existing processes. The process was able to transfer nano-particles down to 100nm in size with a pitch as low as 200nm. The limitation found in the work was the same as the feature size limitation of the patterning recipe and may not be due to limitations of the transfer process itself . The process is currently only suitable for aluminium due to the fact excess metal is transferred during the process. This may easily be removed with a soak in a Decon90 bath, which dissolves the excess Al leaving the PDMS and embedded nano-rods unharmed. The process may transfer other metals but a suitable bath needs to be found to dissolve the excess metal transferred before the process is suitable.

Dynamic Plasmonic Colour pixel by mechanical deformation. Having established a new fabrication process for embedding metallic nano-rods in an elastomeric medium with a high spatial accuracy, the process was applied to creating structural colour which may be modified by the application of a strain to the substrate of the device. The device could potentially be applied in fields such as camouflage, sensing, and displays. In ***chapter 5*** the design of structural colour using nano-rods embedded in PDMS is summarised and compared to that created by nano-hole layers in chapter 4. The nano-rod arrays having been fabricated in PDMS were characterised using a polarising optical microscope setup, with and without a strain applied to the substrate. The patterns showed a significant shift in colour due to mechanical deformation that fitted well with the FDTD modelled results.

A dynamic focal length plasmonic lens. A novel application for metallic nano-structures is in the form of ultra-thin diffractive optical elements such as lenses. Using the unique pattern transfer developed in this thesis dynamic optical zone plates (diffractive lenses, in the form of Fresnel zone plates and photon sieves) were realised in ***chapter 5***. The lenses focus light using transparent and opaque zones to diffract light to a single point at the desired focal length. The transparent and opaque zones are circular, and it is the physical size and spacing of the zones that determine the focal length of the lens. Using plasmonic nano-rod scatters as the fundamental elements of pixels comprising the opaque zones, flat optical lenses were fabricated in PDMS. The focal length and optical power along the axis of light propagation were recorded using a custom optical setup, with and without strain applied to the lens. The change in focal length due to mechanical deformation was found to be proportional to the square of the strain applied, as theory predicts.

Dynamic hologram replay field by mechanical deformation. The wavelength and polarisation dependency of the plasmonic resonances in metallic nano-rods in the near field is transferred into the far field. The results is that nano-rods may be used as scattering elements for holograms with sub-wavelength sized pixels. The result has been used to design metasurfaces of sub-wavelength pixels consisting of nano-rod scatterers to create wavelength and polarisation dependent holograms that produce different far-field images depending on the wavelength and polarisation of the illuminating radiation. By fabricating holograms utilising metallic nano-rods in PDMS in ***chapter 5*** it is experimentally demonstrated that as the pitch of the holograms pixels is altered, so the size of the pixels in the replay field changes with an inversely proportional relationship. The ability to fabricate plasmonic holograms in an elastomeric medium opens up a myriad of opportunities to develop holograms whose replay field may change when the hologram is physically stretched, due to the wavelength, polarisation and proximity dependence of the plasmonic resonance of the nano-rods. The design of pixels whose plasmonic resonance is altered by mechanical deformation was discussed and FDTD simulated pixels were presented. The results show the potential of mechanical deformation of nano-rod array to create dynamic hologram pixels.

6.2 Future work and outlook

Only the surface of the huge potential of dynamic plasmonic metasurfaces has been scratched in this work. What this thesis has shown is that it is possible to create dynamic plasmonic devices, and that these devices have the ability to fit into modern display devices. However, the experimental demonstrations show a proof-of-concept and are far from the final product. The significant amount of computational modelling that has gone into this thesis can, one hopes, diminish the time someone looking to continue the work has to spend on FDTD simulations for the initial design stage of such plasmonic devices and the following are some suggested next steps to take the work presented here to the next stage.

- *Pixel size limitation of nano-hole colour pixels* With dynamic pixels having been demonstrated, the size limitations of both the continuously tunable plasmonic pixel and twisted nematic plasmonic grating cell need to be tested. There will be limitations not only in terms of cross-talk between adjacent pixels, but also of the surface alignment of the LCs to the nano-structures.

- *Increasing the colour gamut* If one were to plot the colours from a regular rectangular array of rectangular nano-holes in a continuously tunable LC-nanohole pixel on a chromaticity diagram, the coverage would be limited to relatively near the centre of the diagram. The reason for this is due to the broad peaks of the experimentally measured transmission spectra. It has been shown in static structural colour pixels that this may be improved using a triangular array [69], which may be applied to the pixels demonstrated in this thesis. Furthermore, the double grating that was shown to improve the vividicity of colours in the twisted nematic device, may also be applied to the continuously tunable nano-hole pixels. Further work is needed to understand the plasmonic and non-plasmonic resonant modes in these structures to aid the progress of this genre of plasmonic pixels.

- *Alternate electro-optic substrates* Whilst the potential of using an electro-optic substrate to tune the plasmonic resonance of a metallic nano-structured surface was demonstrated in theoretical terms using FDTD analysis, the practical implementation was far from successful, with reasons cited including prohibitively large electric fields and fabrication difficulties. If a substrate with a larger electro-optic coefficient could be found, lower electric fields would be needed, and greater movements in the plasmonic resonances may be found. Furthermore fabrication techniques could be developed to encase the nano-structures in the electro-optic substrate, removing the static surface plasmon modes due to the metallic-surrounding medium interface.

- *Development of the PDMS pattern transfer process* There are two main drawbacks of the PDMS pattern transfer process for metallic nano-rods developed in this thesis as it currently stands. The first is the size limitation of nano-rods that may be transferred. This is as much as a constraint of the EBL process as it is the pattern transfer process. Currently ma-N 2405 negative tone resist is used. After spinning the resist layer to be patterned is $\sim$ 400nm thick. High aspect ratio resist pillars will simply fall over once developed, limiting the resolution achievable. By using a different resist, narrower resist pillars may be fabricated, and the feature size limitations of the pattern transfer process may be tested further. The second limitation of the process is that it is limited to one plasmonic metal, aluminium. The process itself will transfer other metals such as Ag, however it is limited by the fact that excess metal transferred, that is not part of the desired nano-rod pattern may not be removed, and efforts so far using nitric acid have not only removed the excess metal, but the Ag nano-rods too. A more dilute acid solution, a mixture of acids, or even sputtering the metal and determining methods of fracturing resist pillars should be explored to maximise the potential of the transfer process and the applications for which it may be used. One of the main advantages for developing the pattern process with Ag is that the size of Ag nano-rods resonant in the visible wavelengths is smaller than those of Al, allowing for greater pixel element densities.

- *Alternative polymers for transfer* PDMS is an excellent polymer for allowing the dynamic tuning of the pitch of plasmonic metasurface. There do however exist polymers, with anisotropic properties, whose optical properties may be altered under application of heat, illumination or by absorption of a solvent. These polymers are called *liquid crystal elastomers* (LCEs), composed of cross-linked polymer chains that are also liquid crystalline. The first step here is to see if the pattern transfer process is compatible with LCEs and if not whether it may be altered to be so. Following evaluation of the compatibility with the transfer process, the applications of combining LCEs with nano-rod arrays may be investigated, with potential routes including their application to devices explored in this thesis such as enhancement of dynamic structural colour and plasmonic holographic pixel switching.

- *Plasmonic holographic switching by mechanical deformation* In ***chapter 5*** the potential for mechanical deformation to alter the plasmonic resonance of a composite scattering pixel element was demonstrated using FDTD simulations. The next step is to fabricate the holograms and test to see if the simulated results can be replicated experimentally. Currently a hologram whose replay field may be altered by mechanical deformation uses a hologram with a 3D replay field with several focal planes. By deforming the hologram, the image in the plane of the camera sensor is changed[134]. This process does not rely on altering the resonance of the individual scattering elements and requires a precise viewing plane to see the switching. Should the experimental results match those modelled, the tuning of the plasmonic scattering of composite pixels would demonstrate a totally new kind of multiplexed hologram.

The suggestions here are but a few routes that may be taken towards the goal of developing dynamic plasmonic metasurfaces in the visible spectrum. As more ways emerge to reliably fabricate nano-sized metallic structures and ways to dynamically exploit their optical properties are found the field will continue to grow.

References

[1] Richard Bartholomew, Calum Williams, Ammar Khan, Richard Bowman, and Timothy Wilkinson. Plasmonic nanohole electrodes for active color tunable liquid crystal transmissive pixels. *Optics Letters*, 42(14):2810, jul 2017.

[2] Jason Geng. Three-dimensional display technologies. *Advances in Optics and Photonics*, 5(4):456, dec 2013.

[3] E a Edirisinghe and J Jiang. Stereo Imaging, An Emerging Technology. In *Proceedings of SSGRR 2000: international conference on advances in infrastructure for E-business, science, and education on the internet*, 2000.

[4] Ozan Cakmakci and Jannick Rolland. Head-Worn Displays: A Review. *Journal of Display Technology*, 2(3):199–216, sep 2006.

[5] Tom Peterka, R.L. Kooima, D.J. Sandin, Andrew Johnson, Jason Leigh, and T.A. DeFanti. Advances in the Dynallax Solid-State Dynamic Parallax Barrier Autostereoscopic Visualization Display System. *IEEE Transactions on Visualization and Computer Graphics*, 14(3):487–499, may 2008.

[6] Armin Schwerdtner and Holger Heidrich. The Dresden 3D Display (D4D) Abstract. In Mark T. Bolas, Scott S. Fisher, and John O. Merritt, editors, *Photonics West'98 Electronic Imaging*, volume 3295, pages 203–210, apr 1998.

[7] David M Hoffman, Ahna R Girshick, Kurt Akeley, and Martin S Banks. Vergence-accommodation conflicts hinder visual performance and cause visual fatigue. *Journal of vision*, 8(3):33.1–30, 2008.

[8] Kalluri Sarma. Recent developments in stereoscopic and holographic 3D display technologies. In Daniel D. Desjardins, Kalluri R. Sarma, Peter L. Marasco, Paul R. Havig, Michael P. Browne, and James E. Melzer, editors, *Proc. SPIE 9086, Display Technologies and Applications for Defense, Security, and Avionics VIII; and Head- and Helmet-Mounted Displays XIX, 908606*, volume 9086, page 908606, jun 2014.

[9] Robert Patterson. Review Paper: Human factors of stereo displays: An update. *Journal of the Society for Information Display*, 17(12):987, 2009.

[10] Cees van Berkel, David W Parker, and Anthony R Franklin. Multiview 3D-LCD. In Mark T. Bolas, Scott S. Fisher, and John O. Merritt, editors, *SPIE Proccedings*, volume 39, pages 32–39, apr 1996.

[11] Richard Stahl, Veronique Rochus, Xavier Rottenberg, Stefan Cosemans, Luc Haspeslagh, Simone Severi, Geert Van Der Plas, Gauthier Lafruit, and Stephane Donnay. Modular sub-wavelength diffractive light modulator for high-definition holographic displays. *Journal of Physics: Conference Series*, 415:012057, feb 2013.

[12] Yunuen Montelongo, Jaime Oscar Tenorio-Pearl, Calum Williams, Shuang Zhang, William Ireland Milne, and Timothy David Wilkinson. Plasmonic nanoparticle scattering for color holograms. *Proceedings of the National Academy of Sciences*, 111(35):12679–12683, sep 2014.

[13] Mehdi Keshavarz Hedayati and Mady Elbahri. Review of Metasurface Plasmonic Structural Color. *Plasmonics*, pages 1–17, oct 2016.

[14] Richard O. Prum, Randall L. Morrison, and Gary R. Ten Eyck. Structural color production by constructive reflection from ordered collagen arrays in a bird (Philepitta castanea: Eurylaimidae). *Journal of Morphology*, 222(1):61–72, oct 1994.

[15] Peter Vukusic, Roy Sambles, Christopher Lawrence, and Gavin Wakely. Sculpted-multilayer optical effects in two species of Papilio butterfly. *Applied Optics*, 40(7):1116, mar 2001.

[16] Tanu Suryadi Kustandi, Hong Yee Low, Jing Hua Teng, Isabel Rodriguez, and Rui Yin. Mimicking Domino-Like Photonic Nanostructures on Butterfly Wings. *Small*, 5(5):574–578, mar 2009.

[17] Yinghong Gu, Lei Zhang, Joel K W Yang, Swee Ping Yeo, and Cheng-Wei Qiu. Color generation via subwavelength plasmonic nanostructures. *Nanoscale*, 7(15):6409–19, 2015.

[18] P. Hariharan. Optical Holography: Principles, Techniques, and Applications, 1996.

[19] D. Gabor. A New Microscopic Principle. *Nature*, 161(4098):777–778, may 1948.

[20] Nanfang Yu and Federico Capasso. Flat optics with designer metasurfaces. *Nature Materials*, 13(2):139–150, jan 2014.

[21] Lumerical. Lumerical Solutions, Inc. www.lumerical.com/tcad-products/fdtd/.

[22] Paolo Biagioni, Jer-Shing Huang, and Bert Hecht. Nanoantennas for visible and infrared radiation. *Reports on Progress In Physics*, 024402:76, 2011.

[23] Stefan a. Maier. Plasmonics: Metal nanostructures for subwavelength photonic devices. *IEEE Journal on Selected Topics in Quantum Electronics*, 12(6):1214–1220, 2006.

[24] C F Bohren and D R Huffman. *Absorption and scattering of light by small particles*, volume 1. Wiley-VCH Verlag GmbH, 1983.

[25] Jacob B Khurgin. How to deal with the loss in plasmonics and metamaterials. *Nature Publishing Group*, 10(1):2–6, 2015.

[26] Jacob B. Khurgin and Greg Sun. Scaling of losses with size and wavelength in nanoplasmonics and metamaterials. *Applied Physics Letters*, 99(21):211106, nov 2011.

[27] William L Barnes, Alain Dereux, and Thomas W Ebbesen. Surface plamons subwavelength optics. *Nature*, 424(August):824–830, 2003.

[28] Andreas Otto. Excitation of nonradiative surface plasma waves in silver by the method of frustrated total reflection. *Zeitschrift fur Physik*, 216(4):398–410, 1968.

[29] B. Hecht, H. Bielefeldt, L. Novotny, Y. Inouye, and D. Pohl. Local Excitation, Scattering, and Interference of Surface Plasmons. *Physical Review Letters*, 77(9):1889–1892, 1996.

[30] H. Ditlbacher, J. R. Krenn, N. Felidj, B. Lamprecht, G. Schider, M. Salerno, A. Leitner, and F. R. Aussenegg. Fluorescence imaging of surface plasmon fields. *Applied Physics Letters*, 80(3):404–406, 2002.

[31] R. H. Ritchie, E. T. Arakawa, J. J. Cowan, and R. N. Hamm. Surface-plasmon resonance effect in grating diffraction. *Physical Review Letters*, 21(22):1530–1533, 1968.

[32] J R Sambles, G W Bradbery, and F Z Yang. Optical excitation of surface plasmons: an introduction. *Contemporary Physics*, 32(3):173–183, 1991.

[33] P. Drude. Zur Elektronentheorie der Metalle; II. Teil. Galvanomagnetische und thermomagnetische Effecte. *Annalen der Physik*, 308(11):369–402, 1900.

[34] A. Sommerfeld. Zur Elektronentheorie der Metalle auf Grund der Fermischen Statistik - I. *Zeitschrift fur Physik*, 47(1-2):1–32, 1928.

[35] A. Sommerfeld. Zur Elektronentheorie der Metalle auf Grund der Fermischen Statistik - II. *Zeitschrift fur Physik*, 47(1-2):43–60, 1928.

[36] Manuel R Gonçalves. Plasmonic nanoparticles: fabrication, simulation and experiments. *Journal of Physics D: Applied Physics*, 47:213001, 2014.

[37] Alessandro Alabastri, Salvatore Tuccio, Andrea Giugni, Andrea Toma, Carlo Liberale, Gobind Das, Francesco De Angelis, Enzo Di Fabrizio, and Remo Proietti Zaccaria. Molding of plasmonic resonances in metallic nanostructures: Dependence of the non-linear electric permittivity on system size and temperature. *Materials*, 6(11):4879–4910, 2013.

[38] Edward D. Palik. *Handbook of Optical Constants of Solids*, volume 2. Academic Press, 1991, 1991.

[39] Aleksandra B Djuris, Jovan M Elazar, Marian L Majewski, a D Rakic, and a B Djurisic. Optical properties of metallic films for vertical-cavity optoelectronic devices. *Applied optics*, 37(22):5271–83, 1998.

[40] Davy Gérard and Stephen K Gray. Aluminium plasmonics. *Journal of Physics D: Applied Physics*, 48(18):184001, 2015.

[41] Gururaj V. Naik, Vladimir M. Shalaev, and Alexandra Boltasseva. Alternative plasmonic materials: Beyond gold and silver. *Advanced Materials*, 25(24):3264–3294, 2013.

[42] Jacob B. Khurgin and Alexandra Boltasseva. Reflecting upon the losses in plasmonics and metamaterials. *MRS Bulletin*, 37(August):768–779, 2012.

[43] Paul R. West, Satoshi Ishii, Gururaj V. Naik, Naresh K. Emani, Vladimir M. Shalaev, and Alexandra Boltasseva. Searching for better plasmonic materials. *Laser and Photonics Reviews*, 4(6):795–808, 2010.

[44] D. A. Bobb, G. Zhu, M. Mayy, A. V. Gavrilenko, P. Mead, V. I. Gavrilenko, and M. A. Noginov. Engineering of low-loss metal for nanoplasmonic and metamaterials applications. *Applied Physics Letters*, 95(15):1–4, 2009.

[45] M G Blaber, M D Arnold, and M J Ford. A review of the optical properties of alloys and intermetallics for plasmonics. *Journal of physics. Condensed matter : an Institute of Physics journal*, 22(14):143201, 2010.

[46] Gururaj V. Naik, Jeremy Schroeder, Xingjie Ni, Alexander Kildishev, Timothy Sands, and Alexandra Boltasseva. Titanium nitride as a plasmonic material for visible and near-infrared wavelengths. *Optical Materials Express*, 2:478–489, 2012.

[47] Yu Yao, Raji Shankar, Mikhail A Kats, Yi Song, Jing Kong, Marko Loncar, and Federico Capasso. Electrically tunable metasurface perfect absorbers for ultrathin mid-infrared optical modulators. *Nano letters*, 14(11):6526–32, nov 2014.

[48] W T Cathey. Phase Holograms , Phase-Only Holograms , and Kinoforms. *Applied optics*, 9(6):1478–1479, 1970.

[49] Janglin Chen, Wayne Cranton, and Mark Fihn. *Handbook of Visual Display Technology.* Springer Berlin Heidelberg, Berlin, Heidelberg, 2012.

[50] Joseph W. Goodman. Introduction to Fourier Optics, Second Edition. *Optical Engineering*, 35(5):1513, may 1996.

[51] A. Giuseppe, Patrick Verdonck, D. Ronaldo, Jose C. Pizolato Jr., B. Daniel, and G. Luiz. Digital Holography: Computer-Generated Holograms and Diffractive Optics in Scalar Diffraction Domain. In *Holography - Different Fields of Application*, chapter 2, pages 29–52. InTech, sep 2011.

[52] G Tricoles. Computer generated holograms: an historical review. *Applied Optics*, 26(20):4351, 1987.

[53] Ting-Chung Poon and Jung-Ping Liu. *Introduction to Modern Digital Holography.* Cambridge University Press, 2014.

[54] B R Brown and A W Lohmann. Computer-generated Binary Holograms*. *IBM J. Res. Develop.*, 13(2):160–168, 1969.

[55] Merck Performance Materials Website. Appearance of Liquid Crystal Phases in a Temperature Profile.

[56] Yanxia Cui, Yingran He, Yi Jin, Fei Ding, Liu Yang, Yuqian Ye, Shoumin Zhong, Yinyue Lin, and Sailing He. Plasmonic and metamaterial structures as electromagnetic absorbers. *Laser & Photonics Reviews*, 8(4):495–520, jul 2014.

[57] Lei Zhang, Shengtao Mei, Kun Huang, and Cheng-wei Qiu. Advances in Full Control of Electromagnetic Waves with Metasurfaces. *Advanced Optical Materials*, 4(6):818–833, 2016.

[58] Anders Kristensen, Joel K. W. Yang, Sergey I. Bozhevolnyi, Stephan Link, Peter Nordlander, Naomi J. Halas, and N. Asger Mortensen. Plasmonic colour generation. *Nature Reviews Materials*, 2(1):16088, nov 2016.

[59] Guangyuan Si, Yanhui Zhao, Jiangtao Lv, Mengqian Lu, Fengwen Wang, Hailong Liu, Ning Xiang, Tony Jun Huang, Aaron J Danner, Jinghua Teng, and Yan Jun Liu. Reflective plasmonic color filters based on lithographically patterned silver nanorod arrays. *Nanoscale*, 5(14):6243–8, 2013.

[60] Tal Ellenbogen, Kwanyong Seo, and Kenneth B. Crozier. Chromatic plasmonic polarizers for active visible color filtering and polarimetry. *Nano Letters*, 12(2):1026–1031, 2012.

[61] Jana Olson, Alejandro Manjavacas, Lifei Liu, Wei-Shun Chang, Benjamin Foerster, Nicholas S. King, Mark W. Knight, Peter Nordlander, Naomi J. Halas, and Stephan Link. Vivid, full-color aluminum plasmonic pixels. *Proceedings of the National Academy of Sciences*, 111(40):14348–14353, oct 2014.

[62] Beibei Zeng, Yongkang Gao, and Filbert J Bartoli. Ultrathin Nanostructured Metals for Highly Transmissive Plasmonic Subtractive Color Filters. *Scientific Reports*, 3:2840, oct 2013.

[63] M. Ye, X. L. Hu, L. B. Sun, B. Shi, Y. Xu, L. S. Wang, J. Zhao, Y. Q. Wu, S. M. Yang, R. Z. Tai, J. Z. Jiang, and D. X. Zhang. Duty cycle dependency of the optical transmission spectrum in an ultrathin nanostructured Ag film. *Journal of Alloys and Compounds*, 621:244–249, 2015.

[64] Alex F. Kaplan, Ting Xu, and L. Jay Guo. High efficiency resonance-based spectrum filters with tunable transmission bandwidth fabricated using nanoimprint lithography. *Applied Physics Letters*, 99(14), 2011.

[65] Dennis W. Dobbs, Irena Gershkovich, and Brian T. Cunningham. Fabrication of a graded-wavelength guided-mode resonance filter photonic crystal. *Applied Physics Letters*, 89(12), 2006.

[66] C Genet and T W Ebbesen. Light in tiny holes. *Nature*, 445(7123):39–46, 2007.

[67] H. F. Ghaemi, Tineke Thio, D. Grupp, T. W. Ebbesen, and H. J. Lezec. Surface plasmons enhance optical transmission through subwavelength holes. *Physical Review B*, 58(11):6779–6782, 1998.

[68] Sozo Yokogawa, Stanley P. Burgos, and Harry A. Atwater. Plasmonic color filters for CMOS image sensor applications. *Nano Letters*, 12(8):4349–4354, 2012.

[69] Daisuke Inoue, Atsushi Miura, Tsuyoshi Nomura, Hisayoshi Fujikawa, Kazuo Sato, Naoki Ikeda, Daiju Tsuya, Yoshimasa Sugimoto, and Yasuo Koide. Polarization independent visible color filter comprising an aluminum film with surface-plasmon enhanced transmission through a subwavelength array of holes. *Applied Physics Letters*, 98(9):2–5, 2011.

[70] Zhibo Li, Alasdair W. Clark, and Jonathan M. Cooper. Dual Color Plasmonic Pixels Create a Polarization Controlled Nano Color Palette. *ACS Nano*, 10(1):492–498, jan 2016.

[71] Zhongyang Li, Serkan Butun, and Koray Aydin. Large-Area, Lithography-Free Super Absorbers and Color Filters at Visible Frequencies Using Ultrathin Metallic Films. *ACS Photonics*, 2(2):183–188, feb 2015.

[72] Ting Xu, Yi-Kuei Wu, Xiangang Luo, and L Jay Guo. Plasmonic nanoresonators for high-resolution colour filtering and spectral imaging. *Nature communications*, 1(5):59, 2010.

[73] Wen-Di Li, Jonathan Hu, and Stephen Y. Chou. Extraordinary light transmission through opaque thin metal film with subwavelength holes blocked by metal disks. *Optics Express*, 19(21):21098, 2011.

[74] Karthik Kumar, Huigao Duan, Ravi S Hegde, Samuel C W Koh, Jennifer N Wei, and Joel K W Yang. Printing colour at the optical diffraction limit. *Nature Nanotechnology*, 7(9):557–561, 2012.

[75] Shawn J. Tan, Lei Zhang, Di Zhu, Xiao Ming Goh, Ying Min Wang, Karthik Kumar, Cheng-Wei Qiu, and Joel K. W. Yang. Plasmonic Color Palettes for Photorealistic Printing with Aluminum Nanostructures. *Nano Letters*, 14(7):4023–4029, jul 2014.

[76] Xiao Ming Goh, Yihan Zheng, Shawn J. Tan, Lei Zhang, Karthik Kumar, Cheng-Wei Qiu, and Joel K. W. Yang. Three-dimensional plasmonic stereoscopic prints in full colour. *Nature Communications*, 5:5361, nov 2014.

[77] Fei Cheng, Jie Gao, Liliana Stan, Daniel Rosenmann, David Czaplewski, and Xiaodong Yang. Aluminum plasmonic metamaterials for structural color printing. *Optics express*, 23(11):14552–60, 2015.

[78] Alexander S. Roberts, Anders Pors, Ole Albrektsen, and Sergey I. Bozhevolnyi. Subwavelength plasmonic color printing protected for ambient use. *Nano Letters*, 14(2):783–787, 2014.

[79] Nanfang Yu, Patrice Genevet, Mikhail a Kats, Francesco Aieta, Jean-Philippe Tetienne, Federico Capasso, and Zeno Gaburro. Light Propagation with Phase Discontinuities Reflection and Refraction. *Science*, 334(October):333–337, 2011.

[80] Francesco Aieta, Patrice Genevet, Mikhail A. Kats, Nanfang Yu, Romain Blanchard, Zeno Gaburro, and Federico Capasso. Aberration-Free Ultrathin Flat Lenses and Axicons at Telecom Wavelengths Based on Plasmonic Metasurfaces. *Nano Letters*, 12(9):4932–4936, sep 2012.

[81] Nanfang Yu, Francesco Aieta, Patrice Genevet, Mikhail A. Kats, Zeno Gaburro, and Federico Capasso. A broadband, background-free quarter-wave plate based on plasmonic metasurfaces. *Nano Letters*, 12(12):6328–6333, 2012.

[82] Shulin Sun, Kuang-yu Yang, Chih-ming Wang, Ta-ko Juan, Wei Ting Chen, Chun Yen Liao, Qiong He, Shiyi Xiao, Wen-ting Kung, Guang-yu Guo, Lei Zhou, and Din Ping Tsai. High-Efficiency Broadband Anomalous Reflection by Gradient Meta-Surfaces. *Nano Letters*, 12(12):6223–6229, dec 2012.

[83] Nanfang Yu and Federico Capasso. Flat optics: Controlling wavefronts with optical antenna metasurfaces. In *2013 IEEE Antennas and Propagation Society International Symposium (APSURSI)*, volume 19, pages 2341–2342. IEEE, 2013.

[84] Yang Zhao and Andrea Alù. Tailoring the Dispersion of Plasmonic Nanorods To Realize Broadband Optical Meta-Waveplates. *Nano Letters*, 13(3):1086–1091, mar 2013.

[85] Xingjie Ni, Alexander V Kildishev, and Vladimir M Shalaev. Metasurface holograms for visible light. *Nature Communications*, 4:2807, 2013.

[86] Kun Huang, Hong Liu, Francisco J. Garcia-Vidal, Minghui Hong, Boris Luk'yanchuk, Jinghua Teng, and Cheng-Wei Qiu. Ultrahigh-capacity non-periodic photon sieves operating in visible light. *Nature Communications*, 6(May):7059, 2015.

[87] Guoxing Zheng, Holger Mühlenbernd, Mitchell Kenney, Guixin Li, Thomas Zentgraf, and Shuang Zhang. Metasurface holograms reaching 80% efficiency. *Nature Nanotechnology*, 10(4):308–312, feb 2015.

[88] Wei Ting Chen, Kuang-Yu Yang, Chih-Ming Wang, Yao-Wei Huang, Greg Sun, I-Da Chiang, Chun Yen Liao, Wei-Lun Hsu, Hao Tsun Lin, Shulin Sun, Lei Zhou, Ai Qun Liu, and Din Ping Tsai. High-Efficiency Broadband Meta-Hologram with Polarization-Controlled Dual Images. *Nano Letters*, 14(1):225–230, jan 2014.

[89] Dandan Wen, Fuyong Yue, Guixin Li, Guoxing Zheng, Kinlong Chan, Shumei Chen, Ming Chen, King Fai Li, Polis Wing Han Wong, Kok Wai Cheah, Edwin Yue Bun Pun, Shuang Zhang, and Xianzhong Chen. Helicity multiplexed broadband metasurface holograms. *Nature Communications*, 6(May):8241, 2015.

[90] Ting Xu, Erich C. Walter, Amit Agrawal, Christopher Bohn, Jeyavel Velmurugan, Wenqi Zhu, Henri J. Lezec, and A. Alec Talin. High-contrast and fast electrochromic switching enabled by plasmonics. *Nature Communications*, 7:10479, jan 2016.

[91] Guoping Wang, Xuechen Chen, Sheng Liu, Chingping Wong, and Sheng Chu. Mechanical Chameleon through Dynamic Real-Time Plasmonic Tuning. *ACS Nano*, 10(2):1788–1794, feb 2016.

[92] Oleksandr Buchnev, Nina Podoliak, Malgosia Kaczmarek, Nikolay I Zheludev, and Vassili A Fedotov. Electrically Controlled Nanostructured Metasurface Loaded with Liquid Crystal: Toward Multifunctional Photonic Switch. *Advanced Optical Materials*, 3(5):674–679, 2015.

[93] Daniel Franklin, Yuan Chen, Abraham Vazquez-Guardado, Sushrut Modak, Javaneh Boroumand, Daming Xu, Shin-tson Wu, and Debashis Chanda. Polarization-independent actively tunable colour generation on imprinted plasmonic surfaces. *Nature Communications*, 6:7337, jun 2015.

[94] Calum Williams, Yunuen Montelongo, Jaime Oscar Tenorio-Pearl, Andrea Cabrero-Vilatela, Stephan Hofmann, William I. Milne, and Timothy D. Wilkinson. Engineered pixels using active plasmonic holograms with liquid crystals. *Physica Status Solidi - Rapid Research Letters*, 9(2):125–129, 2015.

[95] Imogen M. Pryce, Koray Aydin, Yousif A. Kelaita, Ryan M. Briggs, and Harry A. Atwater. Highly strained compliant optical metamaterials with large frequency tunability. *Nano Letters*, 10(10):4222–4227, 2010.

[96] Xueming Li, Lei Wei, René H Poelma, Sten Vollebregt, Jia Wei, Hendrik Paul Urbach, Pasqualina M Sarro, and Guo Qi Zhang. Stretchable Binary Fresnel Lens for Focus Tuning. *Scientific Reports*, 6:25348, 2016.

[97] Li Zhu, Jonas Kapraun, James Ferrara, and Connie J Chang-Hasnain. Flexible photonic metastructures for tunable coloration. *Optica*, 2(3):255–258, 2015.

[98] John B Schneider. Understanding the Finite-Difference Time-Domain Method. *Self Published*, 2012.

[99] Kane S Yee. Numerical Solution of Initial Boundary Value Problems Involving Maxwell's Equations in Isotropic Media. *Antennas and Propagation*, 14(3):302 – 307, 1966.

[100] L Kipp, M Skibowski, R L Johnson, R Berndt, R Adelung, S Harm, and R Seemann. Sharper images by focusing soft X-rays with photon sieves. *Nature*, 414(6860):184–188, 2001.

[101] Geoff Andersen. Large optical photon sieve. *Optics letters*, 30(22):2976–2978, 2005.

[102] Micro resist technology. Negative Tone Photoresist Series ma-N 2400 - Processing Guidlines - www.microresist.de, 2003.

[103] Alee N. Broers, A. C F Hoole Andrew C.F, and Joseph M. Ryan. Electron beam lithography - Resolution limits. *Microelectronic Engineering*, 32(1-4 SPEC. ISS.):131–142, 1996.

[104] Marie Angelopoulos, Jane M Shaw, and Kam-leung Lee. Conducting Polymers as Lithographic Materials. *Polymer Engineering and Science*, 32(20):1535–1540, 1992.

[105] Calum Williams, Richard Bartholomew, Girish Rughoobur, George S D Gordon, Andrew J Flewitt, and Timothy D Wilkinson. Fabrication of nanostructured transmissive optical devices on ITO-glass with UV1116 photoresist using high-energy electron beam lithography. *Nanotechnology*, 27(48):485301, dec 2016.

[106] Khairudin Mohamed, M.M. Alkaisi, and R.J. Blaikie. Surface charging suppression using PEDOT/PSS in the fabrication of three dimensional structures on a quartz substrate. *Microelectronic Engineering*, 86(4-6):535–538, apr 2009.

[107] R Dylewicz, S Lis, R.M. De La Rue, and F Rahman. Charge dissipation layer based on conductive polymer for electron-beam patterning of bulk zinc oxide. *Electronics Letters*, 46(14):1025, 2010.

[108] Benoît Charlot, Gilbert Sassine, Alexandra Garraud, Brice Sorli, Alain Giani, and Philippe Combette. Micropatterning PEDOT:PSS layers. *Microsystem Technologies*, 19(6):895–903, jun 2013.

[109] REO. Understanding Thin Film Process Technologies - REO Precision Optical Solutions - http://www.reoinc.com/technical-resources/cat/78/technical-tutorials.

[110] Hiap Liew Ong, Alan J. Hurd, and Robert B. Meyer. Alignment of nematic liquid crystals by inhomogeneous surfaces. *Journal of Applied Physics*, 57(2):186–192, 1985.

[111] Ho-Seok Ee and Ritesh Agarwal. Tunable Metasurface and Flat Optical Zoom Lens on a Stretchable Substrate. *Nano Letters*, 16(4):2818–2823, apr 2016.

[112] Yongmin Park, Kwanseop Lim, Nokyoung Park, Jin Ho Kimi, and Jong Hoon Hahn. Metal thin-film micropatterns transfer on pdms and its application to capillary electrophoresis electrochemical detection on pdms microchip. *October*, 2003.

[113] Ke Du, Ishan Wathuthanthri, Yuyang Liu, Wei Xu, and Chang Hwan Choi. Wafer-scale pattern transfer of metal nanostructures on polydimethylsiloxane (PDMS) substrates via holographic nanopatterns. *ACS Applied Materials and Interfaces*, 4(10):5505–5514, 2012.

[114] O Buchnev, J Y Ou, M Kaczmarek, N I Zheludev, and V a Fedotov. Electro-optical control in a plasmonic metamaterial hybridised with a liquid-crystal cell. *Optics express*, 21(2):1633–8, 2013.

[115] Hyoki Kim, Jianping Ge, Junhoi Kim, Sung-eun Choi, Hosuk Lee, Howon Lee, Wook Park, Yadong Yin, and Sunghoon Kwon. Structural colour printing using a magnetically tunable and lithographically fixable photonic crystal. *Nature Photonics*, 3(9):534–540, 2009.

[116] Yichen Shen, Veronika Rinnerbauer, Imbert Wang, Veronika Stelmakh, John D. Joannopoulos, and Marin Soljačić. Structural colors from fano resonances. *ACS Photonics*, 2(1):27–32, 2015.

[117] T.W. Ebbesen, H. J. Lezec, H. F. Ghaemi, T. Thio, P. A.Wolff, T. Thio, and P. A.Wolff. Extraordinary optical transmission through sub-wavelength hole arrays. *Nature*, 86(6):1114–7, 1998.

[118] Vivek Raj Shrestha, Sang-Shin Lee, Eun-Soo Kim, and Duk-Yong Choi. Polarization-tuned Dynamic Color Filters Incorporating a Dielectric-loaded Aluminum Nanowire Array. *Scientific Reports*, 5(1):12450, dec 2015.

[119] Qin Chen and David R. S. Cumming. High transmission and low color cross-talk plasmonic color filters using triangular-lattice hole arrays in aluminum films. *Optics Express*, 18(13):14056, 2010.

[120] Luc Duempelmann, Angélique Luu-Dinh, Benjamin Gallinet, and Lukas Novotny. Four-Fold Color Filter Based on Plasmonic Phase Retarder. *ACS Photonics*, 3(2):190–196, feb 2016.

[121] Benny Walther, Christian Helgert, Carsten Rockstuhl, Frank Setzpfandt, Falk Eilenberger, Ernst Bernhard Kley, Falk Lederer, Andreas Tünnermann, and Thomas Pertsch. Spatial and spectral light shaping with metamaterials. *Advanced Materials*, 24(47):6300–6304, 2012.

[122] Ibrahim Abdulhalim. Liquid crystal active nanophotonics and plasmonics: from science to devices. *Journal of Nanophotonics*, 6(1):061001, 2012.

[123] Jana Olson, Alejandro Manjavacas, Tiyash Basu, Da Huang, Andrea E. Schlather, Bob Zheng, Naomi J. Halas, Peter Nordlander, and Stephan Link. High Chromaticity Aluminum Plasmonic Pixels for Active Liquid Crystal Displays. *ACS Nano*, 10(1):1108–1117, jan 2016.

[124] Julia Braun, Bruno Gompf, Georg Kobiela, and Martin Dressel. How holes can obscure the view: Suppressed transmission through an ultrathin metal film by a subwavelength hole array. *Physical Review Letters*, 103(20):1–4, 2009.

[125] Yuan Zhang, Qingkun Liu, Haridas Mundoor, Ye Yuan, and Ivan I. Smalyukh. Metal nanoparticle dispersion, alignment, and assembly in nematic liquid crystals for applications in switchable plasmonic color filters and E-polarizers. *ACS Nano*, 9(3):3097–3108, 2015.

[126] Chin-yu Chen and Yu-lung Lo. Feasibility study on twisted nematic liquid-crystal cell with two cross-embedded wire-grid polarizers as alignment and electrode for projection displays. *Applied Optics*, 48(34):6558, dec 2009.

[127] S. P. Palto, M. I. Barnik, V. V. Artemov, N. M. Shtykov, A. R. Geivandov, S. G. Yudin, and M. V. Gorkunov. Liquid crystal on subwavelength metal gratings. *Journal of Applied Physics*, 117(22):223108, jun 2015.

[128] A. T. M. Anishur Rahman, Peter Majewski, and Krasimir Vasilev. Extraordinary optical transmission: coupling of the Wood-Rayleigh anomaly and the Fabry-Perot resonance. *Optics Letters*, 37(10):1742, may 2012.

[129] Zhicheng Ye, Lindong Guo, Yi She, Nanling Sun, and Han-ping D. Shieh. 69.2: Compact Colorfilter and Polarizer based on Nanowire Grating for Energy Efficient Display. *SID Symposium Digest of Technical Papers*, 44(1):959–961, jun 2013.

[130] Daniel Maystre. *Plasmonics*, volume 167 of *Springer Series in Optical Sciences*. Springer Berlin Heidelberg, Berlin, Heidelberg, 2012.

[131] S. H. Lim and E. T. Yu. Ultraviolet and solar-blind spectral imaging with subwavelength transmission gratings. *Applied Physics Letters*, 95(16):161107, oct 2009.

[132] R S Weis and T K Gaylord. Lithium Niobate: Summary of Physical Properties and Crystal Strucutre. *Applied Physics A*, pages 191–203, 1985.

[133] K.K. Wong. *Properties of Lithium Niobate*. Institution of Engineering and Technology, sep 2002.

[134] Stephanie C Malek, Ho-seok Ee, and Ritesh Agarwal. Strain Multiplexed Metasurface Holograms on a Stretchable Substrate. *Nano Letters*, 17(6):3641–3645, jun 2017.

[135] Mohammad J. Moghimi, Jayer Fernandes, Aditi Kanhere, and Hongrui Jiang. Micro-Fresnel-Zone-Plate Array on Flexible Substrate for Large Field-of-View and Focus Scanning. *Scientific Reports*, 5:15861, 2015.

[136] Lukas Novotny. Effective wavelength scaling for optical antennas. *Physical Review Letters*, 98(26):1–4, 2007.

[137] Sumeet Walia, Charan M. Shah, Philipp Gutruf, Hussein Nili, Dibakar Roy Chowdhury, Withawat Withayachumnankul, Madhu Bhaskaran, and Sharath Sriram. Flexible metasurfaces and metamaterials: A review of materials and fabrication processes at micro- and nano-scales. *Applied Physics Reviews*, 2(1):011303, mar 2015.

[138] Alexandre Larmagnac, Samuel Eggenberger, Hanna Janossy, and Janos Vörös. Stretchable electronics based on Ag-PDMS composites. *Scientific reports*, 4:7254, 2014.

[139] R W R L Gajasinghe, S U Senveli, S Rawal, a Williams, a Zheng, R H Datar, R J Cote, and O Tigli. Experimental study of PDMS bonding to various substrates for monolithic microfluidic applications. *Journal of Micromechanics and Microengineering*, 24(7):075010, 2014.

[140] Nikolas Chronis, Gang Liu, Ki-Hun Jeong, and Luke Lee. Tunable liquid-filled microlens array integrated with microfluidic network. *Optics Express*, 11(19):2370, sep 2003.

[141] B. Berge and J. Peseux. Variable focal lens controlled by an external voltage: An application of electrowetting. *The European Physical Journal E*, 3(2):159–163, oct 2000.